Conference Proceedings of the Society for Experimental Mechanics Series

Gyaneshwar Tandon *Editor*

Composite, Hybrid, and Multifunctional Materials, Volume 4

Proceedings of the 2014 Annual Conference on Experimental and Applied Mechanics

SEM

Springer

Conference Proceedings of the Society for Experimental Mechanics Series

Series Editor
Tom Proulx
Society for Experimental Mechanics, Inc.
Bethel, CT, USA

For further volumes:
http://www.springer.com/series/8922

Gyaneshwar Tandon
Editor

Composite, Hybrid, and Multifunctional Materials, Volume 4

Proceedings of the 2014 Annual Conference on Experimental and Applied Mechanics

Springer

Editor
Gyaneshwar Tandon
University of Dayton
Dayton, OH, USA

ISSN 2191-5644 ISSN 2191-5652 (electronic)
ISBN 978-3-319-06991-3 ISBN 978-3-319-06992-0 (eBook)
DOI 10.1007/978-3-319-06992-0
Springer Cham Heidelberg New York Dordrecht London

Library of Congress Control Number: 2014942919

Printed on acid-free paper

Springer is part of Springer Science+Business Media (www.springer.com)

Preface

Experimental Mechanics of Composite, *Hybrid*, *and Multifunctional Materials*, *Volume 4*: *Proceedings of the 2014 Annual Conference on Experimental and Applied Mechanics* represents one of the eight volumes of technical papers presented at the 2014 SEM Annual Conference & Exposition on Experimental and Applied Mechanics organized by the Society for Experimental Mechanics held in Greenville, SC, June 2–5, 2014. The complete proceedings also includes volumes on: *Dynamic Behavior of Materials*; *Challenges in Mechanics of Time-Dependent Materials*; *Advancement of Optical Methods in Experimental Mechanics*; *Mechanics of Biological Systems and Materials*; *MEMS and Nanotechnology*; *Fracture*, *Fatigue*, *Failure and Damage Evolution*; *Experimental and Applied Mechanics*.

Each collection presents early findings from experimental and computational investigations on an important area within Experimental Mechanics, Composite, Hybrid, and Multifunctional Materials being one of these areas.

Composites are increasingly the material of choice for a wide range of applications from sporting equipment to aerospace vehicles. This increase has been fueled by increases in material options, greater understanding of material behaviors, novel design solutions, and improved manufacturing techniques. The broad range of uses and challenges requires a multidisciplinary approach between mechanical, chemical, and physical researchers to continue the rapid rate of advancement.

New materials are being developed from natural sources or from biological inspiration leading to composites with unique properties and more sustainable sources, and testing needs to be performed to characterize their properties. Existing materials used in critical applications and on nanometer scales require deeper understanding of their behaviors and failure mechanisms. New test methods and technologies must be developed in order to perform these studies and to evaluate parts during manufacture and use. In addition, the unique properties of composites present many challenges in joining them with other materials while performing multiple functions.

Dayton, OH, USA — Gyaneshwar Tandon

Contents

Chapter 1
Characterizing the Mechanical Response of a Biocomposite Using the Grid Method

S. Sun, M. Grédiac, E. Toussaint, and J.-D. Mathias

Abstract This work is aimed at determining the mechanical behavior of a biocomposite made of sunflower stem chips and chitosan-based matrix which serves as a binder. The link between global response and local phenomena that occur at the scale of the chips is investigated with a full-field measurement technique, namely the grid method. Regular surface marking with a grid is an issue here because of the very heterogeneous nature of the material. This heterogeneity is due to the presence of voids and the fact that bark and pith chips exhibit a very different stiffness. Surface preparation thus consists first in filling the voids with soft sealant and then painting a grid with a stencil. The grid images grabbed during the test with a CCD camera are then processed using a windowed Fourier transform and both the displacement and strain maps are obtained. Results obtained show that the actual strain fields measured during compression tests are actually heterogeneous, with a distribution which is closely related to the heterogeneities of the material itself.

Keywords Biocomposite • Chitosan • Displacement • Full-field measurement • Grid method • Strain • Sunflower

1.1 Introduction

This work deals with the mechanical characterization of biocomposites made of chips of sunflower stems and a biomatrix derived from chitosan. This biocomposite is developed for building thermal insulation purposes. However, panels made of this material must exhibit minimum mechanical properties to be able to sustain various mechanical loads such as local stress peaks when mounting the panels on walls. This material also features a very low density (nearly 0.17), so it is necessary to study its specific mechanical properties for other applications than thermal insulation only. Such biocomposites are very heterogeneous because stems are made of stiff bark and soft pith.

The stems are generally ground during sunflower harvest and resulting chips are some millimeters in size. A full-field measurement system was therefore applied during compression tests performed on small briquettes made of this material to collect relevant information on the local response of the bark and pith chips. This can help understand local phenomena that occur while testing the specimens, and establish a link with the global response of the tested specimens. The size of the sunflower chips (some millimeters), the amplitude of the local displacement and strain throughout the specimens reached during the tests and the spatial resolution of full-field measurement systems which are nowadays easily available in the experimental mechanics community make it difficult to obtain reliable information on the sought displacement/strain fields. It was therefore decided to employ the grid method to perform these measurements. This technique consists in retrieving the displacement and strain maps assuming that the external surface of the tested specimen is marked with a regular grid. The grids usually employed for this technique are generally transferred using a layer of adhesive [1]. This marking technique could not be used here because of the very low stiffness of the biocomposite. Grids were therefore painted directly on the surface.

S. Sun • M. Grédiac (✉) • E. Toussaint
Clermont Université, Université Blaise Pascal, Institut Pascal, UMR CNRS 6602, BP 10448,
63000 Clermont-Ferrand, France
e-mail: michel.grediac@univ-bpclermont.fr

J.-D. Mathias
IRSTEA, Laboratoire d'Ingénierie pour les Systèmes Complexes, 9 Avenue Blaise Pascal, CS 20085,
63178 Aubière Cedex, France

G. Tandon (ed.), *Composite, Hybrid, and Multifunctional Materials, Volume 4: Proceedings of the 2014 Annual Conference on Experimental and Applied Mechanics*, Conference Proceedings of the Society for Experimental Mechanics Series,
DOI 10.1007/978-3-319-06992-0_1,

The basics of the grid method employed here to measure displacement and strain maps are first briefly given. The marking procedure is then described. Typical results obtained on specimens subjected to compression tests are then presented and discussed.

1.2 Applying the Grid Method to Measure Displacement and Strain Maps

The grid method consists first in marking the surface under investigation in order to track the change in the geometry of the grid while loading increases, and to deduce the 2D displacement and strain fields from these images. Processing grid images consists first in extracting the phases along directions x and y both in the reference and in the current images. Phase extraction is carried out with the windowed Fourier transform (WFT) [2]. The envelope considered in the present study is Gaussian, as in [3]. The displacements u_i i = x, y are obtained from the phase changes $\Delta\Phi_i$, i = x, y between current and reference grid images using the following equation where p is the pitch of the grid:

$$u_i = -\frac{p}{2\pi}\Delta\Phi_i, \quad i = x, y \tag{1.1}$$

The strain components ε_{ij} i = x, y are deduced using the following equation:

$$\varepsilon_{ij} = -\frac{p}{4\pi}\Delta\left(\frac{\partial\Phi_i}{\partial x_j} + \frac{\partial\Phi_j}{\partial x_i}\right), \quad i, j = x, y \tag{1.2}$$

1.3 Description of the Tested Material

Biocomposites studied here are obtained by mixing bark and pith chips with a biomatrix. Bark provides the main contribution to the mechanical properties of the biocomposite, pith the main thermal insulation properties. A biopolymer based on chitosan is used as a binder [4]. The solvent is merely water containing a low percentage of acetic acid (1 %). In conclusion, it is worth mentioning that this composite material is mainly composed of renewable resources.

1.4 Surface Preparation

There are voids in the biocomposite and some of them are clearly visible to the naked eye on the surface of the specimen, as illustrated in Fig. 1.1.

To avoid any disturbance of the displacement and strain fields measured on the front face of the tested specimen, these voids were filled with a very soft Sikaflex-11FC+ sealant. The impact of this filling material on the response of the specimen is therefore negligible. The surface was then carefully sanded and cleaned. In recent examples of displacement and strain measurements where the grid method was employed, surface marking was generally obtained by transferring a grid, using for instance the technique described in [1]. The problem here is that a layer of adhesive is necessary and this would certainly influence the measured quantity, the stiffness on the substrate being lower than that of the adhesive at some places (pith, voids filled with sealant). This marking technique is therefore not directly applicable here. The grid was painted directly on the surface using a stencil. White paint was first sprayed on the surface of the specimen. The stencil was then placed on this surface and black acrylic ink was sprayed though the stencil with an airbrusher. The lowest size of the square wholes that can be cut in the stencil is the limitation of the technique here. It is equal to 0.4 mm. This finally leads to a grid featuring a frequency of 1.25 lines/mm [5] instead of up to about 10 lines/mm by using the technique described in [1].

Note that the pitch of the grid is not perfectly equal 0.8 mm: it exhibits slight spatial changes which are detected by the WFT (within certain limits). These changes might be considered as caused by a fictitious straining of the tested material beneath the grid. This artifact has been eliminated here by using the procedure described in [3] when processing the grid images.

Fig. 1.1 Front face view of a specimen

1.5 Specimens, Testing Conditions

The specimens were prepared first by moulding small briquettes in which specimens were cut using a saw. The mass percent fraction of chitosan in the biomatrix was equal to 6.25 %. This parameter has an influence on the mechanical response of the specimen [5]. The dimensions of the tested specimens were about 50 × 80 × 122 mm^3. The specimens were subjected to compression tests performed with a 20 kN Zwick-Roell testing machine. The cross-head speed was equal to ~0.02 mm/s. The tested specimens rested on a small plate and the load was applied by imposing a displacement on the upper side. A stiff steel plate was placed on the upper side of the specimen to help obtaining homogeneous imposed displacement and pressure on this side. The lower and upper sides were however not parallel. A 2 mm thin elastomeric sheet was therefore placed between the upper side of the specimen and the moving plate to accommodate displacements imposed on the upper side. The procedure described above was employed to mark the surface with a regular grid after filling the voids with sealant. A Sensicam QE camera was used to grab images of the grid paint on the front face of the specimen during the tests. Nine pixels per period were used to encode one grid pitch.

1.6 Results

A typical mean stress–mean strain curve is shown in Fig. 1.2. A small displacement of the lower support of the specimen being observed, the mean strain is obtained by measuring the average displacement along a line of pixels located 30 pixels under the top face of the specimen to avoid possible edge effects, subtracting it with the average displacement along a line of pixels located 30 pixels above the bottom face of the specimen, and dividing the obtained result by the distance between these two lines. The mean stress is merely the ratio between the applied force and the section of the specimen. In Fig. 1.2, it can be observed that the response is first linear and then non-linear. It is interesting to observe what happens within the material by investigating full-field displacement and strain fields measured on the front face of the specimen.

Figure 1.3 shows a typical vertical displacement field. This displacement is calculated by subtracting the actual displacement and the mean one. It is obtained at the end of the loading phase of the test. As may be seen, the displacement field is irregular. This is due to very local displacement increases due to material heterogeneities. Local strain concentrations can be observed in the vertical strain field shown in Fig. 1.4. On close inspection, they correspond to some zones where the amount of voids is greater than in other zones of the specimen. A more detailed study also shows that the strain level in pith chips is greater than that reached in bark chips, which is certainly due to the difference in stiffness between both constituents [5].

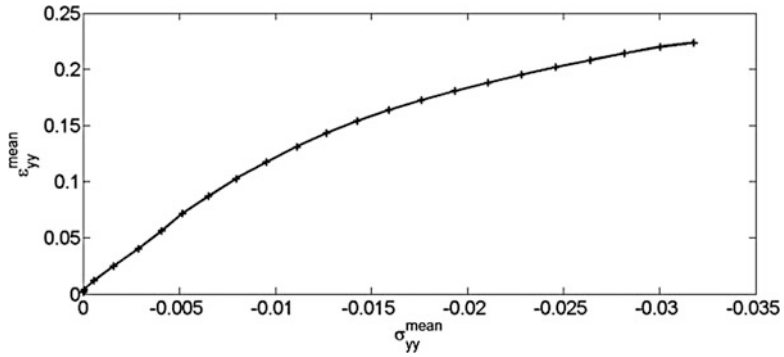

Fig. 1.2 Mean stress–mean strain curve

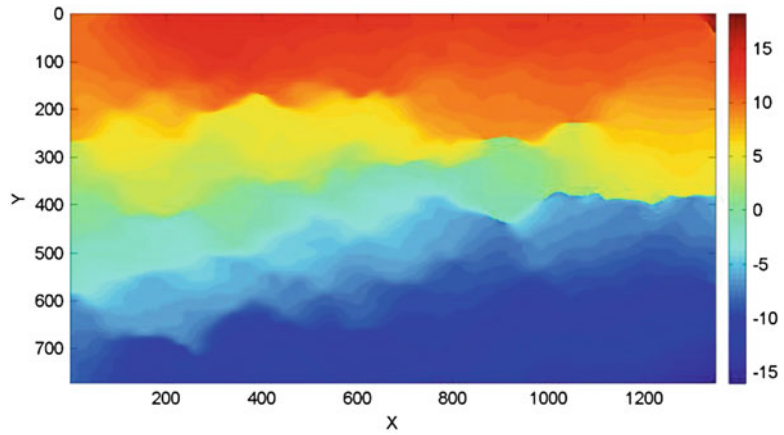

Fig. 1.3 Typical vertical displacement field, in pixels (1 pixel = 40 μm)

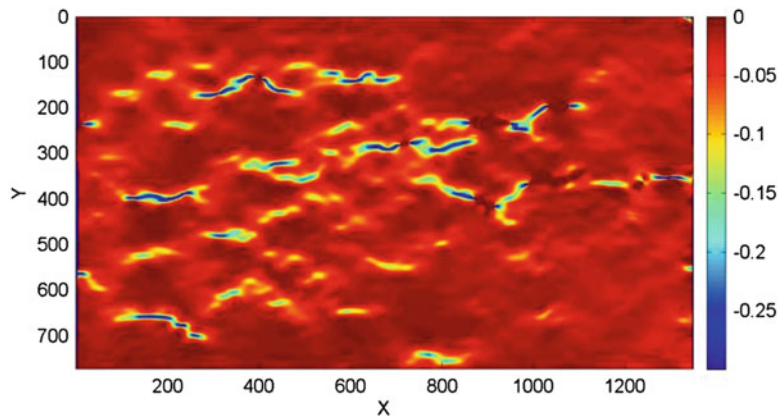

Fig. 1.4 Typical vertical strain field

1.7 Conclusion

The grid method was employed here to characterize the strain field that occurs on the surface of biocomposite specimens. Some very strong heterogeneities are clearly visible. They are closely related to the heterogeneous nature of the material. In particular, the strain level is the highest in zones where voids are present in the material. Even though the measured mechanical characteristics are much greater than the minimum values required for such insulating materials [5], more tests are still necessary to clarify the link between the chitosan volume fraction in the biomatrix, the degree of heterogeneity in the strain field and the strength of the biocomposite. The objective is indeed now to reduce as far as possible the amount of biomatrix in the biocomposite. The reason is that it is the most expensive of all the constituents employed in this material.

References

1. Piro JL, Grédiac M (2004) Producing and transferring low-spatial-frequency grids for measuring displacement fields with moiré and grid methods. Exp Tech 28(4):23–26
2. Surrel Y (2000) Photomechanics, topics in applied physics, vol 77. Springer, Berlin, pp 55–102 (chapter on fringe analysis)
3. Badulescu C, Grédiac M, Mathias J-D (2009) Investigation of the grid method for accurate in-plane strain measurement. Meas Sci Technol 20 (9):095102
4. Patel AK, Michaud P, de Baynast H, Grédiac M, Mathias J-D (2013) Preparation of chitosan-based adhesives and assessment of their mechanical properties. J Appl Polym Sci 127(5):3869–3876. doi:10.1002/app.37685
5. Sun S, Grédiac M, Toussaint E, Mathias J-D, Mati-Baouches N (submitted for publication) Applying a full-field measurement technique to characterize the mechanical response of a sunflower-based biocomposite

Chapter 2
Preliminary Study on the Production of Open Cells Aluminum Foam by Using Organic Sugar as Space Holders

F. Gatamorta, E. Bayraktar, and M.H. Robert

Abstract This work investigates the production of Al foams using organic sugar granulates as space holders. To the Al matrix hollow glass micro spheres were added to constitute a light weight composite material. The process comprises the following steps: mixing of Al powders and organic sugar granulates, compacting of the mixture, heating the green compact to eliminate the sugar and final sintering of the metallic powder. Open spaces left by the volatilization of the sugar granulates constitute a net of interconnect porosity in the final product, which is, therefore, a metallic sponge. It was analyzed the influence of processing parameters in the different steps of production, in the final quality of products. Products were characterized concerning cells distribution and sintering interfaces. Results showed the general viability of producing composites by the proposed technique, based on a simple and low cost procedure.

Keywords Sponge structure • Low cost composites • Organic sugar • Aluminum foam • Sintering

2.1 Introduction

Metal matrix composites (MMCs) are advanced materials; for their production, widely used sintering method is one of the main manufacturing processes to obtain composite products applied for high strength, lightweight materials and mainly as high temperature and wear resistance in aerospace and automotive industry.

Recently, the demands for lightweight materials having a high strength and a high toughness have attracted a lot of attention to the development of composite sponge structures and/or composite reinforced with light materials as nonconventional organic materials such as sugar and/or porous ceramic oxides [1–4, 7] one of our papers on cinasite or vemiculite.

The powder metallurgy (PM) route is known as most commonly used method for the preparation of discontinuous reinforced MMCs. This method is generally used as low—medium cost to produce small objects (especially round), tough, the high strength and resistant materials. Since no melting is involved, there is no reaction zone developed, showing high strength properties. For this reason, in the present work, a simple idea was developed on the production of sponge composites by using a low cost method (mixture of aluminum matrix with organic sugar admixing small size glass bubbles and cold pressing + sintering). In reality, Al-alloy based composites were thought during last 20 years in process when the possibilities of improvement in Al alloys by the then conventional methods of heat treatment and microstructural modification had touched its limit. Consequently, new and attractive processes of composites have replaced a prime as compared to the other processes when the cost and simplicity of manufacturing were compared [1–6]. At the first step of this research, a typical porous structure has been created by using organic sugar particulates and an open spaces created by the volatilization of the sugar particulates constitute a net of interrelate porosity in the final product, called a low cost metallic sponge [5–7].

The scope of this work is to identify and investigate the procedures required for a low cost processing route of MMCs containing glass bubbles reinforcements, for engineering applications. The current research uses a simple sintering

F. Gatamorta • M.H. Robert (✉)
Mechanical Engineering Faculty, University of Campinas, Campinas, SP, Brazil
e-mail: fabiog@fem.unicamp.br; helena@fem.unicamp.br

E. Bayraktar (✉)
Mechanical and Manufacturing Engineering School, SUPMECA—Paris, Paris, France
e-mail: emin.bayraktar@supmeca.fr

G. Tandon (ed.), *Composite, Hybrid, and Multifunctional Materials, Volume 4: Proceedings of the 2014 Annual Conference on Experimental and Applied Mechanics*, Conference Proceedings of the Society for Experimental Mechanics Series,
DOI 10.1007/978-3-319-06992-0_2,

technique under inert environment (mainly Argon gas), which has the certain advantages over liquid state methods. Lower processing temperatures decreases the probability of the matrix reacting unfavorably with the reinforcement, improves glass bubbles and organic sugar particle distribution, presents potentially lower energy consumption, simplified operation methods with a low time scale, etc. The work carried out during this present research project has the following overall aims: to develop the understanding of powder metallurgy techniques in producing sponge aluminum metal matrix composites; to make the persistence of the lowering of costs in the processing of these composites.

2.2 Experimental Conditions

2.2.1 Materials and Green Compact

Four different compositions were prepared for the present work: pure aluminum (99.5 %) matrix was mixed with 30 wt% of white sugar granulates (WS) or 30 wt% of Brown Sugar (BS) granulates as two basic compositions; two other compositions were prepared by addition of 10 wt% Glass Bubbles (GB-hollow glass microspheres produced by the company-3M with a density of 0.227 g/cm^3, specified as S38HSS & K1) on the former two compositions. Finally, for sake of simplicity, these four compositions were classified under the name of the following codes:

1. Al + 30 % BS
2. Al + 30 % BS + 10 % GB
3. Al + 30 % WS
4. Al + 30 % WS + 10 % GB

All of the powders used in this work, Al for the matrix and additional elements, were analyzed in a differential thermal analyzer to determine the critical temperature-transformation points (solid–liquid zone) and mass loss *versus* temperature; they had also their size and geometry analyzed by SEM. All compositions were mixed during 4 h in a stainless steel mixer with addition of 2 % Zinc Stearate to facilitate the lubrication. The role of the sugar granulates used in the matrix is to create nearly homogeneous distribution of empty spaces in the matrix during the sintering process. To prepare green compaction of the powder mixtures, a double action-hydraulic press with a capacity of 100 tons was used. For compaction of the mixture, a stainless steel mold with a diameter of 20 mm was used, resulting in green compacts of same size (diameter: 20 mm and height: 30 mm).

2.2.1.1 Sintering

Samples of green compacts were sintered under inert atmosphere with argon gas. The treatment for solid state sintering was carried out in two steps: firstly, the volatilization of the sugar was made at a temperature of 200 °C for a fixed time of 60 min; at the second step the consolidation of sintering was completed at the temperature of 620 °C for a total period of 180 min. Heating rate was 10 °C/min for both steps. During the first step, removing of the sugar must be complete by allowing the gas created by the melting and volatilization of the sugar granulates to scape, resulting in a porous structure with nearly homogeneous porous distribution. This structure is consolidated by the second step sintering.

2.2.1.2 Measurements of the Density and Porosity of the Compacted Specimens Before and After Sintering

All of the measurements of the density and porosity of the specimens were carried out by pycnometry (digital density meters, Webb and Orr, 1997 work with helium gas) before and after sintering and the results were then compared.

2.2.1.3 Mechanical Tests and Microstructural Analyzes

Sintered products were submitted to compression tests, carried out in a servo-hydraulic INSTRON Universal test device (model Instron 5500R, equipped with a load cell of 25,000 kgf) with a quasi-static low speed (initial rate: 10 mm/min and second rate: 5 mm/min rate). Maximum load endpoint was 4,500 N. All testing parameters are given in Table 2.1.

Table 2.1 General conditions for compression tests of produced composites

Initial speed (mm/min)	10	10	10	10
Load endpoint (N)	4,448	4,448	4,448	4,448
Outer loop rate (Hz)	100	100	100	100
Secondary speed (mm/min)	5.08	5.08	5.08	5.08
Strain endpoint (%)	80	80	80	80

Furthermore, dynamic drop tests were carried out on an universal drop weight test device (Dynatup Model 8200 machine) with a total weight of 10.5 kg, punch height of 600 mm and with an impact velocity of 3 m/s.

Microstructure of produced foams was observed by using Scanning Electron Microscopy (JOEL-SEM).

2.3 Results and Discussion

Results of differential thermal analysis of the Aluminum, Glass Bubbles (GB), White Sugar (WS) and Brown Sugar (BS) powders are shown in Fig. 2.1. In the same figure are also presented images of the powders obtained by SEM.

It can be observed in the DTA curves, the critical temperature-transformation points of the different raw materials: a high energy transformation is observed for Al powders around 650 °C (647.5 °C), without mass loss, related to the melting point of the aluminum. For White and Brown Sugar powders, it is observed in DTA curves a significant transformation starting around 180 °C, followed by a heavy mass loss starting round 220 °C; these points can be assumed as melting and volatilization temperatures, respectively. Both sugar powders present the same behavior.

Related to the Glass Bubbles, Fig. 2.2b shows some reaction when heating from room temperature to 140 °C, with around 5 % of mass addition. This can be related to some chemical reaction in the glass material and must be further investigated.

SEM images show aluminum powders with irregular, elongated shape, with average dimensions ranging from 16 to 300 μm. Hollow glass spheres are perfectly rounded, presenting diameters from 3 to 100 μm; White Sugar and Brown Sugar granulates present polygonal morphology and sizes of 200–300 mm and 400–900 mm, respectively.

Table 2.2 summarizes results of measurements of the density and the porosity of the specimens before (green compact) and after sintering (composite). Results show that the density of all the green compact specimens for the four compositions investigated varies between 2.31 and 2.41 g/cm^3. After sintering these values decrease around 50 %, to the levels of 1.61–1.79 g/cm^3. The effect of the presence of the hollow Glass Bubbles and the type of the sugar granulate used, on the product density is not so remarkable and remains inconclusive. While foams produced from Brown Sugar present lower density when Glass Bubbles are added, foams produced from White Sugar present slightly higher density when this additive is incorporated to the structure. Expected result would be decrease in density with GB addition to the material.

Percentages of free space and massive regions were measured in the green compact specimens as 5–7 % and 92–94 % respectively. After sintering free spaces/massive regions ratio increases as the sugar granulates suffer volatilization, at the same levels for all of four compositions. Sintering treatments is found correct for these compositions.

Microstructural analysis of the obtained products was carried out by using Scanning Electron Microscope (SEM). Figure 2.2 shows pictures taken from surface and transversal sections of the specimens WS30GB10 and BS30GB10.

It can be observed the presence of Glass Bubbles distributed in the structure, as well as the free spaces left by the volatilization of the sugar granulates. Thinner cell walls are present when using coarser sugar particles (BS), compared to those obtained for finer sugar particles (WS). Considering the same weight content of sugar, higher amount of total particles is present for the coarser one.

Results of dynamic compression tests (drop test) of the produced foams, are presented in Fig. 2.3, where the behavior of the materials during impact can be compared among the four compositions investigated. Each curve represents the average of results obtained for four tested samples. Compositions WS30 and BS30 without Glass Bubbles present the higher maximum load capacity (26–27 kN) compared to the values obtained (20 kN) for compositions with Glass Bubbles, i.e. BS30GB10 and WS30GB10. However, both compositions with Glass Bubbles show higher plastic deformation and less brittleness regarding to the compositions without Glass Bubbles. It means that the values of the deflection at maximum load for the specimens containing Glass Bubbles are higher compared to those of the specimens without Glass Bubbles. The behavior of each type of foam can be also related to its density: apart of the high density value for the WS30GB10 condition, it seems that maximum load capacity are obtained for products with higher density, as expected for conventional cellular materials. Higher plastic deformation would also be expected, in general, for lower density foams.

Impact energy, total energy and other information obtained from these tests are indicated in Table 2.3. It can be observed significant energy absorption during impact, in all cases. The values obtained are similar for all products tested.

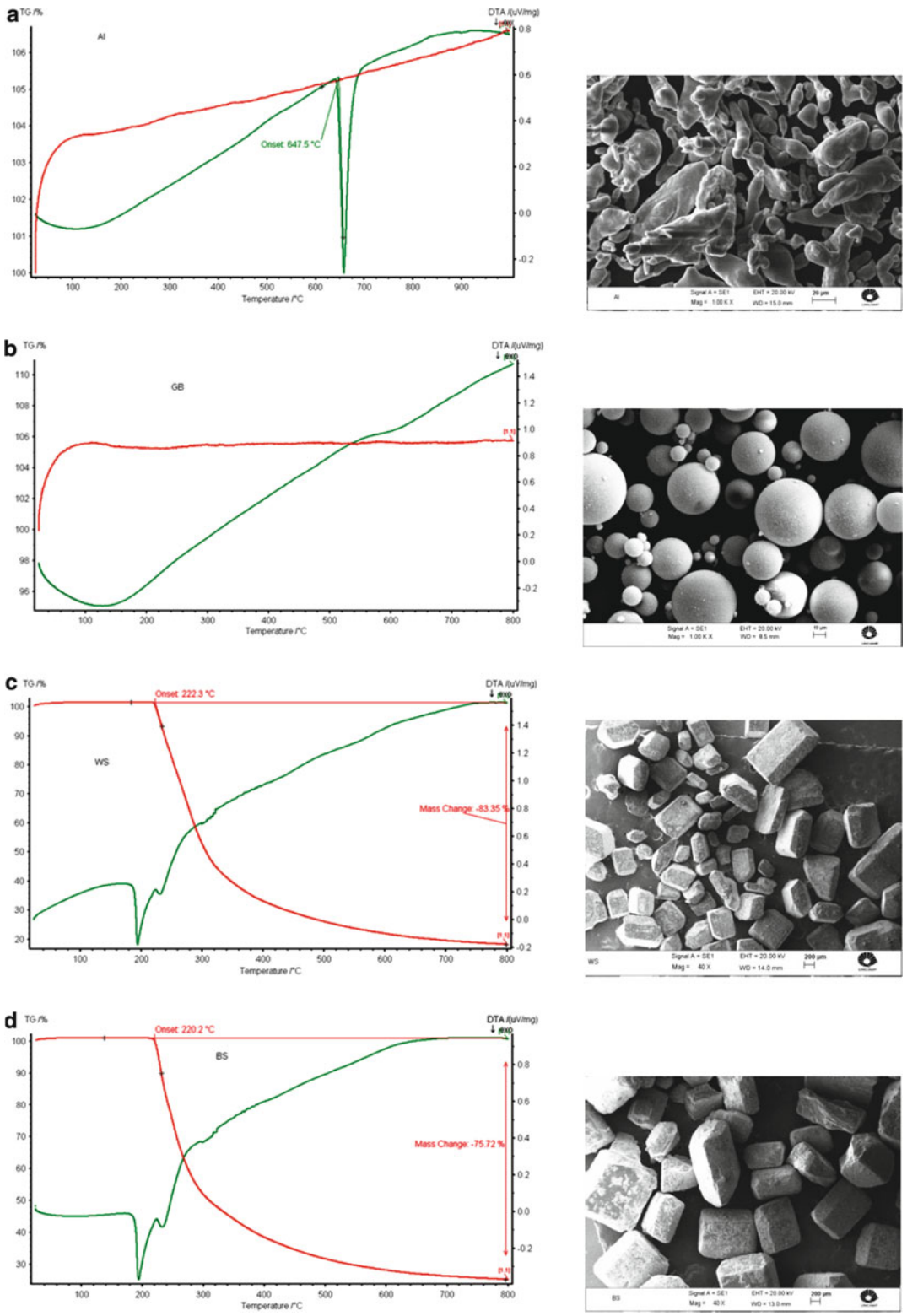

Fig. 2.1 Results of differential thermal analysis (DTA) and thermogravimetry (TG) of the different powders used to produce foams; images by SEM of the corresponding material. (**a**) Aluminum (as matrix), (**b**) glass bubbles (additional element), (**c**) white sugar (space holder) and (**d**) Brown Sugar (space holder)

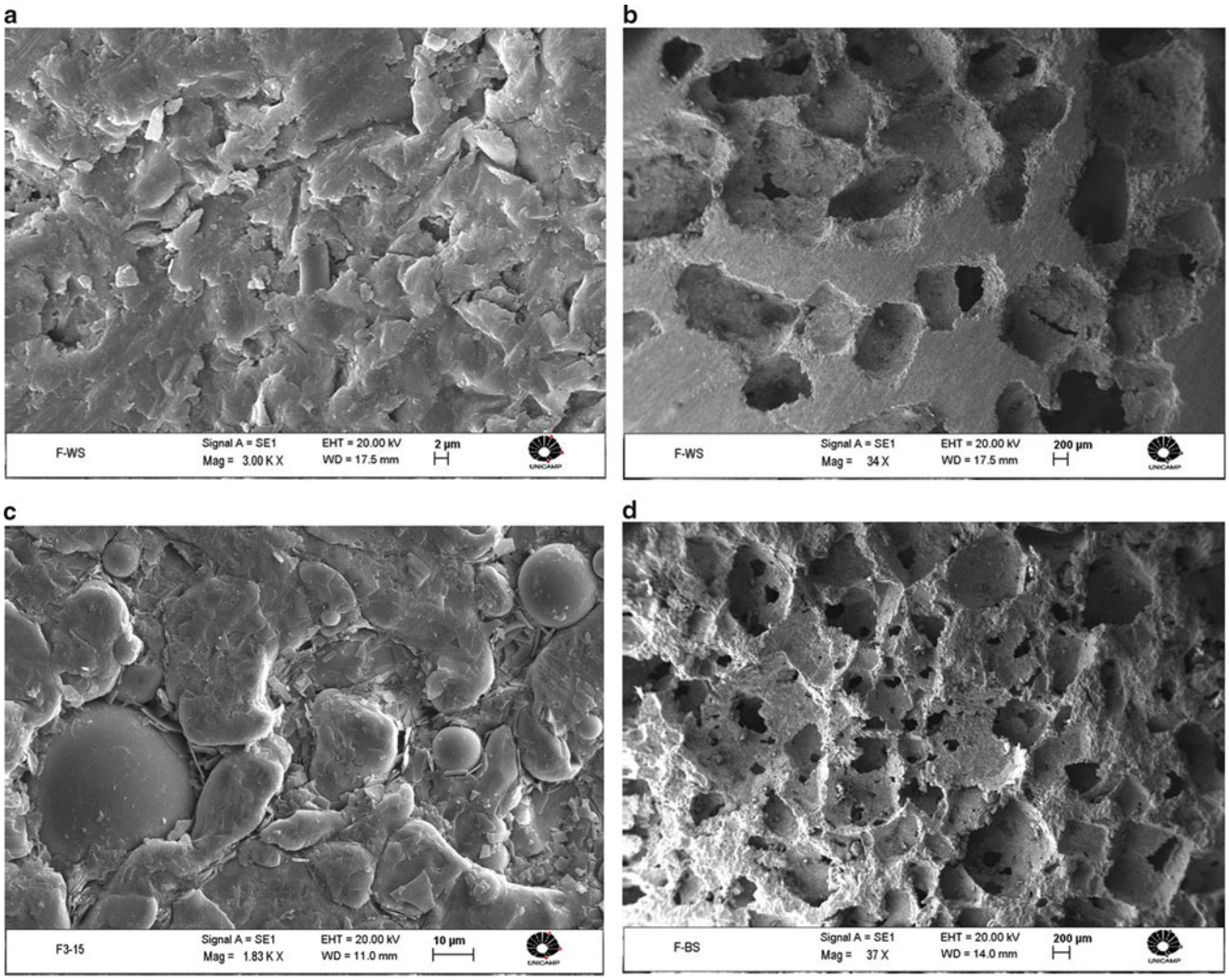

Fig. 2.2 SEM pictures taken from surface and transversal sections of the foams WS30GB10 and BS30GB10. (**a**) WS30GB10; SEM microstructure (surface section), (**b**) WS30GB10; SEM microstructure (transversal section), (**c**) BS30GB10; SEM microstructure (surface section) and (**d**) BS30GB10; SEM microstructure (transversal section)

Table 2.2 Measurements of the density and porosity by He gas pcynometer (digital density meters)

	Condition of specimen	ρ (g/cm^3)	% of empty space	% of massive regions
BS30	Green compact	2.409 ± 0.011	5.42	94.58
	After sintering	1.794 ± 0.025	39.90	60.10
BS3010GB	Green compact	2.358 ± 0.022	5.79	94.21
	After sintering	1.615 ± 0.034	46.39	53.61
WS30	Green compact	2.345 ± 0.010	8.13	92.55
	After sintering	1.713 ± 0.020	42.34	57.66
WS3010GB	Green compact	2.314 ± 0.009	7.93	92.08
	After sintering	1.740 ± 0.022	41.68	58.32

Figure 2.4 shows results of semi-static compression tests for all of the four compositions investigated. Evolution of the stress values depending on the deformation (strain levels as %) were compared with different parameters, for example, peak values (stress as MPa) are found similar levels (45 MPa) for three compositions but only the specimens called BS30 have given much more higher values, around 97 MPa (quasi double). Other test results were summarized in Table 2.4.

From both sorts of compression tests, it seems that the role of Glass Bubbles is relevant on the plasticity of the composites and they give better ductility if they are added in the matrix up to 10–15 %. Some of the test results not given

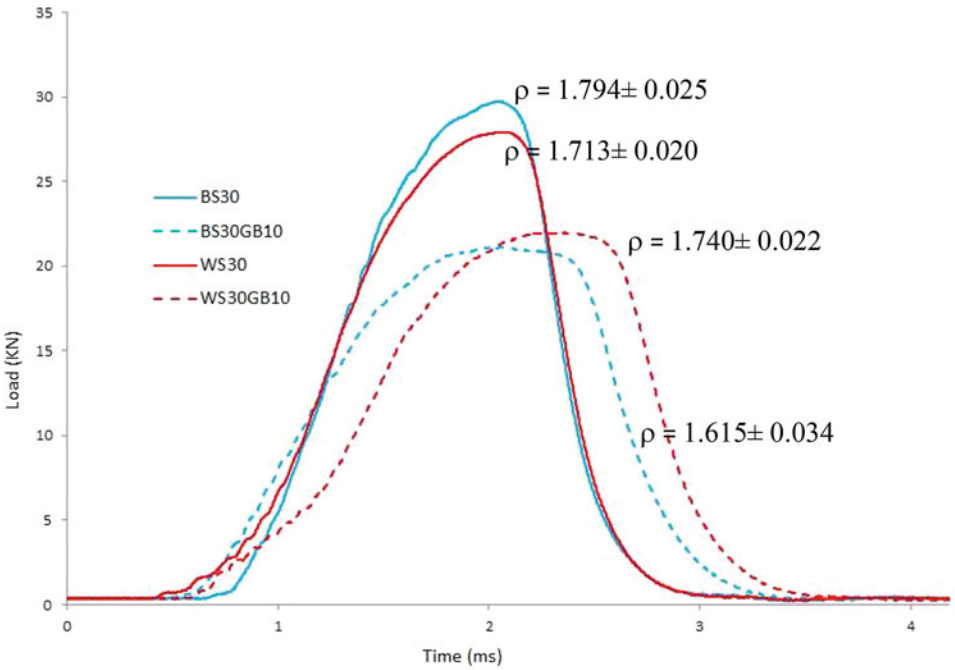

Fig. 2.3 Results of dynamic compression tests (drop test) for the produced foams

Table 2.3 General mechanical characteristics of the produced foams, obtained in dynamic compression tests

Sample	Maximum load (kN)	Time to max load (ms)	Impact velocity (m/s)	Total energy (J)	Total time (ms)	Impact energy (J)	Energy to max load (J)	Total deflection (mm)	Deflection at max load (mm)
BS30	27.8633	2.097	3.1266	48.6261	3.4088	50.7857	49.8731	3.4101	4.1818
BS30 10GB	19.7109	2.0964	3.1301	49.0517	3.8116	50.8994	46.9865	4.4332	4.8798
WS30	26.2176	2.1362	3.1393	49.2017	3.8025	51.1984	50.4654	4.2745	5.0806
WS30 10GB	20.5374	2.1949	3.133	49.2172	4.1687	50.9937	49.0722	4.7298	5.4318

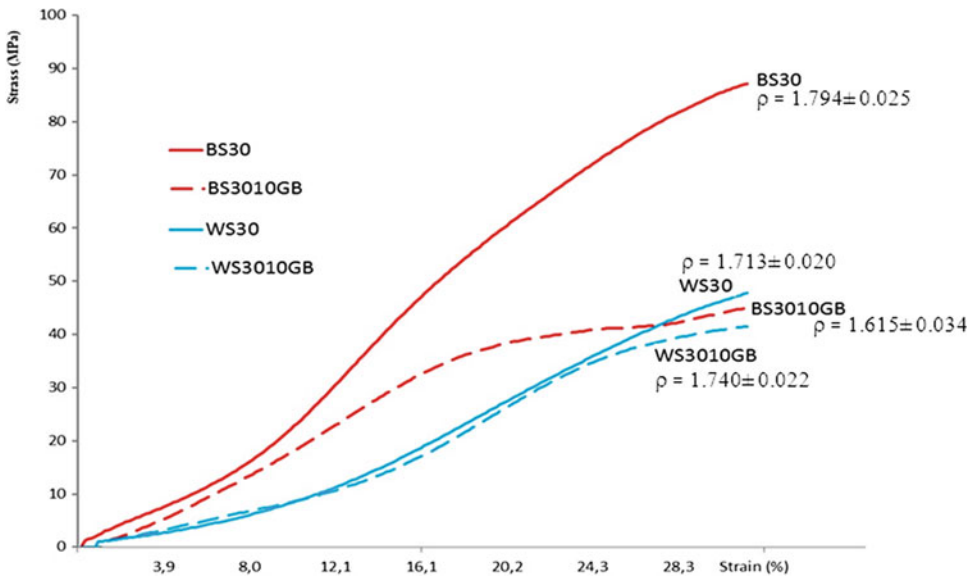

Fig. 2.4 Results of semi-static compression tests for the produced foams

Table 2.4 General mechanical characteristics of the produced foams, obtained in semi-static compression tests

Sample	Modulus (MPa)	Load at offset yield (N)	Stress at offset yield (MPa)	Load at yield (N)	Stress at yield (MPa)	Peak load (N)	Peak stress (MPa)
WS30	243.245	14,194.25	32.72	18,140.73	41.82	19,296.26	44.48
WS30GB10	243.245	14,194.25	32.72	18,140.73	41.82	19,296.26	44.48
BS30	415.947	20,648.17	50.57	-	-	39,834.89	97.56
BS30GB10	261.204	13,514.68	32.52	-	-	18,674.45	44.94

here have shown that beyond these values (>15 % of the Glass Bubbles) the effect is a decrease in ductility; the material become brittle at the higher percentages of this kind of additive.

2.4 Conclusion

In the present work, a simple idea was developed on the production of sponge composites by using a low cost method (mixture of aluminum matrix with organic sugar admixing micro hollow glass bubbles and cold pressing + sintering). Results obtained so far indicates that the method is quite promising in producing foams with open, interconnected cells (sponges) as a result of volatilization of sugar granulates, and glass spheres as closed cells. Acceptable dispersion of both open spaces and closed cells can be achieved when proper mixing/pre-compacting conditions are employed. Product shows low density (relative density around) and ability of energy absorption in impacts.

Results also showed that the two parameters investigated—addition or not of Glass Bubbles and type of sugar granulate (white sugar, fine dimension or Brown Sugar, coarse dimension) presented no conclusive effect on the density and compression behavior of the products. The addition of Glass Bubbles tend to promote decrease in density and to increase plastic deformation of the material (for GB contents up to 15 %).

As a general conclusion, this preliminary study indicates that the technique of producing porous metals containing both open and closed cells, using sugar as space holder for the first and hollow glass spheres for the second, by means of sintering, is worthy investigating.

References

1. Slipenyuk A, Kuprin V, Milman Y, Goncharuk V, Eckert J (2006) Properties of P/M processed particle reinforced metal matrix composites specified by reinforcement concentration and matrix-to-reinforcement particle size ratio. Acta Mater 54(1):157–166
2. Irot FA, Queniss JM, Naslain R (1987) Discontinuously reinforced aluminum matrix composites. Compos Sci Technol 30:155–163
3. Torralba JM, daCost CE, Velasco F (2003) P/M aluminum matrix composites: an overview. J Mater Process Technol 133(1–2):203–206
4. Dasgupta R (2012) Aluminum alloy-based metal matrix composites: a potential material for wear resistant applications, International Scholarly Research Network. ISRN Metallurgy 2012:14 pp. doi:10.5402/2012/594573, Article ID 594573
5. Massol M, Gargiulo J, Gatamorta F (2014) Development of low cost aluminum based composites reinforced with light organic materials and oxides. Final research project (PSYN-2014), Supmeca/LISMMA—Paris, Mechanical and Manufacturing Engineering, Paris—France, 35 pp
6. Ferreira L-P (2013) Production of aluminum metal matrix composites by thixoforming of recycled chips. Thesis for Master of Science, University of Campinas, UNICAMP, Mechanical and Manufacturing Engineering, Campinas—SP, Brazil
7. Robert MH, Jorge AF (2012) Processing and properties of AA7075/porous SiO_2–MgO–Al_2O_3 composite. JAMME 3:1–5

Chapter 3
Characterization of Shear Horizontal-Piezoelectric Wafer Active Sensor (SH-PWAS)

Ayman Kamal and Victor Giurgiutiu

Abstract This paper discusses shear horizontal SH-coupled piezoelectric wafer active sensor (PWAS). The paper starts with a review of the state of the art in modeling SH transducers and their importance in non-destructive evaluation (NDE) and structural health monitoring (SHM). This is followed by basic sensing and actuation equations of shear-poled PWAS transducers. The free SH-PWAS electromechanical (E/M) impedance analytical models are presented, and compared with finite element models (FEM) and experiments. In this study, we extend the analytical development for constrained SH-PWAS bonded to structure on the form of beams. The model is based on normal mode expansion (NME) technique. The interaction between the SH-PWAS and the structure is studied. We developed closed-form equation of structure dynamic stiffness by coupling the mechanical response solution of the SH-PWAS to the structure elasticity solution. Finite element simulations and experiments matched well with analytical predictive model. Impedance spectroscopy is also used in NDE and SHM for composites. We present a predictive FEM for the E/M impedance of bonded SH-PWAS on cross ply GFRP as well as [0/45/45/0]s CFRP plates. The paper ends with summary, conclusion, and suggestions of future work.

Keywords Shear horizontal (SH) waves • Piezoelectric wafer active sensor (PWAS) • Electromechanical (E/M) impedance • Normal mode expansion (NME) • Poling direction • Nondestructive evaluation (NDE) • Structural health monitoring (SHM)

Nomenclature

D_j	Electric displacement vector (C/m^2)
d_{35}	Piezoelectric strain constant for shear mode (m/V) or (C/N)
E_j	Electric field (V/m)
e_{35}	Piezoelectric stress constant for shear mode (N/Vm)
g_{35}	Piezoelectric voltage constant for shear mode (m^2/C) or (Vm/N) or [(V/m)/Pa]
S_{ij}	Strain tensor
s_{55}^D	Mechanical shear compliance at zero electric displacement, D = 0 (m^2/N)
T_{kl}	Stress tensor (N/m^2)
γ	Wave number (1/m)
ε_{jk}^T	Dielectric permittivity matrix at zero mechanical stress, T = 0 (F/m)
ε_{33}^S	Dielectric permittivity in 33 direction measured at zero mechanical strain, S = 0
ε_{33}^T	Dielectric permittivity in 33 direction measured at zero mechanical stress, T = 0
K	Electromechanical coupling factor
μ	Shear modulus (Pa)
ω	Angular frequency (rad/s)

A. Kamal (✉) • V. Giurgiutiu
Department of Mechanical Engineering, University of South Carolina, Columbia, SC 29208, USA
e-mail: kamal@email.sc.edu; victorg@sc.edu

G. Tandon (ed.), *Composite, Hybrid, and Multifunctional Materials, Volume 4: Proceedings of the 2014 Annual Conference on Experimental and Applied Mechanics*, Conference Proceedings of the Society for Experimental Mechanics Series,
DOI 10.1007/978-3-319-06992-0_3,

Introducing some relations $g_{35} = \frac{d_{35}}{\varepsilon_{33}^T}$ $\frac{1}{\varepsilon_{33}^T} = \frac{1}{\varepsilon_{33}^S} - \frac{g_{35}^2}{s_{55}^D}$ $e_{35} = \frac{d_{35}}{s_{55}^E}$ $\varepsilon_{33}^T = \varepsilon_{33}^S + d_{35}e_{35}$

$\frac{\varepsilon^S}{\varepsilon^T} = \frac{s^D}{s^E} = 1 - K^2$ $\frac{e_{35}}{\varepsilon_{33}^S} = \frac{g_{35}}{s_{55}^D}$ $K_{35}^2 = \frac{d_{35}^2}{s_{55}^E \varepsilon_{33}^T} = \frac{e_{35}^2 s_{55}^D}{\varepsilon_{33}^S}$

3.1 Introduction

Piezoelectric materials have been used extensively for structural health monitoring for detecting and identifying damages and flaws in structures. Piezoelectric wafer active sensors (PWAS) are small, thin and inexpensive sensors that can be used in passive mode (direct piezoelectric mode) where the sensors detect guided waves propagating in the structure and output an electric response, or PWAS can be used in active mode (converse piezoelectric mode) in which the transducer excites the structures with mechanical guided waves when it is subjected to electric field. Conventional PWAS is thin rectangular or circular wafer that is poled in thickness direction, with electrodes on top and bottom surfaces; those types of PWAS are either used in the inplane or the thickness mode. In the inplane mode, applying an electric field in thickness direction E_3 causes the sensor lateral dimensions to increase or decrease, a longitudinal strain will occur $\varepsilon_1 = d_{13}E_3$, where d_{13} is the piezoelectric coupling coefficient measured in (m/V). Thickness mode is a mode that occurs simultaneously with extension mode, but dominates at higher frequencies in MHz, in which strain in the thickness direction will occur $\varepsilon_3 = d_{33}E_3$, where d_{33} is the piezoelectric coupling coefficient in thickness direction. A different mode of oscillation can be achieved when the applied electric field is applied perpendicular to the poling direction; and it is referred as shear mode.

For structural health monitoring (SHM) and nondestructive evaluation (NDE) applications, shear horizontal (SH) guided waves showed high potential for quantitatively detecting defects in structures [1, 2]. For most piezoelectric materials, the coupling coefficients associated with shear mode have the largest value of all coefficients [3–5]. The higher values of shear coupling coefficients make SH-PWAS superior in actuation and sensing [6]. SH waves are also preferable because first symmetric mode is non-dispersive, i.e. wave speed is constant at different frequencies. On the other hand, one of the important disadvantages of SH-PWAS is that thicker transducers is needed to sustain and generate the shear actuation and due to high density of piezoceramic materials (≈7,600 kg/m^3 for APC850 piezoceramic Navy II type); using of shear mode piezoelectric elements increases the mass of the system considerably.

An example of using shear mode piezoelectric transducers as actuators was studied as shear element in a cantilever beam setup [7]; where the stress distribution across thickness under mechanical and electrical loading was investigated. A similar study on using shear-type piezoelectric as a shear bender was studied in [8].

In another application, SH polarized waves were used for evaluating the quality of bonding between transducer and the structure [9]. This can be comparable to the method of using imaginary component of PWAS impedance analysis to test the bonding between the transducer and the structure [10]. Shear horizontal waves usually were associated with electromagnetic acoustic transducers or EMAT [11], where SH waves were used to detect weld defects. They have shown superiority over conventional shear vertical (SV) and longitudinal waves [12]. However, it was suggested that piezoelectric based transducers generating SH will show better acoustic generation than EMAT. Also, one point to consider is that EMAT needs conductive structures, while PWAS can be used for conductive metallic structures and non-conductive composites (e.g. glass fiber reinforced polymers), beside the fact that SH-PWAS are much cost efficient. SH waves are associated also with AT-cut quartz resonators. AT-cut quartz resonators were studied in [13], where SH modes were obtained using anisotropic elasticity equations. Thickness shear vibrations of quartz crystal plates were studied using Mindlin plate equations in [14].

This study focuses on electromechanical (E/M) impedance of SH-PWAS, first: analytical development of E/M impedance for (a) free SH-PWAS, (b) when bonded to the structure. The second part presents finite element modeling (FEM) and experimental verification. The third part presents a FEM for the E/M impedance of bonded SH-PWAS on cross ply GFRP as well as [0/45/45/0]s CFRP plates and compared with experiments.

3.2 Theoretical Models of SH-PWAS Impedance Spectroscopy

Impedance spectroscopy has been used for decades to infer the health status of the structure. Shear-mode acoustic wave resonators and (E/M) coupling were studied in numerous studies [15–20]. In this section, an analytical model of impedance and admittance of free SH-PWAS is reviewed, and extended to bonded SH-PWAS case.

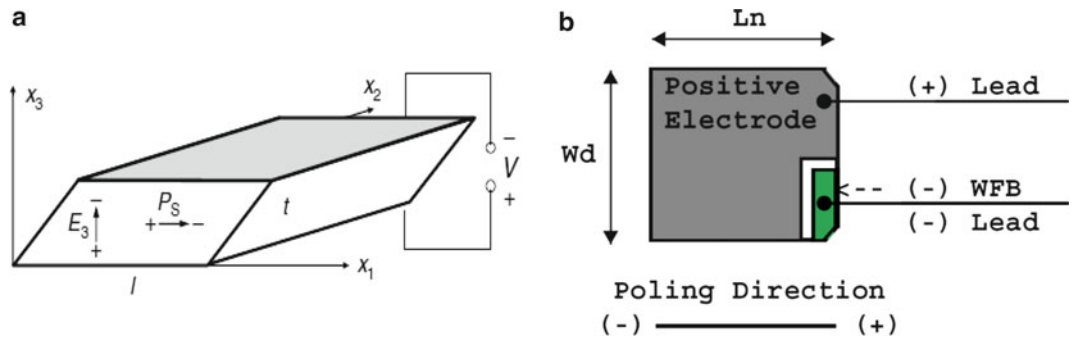

Fig. 3.1 (**a**) Schematic diagram for SH-PWAS, shaded areas are the electrodes. (**b**) Provided transducer schematic from manufacturer. *Source*: APC piezoeceramic Int. Ltd. [4]

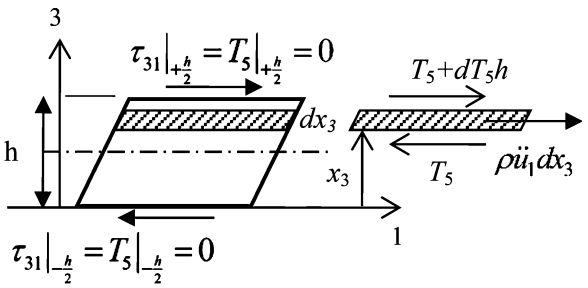

Fig. 3.2 (**a**) Coordinate system and (**b**) free SH-PWAS free body diagram

3.2.1 SH-PWAS Sensing and Actuation Constitutive Relations

Most literature mentioned earlier deal with shear dielectric coupling coefficient d_{15} however this is only applicable if the electric field (E_1) is applied in the in-plane direction and the piezoelectric poling is in thickness direction. In our model and FEM simulations we use d_{35} as the SH-PWAS transducer is having its electrodes on top and bottom and hence electric field is applied along x_3 direction and the poling is applied longitudinally (refer to Fig. 3.1a). For this case, the constitutive equations of piezoelectricity are

$$S_5 = u_1' = s_{55}^E T_5 + d_{35} E_3 \tag{3.1}$$

$$D_3 = d_{35} T_5 + \varepsilon_{33}^T E_3 \tag{3.2}$$

where S_5 is the shear strain component, u_1 is the displacement, s_{55}^E denotes compliance matrix under constant electric field condition, T_5 is shear stress component, d_{35} is piezoelectric coupling coefficients, E_3 represents electric field, D_3 is electric displacement, and ε_{33}^T is the electric permittivity constant of the PWAS material, and $(\ )' = \dfrac{\partial(\ )}{\partial x_3}$.

3.2.2 Free SH-PWAS Electro-mechanical Impedance and Admittance

3.2.2.1 Analytical Modeling Based on Constant Electric Field E_3

The analytical model was studied by the authors in [21]. It starts with the stress free boundary conditions at $\pm\frac{h}{2}$ case, which corresponds to SH-PWAS transducer. Considering Newton law of motion applied to the element in Fig. 3.2, and upon simplification, yields the wave equation for shear waves

$$\mu u_1^{''} = \rho \ddot{u}_1 \tag{3.3}$$

where ρ is piezoelectric material type density, $\ddot{u}_1$ is the second derivative of displacement with respect to time.

Assuming time harmonic solution for displacement, then, the space solution of the differential Eq. 3.3 is

$$\hat{u}_1 = C_1 \sin \gamma x_3 + C_2 \cos \gamma x_3 \tag{3.4}$$

Define speed of SH-wave in the piezoelectric material as c, and the corresponding wave number γ as

$$c^2 = \frac{1}{\rho s_{55}^E}, \quad c = \sqrt{\frac{\mu}{\rho}}, \quad \gamma = \frac{\omega}{c} = \omega \sqrt{\frac{\rho}{\mu}} \tag{3.5}$$

where ω is the circular frequency in rad/s.

Imposing stress free boundary condition $T_5|_{\pm \frac{h}{2}} = 0$ and substitute in Eq. 3.1 to find the constants C_1 and C_2 of Eq. 3.4. This yields the complete displacement and strain response as

$$\hat{u}_1(x_3) = \frac{d_{35}\hat{E}_3}{\gamma} \frac{\sin \gamma x_3}{\cos \frac{1}{2}\gamma h}, \quad \hat{S}_5(x_3) = \frac{\partial \hat{u}_1}{\partial x_3} = d_{35}\hat{E}_3 \frac{\cos \gamma x_3}{\cos \frac{1}{2}\gamma h} \tag{3.6}$$

Electrical Response. Eliminating the stress T_5 between Eqs. 3.1 and 3.2, we obtain electric displacement,

$$D_3 = \frac{d_{35}}{s_{55}^E}\left[u_1^{'} - d_{35}\hat{E}_3\right] + \varepsilon_{33}^T \hat{E}_3 = \varepsilon_{33}\hat{E}_3\left[1 - K_{35}^2\left(1 - \frac{u_1^{'}}{d_{35}\hat{E}_3}\right)\right] \tag{3.7}$$

Integrating the electrical displacement in Eq. 3.7 over electrodes area, results in the electric charge, then integrating over the thickness yields

$$\hat{Q}_{eq} = \frac{\varepsilon_{33}\hat{E}_3 bl}{h}\left[(1 - K_{35}^2)h + K_{35}^2 \frac{\hat{u}_1(x_3)|_{-\frac{h}{2}}^{\frac{h}{2}}}{d_{35}\hat{E}_3}\right] \tag{3.8}$$

where $\hat{Q}_{eq} = \frac{1}{h}\int_{-\frac{h}{2}}^{\frac{h}{2}} Q(x_3)dx_3$. Substituting $\hat{u}_1(x_3)$ from Eq. 3.6. Defining PWAS capacitance as $C = \varepsilon_{33}^T \frac{bl}{h}$, the electric field is related to voltage by $\hat{E}_3 = \frac{\hat{V}}{h}$. The electric current I is defined as the time derivative of electric charge, i.e. $I = \dot{Q} = i\omega Q$, hence the electromechanical (E/M) admittance and impedance of the SH-PWAS can be expressed as

$$Y = \frac{I}{V} = i\omega C\left[1 - K_{35}^2\left(\frac{1 - \tan \frac{1}{2}\gamma h}{\frac{1}{2}\gamma h}\right)\right], \quad Z = \frac{V}{I} = \frac{1}{i\omega C}\left[1 - K_{35}^2\left(\frac{1 - \tan \frac{1}{2}\gamma h}{\frac{1}{2}\gamma h}\right)\right]^{-1} \tag{3.9}$$

3.2.2.2 Analytical Modeling Based on Constant Electric Displacement D_3

The previous constant electric field assumption is usually more appropriate in piezoelectric stacks with internal electrodes, where flow of charge exists (i.e. closed circuit) and the corresponding electric displacement forms a half wave distribution at the resonator [22]. However, in most other cases of single resonators such as thickness shear mode no current flows through the resonator which makes the constant electric displacement assumption (i.e. zero current or open circuit) more realistic. Bar piezoelectric ceramic transformers were studied under constant electric displacement condition [23]; impedance was modeled for the longitudinal mode (d_{31}). The analytical development is similar to one in [24]. Here we show the final results of SH-PWAS E/M admittance and impedance with constant D_3 assumption. Defining $\phi = \frac{1}{2}\gamma h$, the E/M admittance, and impedance are found as

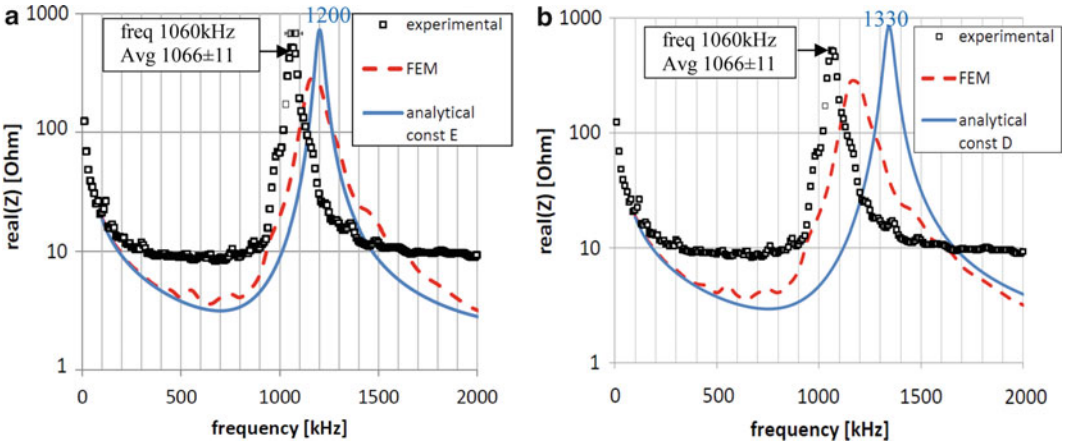

Fig. 3.3 Impedance of free SH-PWAS 15 mm × 15 mm × 1 mm APC 850, analytical model: (**a**) constant E and (**b**) constant D

$$Y = \frac{I}{V} = i\omega C\left[1 - K_{35}^2 \frac{1}{\phi \cot \phi}\right]^{-1}, \quad Z = \frac{1}{i\omega C}\left[1 - K_{35}^2 \frac{1}{\phi \cot \phi}\right] \tag{3.10}$$

The free SH-PWAS capacitance was measured experimentally and found to be 2.76 ± 0.05 nF. SH-PWAS transducers E/M impedance is measured using HP 4194A impedance analyzer. E/M impedance spectroscopy refers to the antiresonances of the free transducer. A sweep of frequency up to 2,000 kHz was performed and the impedance spectrum is compared to FEM and analytical model predictions.

Figure 3.3 shows that the first impedance peak reported experimentally =1,060 kHz (≈1 MHz). Admittance is calculated by inverting the complex value of impedance. From Fig. 3.3b, it is shown that the analytical model with constant electric displacement assumption over predicts the first impedance peak (=1,330 kHz). This draws the conclusion that analytical model with constant electric displacement through thickness is more appropriate for this transducer type.

3.2.3 Bonded SH-PWAS Analytical Model

When the SH-PWAS is bonded to a structure, the displacement of the lower tip of the PWAS can be set equal to u_1^{str} which can be determined from elasticity solution of the bonded structure of thickness $2d$ and then structure dynamic stiffness associated with the transducer can be determined from relation

$$F_{PWAS} = \tau|_{-\frac{h}{2}} A = k_{str} U_1|_{-\frac{h}{2}} \tag{3.11}$$

The bonded SH-PWAS on a plate structure is shown in Fig. 3.4a. Depending on which plane is considered for analysis, the SH-PWAS response can be classified into: (a) axial and flexural response, in 1–3 or z–y plane, (b) SH response, in 2–3 or x–y plane. We start with axial–flexural response in 1–3 plane (Fig. 3.4b).

3.2.3.1 Axial and Flexural Response Solution

Given the boundary conditions and structural properties, then the dynamic structure stiffness $k_{str}(\omega)$ can be evaluated. The applied loads are axial load $f_e(z,t) = \hat{f}(z)e^{i\omega t} \propto F_{PWAS}$ which is acting through structure midplane in addition to the bending moment generated $m_e(z,t) = \hat{m}_e(z)e^{i\omega t} \propto F_{PWAS}d$, where d is the half plate thickness. When incorporating $k_{str}(\omega)$ into consideration; a "constrained PWAS" solution can be developed as follows.

The structure response is evaluated using the normal mode expansion (NME) theory. In NME the loading functions are used to find coefficients C_n which contribute to displacements response at every mode n. The axial force and bending moment can be represented by Heaviside function, $H(z - z_a)$, and linear function of z as shown in Fig. 3.4b, hence the loading functions (shown in Fig. 3.4b) are

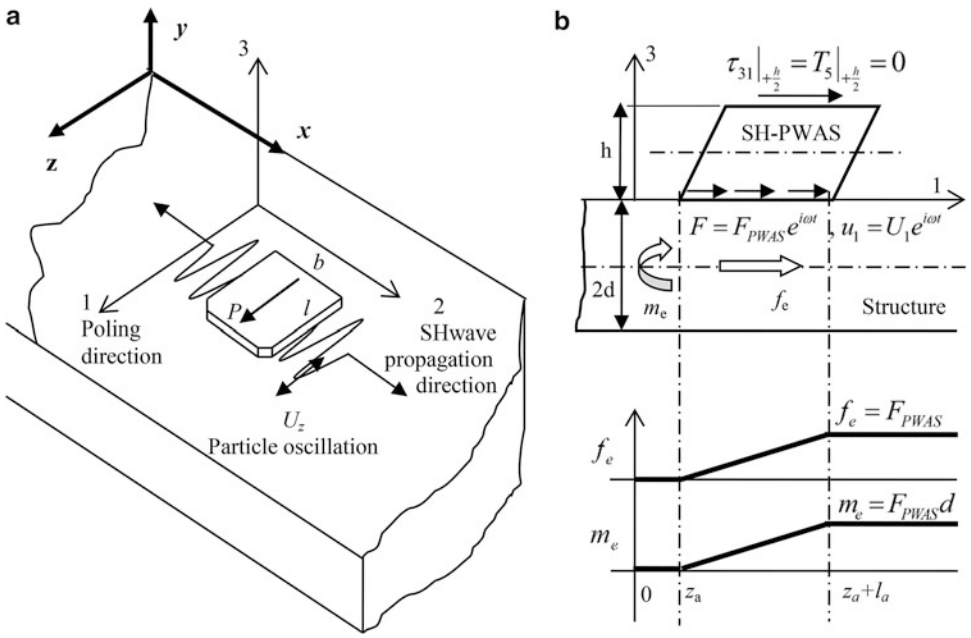

Fig. 3.4 (**a**) Constrained SH-PWAS model and (**b**) interaction between SH-PWAS with the structure, axial and flexural load transfer

$$f_e(z,t) = F_{PWAS}\left\{[(z-z_a)\cdot H(z-z_a)] - \left[\left(z-(z_a+l_a)\right)\cdot H\left(z-(z_a+l_a)\right)\right]\right\}e^{i\omega t} \tag{3.12}$$

$$m_e(z,t) = F_{PWAS}d\left\{[(z-z_a)\cdot H(z-z_a)] - \left[\left(z-(z_a+l_a)\right)\cdot H\left(z-(z_a+l_a)\right)\right]\right\}e^{i\omega t} \tag{3.13}$$

Axial Part. The forced vibration governing equation for axial responses

$$\rho A\ddot{u}(z,t) - EA_u''(z,t) = f_e'(z,t) \tag{3.14}$$

Solving the PDE with the axial loading function yields the factor C_n as

$$C_n = \frac{1}{\left(-\omega^2+\omega_n^2\right)}\frac{F_{PWAS}}{\rho Al}\left[\int_{z_a}^{L} U_n(z)dz - \int_{z_a+l_a}^{L} U_n(z)dz\right] \tag{3.15}$$

And finally the axial displacement can be written as:

$$u_z(x,z,t) = \frac{F_{PWAS}}{\rho Al}\sum_{n=1}^{\infty}\frac{\int_{z_a}^{z_a+l_a} U_n(z)dz}{\left(-\omega^2+2i\zeta\omega\omega_n+\omega_n^2\right)}U_n(z)e^{-i(\gamma_x x-\omega t)} \tag{3.16}$$

Flexural Part. Similarly for flexural response, the forced vibration governing equation is

$$\rho A\ddot{w}(z,t) + EIw''''(z,t) = -m_e''(z,t) \tag{3.17}$$

The final normal mode expanded displacement can be evaluated as

$$w(x,z,t) = \frac{F_{PWAS}d}{\rho A l}\sum_{n=1}^{\infty}\frac{[-W_n(z_a)+W_n(z_a+l_a)]}{\left(-\omega^2+2i\zeta\omega\omega_n+\omega_n^2\right)}W_n(z)e^{-i(\gamma_x x-\omega t)} \tag{3.18}$$

Noting that w displacement is the flexural displacement that is in y-direction in our global co-ordinates. The total axial displacement consists of the part from axial solution as well as the effect of the slope of flexural solution.

$$u_p = u \pm w^{'}d \tag{3.19}$$

Ignoring the x and t terms in Eqs. 3.16 and 3.18, and considering the effective displacement along SH-PWAS length as

$$\left(u_1^{str}\right)_{\text{effective}} = \frac{1}{l_a}\int_0^L u_1^{str}(z)dz \tag{3.20}$$

The dynamic stiffness of the structure $k_{str}(\omega)$ is defined as

$$k_{str}(\omega) = \frac{F_{PWAS}}{\hat{u}_{PWAS}} = \rho_{str}A_{str}l_{str}^2\left\{\sum_{n_a=1}^{\infty}\frac{\left(\int_{z_a}^{z_a+l_a}U_n(z)dz\right)^2}{\left(-\omega^2+2i\zeta_a\omega\omega_{n_a}+\omega_{n_a}^2\right)}+d^2\sum_{n_w=1}^{\infty}\frac{[W_n(z_a+l_a)-W_n(z_a)]^2}{\left(-\omega^2+2i\zeta_w\omega\omega_{n_w}+\omega_{n_w}^2\right)}\right\}^{-1} \tag{3.21}$$

For actual evaluating the dynamic stiffness of the structure, vibration modes need to be determined, and the modes are depending on boundary condition, for instance for free-free structural beam bonded with the SH-PWAS, we have [25]

$$U_n(z) = A_{n_a}\cos\left(\gamma_{n_a}z\right),\quad A_{n_a} = \sqrt{\frac{2}{ml}},\quad \gamma_{n_a} = \frac{n_a\pi}{l},\quad \omega_{n_a} = \gamma_{n_a}c^{str},\quad c_{str} = \sqrt{\frac{E_{str}}{\rho_{str}}},\quad n_a = 1,2,\ldots \tag{3.22}$$

The speed of SH-wave in the piezoelectric material c is different from the axial wave speed in structure, hence the latter is denoted by c_{str}. For flexural modal solution,

$$W_{n_w}(z) = A_{n_w}\left[\cosh\gamma_{nW}z+\cos\gamma_{n_w}z-\sigma_{n_w}\left(\sinh\gamma_{n_w}z+\sin\gamma_{n_w}z\right)\right] \tag{3.23}$$

$$\omega_{n_w} = \gamma_{n_w}^2 a_{flex},\quad a_{flex} = \sqrt{\frac{EI_{str}}{\rho_{str}A_{str}}},\quad A_{nw} = 1/\sqrt{\int_0^l W_{n_w}^2(z)dz} \tag{3.24}$$

where the numerical values for σ_{n_w}, $l\gamma_{n_w}$ can be found from [10], p. 89.

3.2.3.2 Shear Horizontal Response Solution

With similar procedure followed in the axial response, but taking into consideration the plane of analysis containing SH wave propagation direction, i.e. plane 2–3 in Fig. 3.4a. The corresponding setup is shown in Fig. 3.5b. The SH response in this case is

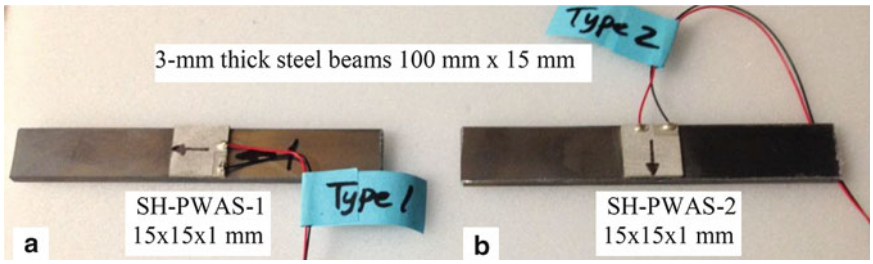

Fig. 3.5 Experimental setup for SH-PWAS bonded on 3-mm steel beams (**a**) orientation-1 and (**b**) orientation-2 (the *black arrow* indicates poling direction)

$$\hat{u}_{PWAS}^{SH} = \frac{F_{PWAS}}{\rho_{str} A_{str} l_{str}^2} \left\{ \sum_{n_a=1}^{\infty} \frac{\left(\int_{z_a}^{z_a+l_a} U_n(z) dz \right)^2}{\left(-\omega^2 + 2i\zeta_a \omega \omega_{n_a} + \omega_{n_a}^2 \right)} \right\} \tag{3.25}$$

where the corresponding eigenvalues will be associated with SH standing waves, i.e

$$U_n(z) = A_{n_a} \cos\left(\gamma_{n_a} z\right), \quad A_{n_a} = \sqrt{\frac{2}{ml}}, \quad \gamma_{n_a} = \frac{n_a \pi}{l}, \quad \omega_{n_a} = \gamma_{n_a} c_{str}^{SH}, \quad c_{str}^{SH} = \sqrt{\frac{G_{str}}{\rho_{str}}}, \quad n_a = 1, 2, \ldots \tag{3.26}$$

Given the boundary conditions and structural properties, the dynamic structure stiffness $k_{shear}(\omega)$ can be evaluated and used in the PWAS solution, to model it as "constrained PWAS". Using the same approach as in Sect. 2.2.1, and using modified "constrained" boundary condition, Eq. 3.11, we get

$$U_1'\big|_{-\frac{h}{2}} = \frac{r}{h} U_1\big|_{-\frac{h}{2}} + d_{35} \hat{E}_3 \tag{3.27}$$

where

$$r = \frac{k_{str}}{k_{PWAS}} \tag{3.28}$$

is defined as the dynamic stiffness ratio, and the transducer stiffness is defined as $k_{PWAS} = \frac{\mu A}{h}$ where $A = bl$

whereas the condition at top surface of the SH-PWAS is

$$U_1'\big|_{\frac{h}{2}} = s_{55}^E . 0 + d_{35} \hat{E}_3 \tag{3.29}$$

With the same analysis, we get the constrained SH-PWAS electromechanical impedance.

3.3 FEM and Experimental Validation of SH-PWAS Impedance Response

3.3.1 Free SH-PWAS FEM

A multiphysics finite element model (FEM) was constructed for free SH-PWAS to show the shear deformation modeshapes. The transducer is modeled with COMSOL multiphysics using coupled physics, where harmonic voltage is applied to the top electrode and the mechanical response is recorded. The free SH-PWAS dimensions are 15 mm ×15 mm × 1 mm. SH-PWAS material is APC850, detailed properties can be found from APC website [4]. From provided information, the transducer capacitance was provided as 3.48 ± 20 % nF. A frequency sweep from 10 to 2,000 kHz is performed

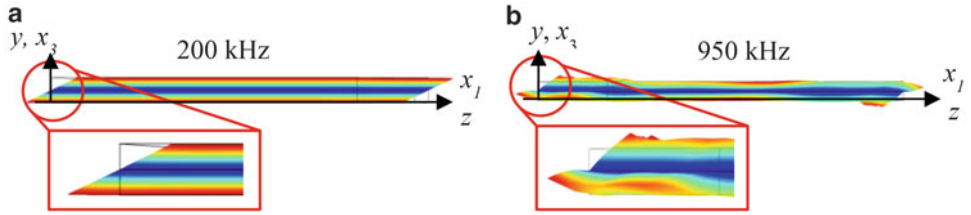

Fig. 3.6 Modeshapes of vibrations for free SH-PWAS using finite element analysis, (**a**) mode shape at 200 kHz and (**b**) modeshape at resonance frequency 950 kHz

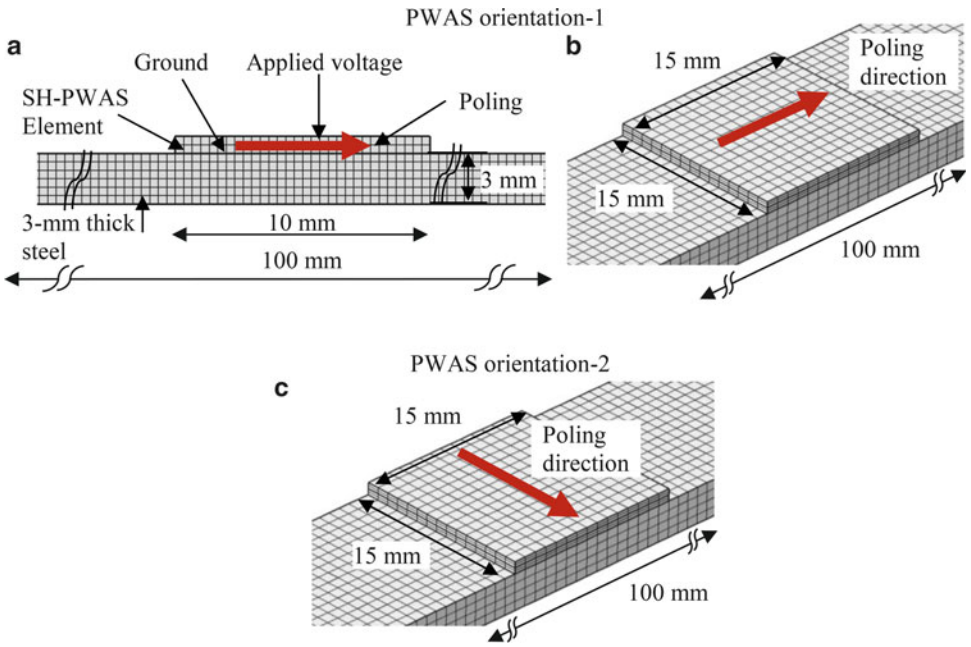

Fig. 3.7 FEM for bonded SH-PWAS on 3-mm thick steel beams: SH-PWAS orientation-1: (**a**) 2-D model, (**b**) 3-D model and (**c**) SH-PWAS orientation-2, 3-D model

in frequency domain solver in the FEM software. The maximum element size is selected 0.5 mm. the coordinate system is defined such that the poling of SH-PWAS is defined along x_1 direction. The deformation modeshapes are captures and the electromechanical (E/M) impedance is calculated to be compared with experimental and analytical results. Figure 3.6 shows the modeshapes of vibration at (a) 200 kHz to show the shear deformation of the transducer, (b) first resonance frequency of the transducer at 950 kHz, where nonlinear effects starts to appear at SH-PWAS ends.

3.3.2 Constrained SH-PWAS Models

Finite element models were constructed for bonded SH-PWAS on 3-mm thick steel beams. Three models are constructed: (1) 2-D model for the case where poling of the SH-PWAS is along beam length, (2) 3-D model for the same case of having poling direction parallel to beam length, and (3) 3-D model for the case of transducer poling perpendicular to the beam length. E/M impedance is calculated for different models for comparison with bonded SH-PWAS analytical models, and experimental results.

Steel beams configurations are used to enhance structure—to—transducer mass ratio. Figure 3.7 shows the two different configurations of SH-PWAS bonded on 3-mm steel beams, 2-D and 3-D models. For PWAS orientation-1, 2-D FEM (Fig. 3.7a) and 3-D FEM (Fig. 3.7b) were constructed. PWAS orientation-2 refers to the situation where the SH-PWAS is

Table 3.1 Dimensions and material properties for FEM of SH-PWAS bonded on steel

	Steel beam	SH-PWAS
Dimensions (mm)	100 × 15 × 3	15 × 15 × 1 on steel
Density ρ (kg/m^3)	7,750	7,600
Modulus (GPa)	E = 200	G = 24.6
Relative dielectric constant $\varepsilon_{33}^T/\varepsilon_0$	–	1,750
Piezoelectric coefficient d_{35} (m/V)	–	590E–12
Hysteresis damping ζ	0.5 %	–
Compliance damping factor η	–	4 %
Permittivity damping δ	–	4 %

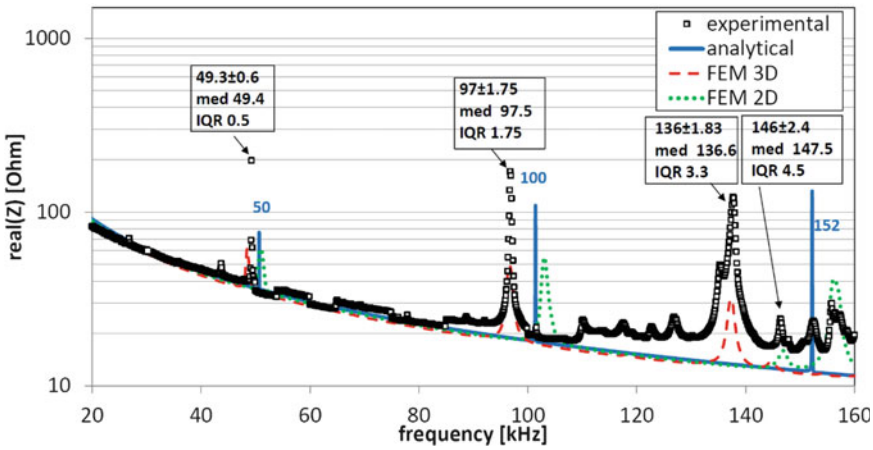

Fig. 3.8 Comparison between experimental results, analytical predictions and finite element simulations for E/M impedance of SH-PWAS bonded on 3-mm thick steel beam (orientation-1)

rotated 90° before bonding on the steel beam, hence, the poling direction in Fig. 3.7c is parallel to beam width, in such situation our analytical model suggests the excitation of shear horizontal standing waves along the beam.

The frequency sweep performed is 1–160 kHz. The maximum element size used is 0.5 mm in the 2-D model. For the 3-D models, transducer is meshed with 1-mm elements and 4-elements per the 1-mm thickness. The steel beam is meshed with 1-mm elements as well and 0.75 mm element size through thickness. The complete listing of model dimensions and material properties are listed in Table 3.1.

3.3.3 Experiments and Comparison with Predictive Models

Experiments were performed on 3-mm thick steel beams. The beam thickness and steel material was selected such that the beam—to—transducer mass ratio is 4 %. The experimental setup for steel beams case is shown in Fig. 3.5.

For the axial–flexural response, comparison between experimental, 3-D finite element simulations, and analytical predictions showed good agreement, as shown in Fig. 3.8. The first fundamental mode impedance peak is measured experimentally as 49.3 ± 0.6 kHz, which agrees with 3-D and 2-D FEM. The second peak is 97 ± 1.75 kHz, with perfect agreement with FEM, analytical prediction is 100 kHz. The third peak needs some investigation. The experimental measurement is 136 ± 1.8 kHz, which matches with 3-D FEM. However the analytical model (152 kHz) shows more agreement with (2-D FEM ≈ 146 kHz).

Referring to 3-D FEM modeshapes at these frequencies (Fig. 3.9), it is noticed that the modeshape of vibration at 137 kHz (which is captured experimentally and by 3-D FEM) involves coupled vibration in the beam length and width. This is not considered in the analytical model, which is 1-D model (beam length and thickness). The analytical model prediction of 151 kHz is more representing the mode shown in Fig. 3.9c (145 kHz by 3-D FEM).

When the SH-PWAS is installed in orientation-2 to generate SH standing waves across beam length, the predicted 3-D FEM modeshapes show the SH motion patterns (Fig. 3.10).

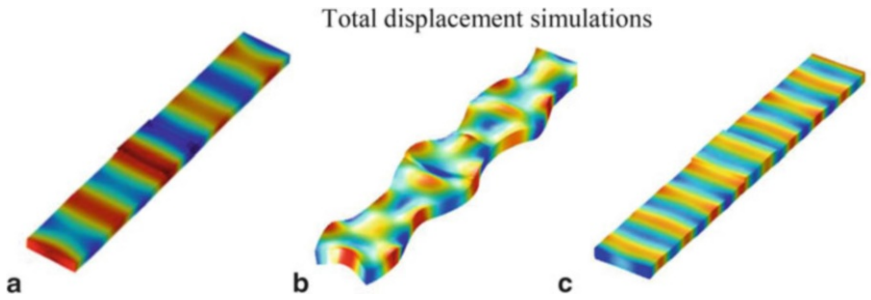

Fig. 3.9 Modeshapes of vibrations of 3-mm thick steel beams with bonded SH-PWAS in orientation-1 (axial–flexural orientation), at excitation frequency: (**a**) 48 kHz, (**b**) 137 kHz, and (**c**) 145 kHz

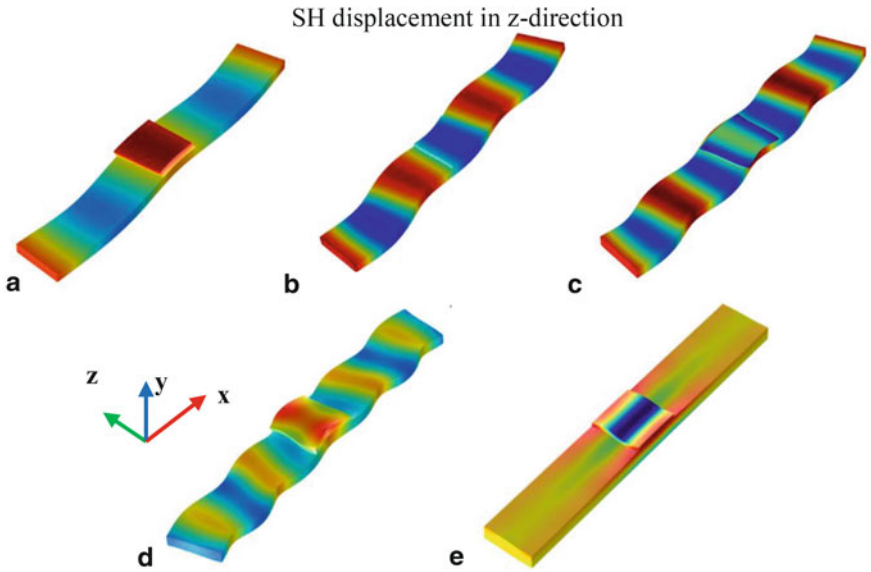

Fig. 3.10 Modeshapes of vibrations of 3-mm thick steel beam with bonded SH-PWAS in orientation-2 (SH orientation) at excitation frequency: (**a**) 30 kHz, (**b**) 60 kHz, (**c**) 90 kHz, (**d**) 123 kHz, and (**e**) 146 kHz

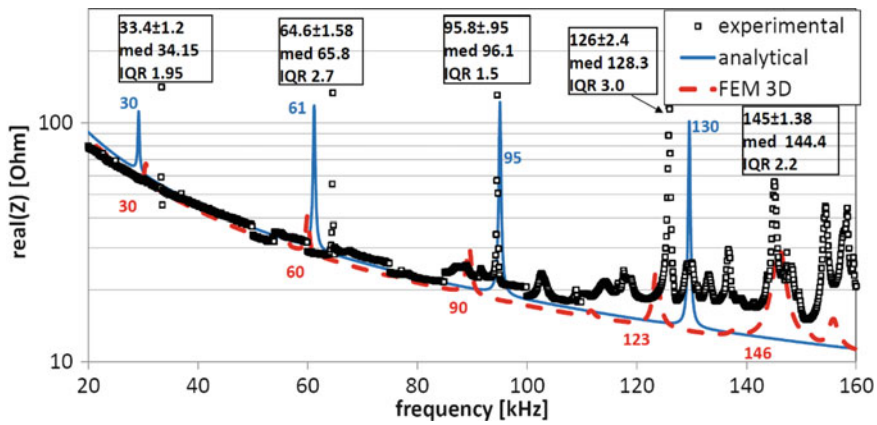

Fig. 3.11 Comparison between experimental results, analytical predictions, and finite element simulations for E/M impedance of SH-PWAS bonded on 3-mm thick steel beam (orientation-2)

Comparison between experimental results, analytical predictions, and finite element simulations (Fig. 3.11) shows good agreement for SH-PWAS orientation-2 that generates SH deformation in the structure. It is noticed that the impedance peaks are multiples of ≈30 kHz. The third peak of 95 kHz shows the best match between experiments and simulations. Also the experimental measurement at 145 kHz shows agreement with 3-D FEM, however this peak is not captured by the analytical prediction. Referring to modeshapes (Fig. 3.10d), it is noticed that the 5th mode of vibration is more or less local mode and it drives the beam into some sort of torsional vibration. The 4th mode starts not to be uniform SH deformation; it may contain coupled modes of vibration.

3.4 SH-PWAS for Composites SHM

3.4.1 Materials

The first material under the study is 1-mm thick woven GFRP plate. It has six plies of woven fabric. The material density is ρ = 1,960 k/m^3. The stiffness matrix [C] provided for this material [26] is

$$C = \begin{bmatrix} 28.7 & 5.7 & 3 & & & & \\ 5.7 & 28.7 & 3 & & & & \\ 3 & 3 & 12.6 & & & & \\ & & & 4.9 & & & \\ & & & & 4.9 & & \\ & & & & & 4.1 & \end{bmatrix} GPa \tag{3.30}$$

For modelling purpose, we use Rayleigh damping with the mass proportional coefficient α_M = 0.2 rad/s and stiffness proportional coefficient $\beta_K = 10^{-8}$ s/rad.

The 2-mm thick CFRP plate is consisting of woven prepreg carbon fabrics in epoxy resin.

There are eight layers with orientation [0/45/45/0]s. the material density is ρ = 1605 kg/m^3. The material mechanical properties for 0-direction ply were provided by Hexcel manufacturer in Table 3.2.

3.4.2 Predictive FEM and Comparison with Experiments

Two models of SH-PWAS bonded on GFRP and CFRP plates were constructed. The plate model had the dimensions 150 mm × 150 mm × 1 mm. The excitation signal amplitude was 10 V and the solver used was frequency domain analysis, where a frequency sweep is performed up to 5 MHz.

The experimental measurements were performed as a sweep up to 5 MHz. The real and the imaginary components of E/M impedance were recorded, we display the measured real (Z) and the corresponding calculated real(Y), where Y is the E/M admittance. The admittance is more representing parameter for resonance of the structure, where the structure vibrates more when the admittance reaches a peak value; while the impedance is the resistance or the anti-resonance situation. Experimental results are compared with FEM simulations and are showed in Fig. 3.12a, b for woven GFRP plate. Electromechanical impedance spectroscopy (EMIS) method is a good candidate for SHM systems to detect small damages in vicinity of the transducer. Exciting the SH-PWAS at relatively smaller frequencies will resonate the whole structure; simulations at such frequencies occurred at 20 and 50 kHz. Similar comparison between experiments and FEM simulations were studied for CFRP plate of same size of 150 mm × 150 mm, but 2-mm thick plate. Results of CFRP plate are shown in Fig. 3.12c, d.

Table 3.2 CFRP layer mechanical properties for 0-direction ply, provided by Hexcel manufacturer (http://www.hexcel.com)

E_{11}	E_{22}	E_{33}	n_{12}	n_{13}	n_{23}	G_{12}	G_{13}	G_{23}
65 GPa	67 GPa	8.6 GPa	0.09	0.09	0.3	5 GPa	5 GPa	5 GPa

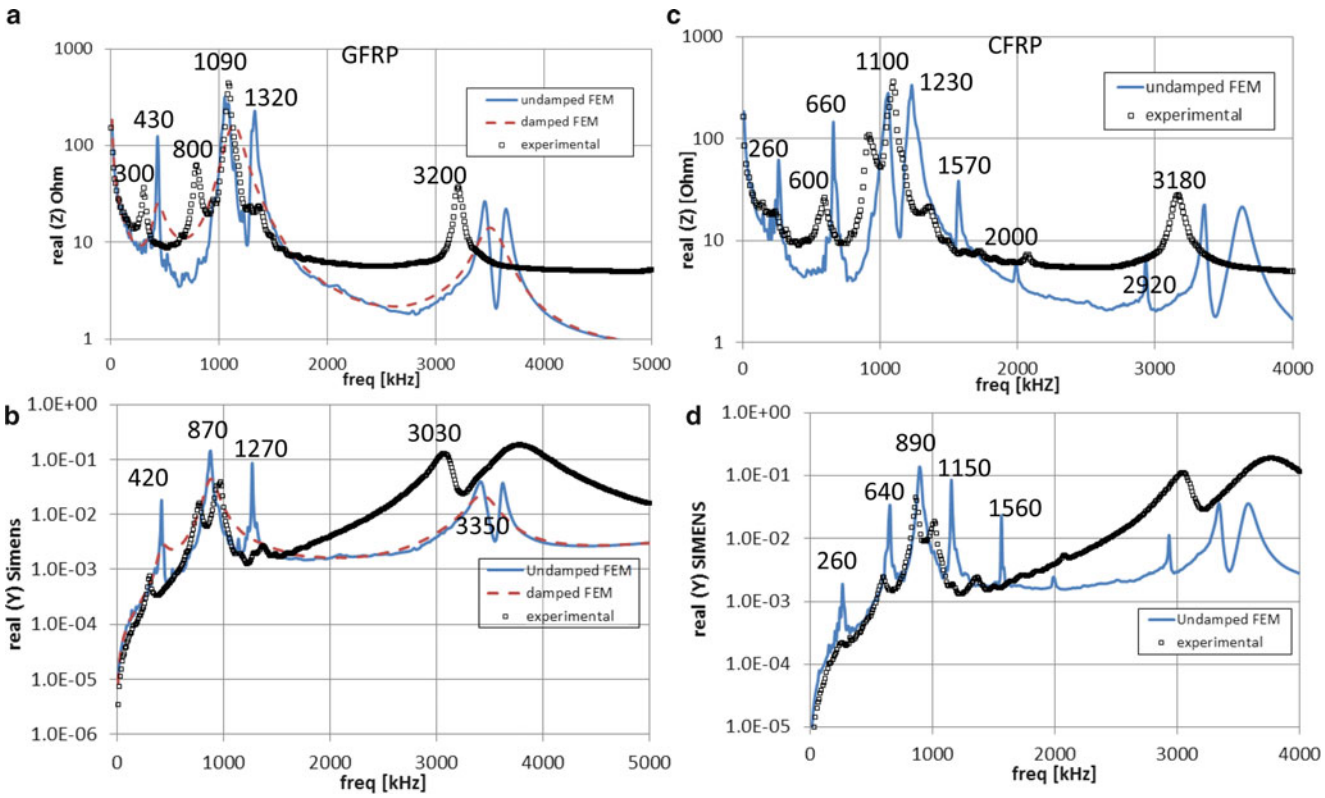

Fig. 3.12 E/M response of SH-PWAS bonded on woven GFRP plate: (**a**) impedance, (**b**) admittance. E/M response of SH-PWAS bonded on [0/45/45/0]s CFRP plate: (**c**) impedance, and (**d**) admittance

3.5 Summary and Conclusions

The study presented predictive analytical models for electromechanical impedance of shear horizontal (SH) coupled piezoelectric wafer active sensor (PWAS) transducers. Investigation of E/M impedance of free SH-PWAS indicated that analytical model with constant electric field assumption is more representing the experimental case and FEM. The first resonance frequency of the free transducer is 950 kHz (admittance). Experiments and FEM of bonded PWAS on structures showed the local resonance effects of the PWAS at frequencies greater than 100 kHz. A case study was performed for SH-PWAS bonded on 3-mm steel beams. The analytical model showed good agreement with FEM simulations and experimental results. SH-PWAS was showed to have directivity effects, where axial–flexural response is obtained when transducer poling direction is parallel to beam length. When the transducer poling direction in perpendicular to beam length, SH response is obtained. The E/M impedance and admittance of SH-PWAS bonded to GFRP and CFRP composites plates was modeled by FEM and compared with experiments. Results have showed good agreement which opens the opportunity to use these predictive models to investigate more parameters and damage condition.

Acknowledgements This work was supported by Air Force Office of Scientific Research grant #FA9550-11-1-0133, program manager Dr. David Stargel; and the Office of Naval Research grant #N00014-11-0271, program manager Dr. Ignacio Perez.

References

1. Fortunko CM, King RB, Tan M (1982) Nondestructive evaluation of planar defects in plates using low-frequency shear horizontal waves. J Appl Phys 53:3450–3458
2. Rose J, Pelts S, Li J (2000) Quantitative guided wave NDE. In: 15th world conference on non-destructive testing, Rome
3. Glazounov A, Zhang Q (1998) Piezoelectric actuator generating torsional displacement from piezoelectric d15 shear response. J Appl Phys Lett 72:2526–2528

4. APC International Ltd. Physical and piezoelectric properties of APC materials. http://www.americanpiezo.com
5. Ferroperm Piezoceramics. http://www.ferroperm-piezo.com/
6. Baillargeon BP (2003) Active vibration suppression of smart structures using piezoelectric shear actuators, Paper 284. Electronic Theses and Dissertations, The University of Maine
7. Sun C, Zhang X (1995) Use of thickness-shear mode in adaptive sandwich structures. J Smart Mater Struct 4:202–206
8. Benjeddou A, Trindade MA, Ohayon R (1997) A unified beam finite element model for extension and shear piezoelectric actuation mechanisms. J Intell Mater Syst Struct 8(12):1012–1025
9. Le Crom B, Castaings M (2010) Shear horizontal guided wave modes to infer the shear stiffness of adhesive bond layers. J Acoust Soc Am 127(4):2220–2230
10. Giurgiutiu V (2008) Structural health monitoring with piezoelectric wafer active sensors. Elsevier Academic Press, Amsterdam
11. Lee J, Kim Y, Cho S (2009) Beam-focused shear-horizontal wave generation in a plate by a circular magnetostrictive patch transducer employing a planar solenoid array. J Smart Mater Struct 18:015009
12. Gao H, Ali S, Lopez B (2010) Inspection of austenitic weld with EMATs. In: Review of progress in quantitative nondestructive evaluation 29B, b
13. Zhu J, Chen W, Yang J (2013) Overtone frequency spectra for x3-dependent modes in AT-cut quartz resonators. IEEE Trans Ultrason Ferroelectr Freq Control 60(4):858–863
14. Du J, Wang W, Chen G, Wu R, Huang D, Ma T (2013) An analysis of thickness-shear vibrations of doubly rotated quartz crystal plates with the corrected first order mindlin plate equations. IEEE Trans Ultrason Ferroelectr Freq Control 60(11):2371–2379
15. Milyutin E, Gentil S, Muralt P (2008) Shear mode bulk acoustic wave resonator based on c-axis oriented AlN thin film. J Appl Phys 104:084508
16. Milyutin E, Muralt P (2011) Electro-mechanical coupling in shear-mode FBAR with piezoelectric modulated thin film. IEEE Trans Ultrason Ferroelectr Freq Control 58:685–688
17. Mueller V, Zhang Q (1998) Shear response of lead zirconate titanate piezoceramics. J Appl Phys 83:3754–3761
18. Yanagitani T (2011) Shear mode piezoelectric thin film resonators. In: Beghi MG (ed) Acoustic waves—from microdevices to helioseismology. InTech, Tokyo, pp 501–520
19. Cheng C, Chen S, Zhang Z, Lin Y (2007) Analysis and experiment for the deflection of a shear-mode PZT actuator. Smart Mater Struct 16:230–236
20. Ji W, Shen L-J (2005) Exact thickness-shear resonance frequency of electroded piezoelectric crystal plates. J Zhejiang Univ Sci 6A(9):980–985
21. Kamal A, Lin B, Giurgiutiu V (2013) Predictive modeling of PWAS-coupled shear horizontal waves, Paper 8695-0F. SPIE NDE Conf Proc 8695:1–15
22. Sherrit S, Djrbashian A, Bradford S (2013) Analysis of the impedance resonance of piezoelectric multi-fiber composite stacks. In: Proceedings of SPIE, non destructive evaluation, 10–14 March, San Diego, CA
23. Erhart J, Pulpan P, Rusin L (2013) Bar piezoelectric ceramic transformers. IEEE Trans Ultrason Ferroelectr Freq Control 60(7):1479–1486
24. Kamas T, Lin B, Giurgiutiu V (2013) Analytical modeling of PWAS in-plane and out-of-plane electromechanicalimpedance spectroscopy (EMIS), Paper 8692-27. SPIE NDE Conf Proc 8692:1–13
25. Giurgiutiu V, Zagrai A (2000) Characterization of piezoelectric wafer active sensors. J Intell Mater Syst Struct 11:959–976
26. Pollock P, Yu L, Sutton MA, Guo S, Majumdar P, Gresil M (2012) Full-field measurements for determining orthotropic elastic parameters of woven glass-epoxy composites using off-axis tensile specimens. Exp Tech 1–11. doi: 10.1111/j.1747-1567.2012.00824.x

Chapter 4
Elastic Properties of CYCOM 5320-1/T650 at Elevated Temperatures Using Response Surface Methodology

Arjun Shanker, Rani W. Sullivan, and Daniel A. Drake

Abstract The structural health of composite structures is dependent on environmental conditions during their service life. Elevated temperatures can reduce the overall stiffness and strength of the composite, thereby increasing the likelihood of premature failure. The effect of elevated temperature on the elastic properties (longitudinal modulus, transverse modulus, shear modulus and Poisson's ratio) of the out-of-autoclave carbon/epoxy prepreg (CYCOM 5320-1/T650) was investigated using a design of experiments approach. Tensile tests at four temperatures (24, 71, 118, and 166 °C) below the glass transition temperature (T_g) (177 °C) of the polymer matrix were performed according to a completely randomized design. Response surface models (RSMs) for predicting the elastic properties were developed using the analysis of variance procedure. The RSMs indicate that elevated temperatures have no significant effect on the longitudinal modulus and Poisson's ratio of the material system. However, the degradation of the transverse and shear moduli due to increasing temperature is successfully represented by a linear and a cubic RSM, respectively.

Keywords Response surface modeling • Out-of-autoclave prepreg • Design of experiments • Polymer matrix composites

4.1 Introduction

Advanced composite materials are widely used in the aerospace industry due to their high strength to weight ratio and their tailorability for various design applications. Composite material properties are highly dependent on the fabrication procedure and composite components are typically cured in an autoclave to achieve aerospace-grade quality required for primary structures. However, access to large autoclaves can be limited and expensive. Out-of-autoclave (OoA) composite materials provide an excellent alternative to autoclaved composites due to their excellent mechanical properties, ease of fabrication, and reduced cost. Typically, OoA prepregs are fabricated using vacuum bag molding techniques and cured at vacuum pressure at low temperatures (93–121 °C); these prepregs ensure even resin distribution, avoiding resin-rich areas that are typically produced with infusion processes [1].

Since OoA prepregs are being used in primary structural components in a variety of service environments, proper material characterization for a wide range of stress and temperature levels is necessary. Studies have shown that the longitudinal moduli of epoxy/carbon composites at elevated temperatures do not vary significantly with temperature [2–5]. However at elevated temperatures, transverse and shear moduli have been shown to decrease by as much as 80 % of their respective room temperature modulus [6].

In this research, the elastic material properties of an OoA epoxy/carbon fiber composite prepreg are experimentally determined at four elevated temperatures (24, 71, 118, and 166 °C) using a design of experiments (DOE) approach. Specimens were fabricated using prepreg layup followed by a vacuum bag cure in a 177 °C oven. The specimens were

A. Shanker
R & D, BST Nano Carbon, 16275 Technology Drive, San Diego, CA 92127, USA

R.W. Sullivan (✉)
Department of Aerospace Engineering, Mississippi State University, Mail Stop 9549, Starkville, MS, USA
e-mail: sullivan@ae.msstate.edu

D.A. Drake
Structural SYS ANLYS & Loads, The Boeing Company, 4000 Lakewood Blvd., Long Beach, CA 90808-1700, USA

G. Tandon (ed.), *Composite, Hybrid, and Multifunctional Materials, Volume 4: Proceedings of the 2014 Annual Conference on Experimental and Applied Mechanics*, Conference Proceedings of the Society for Experimental Mechanics Series,
DOI 10.1007/978-3-319-06992-0_4,

tested in tension to determine their longitudinal, transverse and shear moduli at each temperature. Based upon the DOE approach, response surface models (RSMs) were developed to predict the elastic properties of the composite material for the design temperature range (24–166 °C).

4.2 Design of Experiments (DOE) Approach

A completely randomized design (CRD) was used to develop the RSMs to determine the effect of temperature on the material properties of the OoA epoxy/carbon composite (CYCOM 5320-1/T650). The CRD was chosen due to the flexibility in selecting any number of treatments and repeats. A completely randomized design relies on the randomization of the experimental tests to control the effects of extraneous variations. In a CRD, it is assumed that extraneous factors will affect treatment conditions equally and any significant changes between conditions can be attributed to the independent variables. Three specimens per temperature and specimen configuration were tested and the CRD was chosen with one independent factor (temperature) at four levels (24, 71, 118, and 166 °C). Therefore, a total of 36 tensile experiments were conducted to obtain the elastic moduli (longitudinal, transverse and shear) and Poisson's ratio. The randomized order of the tensile experiments, with three repeats per temperature for each of the three laminate configurations ($[0]_8$, $[90]_{10}$, $[\pm 45_8]_S$), is shown in Table 4.1.

The mathematical model used for the CRD to evaluate the responses from each run can be expressed as [6]

$$\begin{aligned} Y_{ij} &= \mu + \tau_i + e_{ij} \\ i &= 1, 2, \ldots P \\ j &= 1, 2, \ldots r \\ e_{ij} &\sim N(0, \sigma^2) \end{aligned} \tag{4.1}$$

where, Y_{ij} is the measured response on the j^{th} unit to the i^{th} treatment, μ the overall population mean, τ_i is the i^{th} population treatment effect ($\mu_i - \mu$), and e_{ij} is the random error associated with the j^{th} response to the i^{th} treatment. P is the number of treatments and r is the number of repeats.

The formulation of the RSM is dependent on the number of factors being considered. A generalized form of the RSM is

$$\overline{Y}_{ij} = \beta_0 + \beta_1 X_i + \beta_2 X_i^2 + \cdots + \beta_{p-1} X_i^{p-1} + e_{ij} \tag{4.2}$$

Here, $\overline{Y}_i$ is the response of interest (i.e., longitudinal modulus, transverse modulus, shear modulus or Poisson's ratio), X_i is the level of the factor, temperature. The $\beta_0, \beta_1, \ldots, \beta_{p-1}$ are the unknown regression parameters, where $i = 1, 2, 3$. Additionally, e_i is the random error term, which is assumed to be distributed with a zero mean and constant variance.

The method of least squares (LSQ) was used to perform a trend analysis of the mean response relative to the levels of the treatment variable. The LSQ method was used to determine parameter estimates ($b_0, b_1, \ldots, b_{p-1}$) that approximate the unknown regression parameters $\beta_0, \beta_1, \ldots, \beta_{p-1}$.

Table 4.1 Order of tests using CRD for each laminate configuration ($[0]_8$, $[90]_{10}$, $[\pm 45_8]_S$)

Experiment order	Temperature (°C)
1	118
2	166
3	71
4	166
5	24
6	24
7	166
8	71
9	24
10	118
11	118
12	71

$$\overline{\overline{Y}}_i. = b_0 + b_1 X_i + b_2 X_i^2 + \cdots + b_{p-1} X_i^{p-1} + e_i \tag{4.3}$$

where the overbars (=) indicate that the response of interest $\left(\overline{\overline{Y}}\right)$ is an estimate of the "true" response (Y).

4.3 Experimental Method

4.3.1 Material Description

The material used in this study is an out-of-autoclave (OoA) carbon fiber/epoxy prepreg (CYCOM 5320-1/T650, Cytec Industries) with a resin content of 33 %. The toughened epoxy resin CYCOM 5320-1/T650 is typically used for OoA composite manufacturing of primary structural components. The fiber used in the prepreg is the T650 carbon fiber, with a 12 K fiber tow, a fiber areal weight (FAW) of 215 g/m^2. It should be noted that the prepreg used in this study was manufactured in October 2010 and stored at –7 °F until it was used for manufacturing the test articles in April 2013. Therefore, the material was approximately 2.5 years past its shelf life at the time of fabrication.

4.3.2 Specimen Fabrication Process

The specimens were fabricated using a standard prepreg lay-up and vacuum bag technique. Three laminate configurations, $[0]_8$, $[90]_{10}$, and $[\pm 45_8]_S$, were fabricated to obtain the longitudinal modulus E_{11} and Poisson's ratio ν_{12}, transverse modulus E_{22} and shear modulus G_{12}, respectively, as given in Table 4.2 [7, 8].

The test laminates were cured under vacuum bag pressure for 3 h at 121 °C, followed by a post-cure at 177 °C for 2 h. Tab materials were bonded to test laminates using Hysol EA 9394 adhesive which contained glass beads of 1.016 mm diameter to maintain uniform bond thickness. Individual specimens were carefully cut using a wet tile saw.

4.3.3 Testing Procedure

An Instron model 5889 electromechanical test frame with a 100 kN load cell was used to perform tension tests to determine the various mechanical properties. Bi-axial strain gages (CEA-06-125UT-350, Vishay Micromeasurements®) were used to obtain strain measurements in the longitudinal (loading direction) and transverse directions. Tension experiments were performed over a temperature range of 24–166 °C. All tests were conducted in accordance to the CRD, using the appropriate ASTM standard as given in Table 4.2. A constant 2 mm/min head displacement rate was used for all of the testing [7].

4.4 Results

4.4.1 Experimental

Results from tensile tests at 24, 71, 118 and 166 °C for the $[0]_8$, $[90]_{10}$, and $[\pm 45_8]_S$ composite specimens are shown in Figs. 4.1, 4.2, and 4.3, respectively. The elastic properties (longitudinal modulus, transverse modulus, shear modulus, and Poisson's ratio) are summarized in Table 4.3. It is important to note that the $[0]_8$ degree specimens at 166 °C failed

Table 4.2 Specimen description with corresponding ASTM standards to obtain the moduli and Poisson's ratio

Specimen configuration	Dimensions (mm)	Standard	Property
$[0]_8$	w = 12.8, l = 13, t = 1.6	ASTM D3039	Longitudinal modulus and Poisson's ratio [7]
$[90]_{10}$	w = 23, l = 180, t = 2	ASTM D3039	Transverse modulus [7]
$[\pm 45]_{16}$	w = 23.5, l = 145, t = 3.3	ASTM D3518	Shear modulus [8]

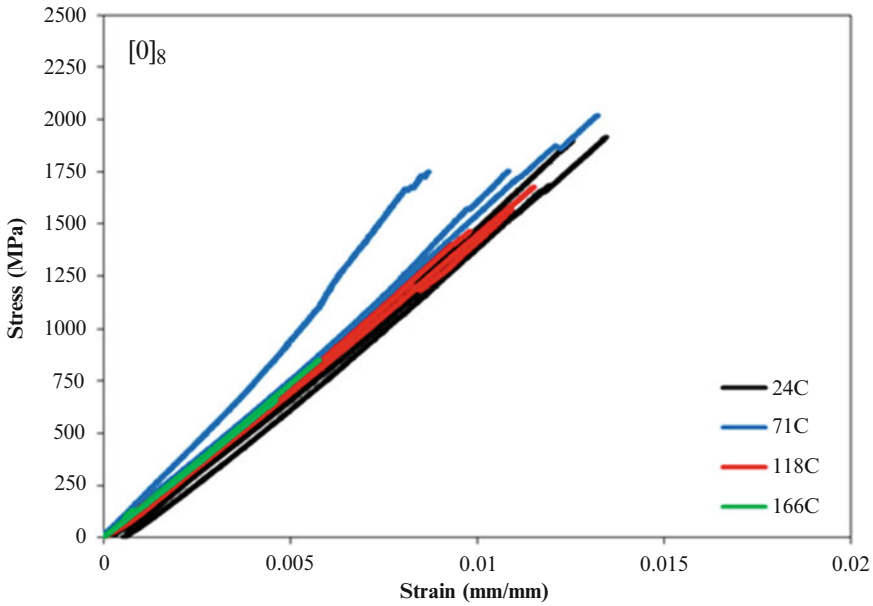

Fig. 4.1 Stress–strain curves at (**a**) 24 °C, (**b**) 71 °C, (**c**) 118 °C, (**d**) 166 °C for the $[0]_8$ specimens (Color figure online)

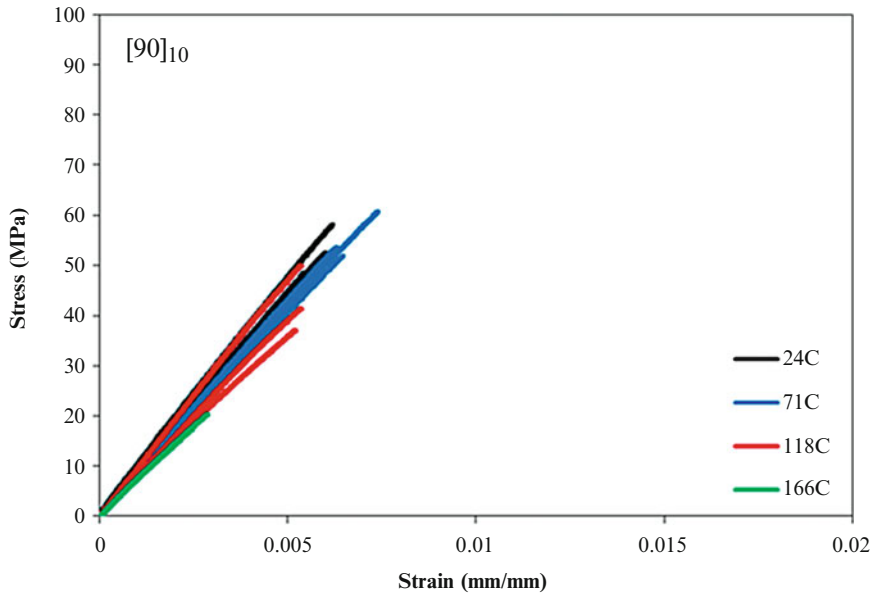

Fig. 4.2 Stress–strain curves at (**a**) 24 °C, (**b**) 71 °C, (**c**) 118 °C, (**d**) 166 °C for the $[90]_{10}$ specimens (Color figure online)

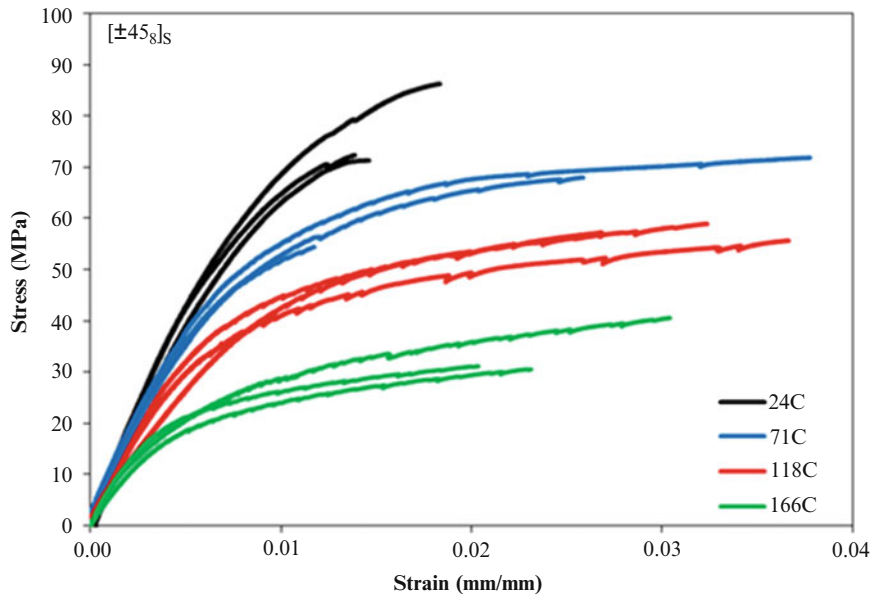

Fig. 4.3 Stress–strain curves at (**a**) 24 °C, (**b**) 71 °C, (**c**) 118 °C, (**d**) 166 °C for the $[\pm 45_8]_s$ specimens (Color figure online)

Table 4.3 Longitudinal, transverse, and shear moduli and Poisson's ratio obtained at 24, 71, 118, and 166 °C

Run	Temperature (°C)	Longitudinal modulus, E_1 (GPa)	Transverse modulus, E_2 (GPa)	Shear modulus, G_{12} (GPa)	Poisson's ratio (ν_{12})
1	118	152.9	7.2	6.4	0.34
2	166	150.7	7.1	4.5	0.29
3	71	152.1	8.4	8.4	0.33
4	166	141.3	7.3	4.4	0.33
5	24	142.0	8.8	9.6	0.31
6	24	146.3	8.9	9.5	0.30
7	166	140.3	7.4	4.8	0.32
8	71	145.2	8.6	8.0	0.33
9	24	147.7	9.4	8.6	0.33
10	118	134.8	7.9	5.4	0.30
11	118	140.9	8.1	4.9	0.31
12	71	132.6	8.1	8.6	0.36

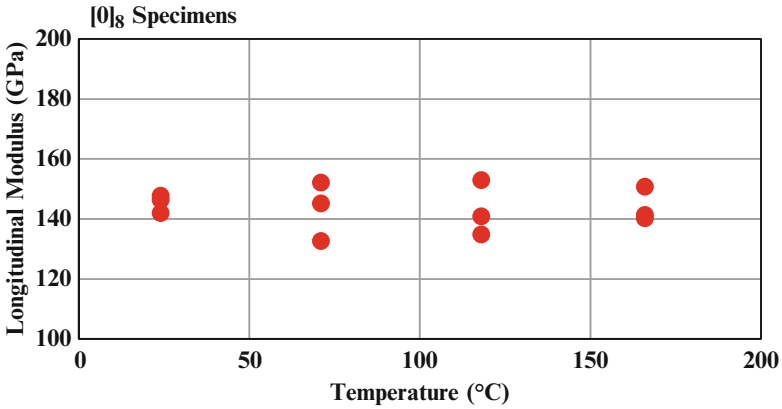

Fig. 4.4 The experimental longitudinal modulus as a function of temperature

prematurely in the grips due to adhesive failure between the tab material and the specimens. However, elastic properties were obtained from these tests. The experimental results for each specimen configuration and temperature were then used to develop the RSMs based on the analysis of variance (ANOVA) procedure.

4.4.2 Analysis of Variance (ANOVA)

The RSMs for predicting the elastic properties as a function of temperature were developed using the statistical software Stat-Ease® Design Expert® V.8 [9]. This software was used to generate the ANOVA tables and to perform the regression analyses to develop the RSMs. Each RSM was calculated for its overall significance to estimate the elastic properties with respect to temperature. The overall significance of each model was evaluated at a 0.05 level of significance. The models were then assessed for lack-of-fit due to possible significant terms not included in the model. The coefficients of multiple determinations, R^2, were also considered in assessing the adequacy of the RSM.

4.4.3 Response Surface Models (RSMs)

Longitudinal Modulus. No significant differences between each consecutive temperature were observed for the longitudinal modulus obtained from the $[0]_8$ specimens, as shown in Fig. 4.4. The ANOVA table for the longitudinal modulus in Table 4.4 shows the model was not significant with a p-value of 0.9781 (greater than 0.05). Hence, no response surface model was obtained for this material property. Experimentally, the longitudinal modulus did not show much variation with respect to increasing temperature. This was expected since the tensile load was applied along the fibers and the fibers are not highly temperature dependent in the range considered (24–166 °C).

Table 4.4 ANOVA table for the longitudinal modulus

Source	df[a]	SS[b]	MS[c]	F_{calc}	F_{stat}	p-value	Conclusion
Longitudinal modulus (E_{11})							
Total (corr)	11	459.56					
Model	3	10.55	3.52	0.063		0.9781	Not significant
Linear (x)	1	2.016	2.016	0.035888	5.32		Not significant
Quadratic (x^2)	1	5.88	5.88	0.104673	5.32		Not significant
Cubic (x^3)	1	0.000125	0.000125	2.23E-06	5.32		Not significant
Pure error	8	449.01	56.13				
R^2	0.0230						
Adj R^2	–0.3434						

[a]Degrees of freedom
[b]Sum of squares
[c]Mean square

Table 4.5 ANOVA table for the transverse modulus

Source	df[a]	SS[b]	MS[c]	F_{calc}	F_{stat}	p-value	Conclusion
Transverse modulus (E_{11})							
Total (corr)	11	6.06					
Model	3	5.26	1.75	17.64		0.0007	Significant
Linear (x)	1	3.82	3.82	40.21053	5.32		Significant
Quadratic (x^2)	1	0.015	0.015	0.157895	5.32		Not significant
Cubic (x^3)	1	0.003	0.003	0.031579	5.32		Not significant
Pure error	8	0.8	0.099				
R^2	0.9765						
Adj R^2	0.9435						

[a]Degrees of freedom
[b]Sum of squares
[c]Degrees of freedom

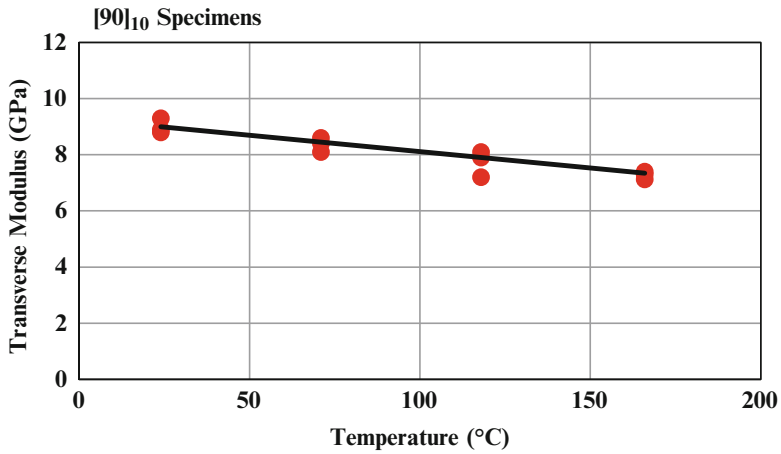

Fig. 4.5 Estimated and experimental transverse modulus as a linear function of temperature

Transverse Modulus. Significant differences in the transverse modulus, obtained from tensile tests of the $[90]_{10}$ specimens, were observed over the complete temperature range. The F-tests and the observed level of significance (p-value) for each model are shown in the ANOVA table (Table 4.5). A linear model was determined to be significant with p-value < 0.05. Therefore, a linear RSM was developed to predict the transverse modulus at temperatures within the design space. Furthermore, the $R^2 = 0.97$ indicates that 97 % of the total variation in the transverse modulus is described by the linear RSM.

Using the LSQ method to determine the parameter estimates, the RSM for estimating the transverse modulus as a function of temperature can be expressed as

Table 4.6 ANOVA table for the shear modulus

Source	df[a]	SS[b]	MS[c]	F_{calc}	F_{stat}	p-value	Conclusion
Shear modulus (G_{12})							
Total	11	46.2					
Model	3	44.16	14.72	57.53		<0.0001	Significant
Linear (x)	1	31.626	31.626	123.62	5.32		Significant
Quadratic (x^2)	1	0.0056	0.0056	0.022	5.32		Not significant
Cubic (x^3)	1	1.485	1.485	5.805	5.32		Significant
Pure error	8	2.05	0.26				
R^2	0.8104						
Adj R^2	0.7795						

[a]Degrees of freedom
[b]Sum of squares
[c]Mean square

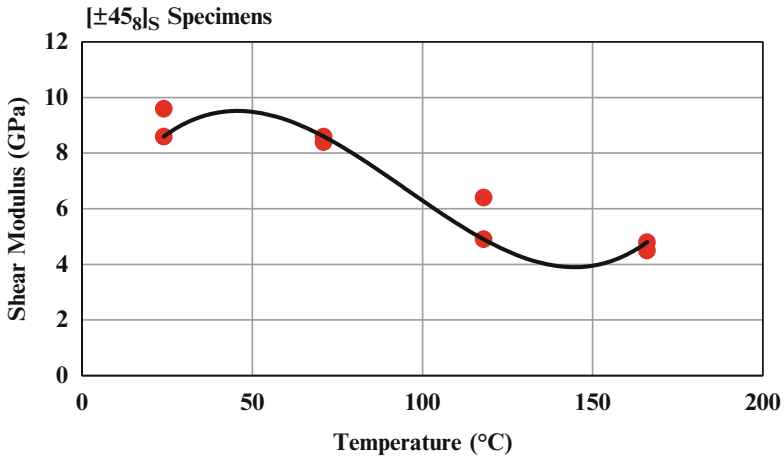

Fig. 4.6 Estimated and experimental shear modulus as a cubic function of temperature

$$\overline{Y} = 9.48 - 0.0064x_i \tag{4.4}$$

The experimentally determined transverse modulus with the predictive RSM is shown in Fig. 4.5. In general, the transverse modulus decreases with increasing temperature.

Shear Modulus. Significant differences between each consecutive temperature were observed in the $[\pm 45_8]_s$ specimens in estimating the shear modulus. The F-tests and the observed level of significance (p-value) for each model are shown in the ANOVA results in Table 4.6. A cubic model was determined to be significant with a p-value < 0.05. Therefore, a cubic RSM was developed to predict the transverse modulus at temperatures dictated within the design space. Furthermore, the $R^2 = 0.81$ indicates that 81 % of the total variation in the shear modulus is described by the RSM.

Using the LSQ method to determine the parameter estimates, the RSM for estimating the shear modulus can be expressed as

$$Y = 2E - 06X^3 - 0.0012X^2 + 0.198X - 0.297 \tag{4.5}$$

Figure 4.6 shows the plot of the experimentally determined transverse modulus with the RSM (Eq. 4.5) as a cubic function of temperature. As shown, the transverse modulus decreases with increasing temperature [3].

Poisson's Ratio. No significant differences were observed in the Poisson's ratio with respect to temperature. The ANOVA results in Table 4.6 show the model for the Poisson's ratio was not significant and therefore, no RSM was developed for this material property (Fig. 4.7).

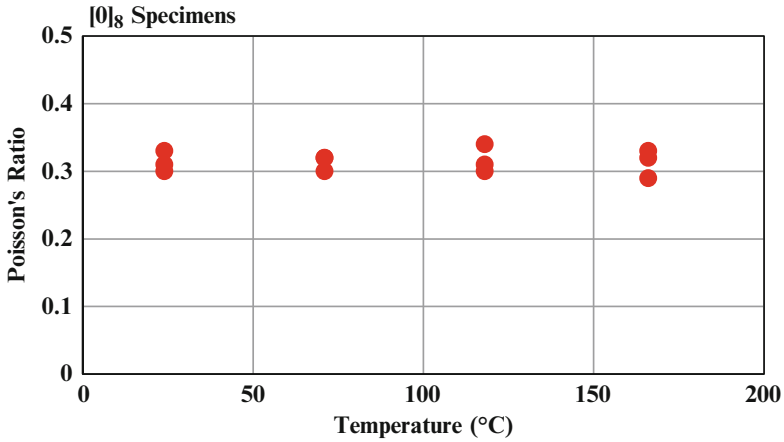

Fig. 4.7 Poisson's ratio as a function of temperature

4.5 Discussion

The matrix dominated elastic properties of an OoA/epoxy composite show significant temperature dependence. The longitudinal modulus and Poisson's ratio, obtained from tensile testing of the $[0]_8$ specimens, are not significantly impacted by temperature variations in the range from 24 to 166 °C. This is expected since the longitudinal modulus is a fiber dominated property and carbon fibers have a high temperature tolerance [2]. The transverse modulus, obtained from the tensile tests of the $[90]_{10}$ specimens, show a linear decrease of the modulus with increasing temperature. Failure is predominantly attributed to a decrease in the fiber-to-matrix adhesion, resulting in low matrix-to-fiber load transfer. Lastly, the temperature dependence of the shear modulus, obtained from tensile tests of the $[\pm 45_8]_s$ specimens, was modeled by a cubic RSM. This is primarily attributed to the decrease in the fiber-to-matrix adhesion and further enhanced by the development of the principal stresses in the ductile matrix at an angle of 45°. It should also be noted that the room temperature average longitudinal modulus and ultimate strength of CYCOM 5320-1/T650 was found to be within 4 % and 2 % of the manufacturer's data, respectively, even though the OoA prepreg was over 2.5 years past its shelf life.

4.6 Summary and Conclusion

Response surface models (RSMs) were developed to investigate the effects of temperature (24–166 °C) on the elastic properties of CYCOM 5320-1/T650, an out-of-autoclave (OoA) prepreg. A completely randomized design (CRD) was used to develop the test matrix in order to control additional variations introduced in the fabrication and testing processes. A linear RSM properly captured the temperature dependent behavior of the transverse modulus. An RSM was not necessary for the longitudinal modulus as minimal temperature dependence was observed, whereas a cubic RSM was developed for the shear modulus, which showed the greatest influence of increasing temperature. This is primarily attributed to an increase in ductility and a decrease in the fiber-to-matrix adhesion with increasing temperature. Using the design of experiments approach, RSMs can be used to predict elastic properties within the design space of the CRD. Additionally, these phenomenological models can be used to develop a more physics-based model based upon RSM predictions.

References

1. Gardiner G. (2011) Out-oautoclave prepregs: hype or revolution? CompositesWorld. http://www.compositesworld.com/articles/out-of-autoclave-prepregs-hype-or-revolution
2. Sun C-T, Yoon KJ (1988) Mechanical properties of graphite/epoxy composites at various temperatures. No. HTMIAC-9. High Temperature Materials Information Analysis Center, West Lafayette, IN
3. Griffis CA, Masumura RA, Chang CI (1981) Thermal response of graphite/epoxy composite subjected to rapid heating. J Compos Mater 15:427–442

4. Chen JK, Sun CT, Chang CI (1985) Failure analysis of a graphite/epoxy laminate subjected to combined thermal and mechanical loading. J Compos Mater 19:408–423
5. Griffis CA, Nemes JA, Stonesifer FR, Chang CI (1986) Degradation in strength of laminated composites subjected to intense heating and mechanical loading. J Compos Mater 20:216–235
6. Montgomery DC (1997) Design and analysis of experiments, 4th edn. Wiley, New York
7. ASTM Standard 3039D/3039M-08 (2008) Standard test method for tensile properties of polymer matrix composite materials. ASTM International, West Conshohocken, PA. doi:10.1520/D3039_D3039M-08. http://www.astm.org
8. ASTM Standard D 3518/D 3519M -94 (2001) Test method for in-plane shear response of polymer matrix composite materials by tensile test of a ±45° laminate. ASTM International, West Conshohocken, PA. doi:10.1520/D3518_D3518M. http://www.astm.org
9. Stat-Ease Design Expert (2010) Getting started with v8 of design-expert software. V.8 Ed

Chapter 5
Coupon-Based Qualification of Bonded Composite Repairs for Pressure Equipment

Michael W. Keller and Ibrahim A. Alnaser

Abstract Bonded composite repairs are increasingly installed on degraded pressure equipment and are frequently treated as permanent repairs. These repairs are installed on both external and internal corrosion defects. For external corrosion, the repair is assumed to halt further corrosion and therefore prevents further metal loss. However, for internal corrosion the damage process can continue and eventually lead to complete loss of the pressure vessel wall. In this scenario, the bonded repair failure mode switches from a tensile-based failure to an interfacial fracture scenario. As such, the current repair codes require the characterization of the interfacial fracture energy of the repair for input into a fracture-mechanics-based design approach. Currently these characterizations are performed on test vessels with a simulated through-wall defect. In this paper we describe a simple coupon-based test using a width-tapered-double-cantilevered beam specimen. Using fracture energy values derived from this test we can successfully predict the failure pressure of pressure vessels with simulated through-wall defects.

Keywords Composite repair • Pressure vessel • Fracture • Adhesive bond • Interface characterization

5.1 Introduction

Bonded composite repairs for damaged pressure equipment have seen significant growth since the introduction of a pre-cured repair in the late 1990s. Since the demonstration of the initial composite repair system, many other systems based on the cured-in-place (CIP) approach have been developed, tested, and marketed. For CIP repairs, a reinforcement fiber is wetted out with a liquid resin in the field and then the uncured composite is wrapped around the pressure vessel over a defect. The CIP-repair is typically allowed to cure before the vessel or pipe is re-pressurized. CIP repairs have one significant benefit over pre-cured composites; the composite can be formed, in place, over complex geometries and curves. This benefit comes, potentially, at the cost of apparent composite mechanical properties when compared to pre-cured systems. However, while many CIP systems use room temperature cured, two-part matrix chemistries leading to material properties below that of elevated cure composites, the pre-cured systems must be bonded to the host-pipe using similar room-temperature cured adhesives.

While the most visible advances in composite repairs of pressure vessels have been in the areas of new materials, the advances in repair design approaches and methodologies are equally important. The first American design guidelines were published in 2000 under the ASME Post Construction Code (PCC) and the recent revision PCC-2 [1]. This repair standard contained both required material characterization as well as design equations for a variety of repair scenarios. There are two critical distinctions in the PCC-2 design methodology, repairs for through-wall defects and repairs for non-through-wall defects. For the case of non-through-wall defects, the design approach is either stress or strain-based and the ultimate tensile properties of the composite are the critical design parameters. Repairs using this approach have been extensively studied in a series of University [2, 3] and industry [4–6] research projects. For the case of through-wall defects, the critical material parameters are no longer ultimate-strength-based, but are now the interfacial fracture behavior of the substrate–composite interface. Design equations for this defect scenario are based on fracture mechanics approaches for an idealized composite–substrate system.

M.W. Keller (✉) • I.A. Alnaser
Department of Mechanical Engineering, The University of Tulsa, 800 S. Tucker Dr., Tulsa, OK 74104, USA
e-mail: mwkeller@utulsa.edu

G. Tandon (ed.), *Composite, Hybrid, and Multifunctional Materials, Volume 4: Proceedings of the 2014 Annual Conference on Experimental and Applied Mechanics*, Conference Proceedings of the Society for Experimental Mechanics Series,
DOI 10.1007/978-3-319-06992-0_5,

The characterization of the substrate–composite bond is codified in the PCC-2 using a simple approach where the interfacial fracture energy is back calculated using the design equations. For the characterization, a short, straight-pipe sample has a circular hole drilled through the pipe wall. A composite is applied over the defect and the repaired pipe is hydrostatically pressurized until failure. The fracture is mathematically modeled as a combination of Mode I and Mode II, but only a single interfacial energy is extracted for the design. This approach has worked well for design, but has limits when attempting to extend or improve the design equations. As such, it is useful to develop and validate a coupon-based sample that would allow for a direct measurement of interfacial fracture toughness of the substrate–composite bond. In this paper we investigate the effectiveness of a width-tapered-double-cantilevered beam fracture specimen for extracting an appropriate fracture energy value for use in the design of repairs for through-wall defects. The test specimen is designed, validated, and the fracture energy value is compared with full-scale tests of through wall defects.

5.2 Experimental Methods

5.2.1 Specimen Manufacture

The WTDCB sample geometry was based off of the design by Jin et al. [7], a schematic of the basic specimen dimensions are shown in Fig. 5.1. Each specimen was comprised of a steel adherend and a composite adherend that was manufactured in-place on the steel adherend. Steel adherends were water-jet cut from A36 steel, which is similar in chemical composition to the steel that would be found in an ASTM 106B pipe. Steel adherends were approximately 6 mm (0.25 in.) thick. This thickness was chosen to simulate the pipe wall of a 6in Schedule 40 pipe. The composite adherend was manufactured by first wetting out a plain-woven carbon-fiber reinforcement using an epoxy from a commercial repair system (Citadel Technologies, Tulsa, OK). Sheets of reinforcement were placed on a waxed platen and built up to the required thickness. Steel adherends that had been grit-blasted to a near-white metal finish had a primer applied to the surface in contact with the repair and Teflon film was inserted at the steel–composite interface to generate a starter crack. The adherend was then placed on the uncured composite layup and a lightweight was applied to compact the composite. This approach has been shown to approximate the composite fiber-volume fraction of a field-installed repair [8]. After curing for at least 24 h at room temperature, the fracture specimens were separated using a carbide-saw blade and then the composite was trimmed to the final shape using a high-speed router. The steel adherend was used as the shaping guide in this step. Finally, a loading block was applied to the composite side using an adhesive (JB-Weld).

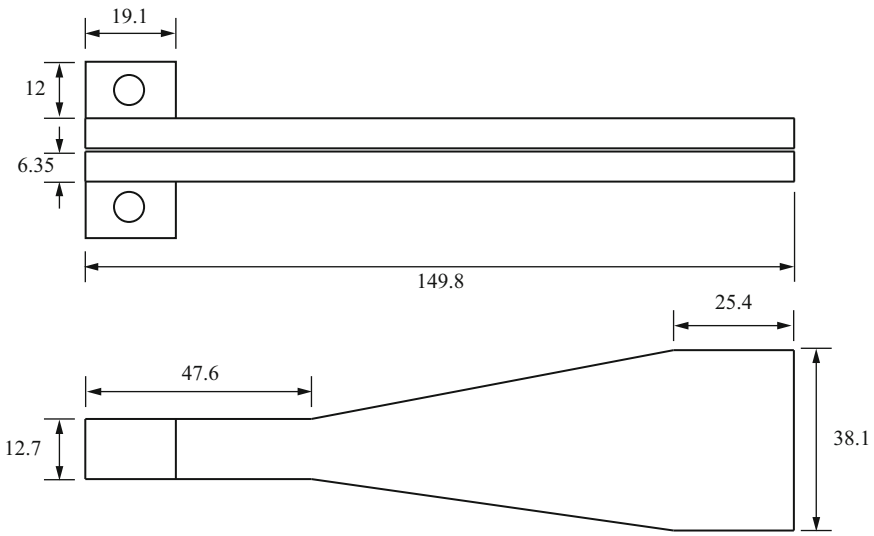

Fig. 5.1 Schematic of a WTDCB, dimensions in mm

5.2.2 Fracture Testing

After specimens were manufactured as described above, they were tested to failure using a servohydrualic load frame (MTS). Samples were pin-loaded in displacement control at a rate of 1.27 mm/min. A group of samples with varying initial crack length, formed by placing Teflon film of varying lengths as the precrack, was used to calibrate the wtdcb specimen geometry using a compliance approach

$$G_{IC} = P^2 \frac{dC}{dA} \tag{5.1}$$

where P is the load, C is the compliance of the specimen, and A is the crack area. Compliance was calculated from the load displacement curve recorded during the fracture test and is given by $C = \delta/P$. After the calibration was performed a series of 13 coupon specimens were tested to determine the G_{IC} value.

5.2.3 Full Scale Testing

Full scale testing of a repair system with a through-wall defect was performed using a 6-inch A106B, schedule 40 pipe spool. Through-wall defects were manufactured by drilling a circular hole through the pipe wall of 10, 15 , and 25.4 mm in diameter. Repairs were installed by first grit-blasting the surface to a near-white metal surface finish. After the surface preparation, a primer was applied to the metal surface followed by the installation of a commercially available composite repair system (Citadel Technologies, Tulsa, OK). After allowing the repair at least 24 h of room temperature curing time, the pipe spools were filled with water and then hydrostatically pressurized to failure. Only samples that failed by debonding were considered to be successful tests. Samples that failed by pinhole leaks or by failure of the wrap over the defect were neglected from the results presented below.

5.3 Model

The design approach adopted by PCC-2 uses an interfacial fracture approach to generate the required design thickness to withstand a prescribed internal pressure. Schematically, the repair is modeled as shown in Fig. 5.2, where the repair is treated as a thin shell spanning a circular defect.

Analysis of the fracture energy of this structure leads to the a relationship between composite material properties, repair thickness t, and internal pressure p

$$G = p^2 \left[\frac{1-\nu^2}{E} \left(\frac{3}{32t^3} a^4 + \frac{2}{\pi} a \right) + \frac{3}{16Gt} a^2 \right] \tag{5.2}$$

For this design equation, the modulus is considered to be a sum squares average $E=\sqrt{E_1 E_2}$, the passion ratio is calculated using a modulus weight $\nu^2 = \nu_{12}^2 E_2/E_1$, and the shear modulus is the through-thickness shear modulus $G = G_{13}$. Equation 5.2 is a mixed mode fracture energy with the first term in the square brackets representing the mode I contribution and the second representing the mode II contribution. The substrate material is considered to be rigid and does not figure into the deformation of the repair–substrate system. For a typical repair design, Eq. 5.2 is solved for p and the resulting solution is used in an iterative fashion to determine the required repair thickness.

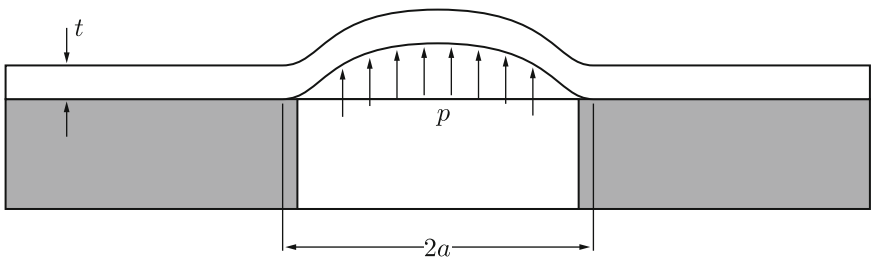

Fig. 5.2 Schematic of a repair over a circular through-wall defect

5.4 Results

5.4.1 Specimen Calibration

A series of six fracture specimens were tested to determine the required form of dC/dA, the results of these calibration samples are presented in Fig. 5.3. As expected, the compliance exhibited a linear relationship to fracture area, which is required for the crack-length independence of the WTDCB sample. The slope of the linear fit is used in the following fracture testing along with Eq. 5.1 to determine the fracture energy for the coupon specimens.

5.4.2 Fracture Testing

Thirteen coupon specimens were tested to determine interfacial fracture energy for use in the design equation given above.

All specimens exhibited an adhesive failure of the primer material, as shown in Fig. 5.4. The primer material is colored grey and can be seen on both the composite adherend and the steel adherend. From the 13 fracture specimens, we determine

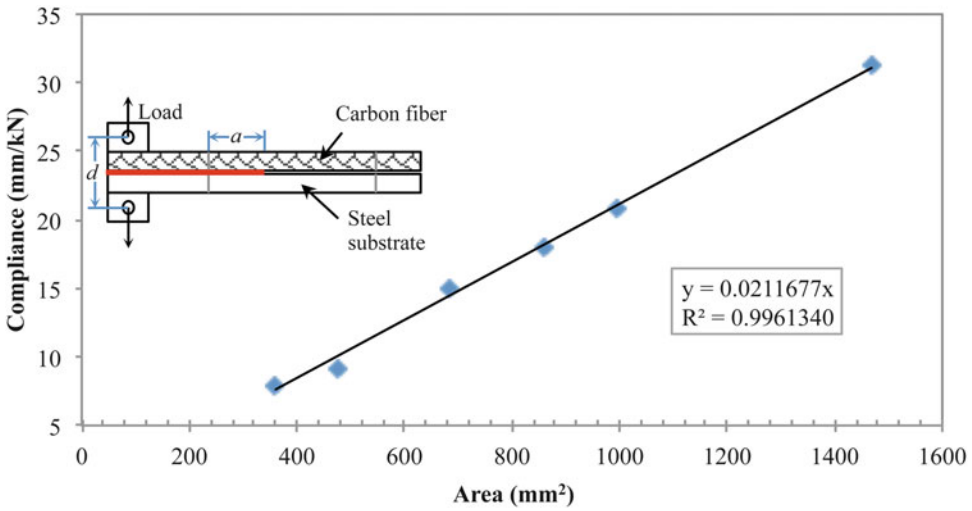

Fig. 5.3 Compliance calibration results for the WTDCB specimen in this work

Fig. 5.4 Image of specimens after fracture

that the apparent fracture energy is $G_C = 1,\ 654 \pm 296$ J/m^2. The error bound represents a 95 % confidence bound on the measured fracture energy.

5.5 Discussion

The fracture energy measured in the coupon testing described above is now used to make failure predictions for model through wall defects. Figures 5.5, 5.6, and 5.7 below present full scale testing values for three defects and a failure prediction curve using Equation 5.2 above. The full-scale testing results were taken from previous work by Wilson [9], the material property values were taken from previous work by Kessler and co-workers [10].

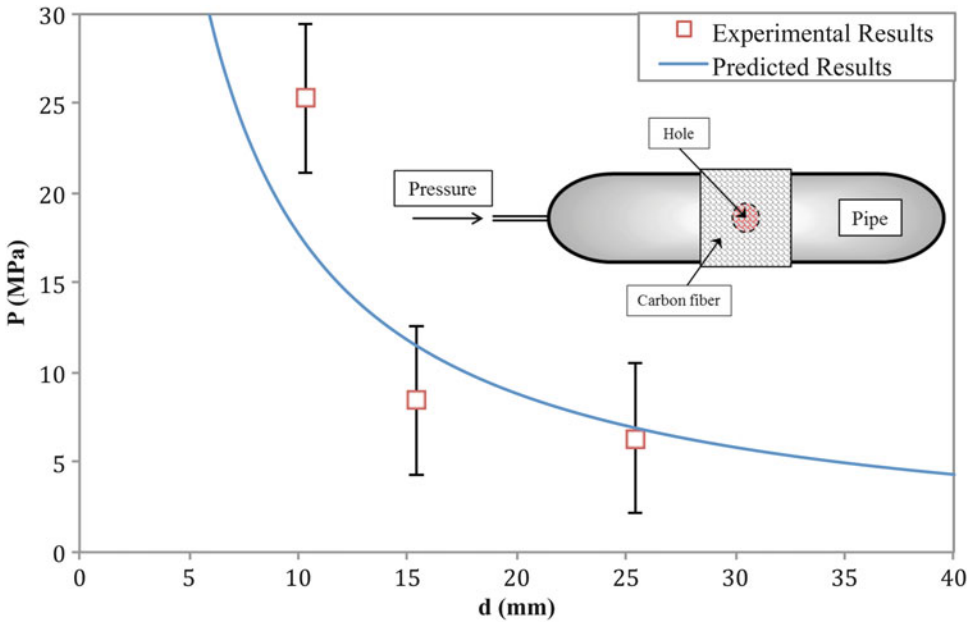

Fig. 5.5 2 plys of 6 K × 3 K repair

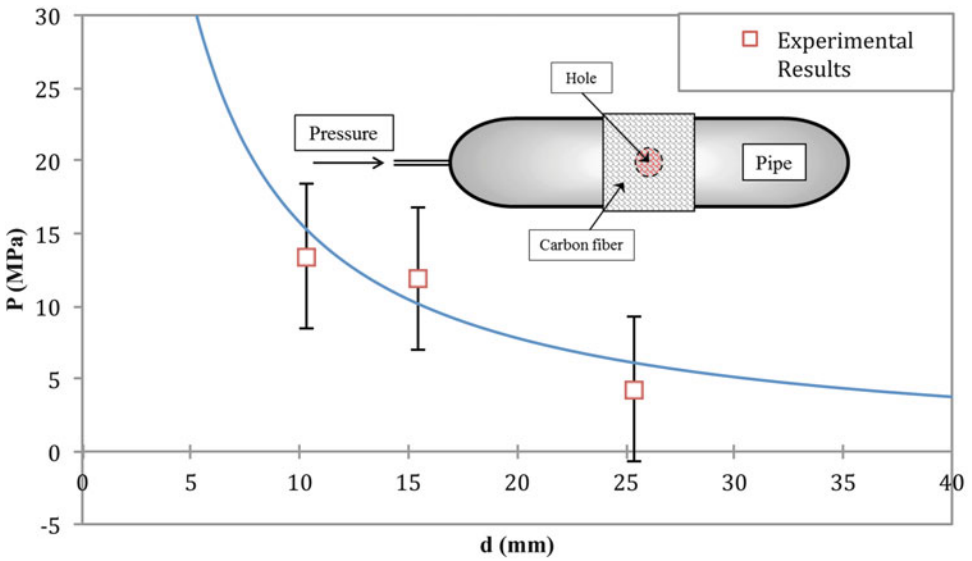

Fig. 5.6 2 plys of 12 K × 3 K repair

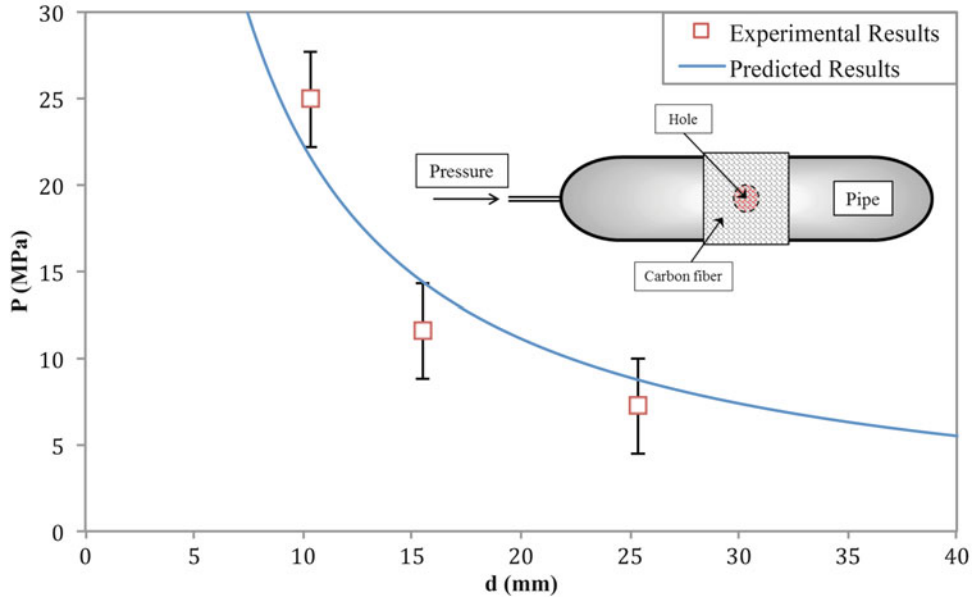

Fig. 5.7 4 plys of 12 K × 3 K

5.5.1 Comparison of Predicted Failure Pressure

Figures 5.5 and 5.6 show the failure pressure prediction and test results for a repair that consisted of two composite plys applied over the simulated through-wall defect. As can be seen from these figures, the prediction line using the values derived from the coupon-based testing show good agreement. All predictions fall within the 95 % confidence bands in the full-scale testing data or fall below the measured failure pressure. A predicted failure pressure below the measured value is considered successful as this ensures a conservative design for any applied repair. Additionally, the prediction holds even when the composite adherend is not made of the same composite as the repair system. Because the stress intensity factor is governed by the elastic mismatch across the crack plane [11], this result is somewhat unexpected. The close agreement between the coupon-based predictions and the full-scale testing may be due to the fact that all materials have similar shear moduli despite have different elastic moduli and the scatter in the full-scale samples may be hiding the dependence.

In Fig. 5.7, a prediction is shown based on a comparison with a 4 ply repair using the same composite material as used in the coupon-based testing. Again, we see good agreement with the prediction using the fracture values derived from the coupon-based test.

The results above indicate that both the coupon-based test and the "large-scale" tests arrive at similar values for fracture energy. The coupon-derived value of $G_C = 1,\ 654 \pm 296$ J/m^2 is similar to the value of $G_C = 1,\ 560$ J/m^2 derived by back calculating from the full-scale test data shown above. The agreement of these two values both validates the coupon specimens and validates the values back-calculated from the full scale tests, indicates that these simple failure tests may be providing valid interfacial fracture values.

5.6 Conclusions

A coupon-based test to extract a design relevant interfacial fracture energy was developed and validated. A fracture energy of $G_C = 1,\ 654 \pm 296$ J/m^2 was determined from the coupon-based testing. Using the design equation in ASME PCC-2, we found that the failure pressures predicted for two reinforcement geometries at two layers agreed closely with values derived from large scale failure testing. The agreement between these two methods likely indicates that both are measuring valid interfacial fracture energies.

References

1. ASME (2011) Post Construction Code. In: Nonmetallic and bonded repairs. ASME, New York
2. Duell JM, Wilson JM, Kessler MR (2008) Analysis of a carbon composite overwrap repair system. Int J Pressure Vessels Piping 85:782–788
3. Wilson JM, Kessler MR, Duell JM (2004) Rupture testing of A-106, grade B steel pipes repaired with carbon/epoxy composites. In: ASME/JSME 2004 Pressure vessels and piping conference, San Diego, pp 175–179
4. Alexander C (2010) Developing stress intensification factors for composite repair systems used to repair damaged pipe. In: ASME 2010 Pressure vessels and piping division/K-PVP conference, Bellevue, pp 283–292
5. Alexander C, Ochoa OO (2010) Extending onshore pipeline repair to offshore steel risers with carbon–fiber reinforced composites. Compos Struct 92:499–507
6. Alexander C, Worth F (2010) Using industry standards for designing composite repair systems for corroded process piping. In: ASME 2010 Pressure vessels and piping division/K-PVP conference, Bellevue, pp 175–184
7. Jin H, Miller GM, Sottos NR, White SR (2011) Fracture and fatigue response of a self-healing epoxy adhesive. Polymer 52:1628–1634
8. Goertzen WK, Kessler MR (2007) Dynamic mechanical analysis of carbon/epoxy composites for structural pipeline repair. Compos B Eng 38:1–9
9. Wilson JM (2006) Characterization of a carbon fiber reinforced polymer repair system for structurally deficient steel piping. Ph.D., The University of Tulsa
10. Kessler MR, Walker RH, Kadakia D, Wilson JM, Duell JM, Goertzen WK (2004) Evaluation of carbon/epoxy composites for structural pipeline repair. In: 2004 International pipeline conference, Calgary, pp 1427–1432
11. Rice JR, Sih GC (1965) Plane problems of cracks in dissimilar media. J Appl Mech 32:418–423

Chapter 6
Compression-After-Impact of Sandwich Composite Structures: Experiments and Simulation

Benjamin Hasseldine, Alan Zehnder, Abhendra Singh, Barry Davidson, Ward Van Hout, and Bryan Keating

Abstract A combined experimental and numerical study of compression-after-impact strength of honeycomb core sandwich composite panels is described. Barely-visible impact damage was induced using quasi-static indentation. Specimens consisted of 16-ply carbon-epoxy facesheets with an aluminum honeycomb core. The facesheet stacking sequence, core geometry and thickness were varied as was the indentor diameter to study the effect of these parameters on damage resistance and post-impact damage tolerance. Computational models of the quasi-static indentation and compression after impact are underway. Results to date compare the experimental and simulate indentations for 25.4 mm diameter indentors. Future work will include modeling the larger, 76.2 mm indentor as well as compression-after-impact.

Keywords Sandwich composites • Low-energy impact • Compression-after-impact • Delaminations • Modeling

6.1 Introduction

The advantages of sandwich composites over monolithic composites, such as increased bending stiffness, low weight and reduced fabrication costs are well documented. The issue of low-energy damage on sandwich composites is however less well understood. Low energy impact can generate internal damage and a residual dent that is barely detectable or undetectable by visual inspection. The resulting damage can affect the post-impact compressive strength, reducing it by as much as 50 % [1–3] or the resulting failure mode. A damaged load carrying component could potentially fail at a fraction of the design load thus it is clearly necessary to study both the resistance to damage and the post-impact damage tolerance of sandwich composite structures.

The aim of this study is to experimentally investigate the damage resistance and post-impact compressive response of sandwich composite structures to low-energy impact at the barely-visible impact damage (BVID) threshold and to develop a computational tool to accurately simulate the results. Experimental data obtained will be used to validate the numerical model.

6.2 Sample Materials and Fabrication

Specimens used in this study were 16-ply graphite-epoxy facesheets adhered to an aluminum honeycomb core. The facesheets were laid from HexPly® IM7/8552 carbon-epoxy unidirectional prepreg and the core was from HexWeb® CR-III 3.2 mm cell size 5052-H39 aluminum honeycomb. Two parameters were varied for this study, the facesheet stacking sequence and the core geometry and thickness. These parameters are shown in Table 6.1. The Q1 and Q2 were used to study the maximum ply angle change while the Q2 and Q3 were used to study the placement of the critical 0° ply. The C1 and C2 cores were used to study the effect of core thickness while the C1 and C3 cores were to study the effect of core density.

B. Hasseldine (✉) • A. Zehnder • W. Van Hout • B. Keating
Sibley School of Mechanical and Aerospace Engineering, Cornell University, Ithaca, NY 14853, USA
e-mail: bph45@cornell.edu

A. Singh • B. Davidson
Department of Mechanical and Aerospace Engineering, Syracuse University, Syracuse, NY 13244, USA

G. Tandon (ed.), *Composite, Hybrid, and Multifunctional Materials, Volume 4: Proceedings of the 2014 Annual Conference on Experimental and Applied Mechanics*, Conference Proceedings of the Society for Experimental Mechanics Series,
DOI 10.1007/978-3-319-06992-0_6,

Table 6.1 Facesheet layup and core geometry

Facesheet	Layup	Core	Density (kg/m^3)	Thickness (mm)
Q1	$[45/0/-45/90/\ -45/0/45/90]_S$	C1	49.7	25.4
Q2	$[45/-45/0/90]_{2S}$	C2	49.7	16.51
Q3	$[45/-45/90/0]_{2S}$	C3	72.1	25.4

Panels were hand-laid with a 3M® AF-555 adhesive film adhering the facesheets to the core. The core was cut and primed using a 3M® EW-5000 structural adhesive primer and the outer loading edges of the final trimmed specimens were reinforced with a 3M® EC-3524A/B potting compound. The purpose of reinforcing the outer loading edges was to inhibit any localized failure of the specimen edges when tested in compression. The core ribbon direction was aligned with the 0° facesheet fiber direction. The final assembly was co-cured in an autoclave following the cure cycle recommended by the prepreg manufacturer.

Post curing, the plate was trimmed to give two edgewise compression (EC) specimens and four compression-after-impact (CAI) specimens per plate. All specimens were ground flat and square to ensure an equal strain distribution when tested in compression. The EC specimens were tested in compression to obtain the undamaged compressive strength. The CAI specimens were first indented and then tested in compression to yield the reduced post-impact compressive strength. This was then normalized by the undamaged EC strength to yield the residual strength for a particular specimen geometry.

6.3 Experimental Results

6.3.1 Quasi-static Indentation

CAI specimens had damage introduced by means of quasi-static indentation (QSI). This was performed using steel spheres of 25.4 or 76.2 mm diameter. QSI was performed in the center of the top facesheet in an Intron® testing machine. Indentation was performed in displacement control up to a maximum force which constituted the threshold for barely-visible impact damage (BVID). This maximum indentation force for each indentor was determined from earlier exploratory studies and decided by consensus of the research group. The load was 2,447 N and 4,306 N for the 25.4 and 76.2 mm diameter indentors respectively.

Post QSI, specimens were inspected nondestructively by means of a 50 MHz pulse-echo ultrasonic C-scan. From the nondestructive evaluation, two damage metrics were obtained; the residual dent profile and the internal facesheet damage (delaminations). From the residual dent profile, the dent depth and the 0° and 90° central dent profiles were measured. The internal damage measurement allowed the ply-by-ply delamination areas to be measured and from this the planar delamination area could be calculated. This is defined as the projected area of all the individual ply-level delamination areas.

6.3.2 Compression-After-Impact Results

The full details of the experimental setup for EC and CAI tests have been previously reported in [4]. The CAI setup included a shadow Moiré [5] that allowed for the out-of-plane displacement of the front indented facesheet to be recorded during compression. This also allowed for the resulting failure mode to be visualized. From the CAI results, three distinct failure mechanisms were evident. For all specimens, progressive dent deepening was seen during compressive loading. For a group of specimens, this progressive dent growth led to increased bending stresses in the front facesheet which eventually lead to micro-buckling of the critical 0° load carrying plies. This buckling and the lack of out-of-plane support from surrounding plies resulted in catastrophic compressive fiber failure (FF). For other specimens, out-of-plane buckling of the facesheet delaminations introduced during QSI led to a local buckled region that occurred above or below the central dent region. This tended to occur close to the critical failure load and eventually the specimen failed by delamination buckling (DB) mode of failure. For specimens with a relatively deep residual dent, seen for the 76.2 mm diameter indented specimens, the dent growth became gradually unstable and expanded rapidly as an elongated ellipse in the direction transverse to the loading direction. This is believed to be due to an instability from the core and is characterized as a global instability (GI) mode of failure.

The CAI strength results plotted against the planar delamination area for the 25.4 mm diameter indentor are shown in Fig. 6.1. There is a decreasing trend of compressive strength with increasing planar delamination area. This trend was not clear from strength comparison with the residual dent depth metric so it is evident that planar delamination area may be a

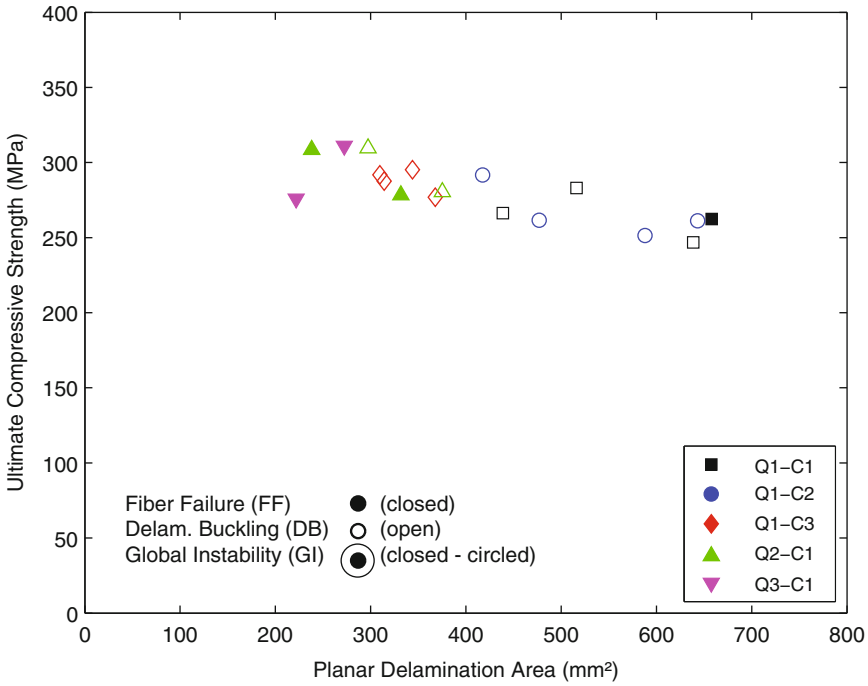

Fig. 6.1 Compression after impact (CAI) strength against planar delamination area for specimens with 25.4 mm diameter indentor

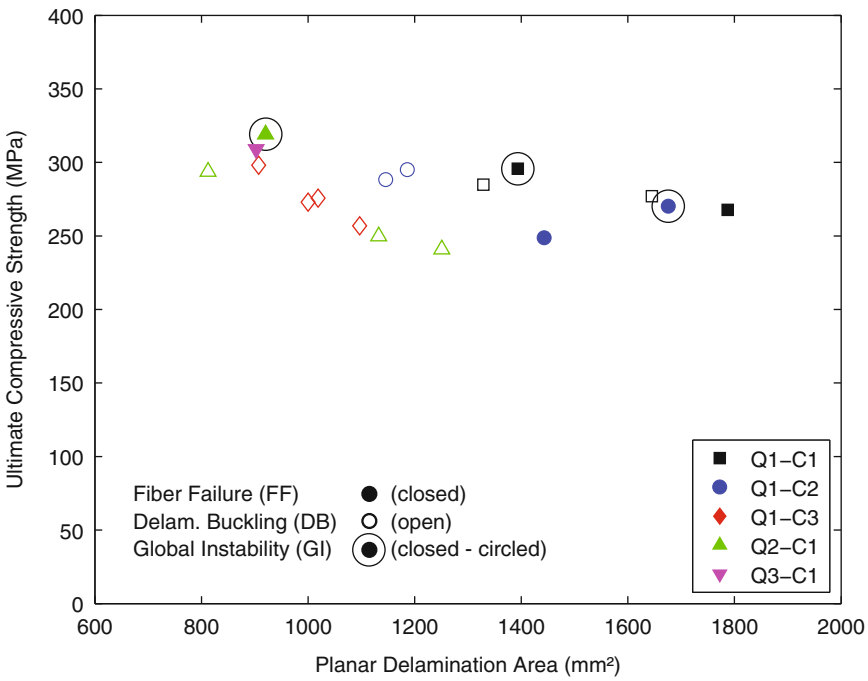

Fig. 6.2 Compression after impact (CAI) strength against planar delamination area for specimens with 76.2 mm diameter indentor

better metric for CAI strength. For the Q1 facesheet, there is a high propensity for delamination buckling mode of failure. The Q2 has an increased occurrence of fiber failure mode and the Q3 facesheet has fiber failure as the dominant mode. The high level of delamination buckling for the Q1 facesheet could be due to the close proximity of the 0° plies to the free surface. The reduced support from the surrounding plies will encourage delamination buckling as the ultimate compressive strength is reached.

The CAI results for the 76.2 mm diameter indentor are shown in Fig. 6.2. From these results, there again is a decreasing trend in CAI strength with increasing planar delamination area. For the large diameter indentor the global instability failure mode appears for specimens with a relatively large residual dent depth. The results also show that the resulting failure mode

influences the ultimate compressive strength. Specimens that failed by delamination buckling tended to have a lower ultimate compressive strength compared with specimens that failed by either fiber failure or global instability modes of failure. This suggests that for CAI modeling, inclusion of the delamination damage mechanism may be required to achieve the necessary fidelity.

6.4 Numerical Modeling

The other major task of this study was to develop a computational tool that will predict damage resistance and post-impact damage tolerance of sandwich composites to a low-energy impact event. The majority of past numerical studies of CAI have simulated a pre-defined state of damage in compression [6]. The goal of this study is to explicitly simulate the QSI damage event and then pass that directly into a CAI simulation to model both the impact event and the resulting compression test. Thus the damage resistance and damage tolerance can be modeled in one simulation. The numerical results will then be validated by the experimental results.

A full-size model was developed using the ABAQUS/Explicit finite element software. The major challenge was to incorporate all the relevant damage mechanisms into the model. From the experimental work, the facesheets exhibited fiber/matrix failure and delaminations, and the core exhibited localized core crushing beneath the indentation site. Facesheet-core debonding was not exhibited from the experimental testing. For this study, we aimed to model the fiber-matrix failure of the facesheets and the localized core crushing of the core. Future work will extend the model to incorporate delaminations introduced during QSI.

The material properties for the constituent materials are shown in Table 6.2. These were obtained from the manufacturer of the prepreg and the honeycomb core [7] or estimated or measured experimentally. The method to experimentally measure these properties is discussed below. Each ply is 0.127 mm thick. The explicit geometry core was modeled using an elastic–plastic material model with E = 70 GPa, $\nu = 0.3$, yield stress of 220 MPa, rising to 282 MPa at 1 % strain and constant thereafter.

The outer facesheets are modeled with continuum-shell elements. A continuum model for the core would be far less computationally expensive than the explicit geometry model used here, but our prior work has shown that the continuum core model was unable to accurately simulate the localized core crushing during QSI. Therefore, the core was split into two regions where the top 30 % of the core adjacent to the top facesheet was modeled using an explicit geometry core. The remaining region that stays elastic during the simulation is modeled with anisotropic 3D continuum elements. The model showing the individual regions including the rigid indentor is shown in Fig. 6.3.

6.4.1 Facesheets

The facesheets were modeled using 8-node continuum-shell (SC8R) elements with a Hashin degradation material model. The ply constituent material properties are based on [7] with modifications to (E_1) to match the simulated and measured in-plane and bending stiffnesses of the 16-ply facesheets. The ply strengths were also modified from the reference values in [8, 9] so that simulations of failure in EC and of four-point bend-to-failure tests match experimental results. The reason for the changes in properties relative to the reference values is that the co-curing process of the sandwich panel assembly, induced fiber waviness, particularly towards the core. The ply stiffnesses and strength are thus reduced relative to a facesheet with negligible fiber waviness.

Table 6.2 Constituent material properties

Material	E_1 (GPa)	E_2 (GPa)	E_3 (GPa)	G_{12} (GPa)	G_{13} (GPa)	G_{23} (GPa)	ν_{12}	ν_{13}	ν_{23}	Density (kg/m^3)
IM7/8552 prepreg	139.5*	12	12	5.17	5.17	3.98	0.32	0.32	0.46	1,570
Continuum core	1.48E−04**	1.47E−04**	1.1*	89E−06**	0.17**	0.127**	1**	1E−05**	1E−05**	49.7

*Measured experimentally
**Estimated

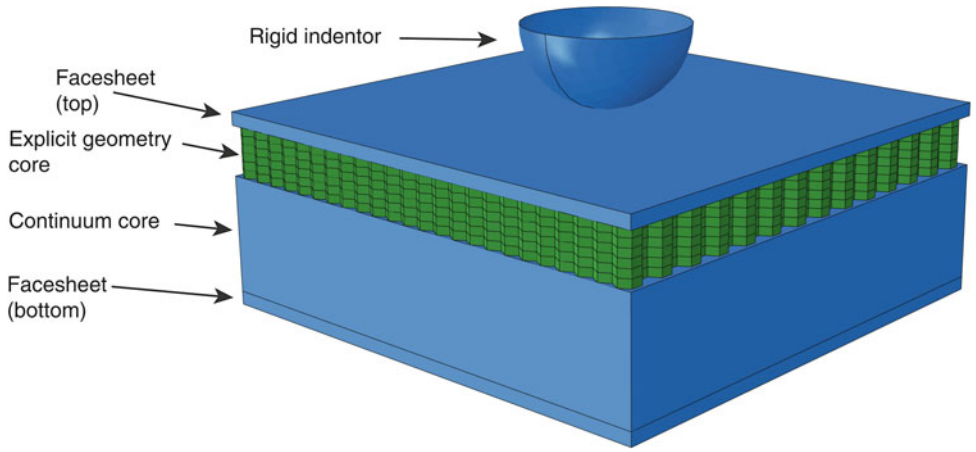

Fig. 6.3 Assembled Abaqus model showing individual parts (25.4 mm diameter indentor)

6.4.2 Explicit Geometry Core

The explicit geometry core is modeled using 4-node linear shell elements (S4RS) with small strain formulation. The aluminum core is modeled with J_2 plasticity using the material parameters described above and a cell wall thickness of 0.018 mm. Note that the thickness is doubled in the ribbon direction of the core. Flatwise compression simulations were performed for all three cores and were validated using experimental flatwise compression tests. The failure stress and constant crushing stress were well matched for the three cores. To improve the accuracy of the geometry, random imperfections of + / – one cell wall thickness was applied to the in-plane coordinates of the explicit geometry core. A mesh convergence study was also performed to find the required mesh density to accurately simulate the flatwise compression tests.

6.4.3 Continuum Core

The continuum core model used linear elastic brick (C3D8R) elements. Material properties and mesh density were taken from a previous study [10]. The benefit of using the continuum core for the majority of the core section is the improved computational efficiency.

6.4.4 Simulation Details

The model was assembled with a tie constraint between the continuum core and bottom facesheet. The coupling of the top facesheet to the explicit geometry core and of the explicit geometry core to the continuum core used shell-to-solid coupling. The indentor was modeled using rigid (R3D4) elements. A general contact algorithm was implemented to deal with the contact of the indentor and facesheet and to avoid any penetrations of adjacent elements. Two explicit-dynamic steps were used, with the first QSI step simulating the indentation of the indentor in displacement control to the maximum QSI force, and the second, CAI step, compressing the sample to final failure. To increase the incremental time step and therefore shorten the overall run time, mass scaling was utilized. A scaling study was conducted to find the maximum mass scaling that could be used without substantially affecting the results.

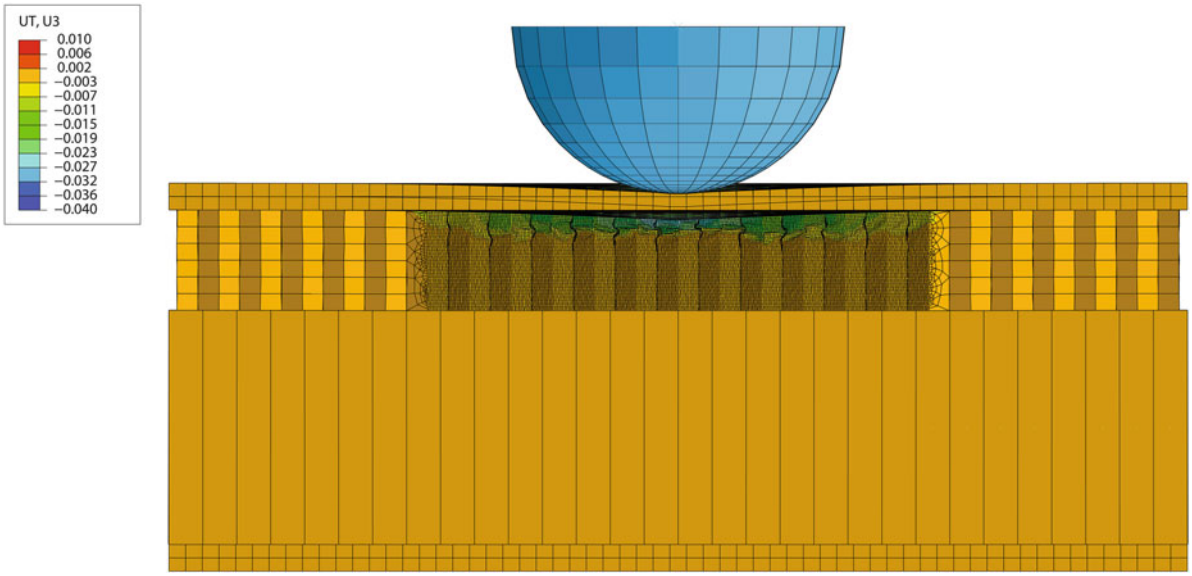

Fig. 6.4 QSI model for 25.4 mm diameter indentor at maximum indentation force. View is cut-through the center showing the localized crushing of the core. Contours show out-of-plane displacement in inches

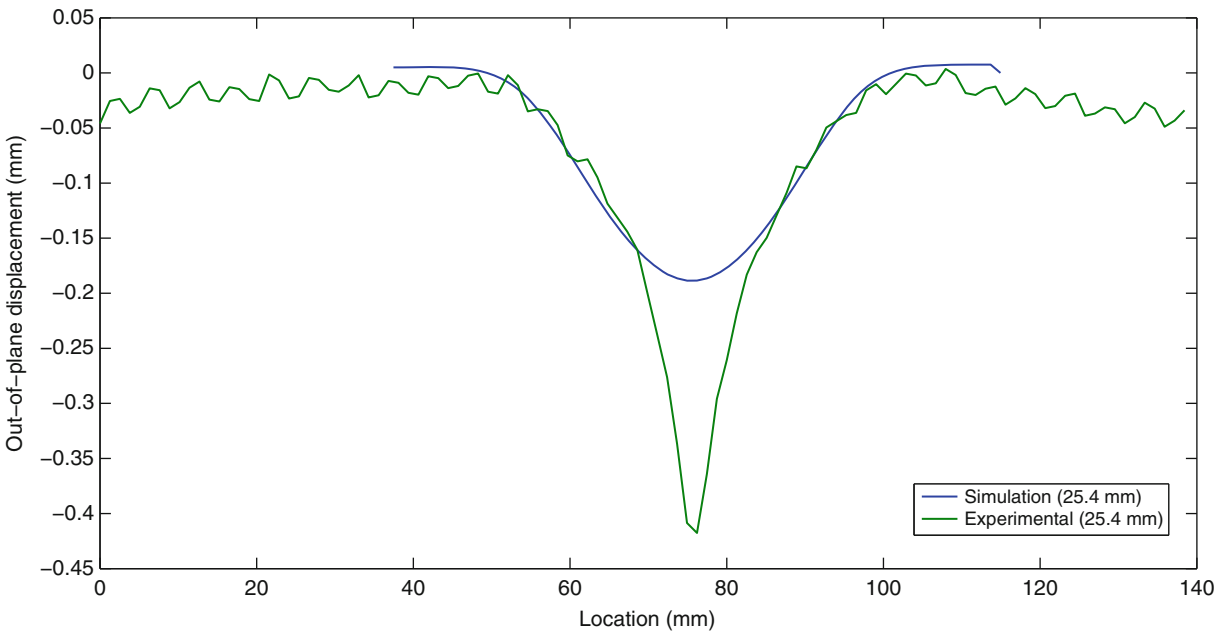

Fig. 6.5 Residual dent profile through the center of the specimen following QSI for the 90° fiber direction. Experimental and FEA numerical results are compared

6.4.5 QSI Results

Qualitative results for the core crushing during the QSI step are shown in Fig. 6.4. The explicit geometry core is clearly able to capture the crushing during the indentation event. The plot shows the out-of-plane displacement contours at the maximum QSI force for the 25.4 mm diameter indentor.

The residual dent profile is shown in Fig. 6.5. The residual dent profile is for the central cut through the top facesheet in the 90° fiber direction. This is compared for the 25.4 mm diameter indentor for the experimental QSI results obtained by C-scan and the numerical results from the FEA simulation. With the exception of the central region the residual dent profiles match up well. Our working hypothesis is that out-of-plane denting of the facesheets, a feature not captured in the FEM model, accounts for the steep experimental dent profile.

6.5 Summary

A combined experimental and numerical study has been conducted for low-energy impact at the BVID threshold of sandwich composite specimens. The numerical results for the 25.4 mm diameter QSI damage are promising. The next steps of the research will simulate BVID damage using the larger 76.2 mm indentor and will simulated the failure after impact damage, or CAI.

Acknowledgements We would like to acknowledge support through the NASA Constellation University Institutes Project (CUIP) grant NCC3-989. This work used the Extreme Science and Engineering Discovery Environment (XSEDE), which is supported by National Science Foundation grant number OCI-1053575. Finally, this work made use of the Cornell Center for Materials Research Shared Facilities which are supported through the NSF MRSEC program (DMR-1120296).

References

1. Kassapoglou C, Jonas P, Abott R (1988) Compressive strength of composite sandwich panels after impact damage: an experimental and analytical study. J Compos Technol Res 10(2):65–73
2. Tomblin J, Lacy T, Smith B, Hooper S, Vizzini A, Lee S (1999) Review of damage tolerance for composite sandwich airframe structures. Federal Aviation Administration Report No. DOT/FAA/AR-99/49. Office of Aviation Research, U.S. Federal Aviation Administration, Washington, DC
3. Moody RC, Vizzini AJ (2000) Damage tolerance of composite sandwich structures. Federal Aviation Administration Report No. DOT/FAA/AR-99/91. Office of Aviation Research, U.S. Federal Aviation Administration, Washington, DC
4. Hasseldine B, Zehnder A, Keating B, Singh A, Davidson B (2013) Compression after impact of thick sandwich composite structures. In: Proceedings of the 54th AIAA structures, structural dynamics, and materials conference
5. Post D, Han B, Ifju P (2000) Moiré methods for engineering and science - moiré interferometry and shadow moiré. In: Photomechanics. Springer, Berlin, pp 151–196
6. Czabaj M, Zehnder A, Davidson B, Singh A, Eisenberg D (2011) Combined experimental/numerical assessment of compression after impact of sandwich composite structures. In: Experimental and applied mechanics, vol 6. Conference proceedings of the society for experimental mechanics series. Springer, New York, pp 793–800
7. Marlett K, Ng Y, Tomblin J (2011) Hexcel 8552 IM7 unidirectional qualification material property data report. National Institute for Aviation, Wichita State University, Wichita
8. Camanho PP, Maimí P, Dávila CG (2007) Prediction of size effects in notched laminates using continuum damage mechanics. Compos Sci Technol 67(13):2715–2727
9. Bisagni C, Vescovini R, Dávila C (2010) Assessment of the damage tolerance of postbuckled hat-stiffened panels using single-stringer specimens. In: 48th AIAA/ASME/ASCE/AHS/ASC structures, structural dynamics, and materials conference, Orlando
10. Czabaj M, Tubbs W, Zehnder A, Davidson B (2011) Compression/shear response of honeycomb core. In: Experimental and applied mechanics, vol 6. Springer, Berlin, pp 393–398

Chapter 7
Compact Fracture Specimen for Characterization of Dental Composites

Kevin Adams, Douglas Ivanoff, Sharukh Khajotia, and Michael Keller

Abstract Dental composites are becoming increasingly popular due to their tooth-like color and appearance. Most short-term failures of dental composites are due to mechanical damage, such as cracking. Therefore, many of these failures might be prevented through the use of a self-healing dental composite. High-quality characterization is critical in the development of self-healing materials. Since healing creates uncertainty about the location of the crack-tip, tapered double cantilever beam (TDCB) specimens are often used for their crack length independence when measuring the fracture toughness and healing efficiency of self-healing materials. Because of the high cost of dental composite materials, small cost-effective TDCB samples, about one third of the standard size, were designed and optimized using rapid prototyping (Objet 3D Printer).

Keywords Composites • Self-healing • Dental • Materials • Microcapsules

7.1 Introduction

The use of resin-based composites in dental restorations has become a prominent alternative to traditional amalgam repairs [1]. This is due mainly to the fact that composites offer a natural tooth appearance, while the metallic appearance of amalgam repairs makes them far more noticeable. Despite this advantage, composite dental restorative materials are more likely to fail due to crack initiation and propagation, reducing their average lifespan relative to amalgam repairs. These failures increase the frequency of costly and time-consuming dental procedures that must be performed in order to prevent further tooth decay through removal and replacement of the original repair. One potential method of mitigating these problems is the use of a microcapsule-based self-healing system embedded within the dental composite, which automatically arrests and repairs cracks before they can propagate to the point of failure. The creation and refinement of such a material requires accurate and consistent testing methods for measuring material properties, such as fracture toughness and healing efficiency. Since a self-healing event repairs a crack using a statistically distributed healing component, accurate location of the healed crack tip is often difficult. This difficulty necessitates the use of fracture specimens that provide a crack-length-independent measure of fracture toughness. One such sample is the tapered double cantilever beam (TDCB) geometry.

The currently accepted size of TDCB specimens is impractical for use with the expensive materials used in modern dental composites, especially since a large testing sample size is desired in order to confidently predict material behavior. Therefore, a new compact TDCB or CTDCB was developed, using rapid prototyping, specifically for use in characterizing self-healing dental composites. Several variations of this design were tested using 3D printed samples, including a linear width taper and a square shaped groove. Lastly, the design was finalized and used to create a mold for making the dental composite specimens.

K. Adams • D. Ivanoff • M. Keller (✉)
Department of Mechanical Engineering, The University of Tulsa, 800 South Tucker Drive, Tulsa, OK 74104, USA
e-mail: mwkeller@utulsa.edu

S. Khajotia
College of Dentistry, The University of Oklahoma, 1100 North Lindsay, Oklahoma City, OK 73104, USA

G. Tandon (ed.), *Composite, Hybrid, and Multifunctional Materials, Volume 4: Proceedings of the 2014 Annual Conference on Experimental and Applied Mechanics*, Conference Proceedings of the Society for Experimental Mechanics Series,
DOI 10.1007/978-3-319-06992-0_7,

7.2 Experimental Method

7.2.1 Specimen Design and Rapid Prototyping

TDCB specimens allow for crack-length-independent fracture testing by tapering the width of the beam such that the change in compliance over change in crack length (dC/da) is constant. The beam shape can be defined using the following relationship [2],

$$3a^2/h^3 + 1/h \propto dC/da \tag{7.1}$$

where a is the crack length and h is the width of the beam. This means that if the complex curve on the left side of Eq. 7.1 is constant throughout the length of the beam, then dC/da will also be constant, making it an acceptable crack-length-independent design. This curve is often approximated by a linear taper in traditional TDCB designs. Figure 7.1 below shows a traditional TDCB as described in [3] along with the compact design adopted in this work.

Figure 7.2 below shows the dimensions of the new CTDCB design.

A linear regression was used to fit a line through the width function defined by Eq. 7.1 in order to design, print, and test CTDCB specimens with a simpler linear taper. Also, CTDCB specimens with a 1 mm square groove instead of the 90° v-shaped groove were designed, printed, and tested. These square groove specimens had the same taper shape as the complex

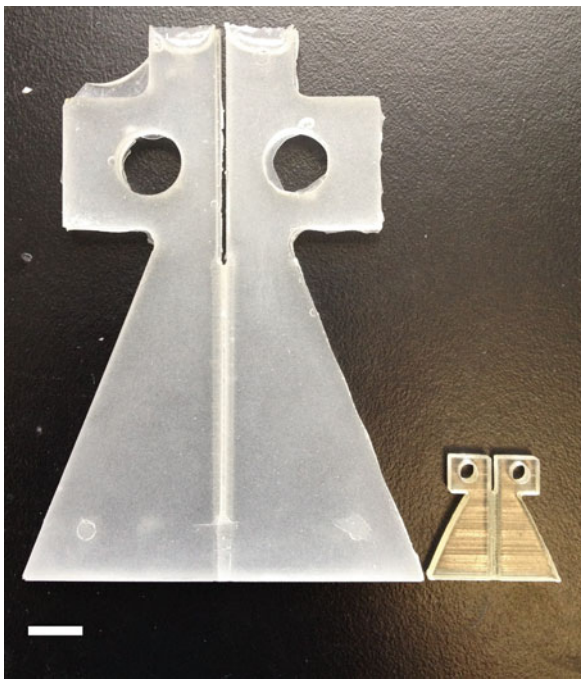

Fig. 7.1 Accepted standard TDCB shape (*larger*) and new CTDCB (*smaller*). Scale bar represents 10 mm

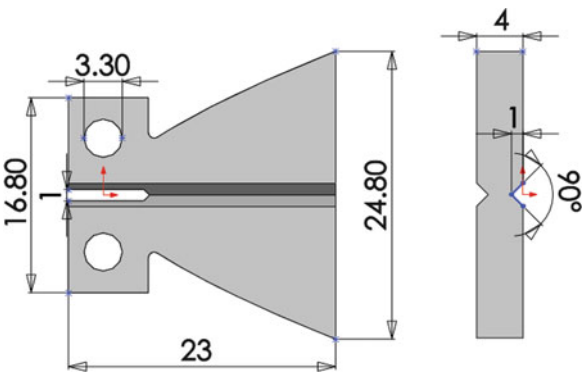

Fig. 7.2 Dimensions of CTDCB design (*complex curve*). All lengths are in mm

curve specimen shown above in Fig. 7.2. For each of the three types of specimens (complex curve, linear taper, and square groove), three specimens were printed for each of the six initial crack lengths tested (4, 5, 6, 7, 8, and 9 mm). This resulted in a total of 18 CTDCB specimens for each of the three types tested. All printed specimens were created using SolidWorks CAD software and printed using high quality settings on an Objet 3D printer.

The geometry of the complex curve CTDCB specimens was chosen to make a mold for dental composite testing. This mold was made using interlocking metal plates that fit into laser-cut acrylic top and bottom pieces. The composite resin was spread into the mold and then cured using exposure to blue light through the transparent acrylic on either side of the mold.

7.2.2 Fracture Testing

CTDCB specimens were tested in displacement control using a load frame controlled by LabVIEW software. Before testing, each specimen was pre-cracked using a razor blade in order to ensure a sharp crack tip. The specimens were loaded in Mode I fracture at a rate of 3 mm/min, while collecting force and displacement data, until failure occurred. Once the samples were tested, a linear regression was performed on the loading portion of the force versus displacement graph in order to find the stiffness and therefore the compliance of the test specimens using,

$$C = 1/k \tag{7.2}$$

where C is the compliance and k is the stiffness. The compliance values of three identical CTDCB specimens were averaged together for each of the six initial crack lengths of the printed specimens. These points were then plotted versus initial crack length in order to find dC/da from a linear regression of the data.

7.3 Results and Discussion

A typical force versus displacement graph that is collected during a CTDCB test is shown below in Fig. 7.3.

Figure 7.4 below shows the compliance versus crack length data for all of the printed CTDCB specimens as well as the five tests run on the current dental composite.

All three specimen geometries, the complex curve, linear taper, and square groove exhibited constant dC/da behavior for the crack lengths that were investigated in this work. Thus, all specimen geometries are acceptable to serve as crack-length-independent fracture specimens. Samples without grooves exhibited frequent arm break-off, as observed by other researcher [4]. The dC/da values shown below in Table 7.1 are the slope values of the linear regressions performed on the data shown in Fig. 7.4.

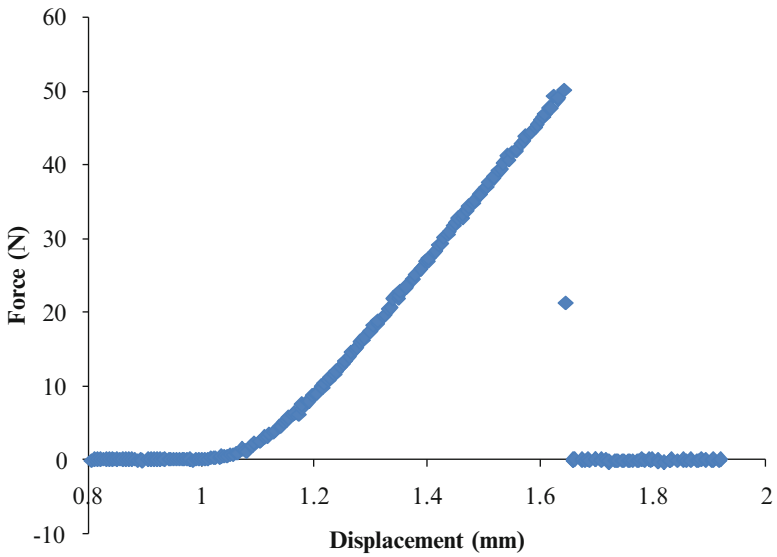

Fig. 7.3 Representative force versus displacement plot for a CTDCB test

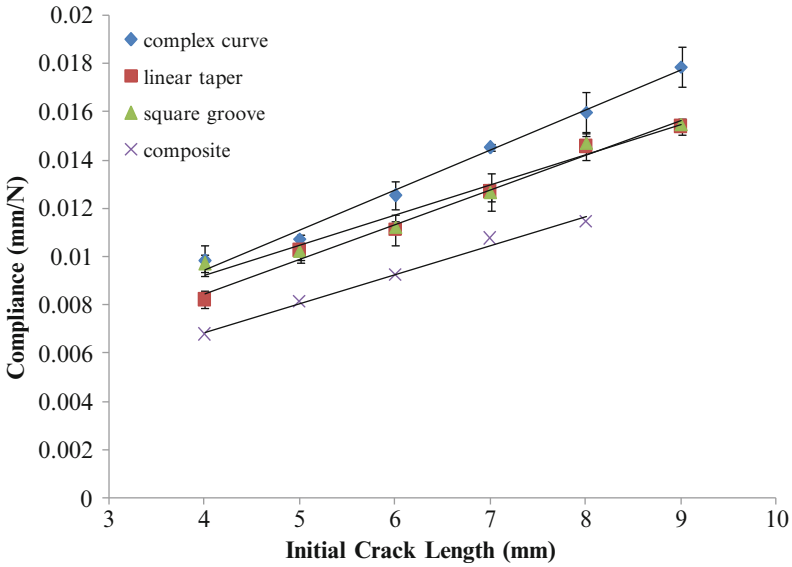

Fig. 7.4 Compliance versus crack length for all printed CTDCB tests as well as five tests on a dental composite material. Error bars represent one standard deviation above and below the mean data point

Table 7.1 dC/da values from linear regression of data

–	Complex curve	Linear taper	Square groove	Composite
dC/da (N^{-1})	0.00166	0.00144	0.00125	0.00119

Because the linear tapered specimen shape only approximates the complex curve shape, its measured dC/da value is slightly lower than that of the complex curve specimens. The square grooved specimens also exhibited a dC/da value lower than that of the v-grooved complex curve specimens. This difference between the dC/da values of the different groove shapes is unexpected. More experiments must be performed in order to better understand this phenomenon.

7.4 Conclusions

Rapid prototyping offers a quick and simple method of comparing various sample geometries and features. All three of the designs tested, complex curve, linear taper, and square groove provided a crack-length-independent measure of fracture toughness for the crack lengths investigated. The linear relationship between compliance and crack length in the dental composite specimens tested produces a constant dC/da and confirms that the new CTDCB design is a valid fracture testing geometry for use in dental composite restorative materials.

References

1. Watanabe H, Khera SC, Vargas MA, Qian F (2008) Fracture toughness comparison of six resin composites. Dent Mater 24(3):418–425
2. Mostovoy S, Crosley PB, Ripling EJ (1967) Use of crack-line-loaded specimens for measuring plane-strain fracture toughness. J Mater 2 (3):661–681
3. Brown EN, Sottos NR, White SR (2002) Fracture testing of a self-healing polymer composite. Exp Mech 42(4):372–379
4. Jung D (1997) Performance and properties of embedded microspheres for self-repairing applications. University of Illinois, Urbana, IL

Chapter 8
Mechanics of Compliant Multifunctional Robotic Structures

Hugh A. Bruck, Elisabeth Smela, Miao Yu, Abhijit Dasgupta, and Ying Chen

Abstract In this investigation, we report on experiments and models we have developed for compliant multifunctional robotic structures using arrays of conducting polymer composites have been developed to form a "nervous system" to sense shape and force distributions. The objective of this research is to enable better training of robots by enabling them to physically communicate via human touch using new compliant multifunctional structures. To achieve this, arrays of conducting polymer composites have been developed to form a "nervous system" to sense shape and force distributions. This sensor array is integrated into compliant composite structures using a scalable additive manufacturing process. These sensor arrays are being developed for a variety of model robotic structures, for example flapping wing MAVs (i.e., bird-like robots) and stair-walking robots. Experimental details of the associated deformation response are quantified in real-time using Digital Image Correlation (DIC). Output from the sensor array is related to shape and force distributions by solving the nonlinear inverse problem using a novel Singular Value Decomposition (SVD) method. This research is leading to new compliant, scalable, sensing structures that simultaneously monitor in real-time both global and local shapes, as well as force distributions. Since compliant multifunctional sensing structures do not yet exist for robots, it is envisioned that it will enable realization of new bio-inspired control principles for training robots. This will significantly advance the ability to make safer interactions and decisions in co-robotics by differentiating robotic interactions with humans from other objects in their environment.

Keywords Contact mechanics • Digital image correlation • Co-robotics • Multifunctional structures • Compliant sensing arrays

8.1 Introduction

The development of compliant sensing structures that integrate multiple functions (e.g., spatially-varying mechanical properties, sensing, wiring, etc.) and that can be produced in large areas is critical to providing the advanced sensing capabilities required for faster and more accurate control in co-robotics. Currently, there are no viable structures for robots that can sense both pressure distributions and shapes simultaneously. By exploiting recent advances in flexible circuits, stretchable sensors, and polymer composites, our research will enable "blind" robots to "touch" and "feel" with flexible limbs that have "nerves" connecting to their "nervous system", analogously to humans. This will also facilitate the integration of polymer actuators and thermal sensors.

Previously, we have been working on developing robots, such as bird-like robots, and understanding the mechanics of structures that control their performance, such as compliant wings [1, 2]. We have been able to realize compliant multifunctional structures by affixing commercial flexible solar cells onto wings for the bird-like robots [3]. Also, stretchable piezo-resistive strain sensors have been applied by spray-coating to measure strains at multiple locations during flapping for self-sensing [4].

In this investigation, we report on experiments and models we have developed for compliant multifunctional robotic structures using arrays of conducting polymer composites have been developed to form a "nervous system" to sense shape

H.A. Bruck (✉) • E. Smela • M. Yu • A. Dasgupta • Y. Chen
Department of Mechanical Engineering, University of Maryland, College Park, MD 20742, USA
e-mail: bruck@umd.edu

G. Tandon (ed.), *Composite, Hybrid, and Multifunctional Materials, Volume 4: Proceedings of the 2014 Annual Conference on Experimental and Applied Mechanics*, Conference Proceedings of the Society for Experimental Mechanics Series,
DOI 10.1007/978-3-319-06992-0_8,

and force distributions. Experimental details of the associated deformation response are quantified in real-time using Digital Image Correlation (DIC). Output from the sensor array can be related to shape and force distributions by solving the nonlinear inverse problem using a novel Singular Value Decomposition (SVD) method.

8.2 Research Approach and Results

The current research approach consists of the following.

(a) Fabrication of multifunctional robotic structures with integrated electronic components.
(b) Design of experiments for characterizing the mechanics of multifunctional robotic structures using load cells and 3D Digital Image Correlation.
(c) Experimental characterization of loads and deformations of multifunctional robotic structures for enhancement of new FEA models for compliant multifunctional robotic structures.

8.2.1 Fabrication of Multifunctional Robotic Structures

We have developed elastomeric electrodes and strain gauges (latex, PDMS, or other elastomeric host polymers loaded with exfoliated graphite) that can be painted onto surfaces (Fig. 8.1). The exfoliation of graphite results in an electrically conductive mixture of graphene and somewhat thicker sheets/flakes of graphite. Mixing the exfoliated graphite (EG) into an elastomeric host produces a conductive composite. The electrical conductivity and the Young's modulus of the composite depend on the amount of EG in the host (the loading), as well as the deformation of the material. Previously, we have investigated similar composites based on carbon nanotubes (CNTs), and have begun looking at the thermal response of these materials as well.

The composites can be applied by spray-coating, brush coating, printing, casting, etc., allowing them to be placed in multiple locations on a deformable surface, such as the small wing of our test-bed. These materials have high gauge factors (change in resistance with strain), yet still maintain a low Young's modulus. The former gives them the high sensitivity required for these applications, while the latter makes the sensor more compliant than the wing material in order not to interfere with the movement of the compliant structure. Traditional strain gauges, such as the metal foil type, do not have the large strain capabilities of these elastomeric composites, nor the necessary compliance, nor the scalability.

Fig. 8.1 (*Top*) Schematic illustration of separation of the layers in graphite by exfoliation, SEM images of exfoliated graphite (EG) showing mixtures of sheets of graphene and multi-layer graphite, and latex strain sensors. (*Center*) Deposition and patterning by spray coating through a stencil. (*Bottom*) Compliant electrode/sensor material on a compliant substrate

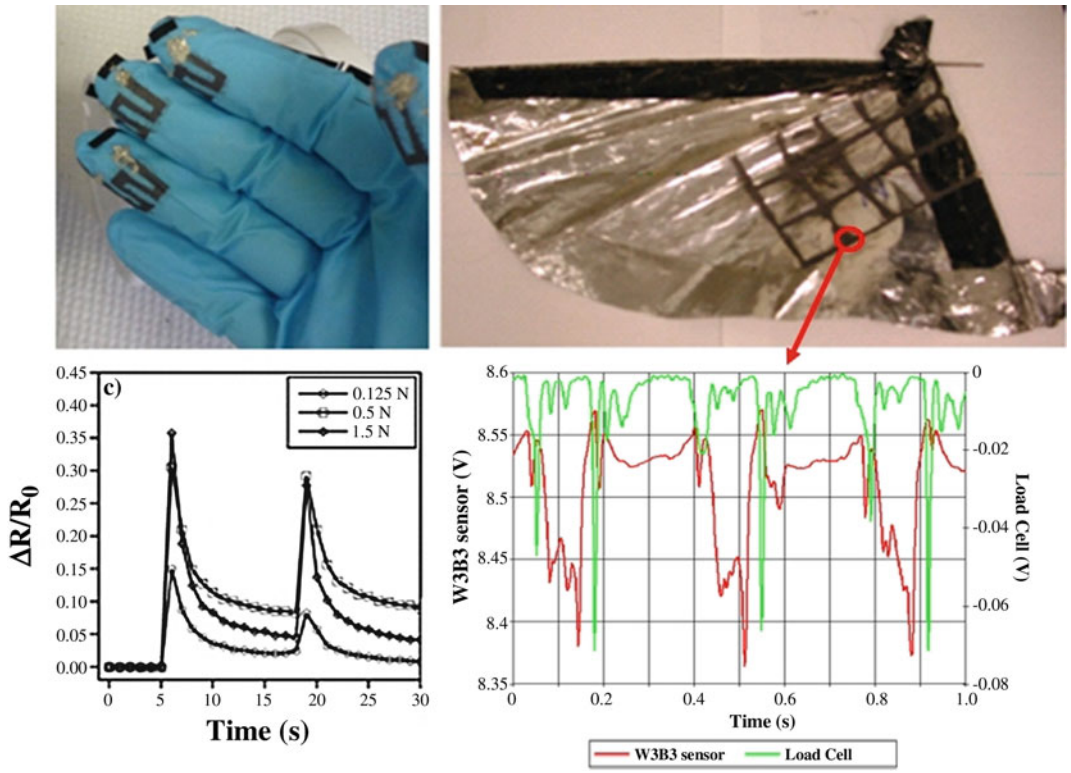

Fig. 8.2 Strain sensors integrated into a nitrile glove and compliant MAV wing, with corresponding data. The glove shows a clear response to pressure (not proportional to load). Data recorded for 1 s from the strain sensor on the wing (*green*) and comparison with measured thrust forces (*red*) [2]

8.2.2 Design of Experiments Using DIC and 6 DOF Load Cell

Prototype tactile sensors have been fabricated by airbrushing the elastomer composite through a stencil onto a nitrile glove, using Neoprene as the host elastomer (Fig. 8.2). The sensor clearly responded upon the hand grasping an object and to loads applied on top of the sensor. These strain gauges were also applied in a grid pattern onto a compliant flapping wing for a micro air vehicle (MAV), and data were recorded during flapping simultaneously with data from a force sensor that measured the generated thrust [1]. The dynamic response was sufficiently fast to respond to changes on this time scale. These sensors allow us to make measurements of the strains in the compliant structures for the determination of the loading applied and will allow us to use optical measurements to calibrate and validate the strain sensor measurements and shape calculations. The strain gauges are calibrated under known loads producing known shapes. A six DOF load cell is utilized to provide a complete characterization of loads acting on the structures, and 3D Digital Image Correlation is used to provide full-field deformation characterization.

8.2.3 Experimental Shape Characterization and Hybrid Numerical Modeling of Forces

3D Digital Image Correlation (DIC) has been used to track the shape of the structures during contact, allowing us to correlate the shape with the measurements at multiple length scales from the integrated sensors to support model development. We have utilized this high-speed shape characterization to track the deformation of wings during the flapping cycle to directly determine the effects of solar cell integration on wing flexibility. The 3D optical tracking of features on the surface enables measurement of shape and of strain fields, in what can be termed an "optical finite element analysis". Figure 8.3 shows 3D DIC shape measurements of compliant multifunctional wings used on a flapping wing MAV we have developed at the University of Maryland known as Robo Raven (http://www.youtube.com/watch?v=mjOWpwbnmTw), that are then incorporated in a CFD modeling to determine the loads that are compared with the measurements using the six DOF load

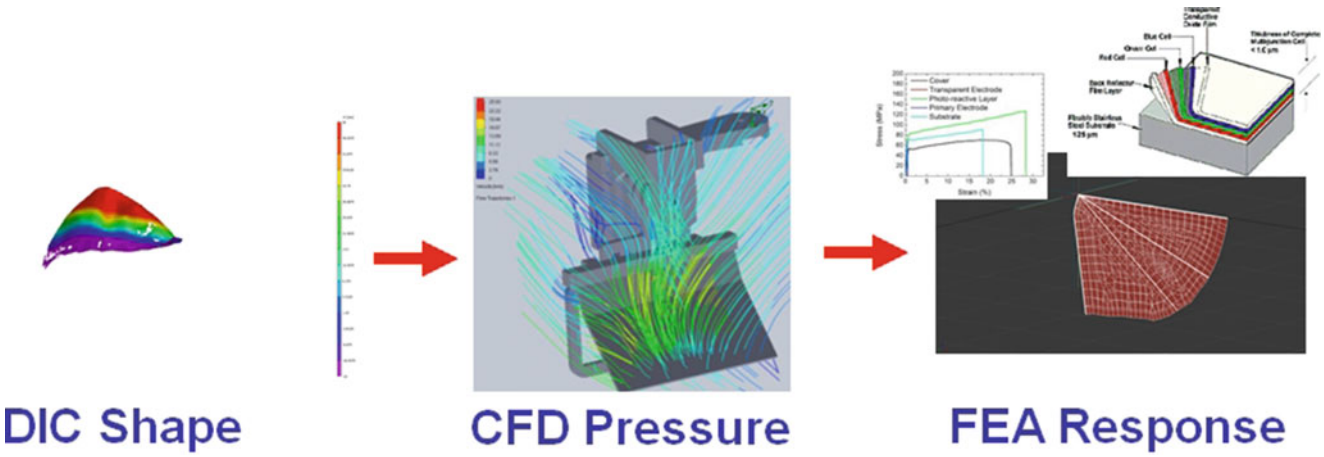

Fig. 8.3 Compliant multifunctional MAV wing with (*left*) measured shape during down flap cycle used in a (*center*) CFD modeling for aerodynamic loads that are then incorporated into a (*right*) detailed FEA model of the structure to predict the deformation response for comparison with measured 3D DIC shape to determine consistency

cell and in predictions of the deformation response from a detailed FEA model of the structure to determine consistency with measured 3D DIC shape.

The deformations being measured are related to *sensor configuration*, *structural material,* and *contact conditions*. Using DIC in this manner can be thought of as performing an "Optical Finite Element Analysis", where the displacement fields can be directly related to mechanical and thermal loading. For example, increasing the thickness or stiffness of the structures will reduce deformations at a given pressure level. This can improve structural integrity, but can concentrate loads when interacting with humans to dangerous levels. We have previously used this approach to characterize thermal strains in rigid polymer structures around embedded resistors. This was done during operation to develop thermo-mechanical FEA models for optimizing thermal and mechanical design through multi-material interfaces [5]. For this research, we have been using it to look at model contact problems for compliant and rigid structures, where we have been able to quantify the variation in the pressure distributions from the DIC strain fields as the contact area varies with the applied loading using a glass slide to visualize contact associated with the foot of a stair-walking robot (see Fig. 8.4a). We have been able to couple the DIC results with FEA models to analyze both the local conditions that influence contact force (see Fig. 8.4b) and the subsequent locomotion of a stair-walking robot developed at the University of Maryland (see Fig. 8.5).

8.2.4 Modeling Flexible Shapes from Strain Measurements

We have previously developed techniques for characterizing the nonlinear dynamics of structures, such as diaphragms in pressure sensors [6, 7]. In previous work, a strain-to-shape algorithm based on Frenet-Serret formulas was studied and used for shape determination of a towed sonar array based on strain measurements at various nodes (Fig. 8.6). In more recent work, an inverse problem was formulated to use the data from discrete strain sensors placed on a beam to determine the beam shape under an arbitrary loading (Fig. 8.7). It was found that the accuracy of the beam shape determination was largely related to the signal-to-noise ratio of the strain sensor data. For applications to compliant multifunctional structures, we are solving a more challenging inverse problem by extending our work to the more complex deformations achievable with compliant multifunctional structures. Models for determination of structure shape and loading distributions are being developed in both linear and nonlinear regimes and the noise in the strain sensor data is being addressed by developing a model based on Bayesian algorithms.

Full-field reconstruction of structure shape from a set of strain measurements represents a challenging inverse problem. Recently, Tessler and Spangler [8] formulated a variational principle for the inverse problem of full-field reconstruction of 3D shell deformations from experimentally measured surface strains, and this approach is applicable to high fidelity linear, as well as nonlinear, static and dynamic motions of plates and shells. However, shape reconstruction has not been demonstrated in the nonlinear regime.

We are currently extending our work to the determination of structure shape and loading distributions in the nonlinear regime, which is encountered with mechanically complex flexible structures and compliant structures. A first approach will follow the lines of Tessler and Spangler to determine the displacement field (shape) of a thin layer in the complaint

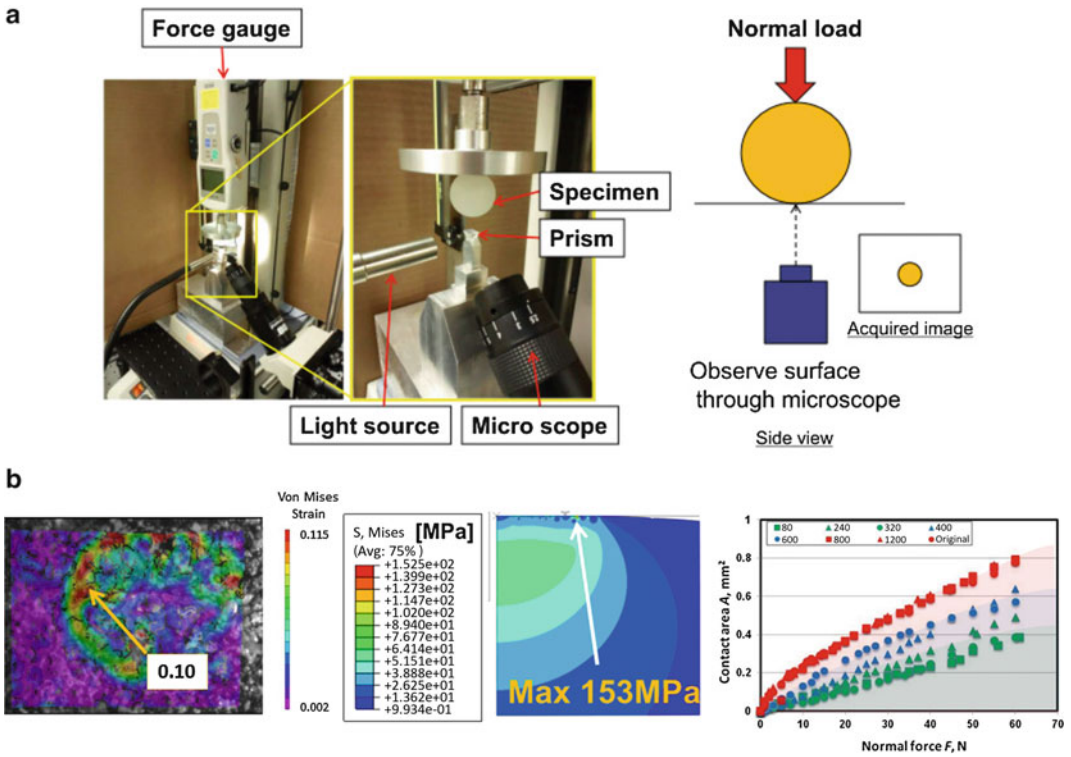

Fig. 8.4 (**a**) Experimental configuration to characterize contact between compliant and rigid structures, and (**b**) DIC strain fields associated with variation in pressure distributions that can be determined as the contact area varies with the applied loading and correlated to FEA simulations based on surface roughness

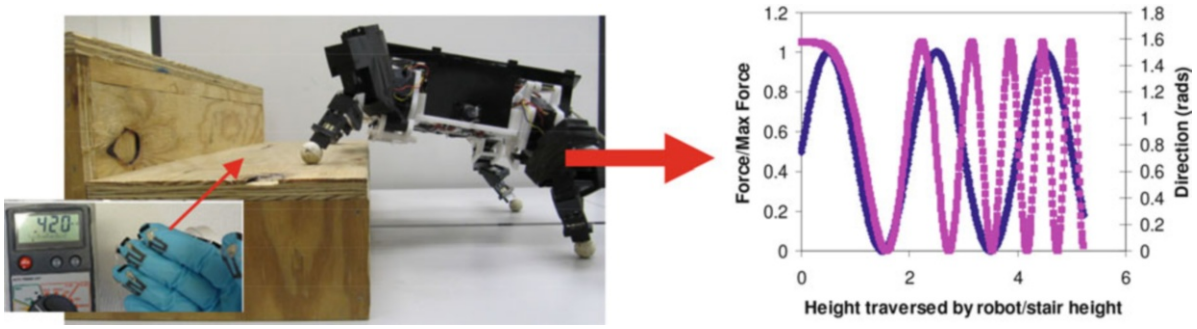

Fig. 8.5 (*Left*) Stair-walking robot where integration of the haptic sensor (*inset*) on the feet will enable (*right*) real-time tracking of the magnitude and direction of forces for enhanced control

multifunctional structure (Fig. 8.8a). The set of discrete measurements from the strain sensors embedded in the structures will be curve fit to obtain a smooth function. This function will be used to formulate a variational problem with the objective of minimizing a cost function defined in terms of the measurements and the predicted values. For this method, a semi-analytical model of the structure is needed to predict the strain–displacement relationship, which will be obtained by using classical thin shell theory along with the appropriate boundary conditions. Geometric nonlinearity will be included in the model to yield the full-field nonlinear out-of-plane deformation, which has never been attempted in previous work. The variational formulation will lead to the displacement fields of interest. The displacements will then be graphically displayed by creating a 3D wire frame mesh, dynamically changing as the layer of interest in the structure deforms during operation. This approach enables fast and real-time shape determination for thin deformable structures, in which strain measurements are required on both surfaces of the thin layer. Since this approach can accommodate any loading applied to the structure, it is especially useful for shape determination of co-robotic structures with deformable shapes, which may experience complex, unsteady loading during their interactions with humans or with their environments.

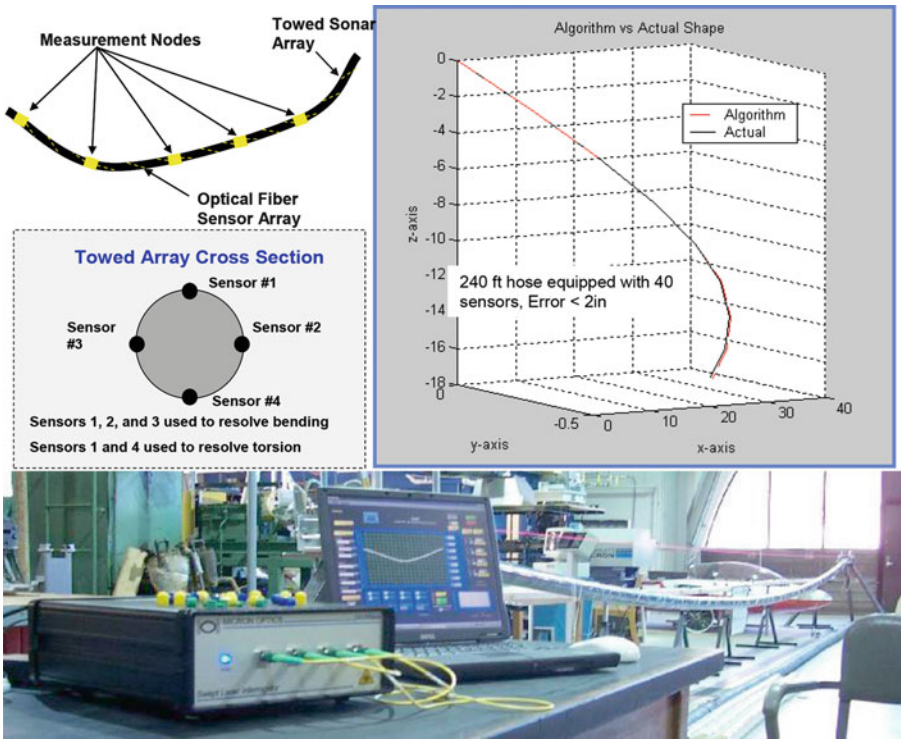

Fig. 8.6 Previous work on shape monitoring of towed sonar array based on distributed strain measurements

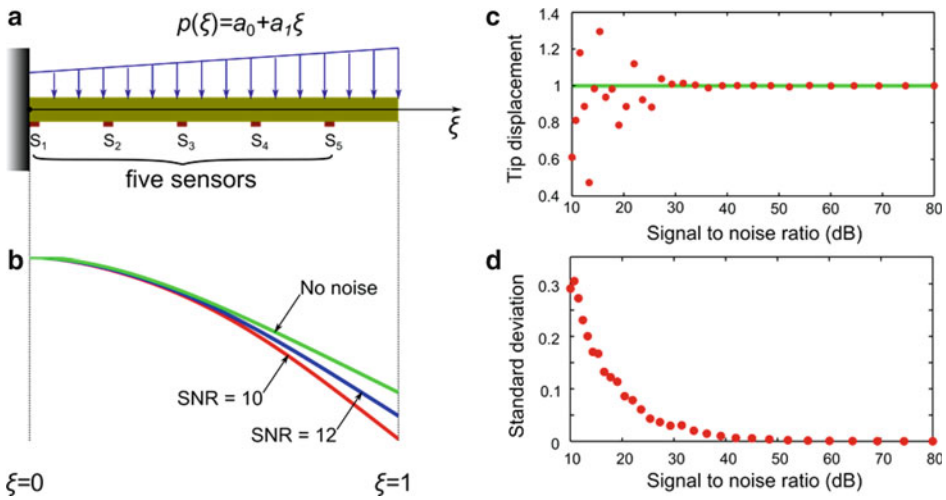

Fig. 8.7 Shape determination of a compliant beam structure with arbitrary loading. (**a**) Schematic of a beam with five strain sensors. (**b**) Determined beam deflection with respect to different noise scenarios. (**c**) Beam tip displacement vs. signal-to-noise ratio (SNR) of the strain sensor. (**d**) Standard deviation of the tip displacement vs. SNR

In a second approach (Fig. 8.8b), the FEA model of the structure will be used with an assumed loading distribution. Under this loading, the strain field can be obtained, which will be used to again formulate a variational problem whose objective is to modify the loading distribution to minimize a cost function defined in terms of the strain measurement data and the modeled strain field. Once the minimum cost function is achieved, the final determined loading distribution will be applied to the FEA model of the structure to obtain the displacement field. Although the limitation of this approach is that the loading applied to the structure should be low frequency as well as mathematically describable, this method is applicable to reconstructing the shape of arbitrary structures (not limited to thin deformable structures) as well as determining the load distributions in both linear and nonlinear regimes. The model can be seeded with experimental data. Determination of the loading distribution will be important for tactile sensing with the multifunctional structures in robotic hands or feet.

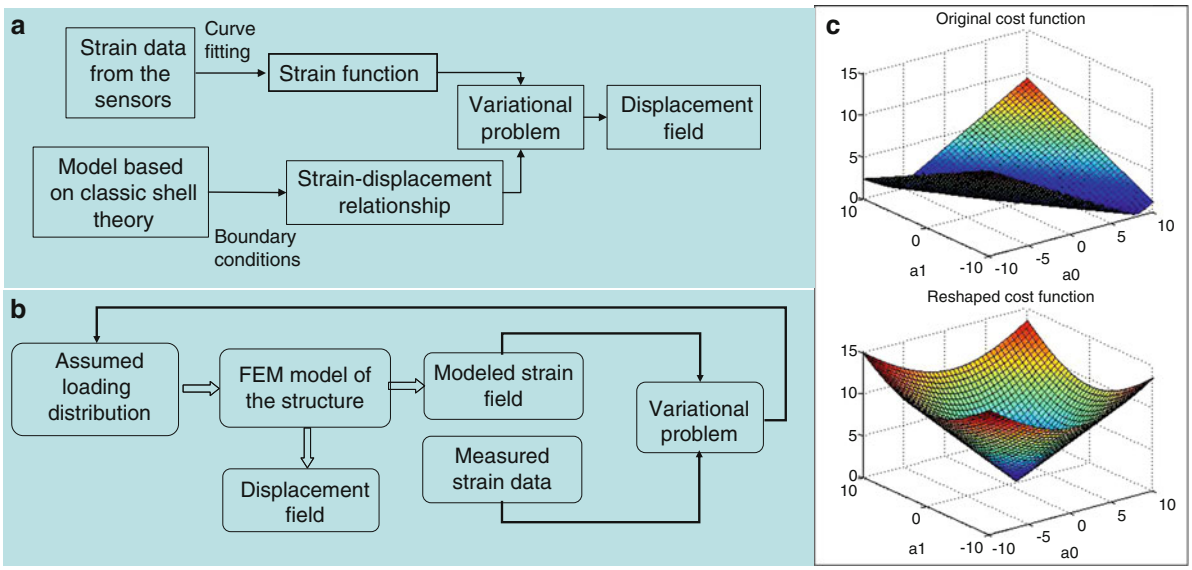

Fig. 8.8 Schematic of proposed shape reconstruction method from strain measurements for (**a**) a thin deformable layer and (**b**) arbitrary structure. (**c**) Example of reshaping cost function using SVD method

In both approaches, the inverse identification will be carried out for both static and dynamic conditions. The computation time must be reduced to achieve real-time monitoring of shape and loading. There are many variational principles that can be used to formulate the problem and obtain the cost function. We will investigate two of them: the conventional least mean-square (LMS) and more advanced differential evolution (DE) scheme [9]. Since LMS does not require correlation function calculation or matrix inversions, it can usually lead to fast convergence for simple structures. However, for more complicated shapes or large areas, DE may be a better solution because it does not require the optimization problem to be differentiable and can be used on optimization problems that are noisy and that change over time discontinuously. However, it has high computational cost and may in some cases not find a solution. To improve performance, we are developing novel approach that makes use of singular value decomposition (SVD) to reshape the cost function, which has never been used to solve the ill-posed inverse problem. SVD is a method for identifying and ordering the dimensions along which the data exhibit the most variation [10]. In a preliminary study, we have applied SVD to determine the shape of a beam structure. As can be seen from Fig. 8.8c, the reshaped cost function eliminated the problem of traditional optimization tools getting stuck in local minima.

In solving the ill-conditioned inversion problem, complications arise when inhomogeneities are introduced into the structure. In addition, even small amount of noise in the strain sensor measurement could lead to unbounded errors in the determination of loading or deformed shape. Nowlin [11] applied the Bayesian algorithm to interpret tactile sensing data for a prototype fingertip, and successfully removed spurious modes, which could not be achieve by using the commonly used linear least-squares inverse. Following this approach, are implementing the Bayesian algorithms to our model. Loading distribution functions are chosen based on the solution to the eigen-value problem of the FEA model, and a target product of probability distribution will be defined. This enables us to construct stable solutions to the inverse problem in the presence of non-perfection of device fabrication and measurement noise.

The methods that we are developing are generic, and can be easily implemented for any robotic structures in which the proposed multifunctional structures can be applied, such as co-robots with dexterous robotic hands for interaction with humans and other highly deformable robotic structures. This represents a significant leap forward from the existing work, which are generally limited to the linear regime or only applicable for certain structures, and have difficulty to solve the ill-posed problem. These models enable us to determine the distributions of contact pressures for co-robotics (the magnitude of force and its directionality, using the second approach). More importantly, since these models incorporates structural dynamics, the time evolution of the loading distributions can be obtained. They allow the robot to sense the change of the loading, thus extract both local and global interaction information with a human. For example, based on the time evolution of the loading distribution, the robot will be able to sense the form of force as well as the change moment applied to its arm. On the other hand, based on the time evolution of the contact shape, the robot will be able to tell the difference when its foot steps on a human foot or a stone. Therefore, incorporating this in a control system with some well-defined communication protocols, the compliant multifunctional structures enable novel interactions with their environment (e.g., training of the robots by human touch).

8.3 Conclusions

We have been able to fabricate compliant multifunctional robotic structures that contain integrated compliant strain sensors that serve as "nerves" for the robot to detect global and local loads. Experiments have been designed to characterize the deformation and loads acting on these structures. In particular, 3D DIC has enabled deformation measurements that are utilized in numerical simulations for model development to provide rigorous validation and design of compliant multifunctional robotic structures. Coupled with new models using FEA, we will solve a singular valued decomposition problem to reconstruct the shapes form the signals generated by the integrated compliant strain sensors, and the subsequent global and local loading associated with those shapes.

Acknowledgements This work has been supported by NSF under grant IIS1317913. The support of the University of Maryland Robotic Center and Toshiba is also greatly appreciated.

References

1. Mueller D, Bruck HA, Gupta SK (2010) Measurement of thrust and lift forces associated with drag of compliant flapping wing air micro air vehicles using a new test stand design. Exp Mech 50:725–735
2. Gerdes J, Cellon KC, Bruck HA, Gupta SK (2013) Characterization of the mechanics of compliant wing designs for flapping wing miniature air vehicles. Exp Mech: 1–11. doi:10.1007/s11340-013-9779-5
3. Bruck HA, Gupta SK, Perez-Rosado A, Philipps A, Roberts L (2013) Compliant multifunctional wing structures for harvesting solar energy. In: Proceedings of ICCM19, Montreal, Canada, pp 1–9
4. Wissman J, Perez-Rosado JA, Edgerton A, Levi BM, Karakas ZN, Kujawski M, Phillips A, Papavizas N, Fallon D, Bruck HA, Smela E (2013) New compliant strain gauges for self-sensing dynamic deformation of flapping wings on miniature air vehicles. Smart Mater Struct 22 (8):085031
5. Gershon AL, Gyger LS Jr, Bruck HA, Gupta SK (2010) In situ characterization of residual strains near electronic components embedded in thermoplastic polymers during processing and operation. In: Gilat R, Banks-Sills L (eds) Advances in mathematical modeling and experimental methods for materials and structures. The Jacob Aboudi Volume. Springer, New York, pp 145–160
6. Yu M, Balachandran B (2005) Exp Mech 45(2):123–129
7. Yu M, Long X, Balachandran B (2008) J Sound Vib 312:39–54
8. Tessler A, Spangler JL (2005) A least-squares variational method for full-field reconstruction of elastic deformations in shear-deformable plates and shells. Comput Meth Appl Mech Eng 194:327–339
9. Storn R, Price K (1997) Differential evolution—a simple and efficient heuristic for global optimization over continuous spaces. J Global Optim 11:341–359
10. Trefethen LN, Bau D III (1997) Numerical linear algebra. Society for Industrial and Applied Mathematics, Philadelphia
11. Nowlin WC (1991) Experimental results on Bayesian algorithms for interpreting compliant tactile sensing data. In: Proceedings of the 1991 IEEE international conference on robotics and automation, Sacramento, California, April 1991

Chapter 9
In Situ SEM Deformation Behavior Observation at CFRP Fiber-Matrix Interface

Y. Wachi, J. Koyanagi, S. Arikawa, and S. Yoneyama

Abstract This paper studies deformation of CFRP at microscopic area and observing technique. Tensile test is carried out for CFRP specimen and digital image correlation (DIC) method is used to observe deformation of microscopic area, especially around its fiber interface. CFRP specimen is loaded by tensile testing machine for investigating deformation around vertical section of fiber. Diameter of carbon fiber used which is mainly interested in the specimen is micro scale, therefore scanning electron microscope (SEM) is used to gain high magnification and resolution pictures as they deforms. To achieve this in situ experiment, testing machine which can be used in SEM is developed. The essential to achieve DIC is selection of random pattern used to follow up change of the area, which greatly influences accuracy of result. Colloidal silica and the other particles are utilized for random pattern with adjustment of concentration. The pattern must be seen clearly and small enough compared to fiber vertical section. Through this research, examination of deformation observation at microscopic area and consideration of starting and fracturing procedure of CFRP are performed.

Keywords DIC • CFRP • Scanning electron microscope • Uniaxial tension experiment • High magnification

9.1 Introduction

Composite material of fiber and plastic is known as FRP, improved strength and formability with excellent stiffness. Therefore, the spread applications in aerospace fields are expected. Reducing weight of aircraft is one of the biggest aims, and this material is an appropriate material to achieve this. Boeing787 uses more than its half weight is made up of composite material. When using composite material in this kind of field, research on deformation and fracture is essential. As a matter of course, composite material is a combination of different materials, so as FRP. Because of this, its deformation and fracture behavior is not uniform. Micron scale fibers effects as an inclusion and stress concentration occurs. When CFRP is loaded, initial damage such as fiber debonding, matrix crack and fiber breaking occurs. Progressing and complex of these are main cause of breaking. Generally, since interlaminar and fiber interface and neighborhood of FRP matrix is very weak compare to other part, it is important to observe about initial damage and fracture progressing there. Both finite element method and observation of actual are held upon investigate the mechanism of destruction of the composite material in detail. However, due to the complex of such Poisson contraction, its measurement is difficult. Further, past research about mechanism of deformation caused in the meantime the process of fracture damage occurs is insufficient.

Study in the region of macro and micro area of FRP has been held since reasons above. In past research, we conducted a study of the temperature/time dependence of the CFRP interface strength [1]. By observing the differences in fracture morphology in strain rate under different temperatures, microscopic fractures of CFRP, crack and matrix interface debonding, are observed. It was found that crack of matrix is dominant at low strain rate and under high temperature.

Y. Wachi (✉) • S. Arikawa • S. Yoneyama
Department of Mechanical Engineering, Aoyama Gakuin University, 5-10-1 Fuchinobe, Sagamihara, Kanagawa 252-5258, Japan
e-mail: c5613140@aoyama.jp

J. Koyanagi
Department of Materials Science and Technology, Tokyo University of Science, 6-3-1 Niijuku, Katsushika-ku, Tokyo 125-8585, Japan

G. Tandon (ed.), *Composite, Hybrid, and Multifunctional Materials, Volume 4: Proceedings of the 2014 Annual Conference on Experimental and Applied Mechanics*, Conference Proceedings of the Society for Experimental Mechanics Series,
DOI 10.1007/978-3-319-06992-0_9,

Regard to this, dominant of interface debonding at high strain rate and low temperature was found. After all, finite element analysis of microscopic area vicinity of fiber and its interface was carried out. Still, need of actual observation was suggested because of gap between the original and analysis.

Present studies of external research organization shows observation of FRP fracture morphology by using optical microscope and SEM [2–5]. These are frequently discussed within analysis of deformation and shear-stress/stress distribution using finite element method. However, deformation occurring at micro area is complicated because of fiber and its interface. Therefore, difference from the actual material is always discussed and suggested. Which means deformation observation of real one is needed and digital image correlation method is used often. Images of microscopic area which is used for digital image correlation are taken by microscopes. Optical microscope is one of the most typical equipment for observing small area, since it is easy to handle and environment condition can be settled in various way. Pattern such as speckle pattern and particles has been used for random pattern for digital image correlation [6]. However, its maximum resolution is limited because of wavelength of visible ray. To observe higher magnification, other microscopes such as SEM [7–13] and atomic force microscope (AFM) image [14, 15] are typically used. Within resolution of this equipment, development of appropriate random pattern for digital image correlation is needed. In past studies, research about development of random pattern for digital image correlation at high resolution has been performed [16]. It is not necessary if a specimen has pattern originally on its surface, which unevenness of surface is typical example of this [11, 14, 15]. Production of pattern on specimen is needed except it has pattern originally. Attaching particles is often used technique for random pattern. Gold sputtering with micron grid is very famous method, but it needs certain equipment which is expensive and requires detailed condition setting.

Above these studies and random pattern settlement, tensile test of laminated CFRP is performed in this paper. At the same time, deformation of fiber interface and around it is observed by using digital image correlation with developed random pattern creating method. Improvement of settlements for observing deformation of micro area using digital image correlation is required to obtain high precious result. This includes development of appropriate random pattern, image acquisition conditions and the other experimental environment. Especially, way of creating random pattern is important. There is no established technique for particular specimen, resolution, and high-vacuum environment. In this paper, chosen particles are placed and stick to the surface of specimen which is very easy and simple compared to gold or platinum sputtering. Since this method is not established yet, try and error of this method is necessary. Different sized colloidal silica and Yttria-stabilized zirconia in suspension are chosen for particle used. Their concentration are adjusted then painted and dried on specimen and surface depositing remaining can be used as random pattern. After developing and preparation of random pattern, SEM images of the before and after loaded are taken and digital image correlation method is adapted. Through this performance, deformation behavior is observed by measuring displacement and strain distribution of CFRP fiber-matrix interface. Also, measurement at microscopic area using digital image correlation is verified.

9.2 Uniaxial Tension Test in SEM

The observation device used is electron probe micro analyzer (EPMA) at center of instrumental analysis of Aoyama Gakuin University. The actual model of the equipment is JXA-8200S from Japan Electron Optics Laboratory (JEOL). By using SEM function of this equipment, high resolution and precision image is taken. Resolution of this equipment is about several nanometers, and fiber which is target of this research is several microns, means it has enough ability. Additionally, observing area is controlled by movement of stage. When specimen deforms or some kind of accident happens and observing area is lost, it is easy to return to the original part by specifying the coordinate. This makes tracking of deformation easy and certain. It is not difficult to take specimen out as to change its load each time, however, due to the character of the equipment, conditions and settlements of the equipment changes. Especially charging up, focus and astigmatism are seen remarkable. Obtaining images at exactly same terms is very difficult, and difference of image caused by these reasons directly effects to the result of digital image correlation. Upon this, the experiment is held without taking specimen out from the equipment until it breaks.

In order to carry this out, there are problems which are known and obvious. The equipment use does not have mechanism to do tensile test, which means production of test machine is necessary. Useable space is only 25 mm height and 100 mm width and length. If any part is out of this range, failure of the equipment is concerned. In this narrow space, control of loading power and measurement of its producing value is required. Therefore, actuator and load cell must be connected from tensile test machine which is inside of the equipment to outside by cable. The atmosphere of the equipment is high vacuumed and settle around 10^{-5} Pa. Since electron beam is used to obtain image, only non-magnetic parts can be used. The biggest problem was loading device to use, but by using ultrasonic actuator it is solved. Features of this are very small, produce

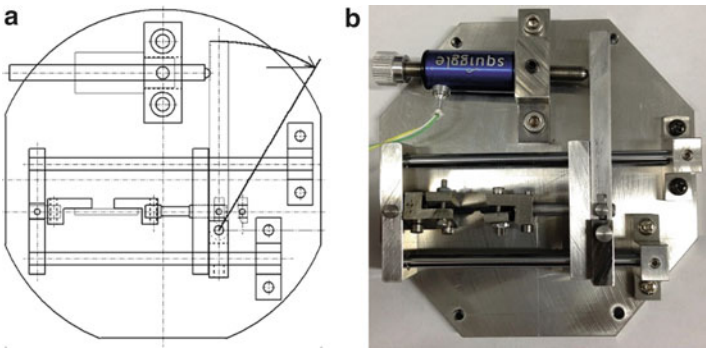

Fig. 9.1 (**a**) Schematic picture and (**b**) photo of tensile test machine

relatively large load, and does not use magnetic part. Schematic illustration and photo of real tensile test machine is shown in Fig. 9.1. Actions of this tensile machine are easy. As actuator moves forward, lever is hit and pushed. As the lever rotates, principle of leverage works and specimen between two posts is pulled. This mechanism brings tensile load and images are gained until specimen breaks.

9.3 Random Pattern for Digital Image Correlation

To observe deformation of CFRP, digital image correlation method is used. This method requires random patterns on the specimen surface. Generally, pigment such as spray paint is used to create dot paint for random pattern on the entire surface when observing range of several tens to several hundred meters. However, the observing area in this study is tens of microns. In this range, spray paints cannot be used since its particle size is not suitable. Therefore, a different approach is needed to create micro pattern.

There are some examples of technique to create micro random pattern from past studies and experiments. In our current examination, particles which are few tens of nanometers in diameter are applied to specimen surface. The appropriate size of particle can be forecast from observation conditions, diameter of the fiber is 7 μm and image is gained from the equipment is about 1,000 pixels in vertically and horizontally with enough resolution. The particle must be bonded on the surface because of following reason. Since inside of the equipment which specimen is placed is settled high vacuum atmosphere and exhaust is held so air is flowing there. If particles are just placed on the specimen, it easily blows away by air flow. As the particle moves other than because of specimen deformation, it directly effects to result of digital image correlation. So the pattern must be stabilized and stabled. Simple solution for this, particle is dissolved in a liquid and then dried on the specimen surface. This produces a sufficient adhesion force. There is a feature of this way, particles are condense and become bigger grain than expected and not aligned as shown in Fig. 9.2. Alumina particle which is smaller than 100 nm in diameter is used in this photo, circle thing shown in the photo is fiber cross section and resin is around it. Each grain is seen much larger than its original size because of cohesion. This is not fine since result of correlation changes depending on the evenness of random pattern. Still, by changing concentration and kind of suspension and application method, it is slightly controllable. Especially the using specimen is polished and repels water and easily cause become uneven during the drying process. Also vapor deposition of platinum adapted to specimen, mainly used to prevent for charge-up, have favorable effect to adhesiveness.

Figure 9.3 shows pattern of particles, which around 30 nm diameter colloidal silica (Snow techs ST-30) is used. This particle is dissolved in alkaline aqueous solution and repelled from the specimen surface. As written in previous paragraph, to solve this problem concentration of the suspension is reduced by mixing with ethanol. By increasing the concentration of ethanol, no longer repelled from polished surface of specimen and cohesion becomes less since drying time is shortened.

9.4 Experiments

Specimen used is unidirectional laminated CFRP. Its mechanical properties are shown in Table 9.1. Length of specimen is 25 mm, 5 mm in width and 2 mm in thickness. Base material of the CFRP is epoxy resin (Mitsubishi Plastics Hyej17HX1 curable 180 °C), and reinforcing material is carbon fiber (TORAYT300). Fibers are settled in width direction and density

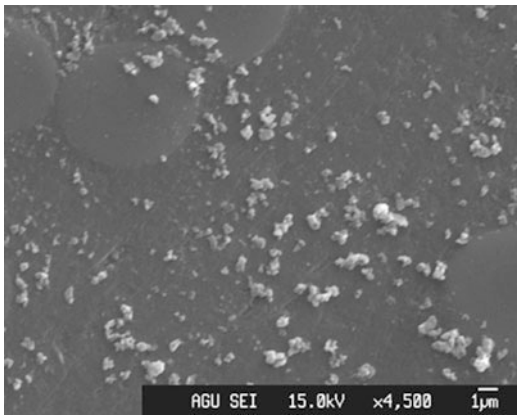

Fig. 9.2 Cohesion of alumina particles

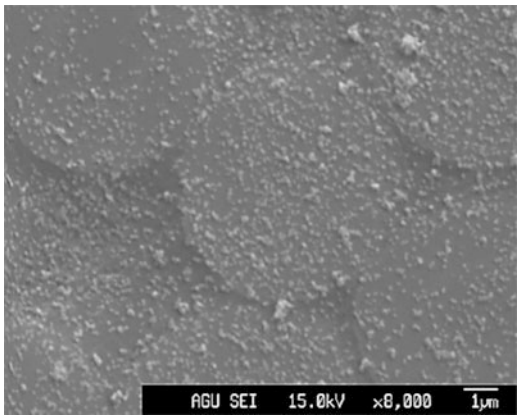

Fig. 9.3 Colloidal silica particles

Table 9.1 Mechanical properties of specimen

	Young's modulus (GPa)	Tensile strength (MPa)	Poisson's ratio
Epoxy	5	80	0.3–0.4
Carbon	230	3,600	0.3
Carbon (vertical)	5–50	–	–

ratio of the reinforcing agent and the base material is 45:55. Diameter of the fibers is 7 μm in average. In the experiment, width direction which can see the fiber cross section is used for observation. Specimen is platinum vapor deposited to prevent for charge-up, the setting is 30 kV in 40 s.

By using observation devices written in previous paragraph and specimen with random pattern prepared specimen, experiment is held. Colloidal silica and ethanol is used to create random pattern as it was in previous paragraph and Fig. 9.3, the concentration is settled at 5 %. The specimen is settled in a tension test machine and photo of observation is taken before loading. Load increases until the specimen breaks and photo is taken at each in constant, then obtained images are used for digital image correlation. As a result, changing process of displacement and strain distribution until fracture can be observed.

9.5 Result of Digital Image Correlation

Obtained SEM images in experiment is shown in Fig. 9.4, they are 1,280 × 1,024 pixels resolution and the magnification is ×5,000. Forced displacement are given to specimen in horizontal direction and it increases from (a) to (d) which is just before specimen breaking. Figure 9.4a shows specimen surface without loading and Fig. 9.4d is taken before the specimen breaks. Gray color circle object appears in photo is cross section of fiber and the darker area around fiber is epoxy resin.

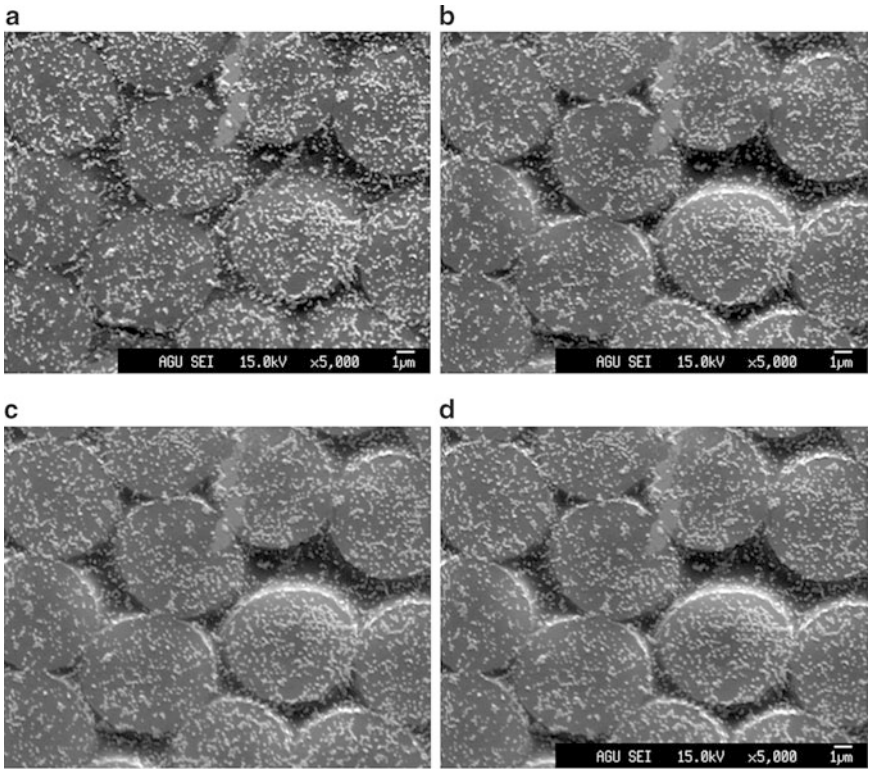

Fig. 9.4 SEM images of specimen surface (**a**) before loaded, (**b–d**) change as load increase

Dots distributed over the entire surface are the colloidal silica particles which are used for random pattern. Compare to Fig. 9.4a, fiber interface of other images are whitened. This is considered as because of charge up and edge effect. When specimen is polished, epoxy resin is easier to scrape compared to fiber. Therefore, edge of fiber becomes distinct and this occurs.

By using digital image correlation method to images in Fig. 9.4, displacement and strain distribution map can be gained. Correlation is performed with image of Fig. 9.4a and the others. Subset size is settle as 51 pixels and outer area of 200 pixels are not used for digital image correlation, since the image contains distortion errors at the area. The result of digital image correlation is shown is Fig. 9.5. Figure 9.4a is chosen as original image and it is compared with Fig. 9.4b–d, result of each correlation are shown in (a)–(c) of Fig. 9.5 as displacement and Fig. 9.6 as strain distribution map.

Approximate location of fiber can be seen in distribution map shown in Figs. 9.5 and 9.6. Distribution on the fiber shows relatively smooth gradient and epoxy resin area shows complicated distribution. It is expected that epoxy resin area indicates trend of stress concentration especially between fibers in loading direction (horizontal). This can be seen in result in Fig. 9.6. The strain of particular area, epoxy resin between fibers in loading direction, increases as the forced displacement enlarges. However, results of digital image correlation shown in both Figs. 9.5 and 9.6 contains obvious errors. Since it is tensile testing, values supposed to be positive. In results of strain distribution, there are specific locations showing negative value (likely blue in maps). This can be seen in all result through (a)–(c) of Fig. 9.6, which means this error is attributed by same reasons.

Precision of digital image correlation is directly affected by state of images used. Image shown in Fig. 9.4 has whitened area around edge of fiber cross section. As written in previous paragraph, cause of this is edge effect and charge up of specimen. There is no effect of these at Fig. 9.4a, has almost no charge up yet. As experiment progress, time elapse and specimen starts to charge up and become whitened as shown in (b), (c) and (d). Since the correlation is performed with luminance distribution, result is affected if there is change of brightness which is cause by other than deformation. Also, unevenness and lack of random pattern will be a cause of error. Colloidal silica particles are adjusted to spread on the surface, but it is hard to distribute uniformly. Adjustment of random pattern creating method is necessary to solve this problem. Especially making more fine and clarity pattern is for the specimen and the observing magnification is important task for this experiment.

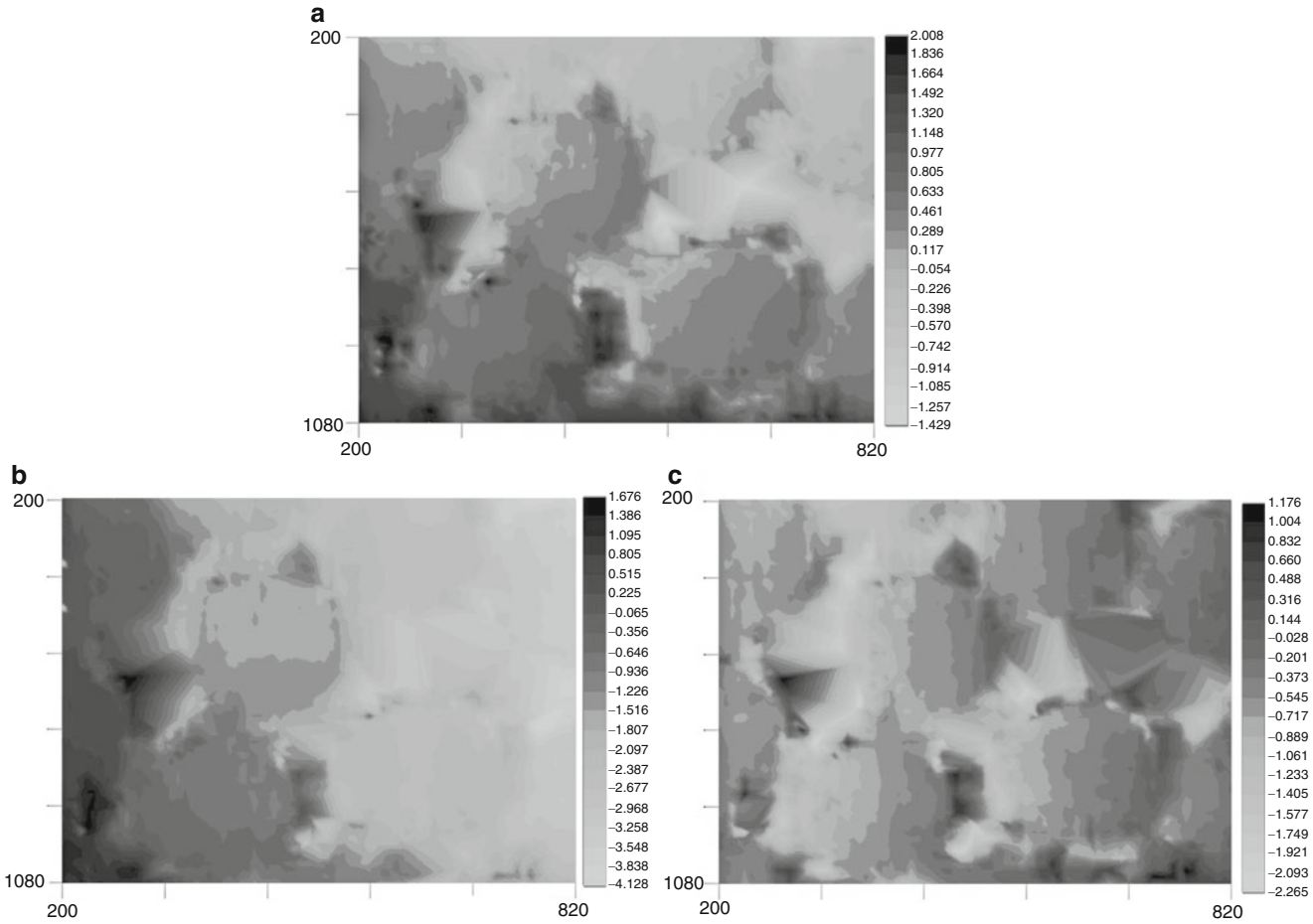

Fig. 9.5 Distribution map of displacement. (**a**–**c**) Showing result between Fig. 9.4a and b–d

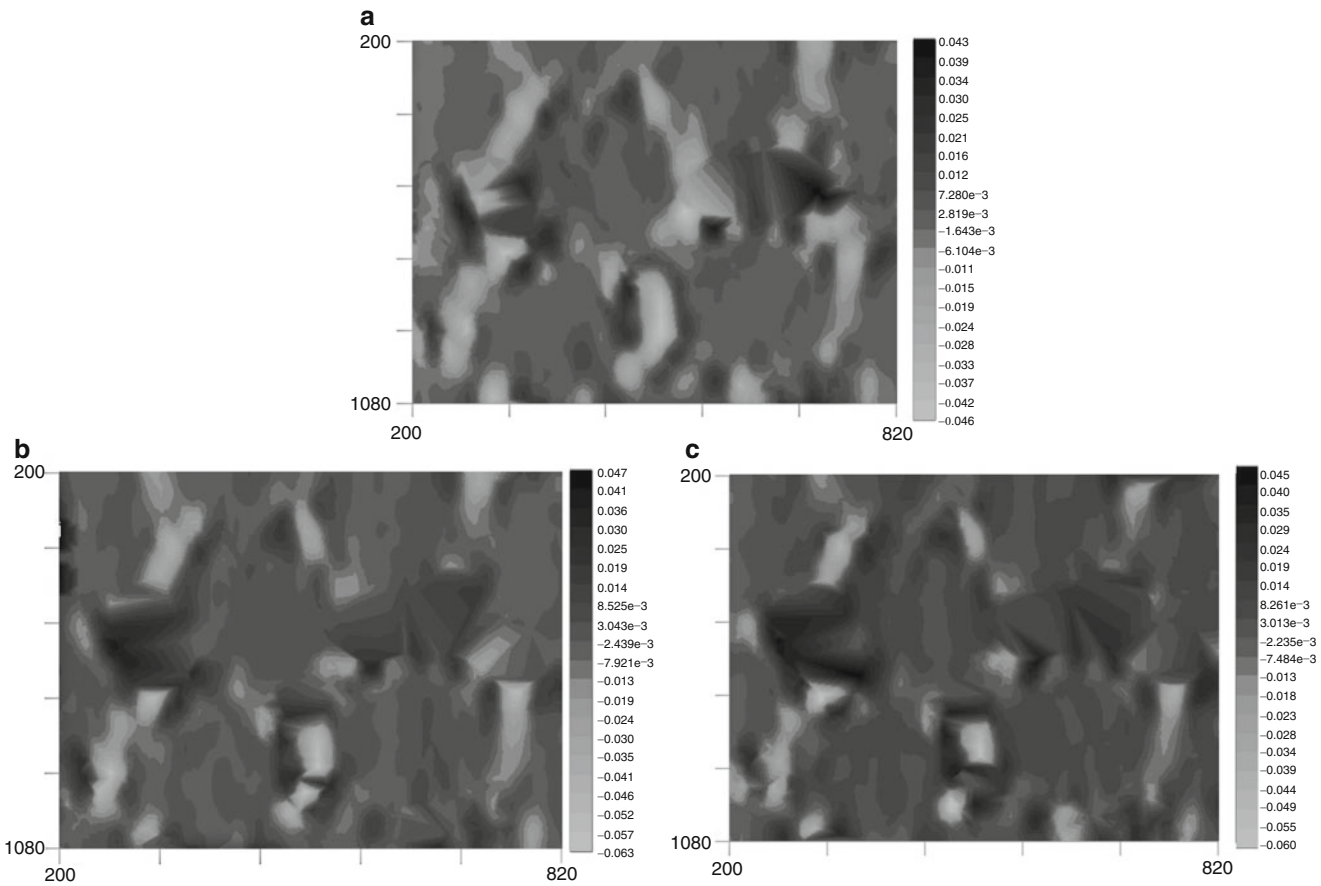

Fig. 9.6 Distribution map of strain. (**a**–**c**) Showing result between Fig. 9.4a and b–d

9.6 Conclusion

A measurement of deformation at micro area of CFRP is performed with digital image correlation method. Tensile testing is developed to perform in scanning electron microscope, and obtained SEM images are used. Charge up and edge effect is seen around edge of fiber cross section, countermeasures must be worked out since it affects to result directly. Random pattern for digital image correlation using colloidal silica particle is proposed and verified. Created pattern is good enough to measure tendency of deformation, but improvement is necessary to discuss accuracy and deformation around fiber interface. It should be smaller, distributed entire observing area, clear, increases amount and placed uniformly. The results of distribution gained shows trend of deformation at epoxy area between fibers at loading direction. However, precision of the result is not sufficient and there must be improvement of experiment.

References

1. Koyanagi J, Adachi Y, Arikawa S, Yoneyama S (2012) Time-dependent internal damage progress and residual strength in notched composite laminates. J Solid Mech Mater Eng 6(6):701–710
2. Totry E, Molina-Aldareguía J, González C, Llorca J (2010) Effect of fiber matrix and interface properties on the in-plane shear deformation of carbon-fiber reinforced composites. Compos Sci Technol 70(6):970–980
3. Hinz S, Omoori T, Hojo M, Schulte K (2009) Damage characterisation of fibre metal laminates under interlaminar shear load. Compos Part A Appl Sci Manuf 40(6–7):925–931
4. Jiménez FL, Pellegrino S (2012) Constitutive modeling of fiber composites with a soft hyper elastic matrix. Int J Solids Struct 49 (3–4):635–647
5. Vaughan TJ, McCarthy CT (2011) A micromechanical study on the effect of intra-ply properties on transverse shear fracture in fibre reinforced composites. Compos Part A Appl Sci Manuf 42(9):1217–1228
6. Lecomte-Grosbras P, Paluch B, Brieu M, Saxcé GD, Sabatier L (2009) Interlaminar shear strain measurement on angle-ply laminate free edge using digital image correlation. Compos Part A Appl Sci Manuf 40(12):1911–1920
7. Wang H, Xie H, Li Y, Zhu J (2012) Fabrication of micro-scale speckle pattern and its applications for deformation measurement. Meas Sci Technol 23:035402
8. Sutton MA, Li N, Joy DC, Reynolds AP, Li X (2007) Scanning electron microscopy for quantitative small and large deformation measurements part I: SEM imaging at magnifications from 200 to 10,000. Exp Mech 47(6):775–787
9. Sutton MA, Li M, Garcia D, Cornille N, Orteu JJ, McNeill SR, Schreier HW, Li X, Reynolds AP (2007) Scanning electron microscopy for quantitative small and large deformation measurements part II: experimental validation for magnifications from 200 to 10,000. Exp Mech 47 (6):789–804
10. Jin H, Lu WY, Korellis J (2008) Micro-scale deformation measurement using the digital image correlation technique and scanning electron microscope imaging. J Strain Anal Eng Des 43(8):719–728
11. Kang J, Jain M, Wilkinson DS, Embury JD (2005) Microscopic strain mapping using scanning electron microscopy topography image correlation at large strain. J Strain Anal Eng Des 40(6):559–570
12. Sutton MA, Li N, Garcia D, Cornille N, Orteu JJ, McNeill SR, Schreier HW, Li X (2006) Metrology in a scanning electron microscope: theoretical developments and experimental validation. Meas Sci Technol 17(10):2613–2622
13. Canal LP, González C, Molina-Aldareguía J, Segurado J, Llorca J (2011) Application of digital image correlation at the micro scale in fiber-reinforced composites. Compos Part A Appl Sci Manuf 43(10):1630–1638
14. Xu Z-H, Li X-D, Sutton MA, Li N (2008) Drift and spatial distortion elimination in atomic force microscopy images by the digital image correlation technique. J Strain Anal Eng Des 43(8):729–743
15. Sun Y, Pang JH (2006) AFM image reconstruction for deformation measurements by digital image correlation. Nanotechnology 17 (4):933–939
16. Winiarski B, Schajer GS, Withers PJ (2012) Surface decoration for improving the accuracy of displacement measurements by digital image correlation in SEM. Exp Mech 52(7):793–804

Chapter 10
High Strain Gradient Measurements in Notched Laminated Composite Panels by Digital Image Correlation

Mahdi Ashrafi and Mark E. Tuttle

Abstract Digital Image Correlation (DIC) was used to measure the in-plane strains induced in laminated graphite-epoxy panels containing a central circular hole and loaded in tension. Panels with three different stacking sequences and two hole diameters (0.25 and 0.375 in.) were tested. Measured strains were compared with predictions based on the Savin solution. Reasonable agreement between predicted and measured whole-field strain patterns was achieved. However, it was found that filtering of the DIC strain data, which is performed routinely to reduce noise, can mask the high strain gradients that actually exist near the edge of the hole. It will be shown that stacking sequence of the composite laminate as well as the hole size in addition to the correlation variables such as subset, step, and filter size have direct effect on strain values measured by DIC. In this study, strain measurements from the predictions were used to tune the correlation variables.

Keywords Digital image correlation • DIC • Notched composite laminate • Strain gradient • Savin solution

10.1 Introduction

Digital Image Correlation (DIC) is a non-contacting optical method in which images of an object before and after external loading are acquired and stored in digital form. Subsequently an image analysis is performed to extract deformations and strains by correlating each image of the deformed pattern to that in the undeformed state [1, 2]. DIC enables full-field strain measurements within 10^{-4} or less with excellent sub-pixel displacement accuracy while being relatively simple in preparation and setup [3–5]; therefore, these attributes make DIC eminently suitable for measuring full-field strains in composite laminates. As a case in point, strain distributions in orthotropic materials such as laminated composites with presence of structural features such as notches or holes can be highly heterogeneous and dependent on the laminates' stacking sequence and shape of the hole/notch [6]. To formulate high-fidelity models of composite damage and failure, it is necessary to find the maximum strain values spatially at a length scale smaller than size of the hole/notch. Subsequently, strain gauges and extensometers lack the requisite spatial resolution to meet these requirements in most cases of practical interest. In this study, it was also found that filtering of the DIC strain data, which is performed routinely to reduce noise, can mask the high strain gradients that actually exist near the edge of the hole. Subsequently, it will be shown that the masked amount depends on the stacking sequence of the composite laminate as well as the spatial resolution (the number of pixels around the hole) in addition to the correlation variables such as subset, step, and filter size.

Numerous studies have utilized digital image correlation to understand the mechanical behavior of fiber composites [5, 7–10]. Lagattu et al. [7] showed that DIC is an effective method to display high strain gradients in heterogeneous materials; however, they did not compare DIC measurements to a corresponding theoretical or finite element models. Rajan et al. [5] briefly looked at the step and filter size effects on the strains measured using DIC in an Aluminum sample with a circular hole. However, there are no studies in authors' knowledge to emphasize the effect of stacking sequence and geometry features on the high local strain gradients measured by DIC in fiber composites.

The following paper reports an experimental investigation on examining high local in-plane strain gradients near a circular hole in laminated composite materials with different stacking sequences. Subsequently, in order to account for

M. Ashrafi • M.E. Tuttle (✉)
Department of Mechanical Engineering, University of Washington, Stevens Way, Box 352600, Seattle, WA 98195, USA
e-mail: ashrafi@u.washington.edu; tuttle@u.washington.edu

G. Tandon (ed.), *Composite, Hybrid, and Multifunctional Materials, Volume 4: Proceedings of the 2014 Annual Conference on Experimental and Applied Mechanics*, Conference Proceedings of the Society for Experimental Mechanics Series,
DOI 10.1007/978-3-319-06992-0_10,

spatial resolution effect on capturing the peak strain values, two different hole sizes were studied. Furthermore, strain measurements by DIC were then compared to closed-form elasticity solution available for each model. These comparisons could help the DIC user to set the correlation variables such as subset, step, and filter size.

10.2 Experimental Setup

10.2.1 DIC Equipment

In this study in-plane strains were measured using three-dimensional DIC. Specifically, the Vic3D package commercially available from Correlated Solutions Inc, was used. The package includes two Point Grey digital cameras that are able to produce images with pixel resolution of 2,448 × 2,048, a pair of Schneider Xenoplan lenses (focal ratio: 1.9 and focal length: 34.9 mm), stereo camera mounting, and the Vic-3D post-processing software. The cameras were positioned symmetrically about the specimens (as shown in Fig. 10.1a) as suggested, and the angle between the cameras was set to 22°. Figure 10.1b shows the schematic of the DIC test setup.

10.2.2 Sample Preparation

In this study, IM7/5260 graphite/bismalemide pre-pegs with ply thickness of 0.0058 in. were used to manufacture composite laminates with $[90/\pm45/90]_{2S}$, $[0/\pm45/0]_{2S}$, and $[10]_{16}$ stacking sequences. Test samples were 12 in. × 1.5 in. in size. To generate high quality speckle patterns, a MATLAB computer program was produced to create random speckle patterns from black circles ranging from 2 to 3 pixels in diameter. The black/white color ratio was set to 40/60. The plotted result was then printed on traditional computer paper using a normal laser printer, and cut into 2 in. × 1.5 in. size pieces, then bonded to the surface of the specimens using M-Bond 200 (Micro-Measurements, NC) strain gage adhesive. Before bonding, the surfaces

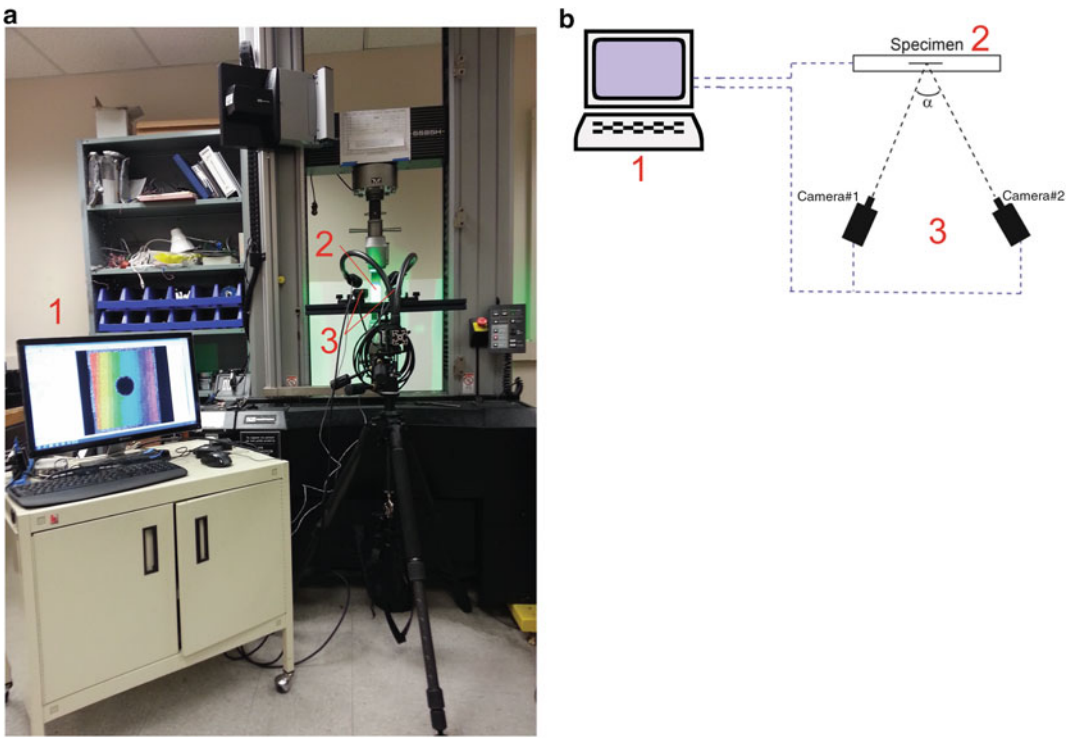

Fig. 10.1 (**a**) Experimental setup for measuring strains using three-dimensional DIC. (**b**) Schematic of the three-dimensional DIC setup

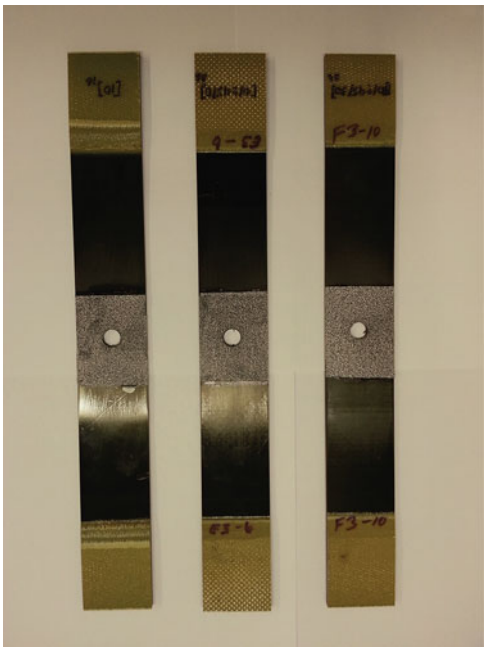

Fig. 10.2 Speckled test samples with 0.375 in. diameter

of the samples were sand blasted and cleaned using acetone. Additional care was needed in order to ensure perfect bonding between the speckled paper and test specimen. Circular holes of 0.25 and 0.375 in. in size were drilled into the samples using a table drill machine. Figure 10.2 shows test samples after speckling.

10.3 Testing

An Instron universal tensile tester, model 5585H, was used to apply tensile load to the samples. The maximum load applied was 1,000 lb at the load rate of 0.5 in./min. Images were taken from the samples, prior to loading, and every 250 lb of tensile load.

10.4 Theoretical Solutions

DIC measurements for the rectangular composite laminates with circular holes were compared to strains predicted by the Savin solution [11, 12] for an infinite plate with a circular hole subjected to uniaxial tensile loads. Effective properties for each laminate required by the Savin solution were calculated using Classical Lamination Theory (CLT). The strain resultants were then plotted by MATLAB. In DIC, measurements are reported in the center of the subsets, therefore the displacements are calculated half a subset away from the edges of each sample. To be consistent predicted strain fields were also calculated and plotted a half-subset away from the edges.

10.5 Results and Discussions

The images taken during the test were post-processed using the commercially available Vic-3D software package. Attempts were made to minimize the subset size in order to measure the strain peaks close to the edges of the samples. Full image correlation requires that each subset in the deformed image contain sufficient unique information. Therefore, limitations in

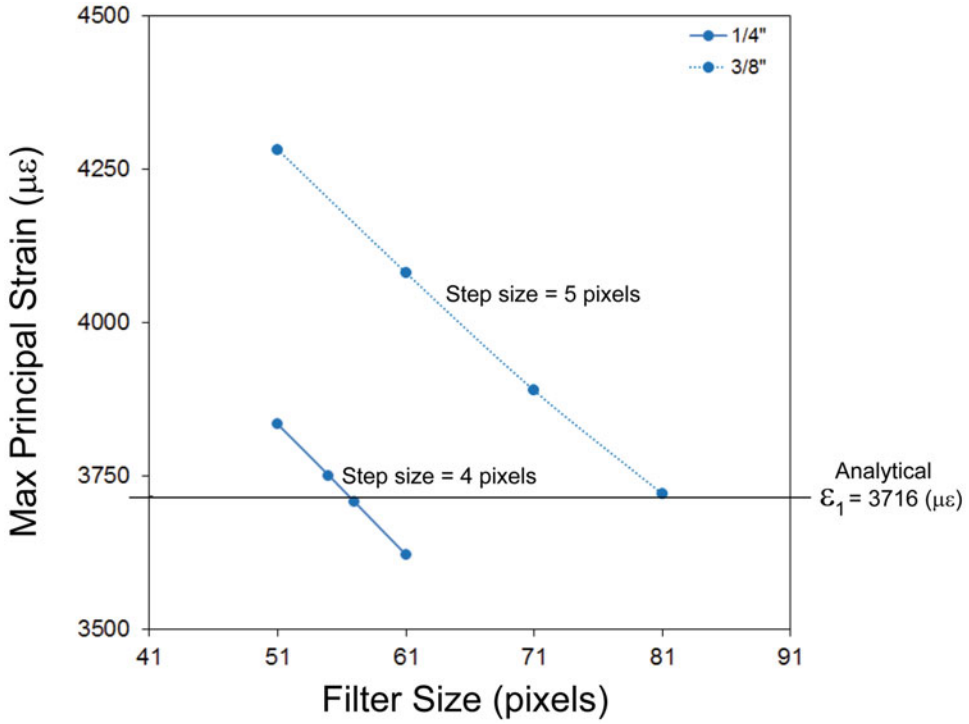

Fig. 10.3 Maximum principal strain for different filter sizes in $[90/\pm45/90]_{2s}$ laminate measured by DIC for two different hole sizes

minimizing the subset size are: speckle size, camera resolution, and noise level [1]. In practice, images are always contaminated by some noise. Noises are formed from imaging sensors, or during the correlation process [1]. A simple test was performed to find the noise level by correlating two identical images, and the noise level was found to be ±150 με. Filtering (averaging) is therefore employed. Setting the filter size too high will eliminate the high local strain gradients, and too small filter size will lead to noisy strain fields. In this study, filter size was chosen by comparing the maximum principal strain (ε_1) measured from DIC and theoretical solution for the laminate with $[90/\pm45/90]_{2S}$ stacking sequence. Figure 10.3 shows that peak principal strains were linearly related to the filter size. Subsequently, filter sizes which resulted to the best agreement between DIC measurements and theoretical solution for $[90/\pm45/90]_{2S}$ laminate were also used for laminates with $[0/\pm45/0]_{2S}$ and $[10]_{16}$ stacking sequences.

A comparison between the strain gradients around the hole on the notched composite laminates on Fig. 10.4 shows good agreement between the DIC measurements and the predicted strains for two different hole sizes. Note that the magnitudes of measured and predicted ε_x are relatively low in comparison to the magnitudes of ε_y and γ_{xy}. Consequently the noise level in ε_x measurements appears to be higher than that of ε_y and $\gamma_{xy.}$ In reality the noise level is comparable in all three images.

An adequate stain-sensing system should exhibit a linear response to strain over a wide range [13]. Figure 10.5 shows that maximum principal strains (ε_1) resultants measured by DIC are linear in a wide range of tensile loads. Maximum principal strains measured for laminates with $[0/\pm45/0]_{2S}$ stacking sequence are relatively close to the noise level of DIC systems; therefore ε_1 measurements for the mentioned stacking sequence did not show a linear response to the corresponding tensile load. Rajan et al. [5] showed that within a reasonable strain error, DIC parameters such as subset, step, and filter size cannot be chosen to comply with the concurrent requirements of capturing the strain gradient near the notch and mitigating the numerical differentiation noise. Subsequently, Fig. 10.6 depicted that in the same experimental setup, higher peak strains were captured by DIC measurements for the samples with larger hole sizes.

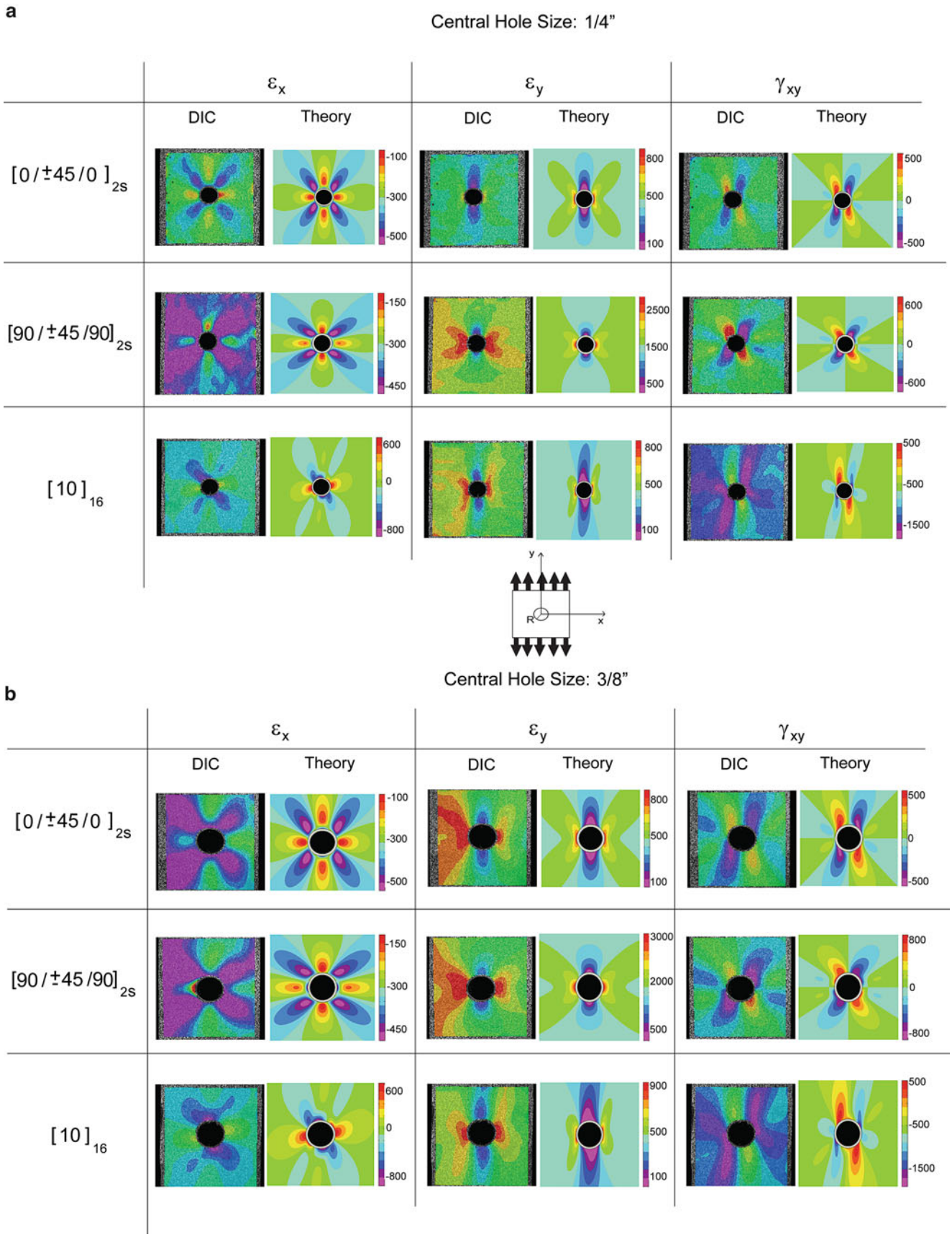

Fig. 10.4 (**a**) ε_x, ε_y, and γ_{xy} resultants for rectangular plate with 0.25 in. hole under uniaxial loading in the *y*-direction. (**b**) ε_x, ε_y, and γ_{xy} resultants for rectangular plate with 0.375 in. hole under uniaxial loading in the *y*-direction

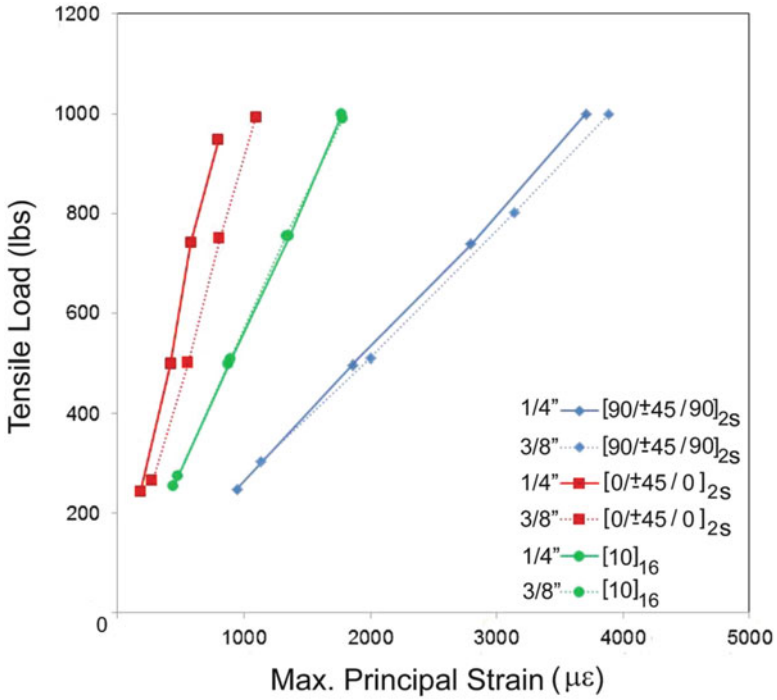

Fig. 10.5 Maximum principal strain measured at every 250 lb for all of the test samples

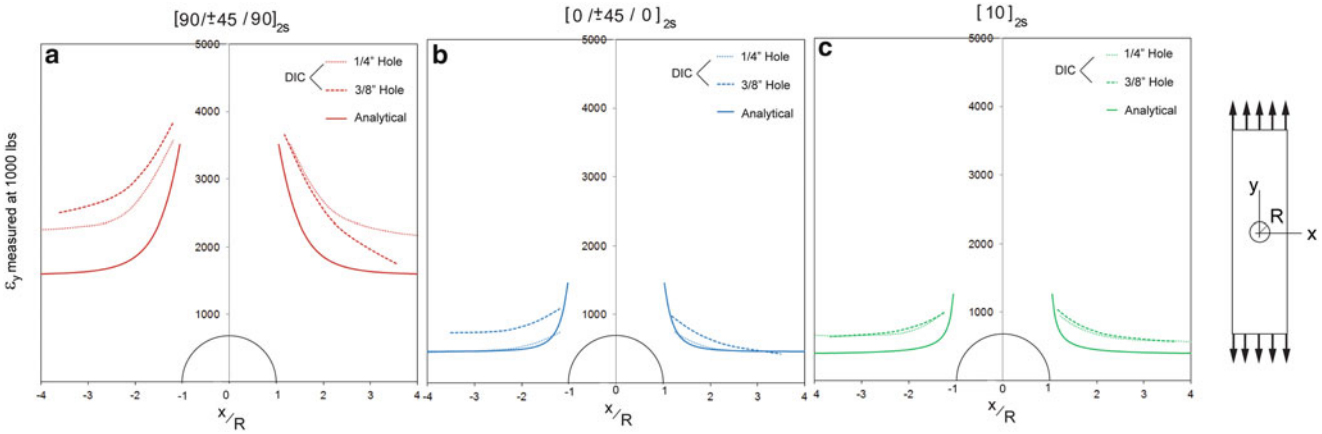

Fig. 10.6 Line scans for ε_y measured for 1,000 lb tensile load in the y-direction for composite laminate with (**a**) $[90/\pm45/90]_{2S}$, (**b**) $[0/\pm45/0]_{2S}$ and (**c**) $[10]_{16}$ stacking sequence

10.6 Summary and Conclusions

Digital image correlation is capable of measuring full-field displacements and strains with accuracy and spatial resolution superior to strain gages and extensometers in composite laminates with different stacking sequences. However, strain measurements by DIC are heavily dependent on camera, correlation parameters (subset, step, and filter size), and spatial resolution. Yet, DIC is the most convenient method to measure full field strains in laminated composite materials. In this paper, it is shown that for notched composite laminates, correlation variables could be set by comparing DIC measurements with an available theoretical prediction. To illustrate the feasibility of this methodology, strain gradients on composite laminates with different stacking sequence and hole size were measured by DIC method and compared to theoretical predictions. The results showed good overall agreement in strain gradient patterns and magnitudes.

References

1. Sutton MA, Orteu JJ, Schreier HW (2009) Image correlation for shape, motion and deformation measurements: basic concepts, theory and applications. Springer, London
2. Pan B, Qian K, Xie H, Asundi A (2009) Two-dimensional digital image correlation for in-plane displacement and strain measurement: a review. Meas Sci Technol 20:1–17
3. University of South Carolina Correlated Solutions, Inc. (2009) Digital image correlation: overview of principles and software. In: 2009 SEM annual conference on experimental mechanics, Albuquerque
4. Zhou P, Goodson KE (2001) Subpixel displacement and deformation gradient measurement using digital image/speckle correlation (DISC). Opt Eng 40:1613–1620
5. Rajan VP, Rossol MN, Zok FW (2012) Optimization of digital image correlation for high-resolution strain mapping of ceramic composites. Exp Mech 52:1407–1421
6. Pagliaro P, Zuccarello B (2007) Residual stress analysis of orthotropic materials by the through-hole drilling method. Exp Mech 47:217–236
7. Lagattu F, Brillaud J, Lafarie-Frenot M-C (2004) High strain gradient measurements by using digital image correlation technique. Mater Char 53:17–28
8. Kazemahvazi S, Kiele J, Zenkert D (2010) Tensile strength of UD-composite laminates with multiple holes. Compos Sci Technol 70:1280–1287
9. Bisagni C, Walters C (2008) Experimental investigation of the damage propagation in composite specimens under biaxial loading. Compos Struct 85:293–310
10. Ramault C, Makris A, Van Hemelrijck D, Lamkanfi E, Van Paepegem W (2011) Comparison of different techniques for strain monitoring of a biaxially loaded cruciform specimen. Strain 47:210–217
11. Savin GN (1961) Stress concentration around holes. Pergamon, Oxford
12. Chern SM, Tuttle ME (2000) On displacement fields in orthotropic laminates containing an elliptical hole. J Appl Mech 67:527–539
13. Shukla A, Dally JW (2010) Experimental Solid Mechanics. College House Enterprises, LLC, Knoxville, TX

Chapter 11
Intermittent Deformation Behavior in Epitaxial Ni–Mn–Ga Films

Go Murasawa, Viktor Pinneker, Sandra Kauffmann-Weiss, Anja Backen, Sebastian Fähler, and Manfred Kohl

Abstract This study is conducted to measure intermittent and continuum deformation behaviors in epitaxial Ni–Mn–Ga films under uniaxial tensile loading. First, epitaxial Ni–Mn–Ga film is prepared on a substrate by magnetron sputtering. Secondly, the constraint film is released from substrate by wet-chemical etching of Cr. Thirdly, we simultaneously measure phase transformation band nucleation and strain field arising in epitaxial freestanding Ni–Mn–Ga films. The band nucleations are measured using Stress Drop Analysis (SDA) in macroscopic stress–strain curve, and strain fields are measured using Digital Image Correlation (DIC) method. Results show that smaller size bands nucleated on the beginning stage of stress induced martensite transformation in stress–strain curve, then larger size bands did on the latter stage. The strain field shows macroscopic inhomogeneity under tensile loading. Especially in the latter stage of stress induced martensite transformation in stress–strain curve, the inhomogeneous region propagates along to loading direction although the shape is not distinct. Present Ni–Mn–Ga film microstructure has an order structure with some disorder structures consisting of some martensite arrangements. Their structures will affect intermittent and continuum deformation behaviors in epitaxial Ni–Mn–Ga film.

Keywords Intermittent deformation • Continuum deformation • Phase transformation band nucleation • Strain field • Epitaxial Ni–Mn–Ga film • Stress Drop Analysis • Digital Image Correlation

11.1 Introduction

In recent years, considerable attention has been devoted to magnetic shape memory alloys. Early reports from Ullakko et al. [1, 2] described field-induced changes of shape in the single-crystal Ni–Mn–Ga system. They demonstrated reversible field-induced strains of about 0.2 %. Then, Tickle et al. [3] reported field-induced strains of about 0.5 % during cyclic application of the magnetic field below the austenite/martensite transformation temperature, and strains of 1.3 % upon application of a field from a stress-biased state at similar temperatures. Furthermore, giant magnetic-field-induced strain has been reported by several researchers [4–6]. In those studies, greater than 9 % magnetic-field strain was observed at room temperature. Single-crystal Ni–Mn–Ga alloy especially shows large magnetic field-induced strain and fast response compared with conventional shape-memory alloys such as NiTi alloy [1–6]. Single-crystal Ni–Mn–Ga can be a promising material for use in future microactuator elements [7–12].

Murasawa et al. [13] and Kohl et al. [14–16] investigated macroscopic continuum inhomogeneous deformation behavior arising in Ni–Mn–Ga foil under uniaxial tensile loading using Digital Image Correlation (DIC). They reported that the measured strain band propagated under deformation, and that their behavior was changed by the specimen's pre-treatment

G. Murasawa (✉)
Department of Mechanical Engineering, Yamagata University, 4-3-16 Jonan, Yonezawa, Yamagata 992-8510, Japan
e-mail: murasawa@yz.yamagata-u.ac.jp

V. Pinneker • M. Kohl
Institute for Microstructure Technology, Karlsruhe Institute of Technology, P.O. Box 3640, 76021 Karlsruhe, Germany

S. Kauffmann-Weiss • A. Backen • S. Fähler
Institute for Metallic Materials, IFW Dresden, P.O. Box 270116, 01171 Dresden, Germany

G. Tandon (ed.), *Composite, Hybrid, and Multifunctional Materials, Volume 4: Proceedings of the 2014 Annual Conference on Experimental and Applied Mechanics*, Conference Proceedings of the Society for Experimental Mechanics Series,
DOI 10.1007/978-3-319-06992-0_11,

such as thermomechanical training and magnetomechanical training. However, it remains difficult to explain the inhomogeneous strain field formation mechanism solely considering the information of initial microstructure and macroscopic deformation behavior phenomenologically.

Single-crystal materials usually show many stress drops on the plastic deformation region or stress-induced martensite transformation region in a stress–strain curve [4, 5], which are caused by dislocation slip or twinning band occurring across specimen widths. Such band nucleation reflects phenomena such as intermittent behavior [17], spatial clustering and avalanche behavior [18–21], and self-similar or scale free [22] under deformation. Thereby, their behavior generates macroscopic-continuum-inhomogeneous deformation behavior. It is extremely effective for elucidating deformation mechanisms in single-crystal shape memory materials to measure the macroscopic strain field and microscopic band nucleation behavior simultaneously.

This study was conducted to measure intermittent and continuum deformation behaviors in epitaxial Ni–Mn–Ga films under uniaxial tensile loading. First, epitaxial Ni–Mn–Ga film was prepared on a substrate by magnetron sputtering. Secondly, the constraint film was released from substrate by wet-chemical etching of Cr. Thirdly, we simultaneously measured phase transformation band nucleation and strain field arising in epitaxial freestanding Ni–Mn–Ga films. The band nucleations were measured using Stress Drop Analysis (SDA) in macroscopic stress–strain curve, and strain fields were measured using Digital Image Correlation (DIC) method. Then, we discuss the intermittent and continuum deformation behaviors of epitaxial Ni–Mn–Ga films.

11.2 Materials and Methods

11.2.1 Material

The material is an epitaxial Ni–Mn–Ga film by magnetron sputtering from an alloyed Ni44Mn32Ga24 target. The single crystalline MgO(1 0 0) substrate is first covered with an epitaxial Cr buffer (70 nm). The Ni–Mn–Ga (2 μm) is deposited at a substrate temperature of 400 °C in order to enable epitaxial growth and chemical ordering. Figure 11.1 presents the microstructure of an epitaxial Ni–Mn–Ga film deposited on MgO substrate.

Engineering stress–strain curves are measured on the freestanding film. The film is prepared as lamellar stripes by photolithography and wet-chemical etching from epitaxial Ni–Mn–Ga film deposited on MgO substrate. Figure 11.2 shows the schematic illustration of tensile loading test specimen. Specimen both ends are glued to ceramic plates that serve as an interface for the tensile machine grips. Both ceramic plates are supported with two additional support layers, as depicted in Fig. 11.2. The loading direction is adjusted to be parallel to the long edge of the sample. Then, two paper parts are cut before tensile loading tests.

11.2.2 Stress Drop Analysis (SDA)

Figure 11.3 presents a typical stress–strain curve in single-crystal Ni–Mn–Ga. As the figure shows, it has numerous small stress drops and fewer large ones. As discussed below, this feature results from the martensite band nucleation. Using this stress–strain curve, we attempt to conduct SDA using the following method.

1. Stress drops can be extracted from the stress–strain curve as presented in Fig. 11.3

$$[\Delta\sigma(t),\ \ t = 1, 2, \ldots, N] \tag{11.1}$$

   Therein, $\Delta\sigma$ is the amplitude of stress drop. t denotes time.
2. Fast Fourier Transform (FFT) analysis is conducted for the set of $\Delta\sigma$. This result shows whether the stress drops are noise or not.
3. Using a series of $\Delta\sigma$, the distribution of the magnitude of stress drop is obtainable to evaluate static information of the stress drop.
4. Cumulative stress drop counts–strain and stress drop magnitude–strain provide the history of martensite band nucleation speed and size.

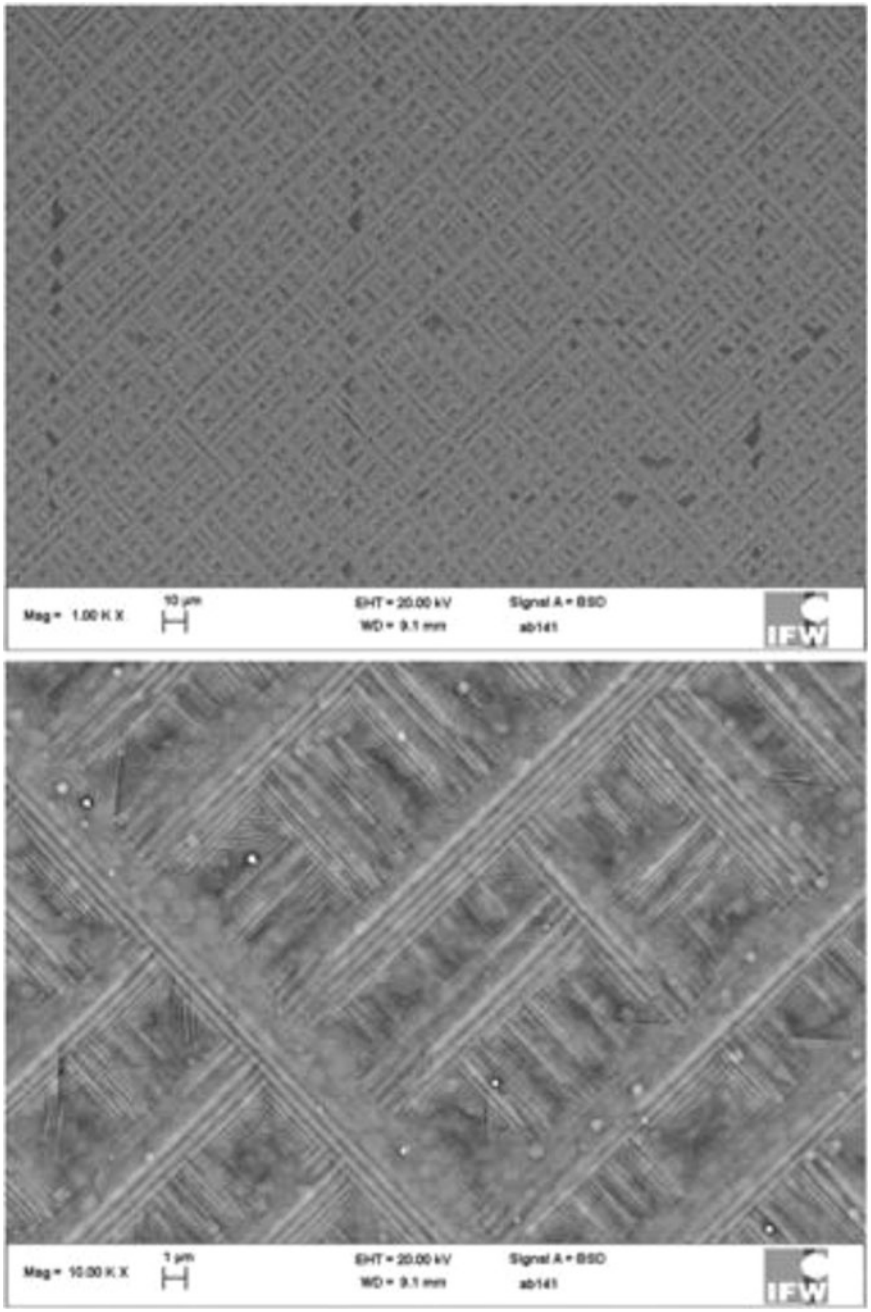

Fig. 11.1 SEM image of microstructure for an epitaxial Ni–Mn–Ga film deposited on MgO substrate

11.2.3 Strain Field Measurement Method

DIC measurement is conducted on a part of the specimen surface for measuring the strain field. DIC software was produced in-house. Details of DIC are reported in the literature [23–25]. A test system, a local strain field measurement system, was also constructed based on DIC as in-house software on a LabVIEW platform. We can measure the strain field semi-automatically using this system. Its details have been presented in earlier reports [26, 27].

11.2.4 Experimental Setup

The mechanical properties of the Ni–Mn–Ga film specimens are investigated in a tensile testing machine (Instron Corp.) in strain control mode. The loading rate is set to 0.015 mm/min. During tensile experiments, the intensity pattern on the surface of the Ni–Mn–Ga foil specimen is monitored using a CCD camera. For this purpose, the surface is covered with a graphite layer to prevent undesired reflections.

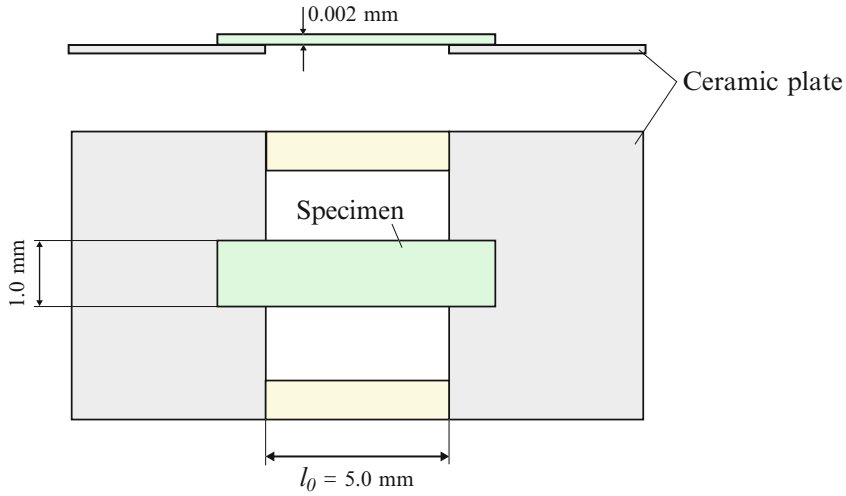

Fig. 11.2 Schematic illustration of epitaxial Ni–Mn–Ga film tensile loading specimen

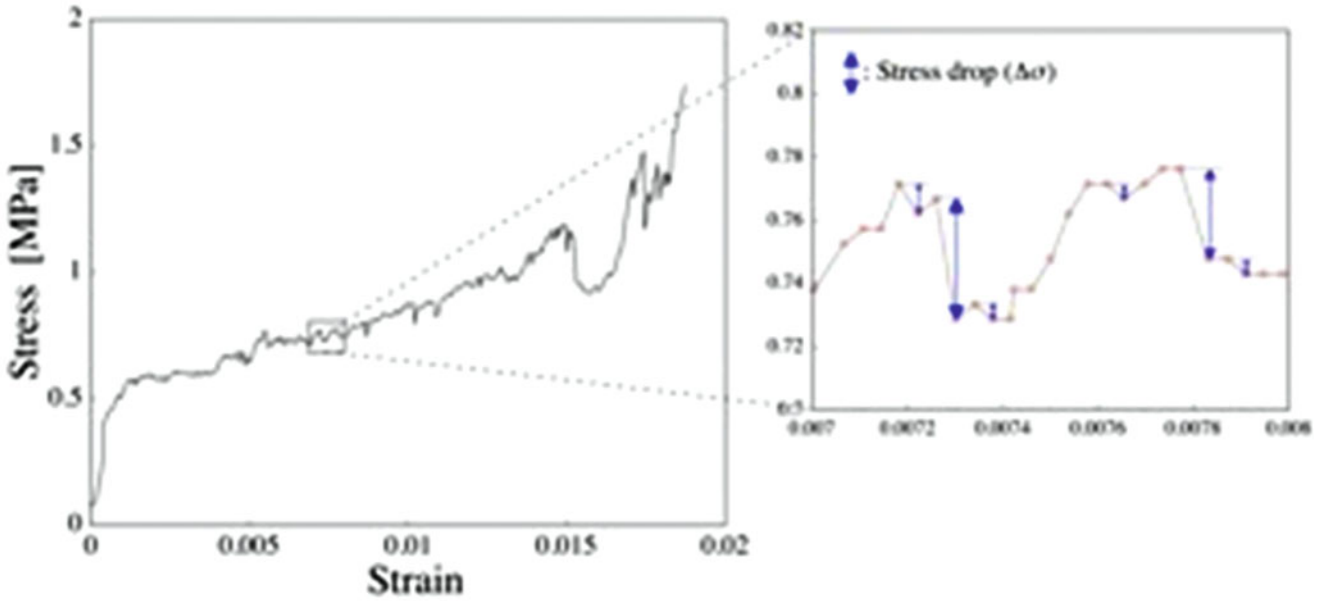

Fig. 11.3 A typical stress–strain curve in single-crystal Ni–Mn–Ga

11.3 Results and Discussion

11.3.1 Macroscopic Stress–Strain Curve

Figure 11.4 displays stress–strain curve. As shown in this figure, deformation behavior can be broadly divided into two parts as early stage and latter stage. In early stage, small stress drops happen. On the other hand, large stress drops appear in latter stage.

11.3.2 Intermittent Deformation Behavior

Figure 11.5 demonstrates the SDA analysis results. Figure 11.5a–c show stress–time curve, intermittent deformation behavior such as martensite band nucleation, and martensite band size distribution during stress induced martensite transformation under uniaxial tensile loading. Results show that small martensite bands nucleate at early stage of stress

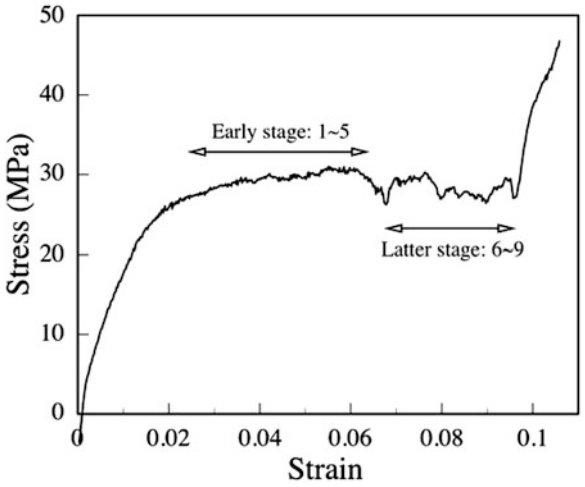

Fig. 11.4 Stress–strain curve of epitaxial Ni–Mn–Ga film

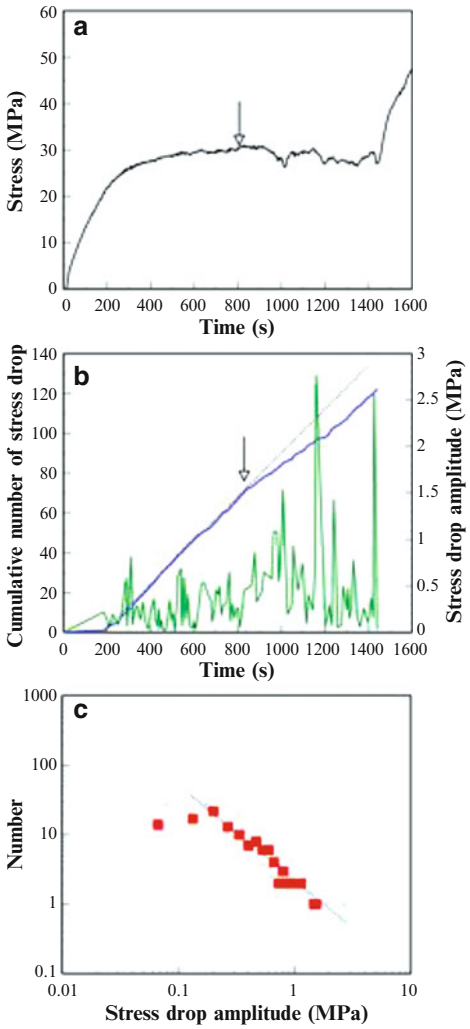

Fig. 11.5 SDA analysis results of epitaxial Ni–Mn–Ga film

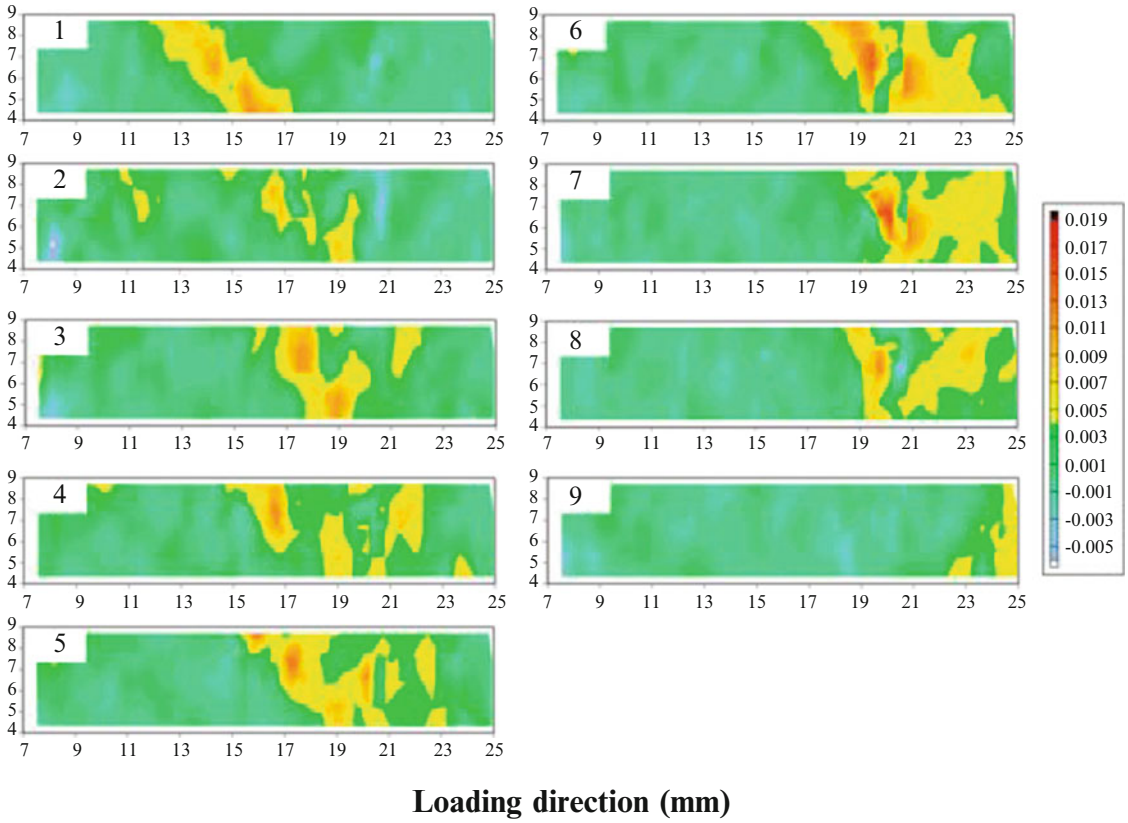

Fig. 11.6 Strain fields of epitaxial Ni–Mn–Ga film

induced martensite transformation and large ones nucleate at latter stage of that. In addition, its nucleation speed becomes low at latter stage as compared with early stage. Furthermore, martensite bands up have scaling behavior, as shown by the dashed line. This implies that a lot of small martensite bands form subsequent lage martensite bands.

11.3.3 Macroscopic Strain Field

Figure 11.6 shows strain field results of the Ni–Mn–Ga film specimens under uniaxial tensile loading. The results indicated in number 1–5 are typical strain field results during early stage of stress induced martensite transformation and ones in number 6–9 are typical one during in latter stage of that. From these results, we can see that narrow strain bands or scatter ones appear at early stage, and more wide bands happen or bands not appear. These macroscopic strain field experimental results correspond with microscopic SDA analysis results.

11.4 Conclusions

In present study, we simultaneously measured phase transformation band nucleation and strain field arising in epitaxial freestanding Ni–Mn–Ga films under uniaxial tensile loading. The band nucleations were measured using Stress Drop Analysis (SDA) in macroscopic stress–strain curve, and strain fields were measured using Digital Image Correlation (DIC) method. The results are following ones.

1. From the results of stress–strain curve, we can see that the deformation behavior can be broadly divided into two parts as early stage and latter stage.

2. From the results of SDA analysis, we can see that small martensite bands nucleate at early stage of stress induced martensite transformation and large ones nucleate at latter stage of that. In addition, its nucleation speed becomes low at latter stage as compared with early stage. Furthermore, martensite bands up have scaling behavior, as shown by the dashed line. This implies that a lot of small martensite bands form subsequent lage martensite bands.
3. From the results of strain field, narrow strain bands or scatter ones appear at early stage, and more wide bands happen or bands not appear.

References

1. Ullakko K, Huang J, Kantner C, O'Handley R, Kokorin V (1996) Large magnetic-field-induced strains in Ni_2MnGa single crystals. Appl Phys Lett 69:1966
2. Ullakko K, Huang J, Kokorin V, OHandley R (1997) Magnetically controlled shape memory effect in Ni_2MnGa intermetallics. Scripta Mater 36:1133
3. Tickle R, James R, Shield T, Wuttig M, Kokorin V (1999) Ferromagnetic shape memory in the NiMnGa system. IEEE Trans Magn 35:4301
4. O'Handley R, Murray S, Marioni M, Nembach H, Allen S (2000) Phenomenology of giant magnetic-field induced strain in ferromagnetic shape-memory materials. J Appl Phys 87:4712
5. Murray S, Marioni M, Allen S, O'Handley R, Lograsso T (2000) 6% magnetic field-induced strain by twin-boundary motion in ferromagnetic Ni-Mn-Ga. Appl Phys Lett 77:886
6. Sozinov A, Likhachev A, Lanska N, Ullakko K (2002) Giant magnetic-field-induced strain in NiMnGa seven-layered martensitic phase. Appl Phys Lett 80:1746
7. Kohl M, Agarwal A, Chernenko VA, Ohtsuka M, Seemann K (2006) Mater Sci Eng A—Struct 438:940
8. Kohl M, Brugger D, Ohtsuka M, Takagi T (2004) Sensor Actuat A 114:445
9. Kohl M, Brugger D, Ohtsuka M, Krevet B (2007) A ferromagnetic shape memory actuator designed for large 2D optical scanning. Sensor Actuat A 135:92
10. Backen A, Yeduru SR, Kohl M, Baunack S, Diestel A, Holzapfel B, Schultz L, Faehler S (2010) Comparing properties of substrate-constrained and freestanding epitaxial Ni-Mn-Ga films. Acta Mater 58:3415
11. Khelfaoui F, Kohl M, Buschbeck J, Heczko O, Faehler S, Schultz L (2008) A fabrication technology for epitaxial Ni-Mn-Ga microactuators. Eur Phys J Spec Top 158:167
12. Auernhammer D, Schmitt M, Ohtsuka M, Kohl M (2008) NiMnGa nanostructures produced by electron beam lithography and Ar-ion etching. Eur Phys J Spec Top 158:249
13. Murasawa G, Yeduru SR, Kohl M (2012) Exp Mech, under revision process
14. Pinneker V, Yin R, Eberl C, Sozinov A, Ezer Y, Kohl M (2013) Evolution of local strain bands of different orientation in single crystalline Ni–Mn–Ga foils under tension. J Alloys Compd 577(1):S358–S361
15. Kohl M, Krevet B, Yeduru SR, Ezer Y, Sozinov A (2011) A novel foil actuator using the magnetic shape memory effect. Smart Mater Struct 20:094009
16. Krevet B, Pinneker V, Kohl M (2012) A magnetic shape memory foil actuator loaded by a spring. Smart Mater Struct 21:094013
17. Dimiduk D, Woodward C, LeSar R, Uchic M (2006) Scale-free intermittent flow in crystal plasticity. Science 312:1188
18. Weiss J, Marsan D (2003) Three-dimensional mapping of dislocation avalanches: clustering and space/time coupling. Science 299:89
19. Richeton T, Weiss J, Louchet F (2005) Breakdown of avalanche critical behaviour in polycrystalline plasticity. Nat Mater 4:465
20. Richeton T, Weiss J, Louchet F (2005) Dislocation avalanches: role of temperature, grain size and strain hardening. Acta Mater 53:4463
21. Murasawa G, Morimoto T, Yoneyama S (2011) Nucleation and growth behavior of twin region around yield point of polycrystalline pure Ti. Exp Mech 52:503
22. Miguel M, Vespignani A, Zapperi S, Weiss J, Grasso J (2001) Intermittent dislocation flow in viscoplastic deformation. Nature 410:667
23. Yoneyama S, Morimoto Y (2003) Accurate displacement measurement by correlation of colored random patterns. JSME Int J Ser A—Solid Mech Mater Eng 46(2):178–184
24. Yoneyama S, Morimoto Y, Takashi M (2006) Automatic evaluation of mixed-mode stress intensity factors utilizing digital image correlation. Strain 42(1):21–29
25. Yoneyama S, Kitagawa A, Iwata S, Tani K, Kikuta H (2007) Bridge deflection measurement using digital image correlation. Exp Tech 31 (1):34–40
26. Murasawa G, Yoneyama S, Sakuma T (2007) Nucleation, bifurcation and propagation of local deformation arising in NiTi shape memory alloy. Smart Mater Struct 16(1):160–167
27. Murasawa G, Kitamura K, Yoneyama S, Miyazaki S, Miyata K, Nishioka A, Koda T (2009) Macroscopic stress-strain curve, local strain band behavior and texture of NiTi thin stress. Smart Mater Struct 18(5):055003

Chapter 12
Experimental Analysis of Repaired Zones in Composite Structures Using Digital Image Correlation

Mark R. Gurvich, Patrick L. Clavette, and Vijay N. Jagdale

Abstract Reliable understanding of load transfer in repaired zones of composite structures is needed for optimization of repair solutions and enhancement of post-repair behavior. Specific interest is in the analysis of local stress-strain states of composite repair, where digital image correlation (DIC) technique seems to be especially helpful. Thus, the objective is to develop and demonstrate a DIC-based experimental approach for analysis of repaired zones in composite structures including characterization of damage initiation and growth. The approach is based on experimental analysis of through-thickness distributions of internal strains as a function of applied load. Corresponding test coupons are either cut from actual repaired structures or specifically manufactured to represent topology, geometry, lay-up and properties of repaired structures. Demonstration of the approach is considered on an example of generic laminated carbon fiber composites IM7-977-3 with different lay-ups and geometrical configurations of repaired solutions. It is shown that distributions of internal strains, areas of strain concentrations, locations of damage initiation, and processes of damage growth can be experimentally observed and quantified with good accuracy.

Keywords Composite • Repair • DIC • Damage • Crack

12.1 Introduction

Existing modeling capabilities to predict damage tolerance (DT) of composites are primarily applied to new, i.e., undamaged components. However, typical composite structures (both defense and commercial) are usually susceptible to numerous types of damage in operation, transportation, maintenance, etc. Therefore, reliable modeling approaches to understand and quantify DT of repaired composite components and structures could provide significant cost and labor benefits by avoiding expensive component replacement, increasing residual post-repair life, simplifying repair solutions, etc. The problem is that repair-related decisions are still mainly empirical and based primarily on generated field experience, common sense, and design over-conservatism. Available modeling solutions and main ideas in this area are briefly discussed below on examples of representative publications.

Repaired zones in composite structures are often analyzed using solutions applied to adhesive joints (see, for example, [1, 2]). These solutions are based on the assumption that interfaces between repaired parts are the weakest elements. Therefore, the interfaces can be treated similarly to bonded joints. With respect to modeling approaches of failure mechanisms at such surfaces, they can be schematically separated [3] as (a) continuum mechanics based, (b) fracture mechanics based, and (c) progressive damage based approaches. Continuum mechanics approaches are demonstrated, for example, with different criteria, such as maximum stress [4, 5], as well as strain or plastic energy density. To capture stress concentrations at interface edges, "stress or strain at a distance" approaches are sometimes used [6]. Still, the challenge of singularity and sensitivity to FEA implementations (primarily, mesh density) may require application of methods based on fracture mechanics (see, for example [7, 8]). Such approaches apply criteria in the form of critical mixed mode energy release rate [7] or generalized stress intensity factor [8] and may require additional input information on damage initiation. Progressive damage based solutions, however, are used to capture the entire process of damage including consideration

M.R. Gurvich (✉) • P.L. Clavette • V.N. Jagdale
United Technologies Research Center, 411 Silver Lane, MS 129-73, East Hartford, CT 06108, USA
e-mail: GurvicMR@utrc.utc.com; ClavetPL@utrc.utc.com; JagdalVN@utrc.utc.com

G. Tandon (ed.), *Composite, Hybrid, and Multifunctional Materials, Volume 4: Proceedings of the 2014 Annual Conference on Experimental and Applied Mechanics*, Conference Proceedings of the Society for Experimental Mechanics Series,
DOI 10.1007/978-3-319-06992-0_12,

of both damage initiation and growth. Such solutions are closer to the actual physics of observed failure processes but are more challenging for analysis. Cohesive element based (CE) FEA modeling approaches [3, 9–13] seem to be among the most promising ways to mitigate these challenges. In CE-based FEA of repaired parts, simulation of damage along a predefined crack path is considered. In this case, a traction-separation response is specified between initially coincidental nodes on either side of the path. Such modeling considers both damage initiation and its potential growth through understanding of the strength and toughness response, respectively.

Although corresponding computational CE-based solutions are rapidly developed [3, 9–14], their experimental validation is still a much less explored area. In addition, reliable characterization of input data for such analysis is an equally challenging issue requiring development of test methods specifically for repaired zones, where more traditional methods of fracture mechanics characterization have only marginal applicability. Thus, the main motivation of this study is the development of test implementations to understand and quantify processes of both damage initiation and growth at repaired surfaces. Digital Image Correlation (DIC) technique provides invaluable opportunity for non-contact 2D assessment of strain fields and seems to be especially helpful in analysis of progressive damage networks. Thus, the objective is the development of a DIC-based experimental approach for analysis of repaired zones in composite structures including its demonstration for typical composite materials and parameters of repair design.

12.2 Approach

Major interest is focused on the understanding of processes controlling damage initiation and growth and, especially, behavior at load levels *before* any visible damage occurs. It can help to understand redistribution of local strains as functions of applied load, assess inevitable local statistical variability, and clearly identify the weakest points or areas. In addition to the damage process itself, characterization of *pre*-damage behavior can also be used for understanding of the actual interaction between bonded composite materials for purposes of potential optimization. For these purposes, direct application of *in-plane* DIC has some limitations (here, "in plane" is defined as at either outer or inner surfaces of the composite zone). The key disadvantage of in-plane DIC is a relatively small area to be observed, i.e., relatively low sensitivity to any changes in strain fields. It is suggested, therefore, in this study to consider *through-thickness* DIC-based characterization of repaired zones.

This approach is schematically illustrated in Fig. 12.1, where cross-sectional slices of repaired zones are the surfaces to be analyzed by DIC (let's emphasize that this approach is suggested for experimental characterization in laboratory conditions

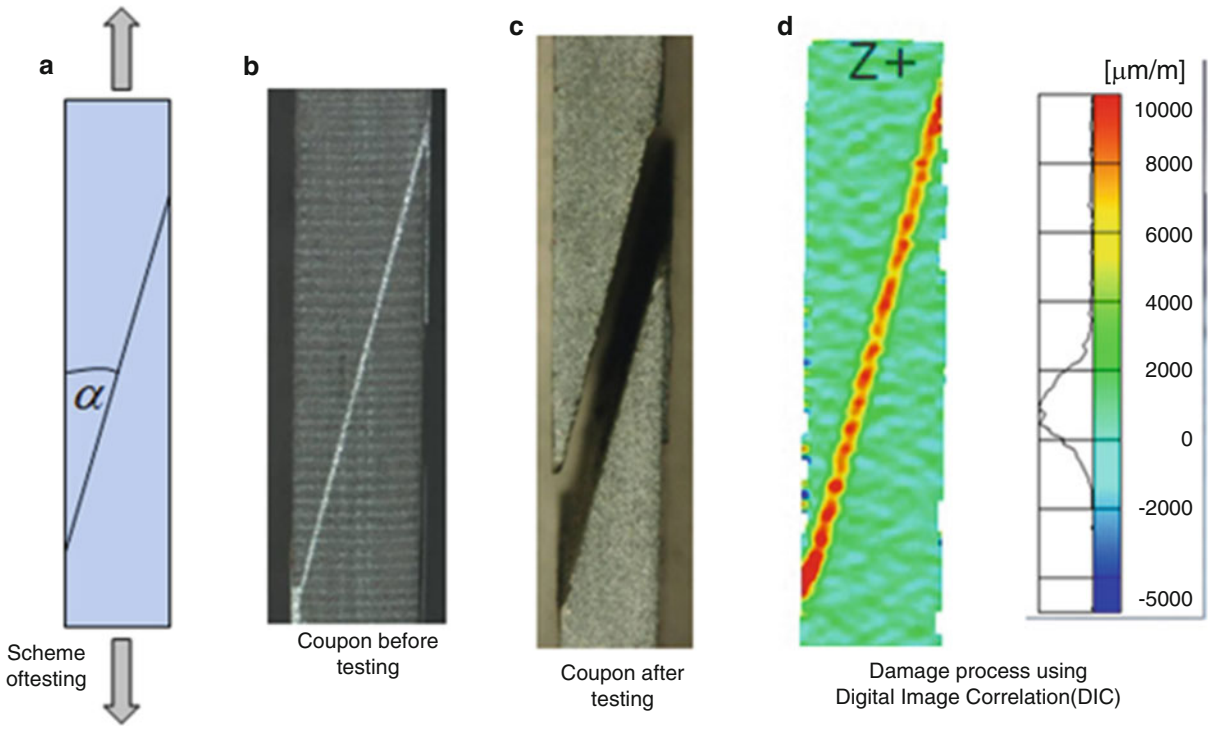

Fig. 12.1 Scheme of testing (**a**), typical coupon (**b**), its post-damage view (**c**), results of representative test (**d**)

and is not proposed as in situ method of actual structures in service). Figure 12.1a indicates a representative cross-sectional view of a repaired surface defined in this example by angle of orientation α. In general, much more complex repair solutions with multiple repaired surfaces can be similarly analyzed. A representative fabricated coupon before and after testing is shown in Fig. 12.1b, c, respectively. The tested coupon (Fig. 12.1c) can be used for analysis of *post*-damage characterization, however, *pre*-damage processes can be missed. This shortcoming can be overcome through the use of DIC (Fig. 12.1d), showing the development of strains throughout the load spectrum. Clear definition of high strains can be noted including their statistical distribution along the repaired bonded surface as well as identification of the weakest points. (With higher DIC resolution, statistical variability of strains through the thickness of the adhesion layer can be potentially captured as well). As the representative image indicates (Fig. 12.1d), there is significant potential to gain additional information on pre-damage behavior and use these results to characterize interfacial allowables needed for modeling of repair zones. A more systematic implementation of this approach is discussed below in detail.

12.3 Experimental Implementation

For the experimental demonstration of the developed solution, a test matrix with two representative lay-ups and two representative geometries is considered. The materials are laminated carbon-fiber composite coupons with lay-up of $[0]_{20}$ and $[[+45/-45]_4/[0]_3]_{2s}$, respectively. The 25 × 200 mm coupons were prepared using IM7 12,000 filament count tow uni-directional carbon tape from Hexcel impregnated with Cycom 977-3 resin (ply thickness = 0.005″; the fiber volume fraction = ~63 %). To simulate a relatively simple repair, scarf joints were created by grinding at angles of 15° and 30°. Hysol EA9394 structural adhesive was used for the repair joint, using a fixture to control the bondline thickness. Tensile tests were conducted on a 90 kN servo-hydraulic MTS load frame with hydraulic grips. A displacement rate of 1.25 mm/min was applied in a tensile mode to the specimens. The displacement was increased at a constant rate until specimen failure. The $[0]_{20}$ specimens were tested in the 0° direction and the $[[+45/-45]_4/[0]_3]_{2s}$ specimens were tested in the 90° direction. Three specimens for each layup and scarf joint configuration were tested for repeatability assessment.

During the test, full field DIC-based measurement was conducted to observe the behavior of the repaired area. The DIC equipment was a GOM Aramis 5M (5 megapixel) stereo system. The DIC imaging frame rate was 7 fps (frames per second) for the $[0]_{20}$ specimens and 5 fps for the $[[+45/-45]_4/[0]_3]_{2s}$ specimens. The imaged region was an area of ~25 mm length in the center of the approximately 150 mm long gage section. For the purposes of the analysis, a coordinate transformation was imposed to align (a) the axial direction with the left edge of the specimen; (b) the long transverse direction normal to the imaged surface and (c) the short transverse direction approximately aligned to the bottom of the imaged area.

12.4 Representative Test Results

The test results (Figs. 12.2 and 12.3) showed very good repeatability amongst the population of each type of sample. Notwithstanding the mechanical test frame slack at low loads, the $[0]_{20}$ tests showed essentially a linear-to-failure behavior with no obvious indications of plasticity. In comparison, some plastic-like behavior was seen with the $[[+45/-45]_4/[0]_3]_{2s}$ specimens at higher load. In both cases, the 15° scarf joint was significantly stronger than the 30° joint. This effect can be explained by the difference in shear and tensile properties of the adhesion layer and, of course, obvious re-distribution of stresses as function of angle α. This provides an argument for the use of shallow taper angle scarf joint repairs for tension loading to maximize the bond area. However, such a consideration is balanced by manufacturability as it becomes increasingly difficult to control preparation of low angle scarf joints. It should also take into consideration actual load conditions (e.g., combined bending/tension), where effects of the repair geometry can be more sophisticated.

Figure 12.4 illustrates distribution of displacements for a $[[+45/-45]_4/[0]_3]_{2s}$ coupon just prior to fracture ($\alpha = 15°$). Although the displacement maps do capture orientation of the adhesion layer, strain distributions provide much more information as shown in Figs. 12.5, 12.6, 12.7, and 12.8 (these strain distributions are shown as function of applied load where load just prior to fracture is defined as 100 %). In the case of the $[0]_{20}$ lay-ups, there were no indications of measurable transverse strains in the composite material. The transverse and shear strains were concentrated in the joint for both the 15° and 30° case (Figs. 12.5 and 12.6, respectively). A similar condition was seen for the axial strain and can also be explained by much lower stiffness of the adhesive layer vs. the stiffness of composite in the axial orientation. Also the magnitude of the transverse strain was much higher for the 15° case as compared to the 30° case.

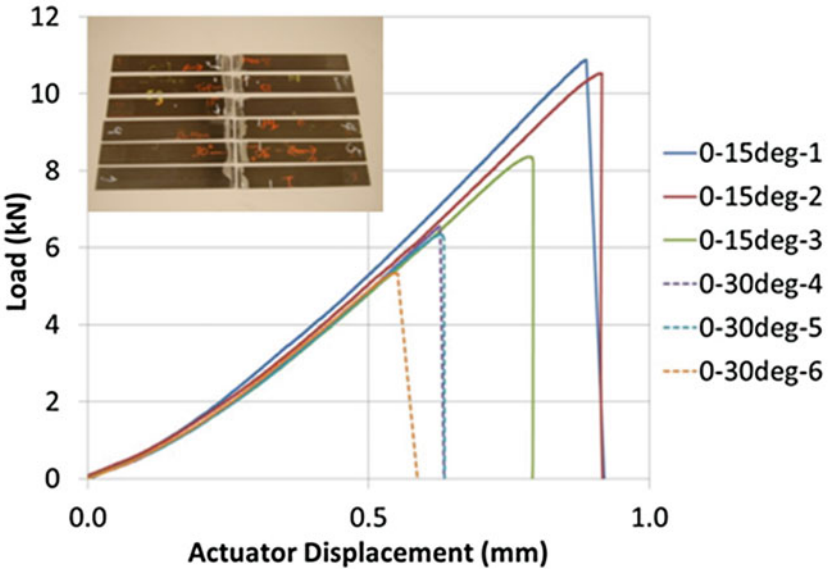

Fig. 12.2 Representative test results for $[0]_{20}$ coupons under tension in the 0 direction

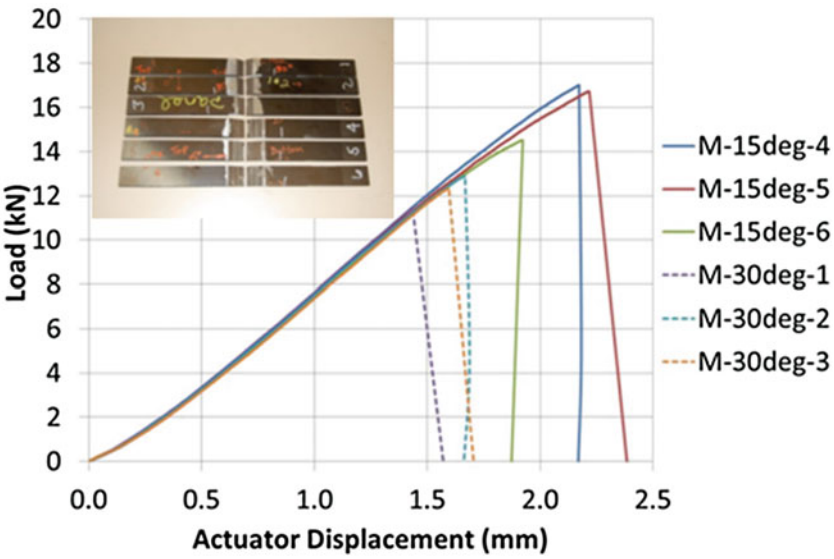

Fig. 12.3 Representative test results for $[[+45/-45]_4[0]_3]_{2s}$ coupons under tension in the direction

Strain distributions for the $[[+45/-45]_4/[0]_3]_{2s}$ coupons were more complex. In this case, the effect of heterogeneous structure was observed very early in the loading spectrum (Figs. 12.7 and 12.8). Testing in the 90° direction resulted in matrix dominated strains, since the deformation was mainly concentrated in the plies with fiber oriented perpendicular to the loading direction. This was particularly evident in the center of the coupon due to the symmetric lay-up. The "plastic-like" behavior seen in Fig. 12.3 was a result of partial fracture of the matrix resin due to high effective strain, primarily concentrated in the central band of 0° plies. Multiple fractures of this region were noted in the field of view for the case of $\alpha = 15°$. However, only two fractures were noted at $\alpha = 30°$. Overall, results demonstrated in Figs. 12.5, 12.6, 12.7, and 12.8 indicate that the suggested through-thickness DIC can be applicable to a range of composite designs and repair implementations.

A qualitative comparison with FEA modeling predictions can also be performed. CE-based FEA approach [3] was applied to understand processes of damage initiation and growth for similar repair implementations. A representative FEA prediction shown in Fig. 12.9 indicates that fracture of the coupon can be clearly predicted, and generated force/displacement diagrams are quite similar to the experimentally observed dependences (Figs. 12.2 and 12.3). A more systematic analysis of test/model correlations will be considered in a follow-up study specifically focused on quantification of allowables controlling damage of the adhesive repair interface.

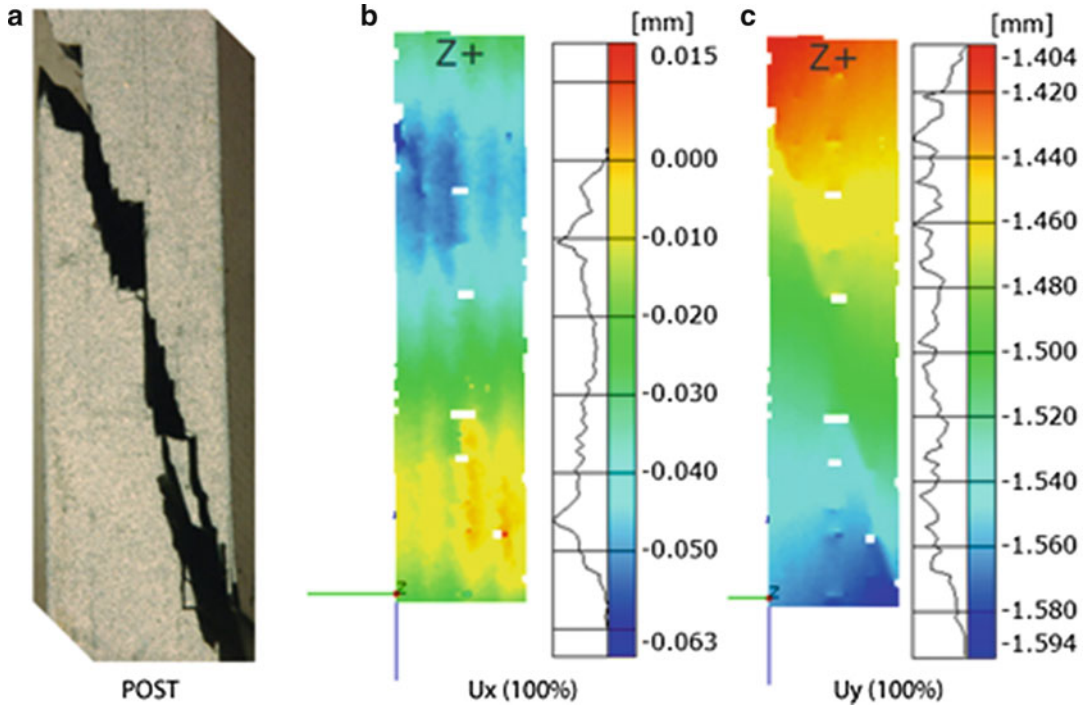

Fig. 12.4 Representative (**a**) post-damage coupon $[[+45/-45]_4[0]_3]_{2s}$ and distributions of displacements just prior to fracture (**b**) U_x and (**c**) U_y under tension in the 90 direction ($\alpha = 15°$)

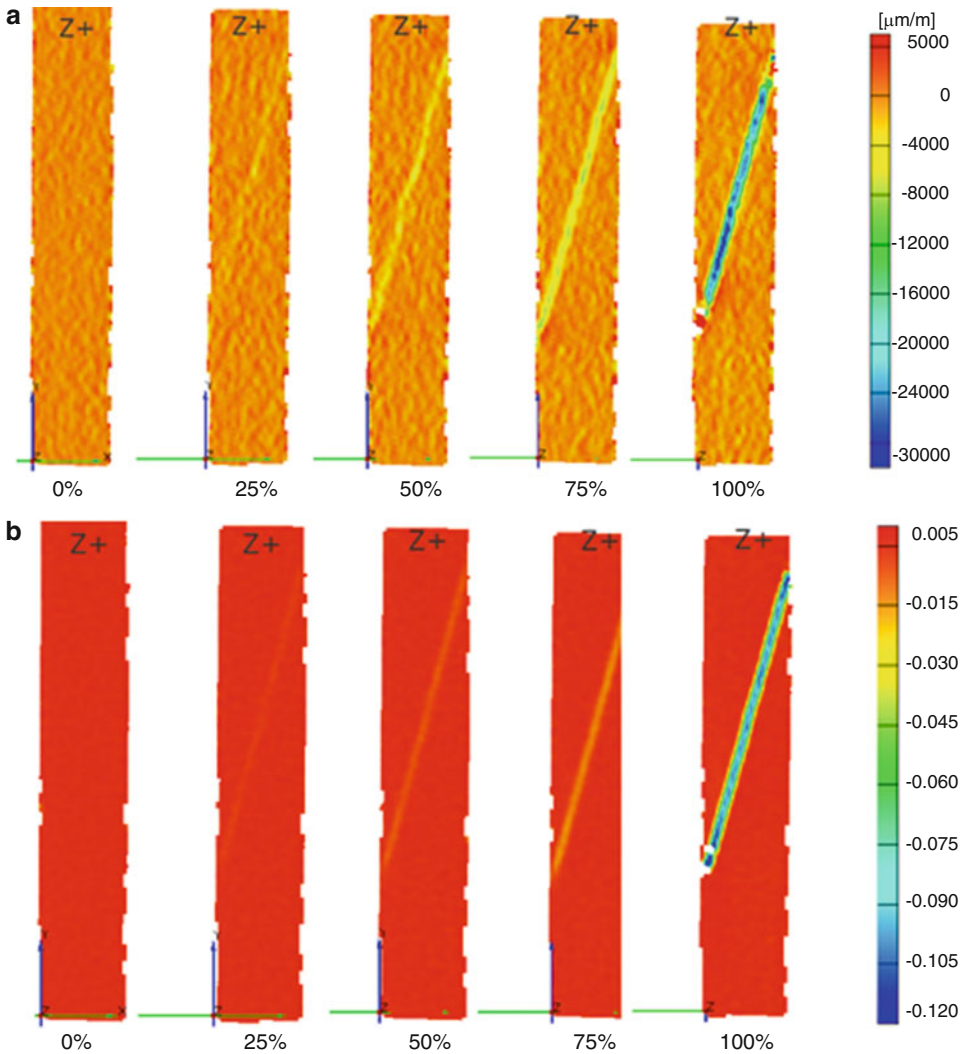

Fig. 12.5 Representative distributions of (**a**) ε_{xx} and (**b**) ε_{xy} for $[0]_{20}$ coupons under tension in the 0 direction ($\alpha = 15°$)

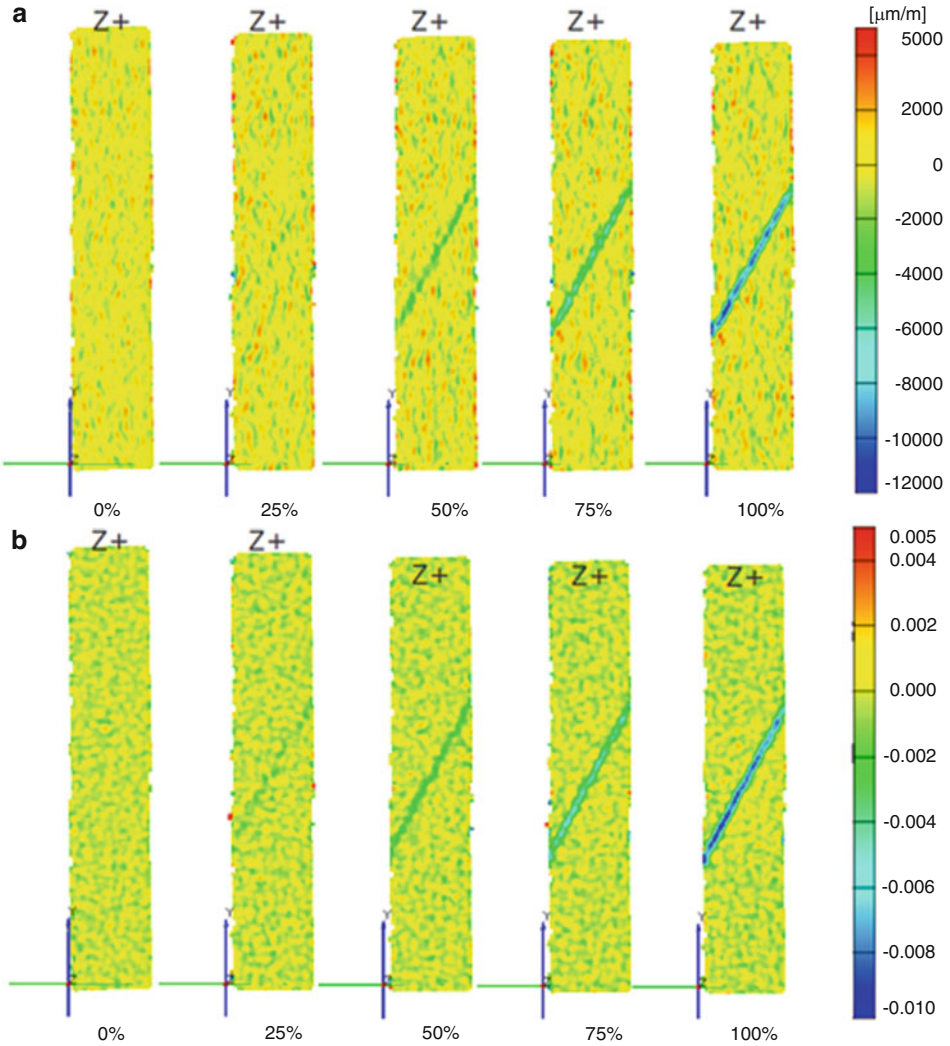

Fig. 12.6 Representative distributions of (**a**) ε_{xx} and (**b**) ε_{xy} for $[0]_{20}$ coupons under tension in the 0 direction ($\alpha = 30°$)

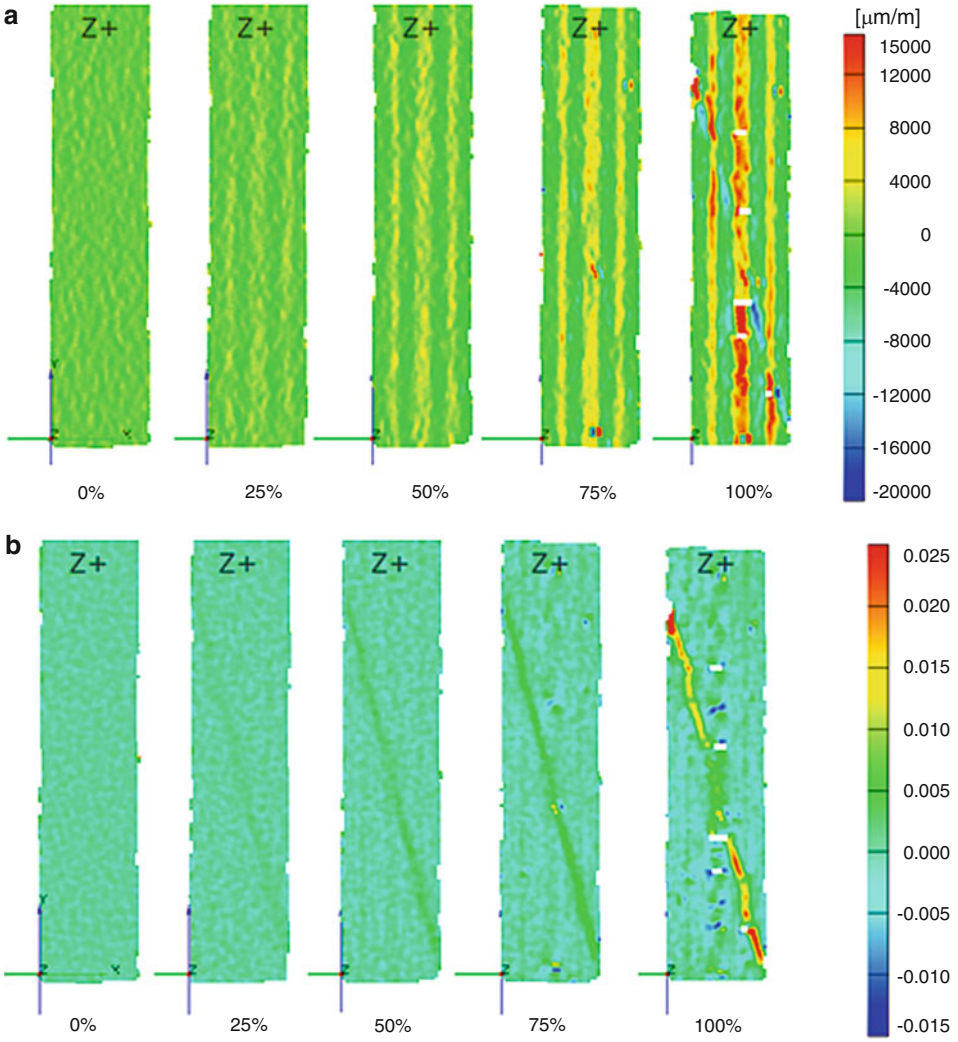

Fig. 12.7 Representative distributions of (**a**) ε_{xx} and (**b**) ε_{xy} for $[[+45/-45]_4[0]_3]_{2s}$ coupons under tension in the 90 direction ($\alpha = 15^\circ$)

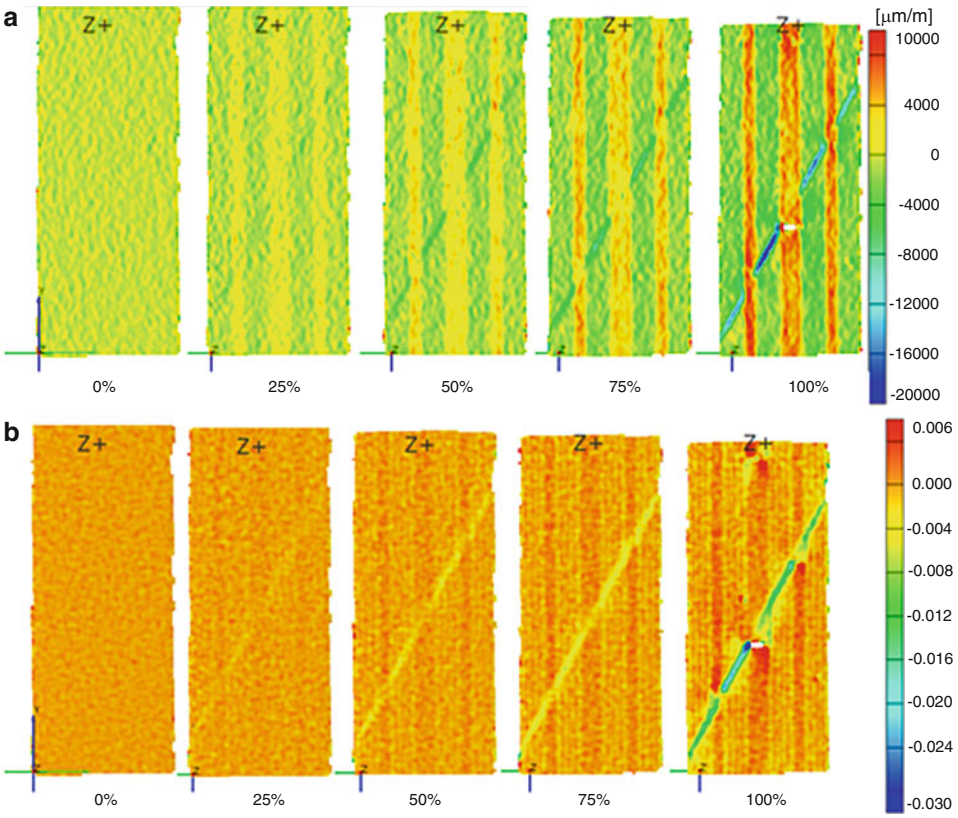

Fig. 12.8 Representative distributions of (**a**) ε_{xx} and (**b**) ε_{xy} for $[[+45/-45]_4[0]_3]_{2s}$ coupons under tension in the 90 direction ($\alpha = 30°$)

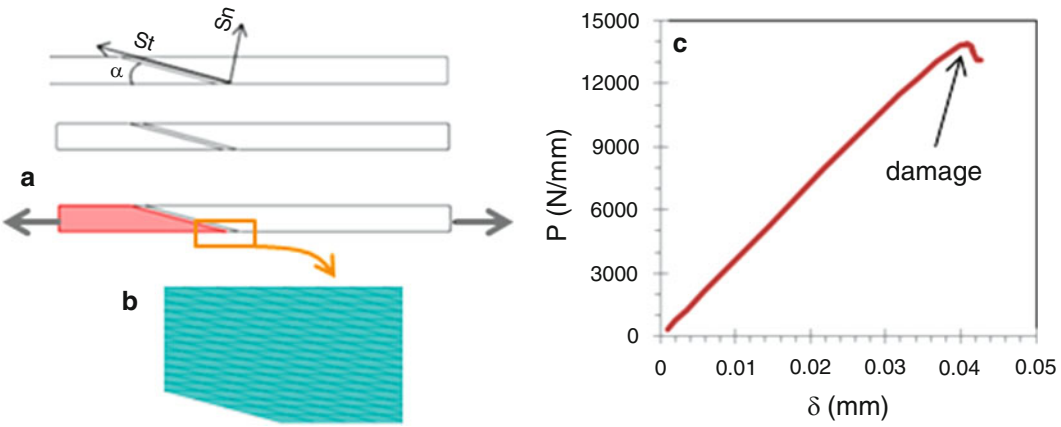

Fig. 12.9 Scheme of modeling (**a**), detail of FEA implementation (**b**) and typical predictions (**c**) of force–displacement correlations under uniaxial tension

12.5 Conclusions

A relatively simple approach for DIC-based experimental analysis of repaired zones in composites is suggested and demonstrated. It is shown that through-thickness characterization is a promising way to understand processes of strain distributions as well as damage initiation and growth. Demonstration on two different lay-ups and two different geometries indicates its applicability to other materials and repair implementations. Although this approach was demonstrated under static load conditions, it seems that other implementations can be similarly applied under cyclic or dynamic loads to characterize fatigue and impact behaviors, respectively. Integration of this experimental approach with FEA modeling (e.g., [3]) for characterization of interfacial allowables will be considered in a separate follow-up publication.

Acknowledgement The authors thank the United Technologies Research Center for support of this study and permission for publication.

References

1. Yang C, Huang H, Tomblin JS, Sun W (2004) Elastic–plastic model of adhesive-bonded single-lap composite joints. J Compos Mater 38:293–309
2. Zhang J, Bednarcyk BA, Collier C, Yarrington P, Bansal Y, Pindera MJ (2006) Analysis tools for adhesively bonded composite joints, part 2: unified analytical theory. AIAA J 44:1709–1719
3. Gurvich MR, Jagdale VN (2012) Damage tolerance analysis of repaired composite structures: engineering approach and computational implementation. In: 2012 3DS SIMULIA community conference, providence, RI, 15–17 May 2012, pp 48–62
4. Adams RD, Atkins RW, Harris JA, Kinloch AJ (1986) Stress analysis and failure properties of carbon-fibre-reinforced-plastic/steel double-lap joints. J Adhes 20:29–53
5. Kumar SB, Sridhar I, Sivashanker S, Osiyemi SO, Bag A (2006) Tensile failure of adhesively bonded CFRP composite scarf joints. Mater Sci Eng B 132:113–120
6. Towse A, Potter KD, Wisnom MR, Adams RD (1999) The sensitivity of a Weibull failure criterion to singularity strength and local geometry variations. Int J Adhes Adhes 19:71–82
7. Hutchinson JW, Suo Z (1992) Mixed-mode cracking in layered materials. Adv Appl Mech 29:63–191
8. Gleich DM, Van Tooren MJL, Beukers A (2001) Analysis and evaluation of bondline thickness effects on failure load in adhesively bonded structures. J Adhes Sci Technol 15:1091–1101
9. Kafkalidis MS, Thouless MD (2002) The effects of geometry and material properties on the fracture of single lap-shear joints. Int J Solids Struct 39:4367–4383
10. Campilho RDSG, de Moura MFSF, Ramantani DA, Morais JJL, Domingues JJMS (2009) Tensile behaviour of three-dimensional carbon-epoxy adhesively-bonded single and double-strap repairs. Int J Adhes Adhes 29:678–686
11. Campilho RDSG, de Moura MFSF, Pinto AMG, Morais JJL, Domingues JJMS (2009) Modelling the tensile fracture behaviour of CFRP scarf repairs. Compos Part B Eng 40:149–157
12. Li S, Thouless M, Waas A, Schroeder J, Zavattieri P (2006) Competing failure mechanisms in mixed-mode fracture of an adhesively bonded polymer–matrix composite. Int J Adhes Adhes 26:609–616
13. Pinto AMG, Campilho RDSG, de Moura MFSF, Mendes IR (2010) Numerical evaluation of three-dimensional scarf repairs in carbon-epoxy structures. Int J Adhes Adhes 30:329–337
14. de Moura MFSF, Gonçalves JPM, Chousal JAG, Campilho RDSG (2008) Cohesive and continuum mixed-mode damage models applied to the simulation of the mechanical behaviour of bonded joints. Int J Adhes Adhes 28:419–426

Chapter 13
Mechanics of Curved Pin-Reinforced Composite Sandwich Structures

Sandip Haldar, Ananth Virakthi, Hugh A. Bruck, and Sung W. Lee

Abstract Pin-reinforced sandwich composites have recently attracted the attention in lightweight structural applications where it substantially improves out-of-plane and shear properties for sandwich composites. However, there is not a great deal of understanding in regards to how shaping these composites affects their mechanical performance when the orientation of the pin-reinforcement may change due to the shaping process. In this investigation, singly curved pin-reinforced sandwich composites using K-Cor have been fabricated using a bend fixture to curve the specimen and heat treatment to soften the core during before bonding with the composite face sheets in order to prevent any damage to the core during the shaping process. Experiments were then performed on the curved sandwich specimens using different boundary conditions on the edges. The boundary conditions were found to result in increased load bearing capacity when supported at the edge compared to support at the bottom due to increased lateral constraint that delayed the onset of bending shear failure. Digital Image Correlation (DIC) was also used to determine the deformation fields from the images captured during deformation to quantify the effects of boundary conditions on the onset of failure initiation, and the results were used to develop a new Finite Element Analysis (FEA) model that is capable predict the mechanical behavior of the curved K-Cor sandwich composites.

Keywords K-Cor sandwich composites • Curved sandwich structures • Digital image correlation • Finite element analysis

13.1 Introduction

Sandwich composites have been very popular in many lightweight structural applications due to their high stiffness/strength to weight ratio and the ability to easily tailor core properties through orientation, properties, and density of pins. Sandwich composites are generally made of two stiff facesheets separated by a light weight porous core. The facesheets predominantly carry in-plane loading, whereas the light weight foam core controls the shear response and subsequent flexural strength and stiffness of the structure. However, due the soft core, the out-of-plane properties are substantially lower than the in-plane, which limits the application of the sandwich composites in panel structures. To overcome this limitation, through thickness reinforcement in the core material has been implemented using pins. The pins are integrated with the facesheets in two different configurations, known as X-Cor or K-Cor. In X-Cor, the pins penetrate into the facesheets, while in K-Cor the pins are bent at an angle so they can be bonded to the surface of the face sheets. Popular choices for pin materials include pultruded carbon rod or metallic pins.

The pin reinforcement has been found to significantly improve the compressive and shear properties compared to the unreinforced sandwich composites. Reinforcement in natural and synthetic composites has been found to enhance its properties compared to their unreinforced counterpart [1–3]. Earlier, several studies have been performed to characterize the effect of through thickness reinforcement on compressive [4–6], flexural [7], shear properties [8] of sandwich composites. The effect of pin reinforcement on compressive behavior was studied using the Finite Element Analysis and modeled by introducing pin-facesheet interaction [6]. For many applications, curved sandwich composites are required to

S. Haldar (✉) • H.A. Bruck
Department of Mechanical Engineering, University of Maryland, College Park, MD 20742, USA
e-mail: shaldar@umd.edu; bruck@umd.edu

A. Virakthi • S.W. Lee
Department of Aerospace Engineering, University of Maryland, College Park, MD 20742, USA

G. Tandon (ed.), *Composite, Hybrid, and Multifunctional Materials, Volume 4: Proceedings of the 2014 Annual Conference on Experimental and Applied Mechanics*, Conference Proceedings of the Society for Experimental Mechanics Series,
DOI 10.1007/978-3-319-06992-0_13,

achieve desired structural features. Due to the fact that shaping the sandwich composite may change pin orientation, it is essential that the mechanical behavior of curved sandwich composites be studied in material.

In this study, we report preliminary results on the flexural performance of singly curved K-Cor sandwich composites. The curved K-Cor sandwich composites have been fabricated by using a specially designed bend fixture to curve the specimen and a controlled heat treatment process that softens the core and prevents damage from occurring during the shaping process when it is bonded to the composite facesheets. The flexural response of the curved sandwich composites was studied using different boundary conditions at the ends of the specimen. The deformation behavior and failure mechanisms were investigated in greater detail by using Digital Image Correlation (DIC). The behavior of pin-reinforced sandwich composites under different boundary conditions, as well as with and without foam in the core, were compared. Using the experimental results, a new Finite Element Analysis (FEA) model was developed to predict the mechanical response of the pin-reinforced sandwich composites.

13.2 Specimen Fabrication and Experimental Method

13.2.1 Specimen Fabrication

A shaping fixture was designed that allowed for fabricating curved K-Cor sandwich composite beam specimens in bending, where Rohacell foam cores reinforced with pultruded T650-35/8606 carbon fiber pins are adhesively bonded to composite facesheets inside of an oven (Fig. 13.1). To prepare the specimens, they are first heated to 200 °C, which is the upper softening point for Rohacell foam. This allow the foam to deform without fracturing, which is evident in the figure. While the figure shows a specimen in three-point bend, a more uniform loading was obtained by applying loads at periodic locations along the specimen. This enabled more intimate contact between the face sheets and specimen all along the length. Curved sandwich specimens were prepared by repetitive heating of the woven fabric carbon fiber-epoxy facesheet obtained from DragonPlate and K-Cor foam to achieve the curved shape. The K-Cor has reinforcement of pultruded carbon rod of 0.5 mm diameter. The curved components were then glued together by West System epoxy resin 105 and slow hardener 206 at 5:1 ratio by mass. The epoxy adhesive was then cure at 80 °C for around 24 h. Specimens were prepared with a curvature of 0.167 cm^{-1}. A core with a pin density of 1.8 lb/ft^3 was used. Ends of the specimen were cut flat to permit total contact with the bottom of the test frame. A central load was applied to the specimen. The foam core of the composite sandwich specimen was then dissolved to obtain the specimen with only pin structure. The representative curved specimen dimensions are shown in Fig. 13.2c. All the specimens were of approximately same dimensions (i.e., support span of 120 mm, thickness 15.5 mm, and width of 20 mm).

13.2.2 Experimental Method

Displacement controlled flexural tests of the K-Cor composite sandwich specimens were performed in an Imada MX 500 load frame equipped with a Z2H-440 2 kN load cell that has a load resolution of 0.1 kg and a caliper to measure the loading point displacement. During the test, in situ imaging was performed by POINT GREY CCD cameras for using Digital Image Correlation (DIC) for deformation measurement. Images were captured at the specimen face to observe the failure

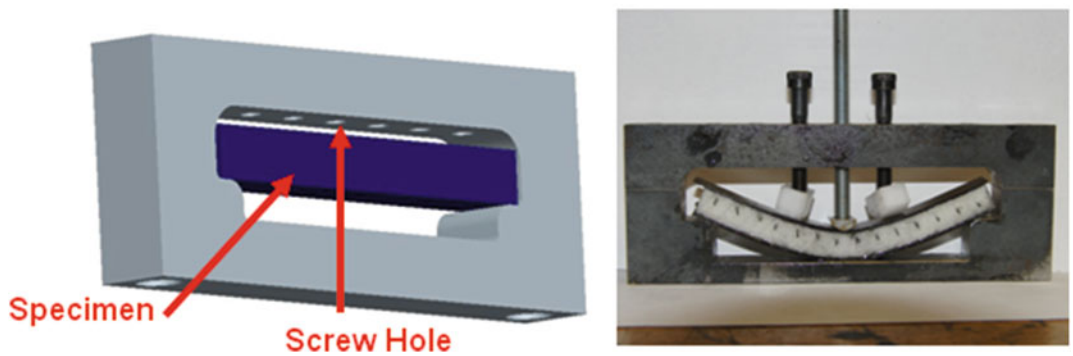

Fig. 13.1 The fixture to shape the sandwich composite through heat treatment to fabricate sandwich composite with constant curvature

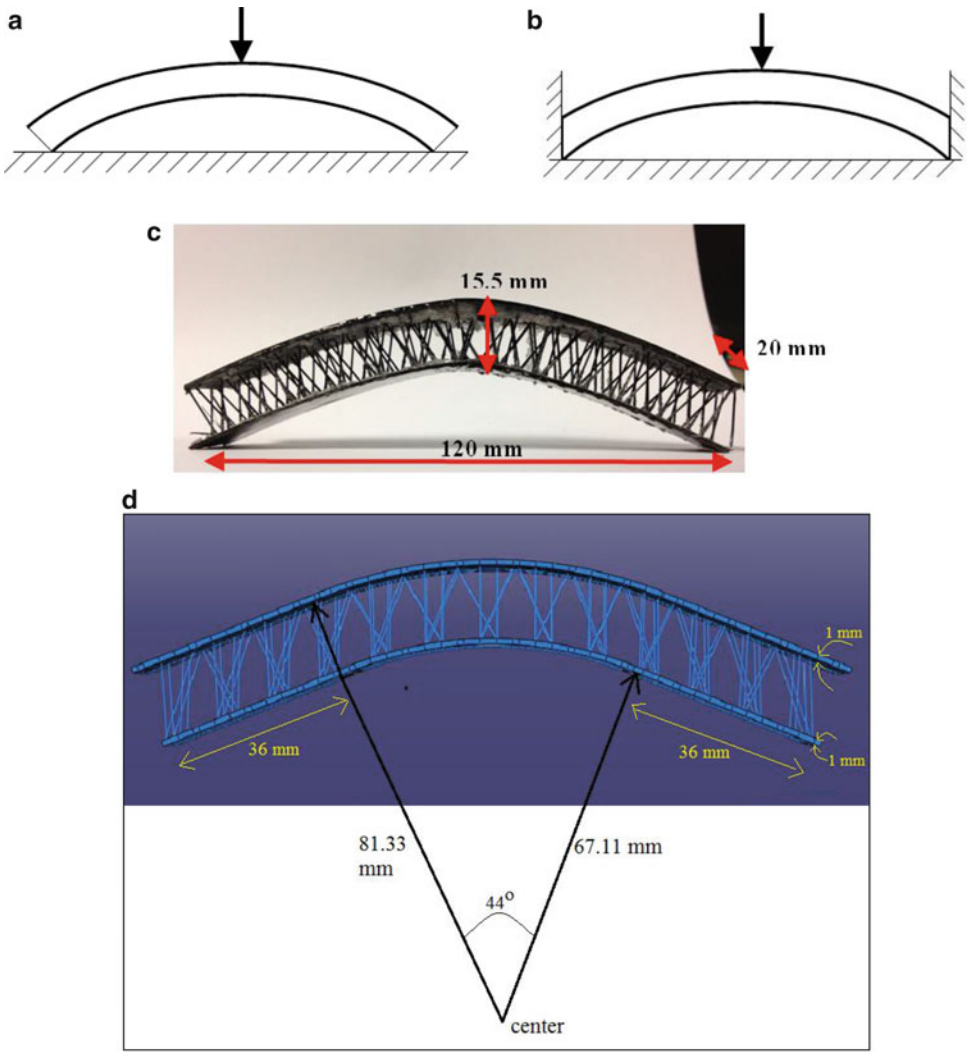

Fig. 13.2 Schematic of the end conditions and loading of the flexural test of the K-Cor sandwich composite under flexure (**a**) specimen supported at the bottom, (**b**) specimen supported at the bottom and edge, and (**c**) representative specimen with dimensions, (**d**) model for Finite Element Analysis (FEA)

mechanism and to obtain the deformation in the through thickness direction of the sandwich by 2D DIC. Two cameras were used to capture the images of the top face of the specimen for 3D DIC. The specimens were illuminated by MI-150 high intensity fiber optic illuminator from Edmund Optics (Barrington, NJ, USA). DIC was performed with the images captured during deformation to obtain the displacement and strain fields in the specimen during bending using commercially available software by Correlated Solutions Inc, Columbia, SC.

Flexural tests were performed with two types of boundary conditions: (1) supported only at the bottom, and (2) supported at the bottom and edge. Three types of K-Cor composite sandwich specimens were also investigated: (1) curved specimen with foam, (2) curved specimen without foam, and (3) flat specimens with foam. The schematics of the end conditions of the specimens and loading are shown in Fig. 13.2a, b. The specimen size was maintained same for all the tests.

13.2.3 Finite Element Analysis

A Finite Element Analysis (FEA) model of the curved sandwich is developed in ABAQUS, as shown in Fig. 13.2d. The geometry of the structure was obtained by curve fitting several points on the outline of the real structure to the desired shape. The top and the bottom facesheets of the sandwich are constructed as two concentric arcs subtending an angle of 44° in the center with rectangular overhangs at the end of lengths equal to 36 mm. The thickness of each facesheet is 1 mm. The curved

sandwich specimen is prepared by bending the flat sandwich specimen as described above. In modeling the sandwich structure the endpoints of the pins on the facesheet are assumed to lie at the same points as they would lie on the originating flat sandwich structure. That is, the end points of the pins are separated by a uniform curve length between them equal to the pin spacing in the flat sandwich specimen. This length is equal to 10 mm. In the model, the pins at the ends that overshoot the boundaries of the structure are not included. In the initial study, linear elastic simulation is performed for the bending of the curved K-Cor sandwich without foam in the core. Linear elastic material properties with $E_L = 156.5$ GPa, $E_T = 12.96$ GPa, $G_{LT} = 6.96$ GPa, $G_{TT} = 4.3$ GPa, $\nu_{LT} = 0.23$, and $\nu_{TT} = 0.55$ for the facesheet, and $E = 156.5$ GPa, $\nu = 0.23$ for the pin have been used in the simulation. The pins are meshed using three-noded quadratic beam elements (B32). The facesheets are meshed into 20 noded brick elements (C3D20). The force–displacement slope was obtained by applying a uniform line load on the top facesheet. For the boundary conditions, only vertical displacements were constrained on the left and right bottom edges allowing the structure to deform along the length direction.

13.3 Experimental Results

13.3.1 Global Flexural Response

Flexural tests are performed with different end conditions and specimens to determine the effect of the end supports of the specimen and foam in the deformation and failure initiation. The global flexural load–displacement response of the specimens under two different end conditions is depicted in Fig. 13.3. Further detail observations will be discussed in

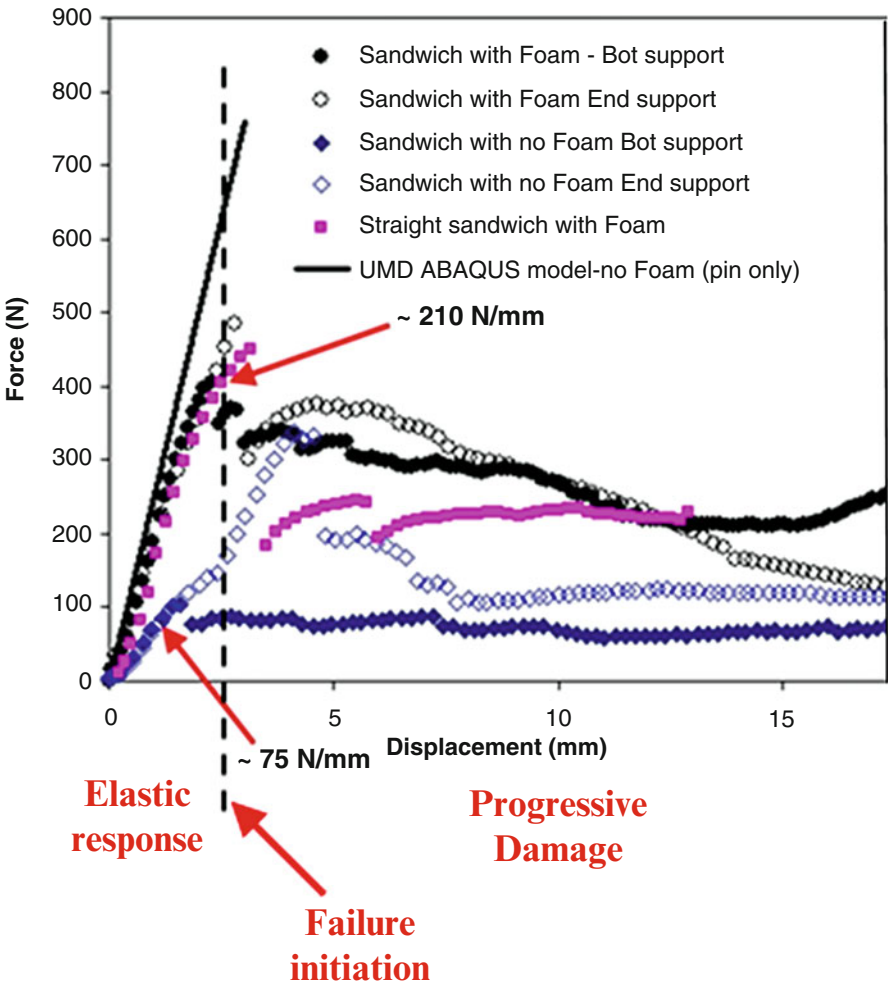

Fig. 13.3 Global flexural response of the curved K-Cor sandwich specimens and comparison with straight sandwich and FEA simulation. The elastic regime and failure initiation point where the mechanical response transitions to progressive damage accumulation is indicated

reference to the deformation fields obtained by DIC. The global stiffness of the curved specimen with foam was determined to be around 210 N/mm and that of the specimen without foam was around 75 N/mm. It is noted that the end conditions (supported at the bottom where only the bottom facesheet is supported, and supported at the bottom and edge where both facesheets are supported) did not significantly affect the global flexural response in terms of the flexural stiffness. The global response of a curved sandwich was found to be comparable to the response of a straight K-Cor sandwich during the initial deformation, which is also shown in the figure. The curved specimens exhibit a gradual decrease in the load bearing capacity, whereas the straight sandwich exhibited a more abrupt decrease in the load bearing capacity after failure initiation.

The linear elastic response obtained from the FEA model was found to be in close agreement with the experimental measurements. The deformation displacements of the top and bottom facesheets near the loading area were observed to be non-identical. The slope of the load–displacement response obtained from the FEA model was equal to 253 N/m. The strength and non-linear response were not studied in the FEA model.

The effect of the end supports was most significant on the non-linear response where failure initiates and the mechanical response transitions to progressive damage accumulation. In cases where the pin-reinforced sandwich specimens were with and without foam, the maximum load bearing capacity was found to be higher when the ends of the sandwich were supported (both the facesheets are supported). However, since the specimens are curved, the presence of foam in the core has a more significant role in the shear resistance it provides. Thus, the load bearing capacity is significantly increased by end support when foam is not present in the core due to the "arch" profile of the curved structure, which produces more thrust load through the face sheets rather than the more shear through the core, as is the case when the bottom of the specimen is supported. It was also determined that this allowed the curved shape to provide more load bearing capacity than the flat specimen in the non-linear region when foam was present in the core.

13.3.2 DIC Measurements for Curved Specimens

The strain fields obtained from DIC of the images captured during the deformation is shown in Fig. 13.4 below for the K-Cor sandwich specimen with foam and supported at the edges as per Fig. 13.2b. DIC results could only be obtained from the specimens with foam, since the foam core provided a continuous media suitable for subset correlation. The strain fields were found to be consistent with the classical three-point bending deformation fields within the elastic regime corresponding to point A (Fig. 13.4a) with a concentration of local deformation below the loading indenter. At point B, right after the core shear failure initiates, the shear crack progresses to the facesheet-core interface and the load bearing capacity can be attributed to the resistance at the core-facesheet interface and buckling of the top facesheet. The strain magnitudes increased by an order of magnitude around the failure initiation, and the core shear strain was found to be 7 % at the failure location.

13.3.3 Failure Mechanism in K-Cor Sandwich Under Different Conditions

The core shear failure was observed to be dominant in the K-Cor sandwich specimens with foam in both end support conditions, as shown in Fig. 13.5a. Apart from the consistent core shear failure, facesheet buckling was observed in the top facesheet only when the edge was supported. When foam was not present in the core, the entire shear load is carried during bending by the pin reinforcement in the core. Thus, detachment of the pins from the facesheet was observed to precede any facesheet failure, as shown in Fig. 13.5b, without any observation of pin buckling as in the case of the DIC results from the specimens with foam. It has been observed that the boundary conditions do not significantly affect the failure initiation location. The failure initiation always occurred around the mid-section of the specimen, and was asymmetric due to the localized load distribution from the pin configuration.

The undeformed and deformed shapes of the FEA model are also shown in Fig. 13.5c. Although, the FEA model was only developed to predict the elastic response of the structure without accounting for any failure mechanisms, the concentration of deformation that was predicted by the model correlated well with the observed asymmetric progression of damage observed in the specimen due to localized load distributions from the pin configuration.

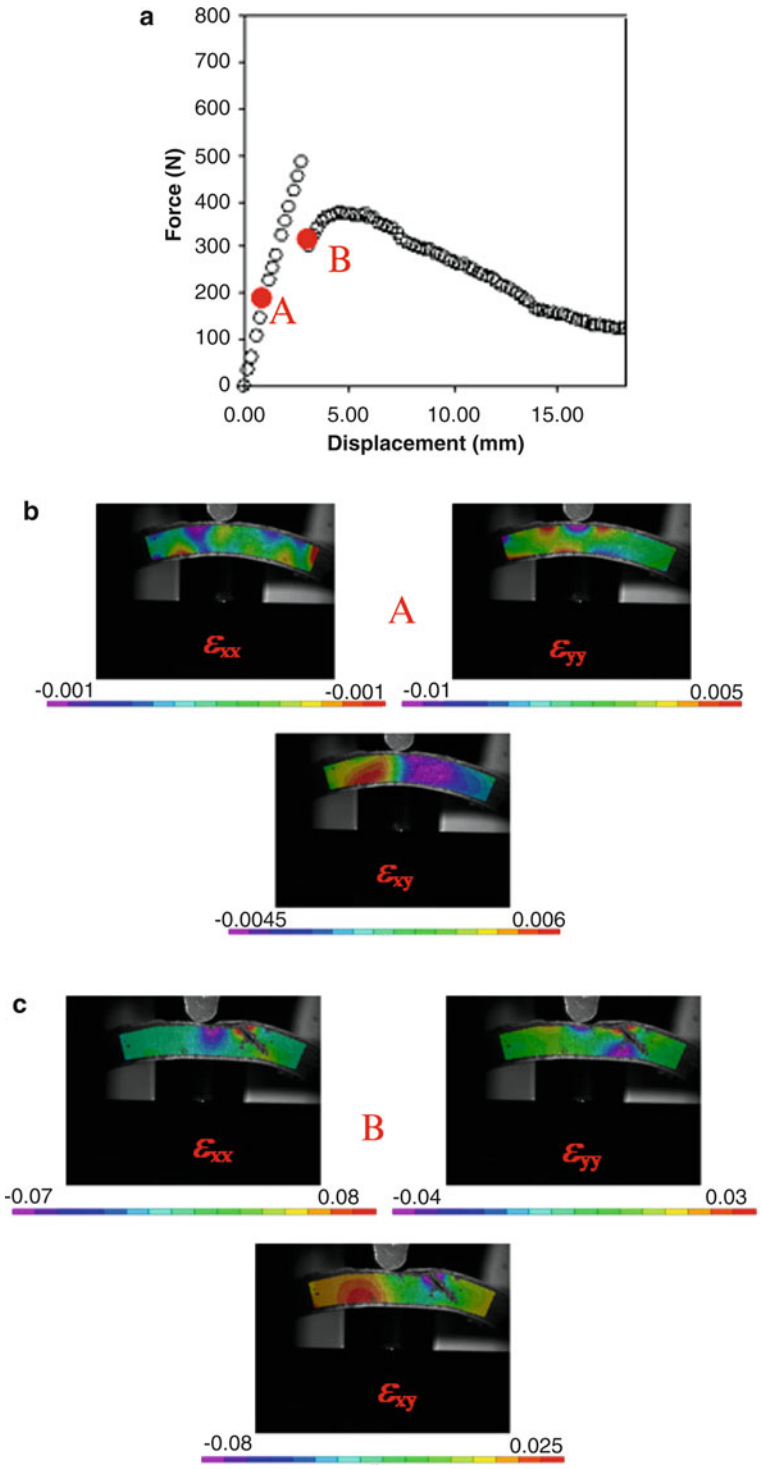

Fig. 13.4 Flexural response and deformation behavior in K-Cor sandwich composite: (**a**) load–displacement response of sandwich with support at the edge, (**b**) strain fields obtained by DIC within the elastic regime, and (**c**) strain fields obtained by DIC right after core shear failure initiation

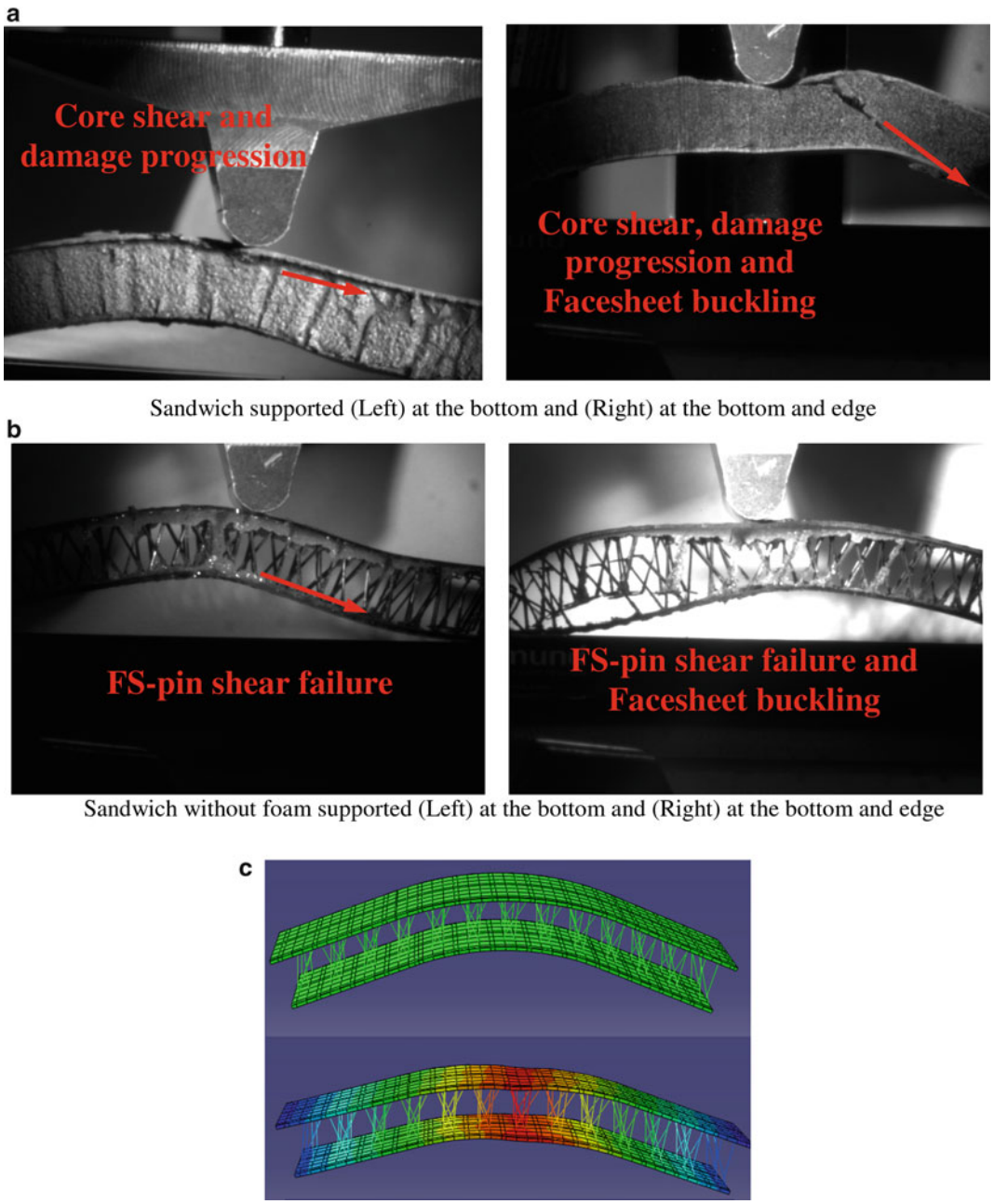

Fig. 13.5 Failure initiation, progressive damage and facesheet buckling under different end supports in the specimens: (**a**) with foam, (**b**) without foam, and (**c**) undeformed and deformed shape (within elastic regime) of curved K-Cor sandwich composite obtained from FEA under unit applied displacement

13.4 Conclusions

Curved K-Cor sandwich composite specimens were fabricated with a reasonably high level of curvature. Three-point bending experiments were performed on curved K-Cor sandwich specimens with and without foam at the core. Curved K-Cor sandwich specimens were tested under two end support condition: (1) supported at the bottom, and (2) supported at the bottom and edge (i.e., end constraint).

The resulting load–displacement curve for curved specimens with foam exhibited a response similar to flat specimens in both end support conditions. However, after reaching the elastic limit there was a gradual decline in load bearing capacity rather than an abrupt drop. Also, there was approximately a similar elastic load limit that was most likely due to the arching

of the specimen inducing a bending moment similar to that of a flat specimen in three-point bending. The non-linear behavior after failure was much different than observed with flat specimens in three point bending, which exhibit abrupt load reduction at the elastic limit and core shear failure and much lower load bearing capacity during progressive damage accumulation. For specimens without foam, there was a much greater sensitivity to the end conditions due to the fact that the core could not sustain as much shear without the foam. Thus, having the ends constrained allowed for more thrust load through the facesheets, and a much greater load bearing capacity than was observed when only the bottom of the specimen was supported and more shear was conducted through the core.

DIC strain fields were found to be consistent with classical three-point bending deformation, and a core shear strain of 7 % was measured at the location of failure initiation. The dominant failure mechanism for specimens with foam was observed to be core shear failure, which progressively propagated to the facesheet-core interface when foam was present in the core. There was also significant accumulation of shear strain on one side of the specimen that led to delamination occurring on only one side of the central loading point as the load was shed. For specimens without foam, shear failure at the pin-facesheet joint was observed to be the dominant mechanism. Due to the shear failure at the pin-facesheet joint, the pin buckling mode was not observed as in the case of specimens with foam.

Acknowledgements The authors would like to acknowledge support from NAWCAD in Pax River, MD through cooperative agreement N00421-98-H-1116 with the University of Maryland.

References

1. Cartié DDR, Fleck NA (2003) The effect of pin reinforcement upon the through-thickness compressive strength of foam-cored sandwich panels. Compos Sci Technol 63(16):2401–2409
2. Haldar S, Bruck HA (2014) Mechanics of composite sandwich structures with bioinspired core. Compos Sci Technol. http://dx.doi.org/10.1016/j.compscitech.2014.02.011. doi:10.1016/j.compscitech.2014.02.011#doilink
3. Haldar S, Bruck HA (2011) Characterization of dynamic damage mechanisms in palmetto wood as biological inspiration for impact resistant polymer composites. Mech Mater 57:97–108
4. Nanayakkara A, Feih S, Mouritz AP (2011) Experimental analysis of the through-thickness compression properties of z-pinned sandwich composites. Compos Part A Appl Sci Manuf 42(11):1673–1680
5. Haldar S, Bruck HA (2013) A new methodology for scaling the mechanics of pin-reinforcement in composite sandwich structures under compression using digital image correlation. Exp Mech, submitted for publication
6. Virakthi A, Lee SW, Haldar S, Bruck HA, Rahman A (2013) Modeling of pin-facesheet interactions in K-Cor sandwich structures under compressive loading. In: 54th AIAA/ASME/ASCE/AHS/ASC structures, structural dynamics, and materials conference, Boston, Massachusetts
7. Rice MC, Fleischer CA, Zupan M (2006) Study on the collapse of pin-reinforced foam sandwich panel cores. Exp Mech 46(2):197–204
8. Du L, Guiqiong J, Tao H (2009) Z-pin reinforcement on the core shear properties of polymer foam sandwich composites. J Compos Mater 43 (3):289–300

Chapter 14
Experimental Investigation of Free-Field Implosion of Filament Wound Composite Tubes

M. Pinto and A. Shukla

Abstract The mechanisms and energies associated with the hydrostatic implosion of composite cylinders are investigated experimentally and numerically. Experiments are conducted in a large pressure vessel, designed as to provide an adequate reflection-free window to best capture pressure waves resulting from the collapse. Both glass-fiber/polyester and carbon-fiber/epoxy filament wound thin-walled ($R/t > 15$) tubes are tested with varying L/D ratios to explore the effect of geometry on the collapse pressure and mechanics of the collapse. 3D Digital Image Correlation (DIC) is used to capture the full-field displacements and strains during the implosion event, and dynamic pressure transducers are employed to measure the pressure pulse generated by the collapse. Computational models are developed to verify and better understand key mechanisms of failure during hydrostatic buckling.

Keywords Composite cylinders • Hydrostatic implosion • Filament winding • Digital image correlation • High-speed photography

14.1 Introduction

The use of composites has attracted attention in underwater marine applications due to the array of advantages offered by these materials. Composite materials offer alternatives with reduced weight, improved corrosion resistance, and for submerged structures, greater potential operating depths. In addition, these materials provide improved stealth qualities by having very low thermal, acoustic, and magnetic signatures, increasing their appeal for military applications. For these reasons, the presence of composite materials in marine industries is increasing, and they are currently used in several naval applications, such as sonar domes, masts, and hull sheathings [1]. One of the biggest obstacles to widespread adaptation of composite materials is a lack of complete understanding and simple design rules for these materials, especially under extreme loading conditions [1]. For this reason, this work looks to expand the current knowledge of composite behavior by examining the problem of implosion.

The implosion of a submerged structure occurs when external pressure reaches a critical value, causing an instability in the structure and resulting in a rapid and often catastrophic collapse. During this collapse, the boundaries of the volume and the surrounding fluid are accelerated to high velocities and stop suddenly once the collapse is completed. This abrupt change in momentum releases a pressure wave into the surrounding fluid, which can have the potential to damage nearby structures [2, 3]. For this reason, the implosion problem has gained much attention in recent decades. The implosion of glass spheres has been studied by several authors who characterized the pressure pulse emitted during collapse as well as its potential for damage to nearby structures [4–6]. The implosion of aluminum cylinders has also been studied in recent work. Turner identified key stages of the implosion event in relation to the local pressure about the collapsing structure [7]. Farhat et al. studied the implosion of aluminum cylinders with varying L/D ratios to produce both mode 2 and mode 4 failures [8].

M. Pinto • A. Shukla (✉)
Dynamics Photomechanics Laboratory, Department of Mechanical, Industrial and Systems Engineering, University of Rhode Island, Kingston, RI 02881, USA
e-mail: mpinto@umassd.edu; shuklaa@egr.uri.edu

G. Tandon (ed.), *Composite, Hybrid, and Multifunctional Materials, Volume 4: Proceedings of the 2014 Annual Conference on Experimental and Applied Mechanics*, Conference Proceedings of the Society for Experimental Mechanics Series,
DOI 10.1007/978-3-319-06992-0_14,

In this work, the authors were able to observe the differences in the emitted pressure pulse as well as the collapse progression due to the change in buckling mode. In both works by Turner and Farhat, robust fluid–structure computational models were developed which correlated quite well with experimental data.

Though several analytical treatments exist on the subject, the implosion of composite cylinders under hydrostatic loading has also been experimentally studied in a few previous publications. Moon et al. examined implosion of filament-wound carbon/epoxy composite tubes with different winding angles both experimentally and computationally to determine collapse pressures and modes [9]. Both Ross and Smith performed experiments on carbon/E-glass tubes to determine critical buckling pressure, buckling modes, and create design tables for these structures [10, 11]. Hernández-Moreno et al. tested filament-wound glass/epoxy composite tubes with a winding angle of 55° to examine effects of winding pattern on the collapse pressure [12]. Hur et al. examined the buckling modes, loads, and ply failure of carbon/epoxy tape layup tubes both experimentally and computationally [13]. Yang et al. developed an analytic model for critical buckling pressure based on anisotropic laminate theory and performed experiments on E-glass/epoxy tubes to test predictions [14]. However, in none of these studies was the pressure pulse from the collapse measured, nor were high speed images of the collapse event captured. This study addresses the current gap in knowledge by examining the pressure pulses emitted in collapse of filament wound composite tubes and capturing full-field displacements during the implosion event along with a high-speed photographic record of the failure process.

14.2 Materials

The impodable volumes in this study are carbon/epoxy and glass/polyester (PE) filament wound composite tubes. The carbon/epoxy tubes consist of seven layers of unidirectional carbon fabric reinforcement arranged in a [±15/0/±45/±15] layup with a 60.3 mm inner diameter and 305 mm length. These cylinders are manufactured by Rock West Composites (West Jordan, UT) with a nominal wall thickness of 1.63 mm and are thoroughly sanded on the exterior surface for excellent finish and tolerances. The glass/PE tubes consist of five layers of unidirectional E-glass fabric reinforcement arranged in a [±55/±55/0] layup with a 57.2 mm inner diameter and 406 mm length. These cylinders are manufactured by Nor'Easter Yachts (Milford, CT) with a nominal wall thickness of 2 mm The dimensions are selected as to provide specimens with a relatively low expected collapse pressure, and a high R/t ratio so that thin-wall assumptions may be utilized.

14.3 Experimental Methods

All implosion experiments are conducted in a large (2.1 m dia. × 2.1 m height) pressure vessel with a maximum pressure rating of 6.89 MPa to simulate free-field conditions to monitor the evolution of pressure waves, and to provide constant hydrostatic pressure throughout the collapse event (see Fig. 14.1). Several Plexiglass windows mounted about the midspan of the pressure vessel allow the specimens to be viewed by cameras and adequately lit by two high powered light sources.

The specimens are sealed using two aluminum end caps, each inserted 12.7 mm into the tube, thereby reducing the unsupported length by 25.4 mm. The sealed tube is then suspended horizontally in the center of the pressure vessel using several steel cables attached to the inner walls of the vessel. A random speckle pattern is applied to a region spanning the entire length of the specimen and approximately half of the circumference using flat black paint. This region is painted white prior to speckling to enhance the contrast of the pattern. The tubes are secured in such a way that they cannot move or float during the filling process and the painted surface is faced toward the viewing windows. To measure the changes in local pressure during the collapse event, several high pressure blast transducers (PCB 138A05, PCB Piezotronics, Inc., Depew, NY) are mounted at different locations about the specimen both axially and circumferentially. The amplified outputs of these sensor are monitored by an Astro-med Dash® 8HF-HS portable data recorder (Astro-Med Inc., West Warwick, RI) at a sampling rate of 2 MHz.

The vessel is then flooded with water that is first filtered for maximum optical clarity, leaving a small air pocket at the top. Once the vessel is filled, nitrogen gas is introduced into the air pocket to pressurize the enclosed water. The pressure inside the vessel is increased at a gradual rate (83 kPa/min) until the specimen collapsed. At this point, the cameras and pressure sensors are end triggered to record the data occurring 1 s prior to triggering. In this way, data is collected for the entire collapse event by all recording devices. Post-mortem images are taken immediately after removal using a Nikon D90 DSLR camera to minimize potential creep.

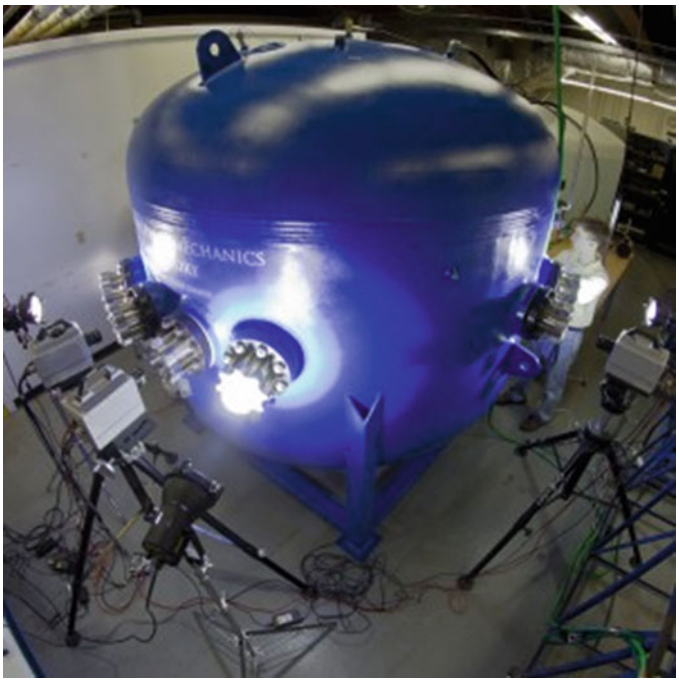

Fig. 14.1 Pressure vessel used for implosion experiments

Two high-speed cameras (Photron SA1, Photron USA, Inc.), offset by 16° are used to capture stereo images of the patterned region of the specimen at 20,000 frames/s for glass/PE tubes, and 36,000 frames/s for carbon/epoxy tubes. The stereo images are analyzed using a commercially available digital image correlation (DIC) software, VIC3D 2012 (Correlated Solutions, Inc., Columbia, SC) to determine real-time, full-field displacements across the viewable surface of the specimen throughout the implosion event with a spacial resolution of 0.5 mm. The digital cameras have a resolution of 1,024 × 1,024 pixels. The lenses used for each experiment are selected as to image the entire width of the specimen throughout the collapse process, and to capture the full unsupported length of the cylinders.

14.4 Results

The glass/PE tubes imploded at a critical pressure of 2.03 MPa, while the carbon/epoxy tubes collapsed at a pressure of 1.61 MPa. These observed buckling pressures are reasonably close to the predictions made based on the methods of Rasheed [15] and Koudela [16]. Both specimen types collapsed completely in a mode 2 buckling shape, and regained some of their original circularity after pressure is removed.

Figure 14.2 shows typical pressure histories about the midspan of glass/PE tubes. This trace shows a fairly smooth drop in local pressure, followed by a sharp spike which decays gradually and is followed by many oscillations. This is consistent with previous work done by Turner [7] and Farhat [8] on metallic cylinders and shows that some of the same mechanisms are at play. The drop in pressure between points A and B are a result of the cylinder walls collapsing in toward each other. Surrounding fluid accelerates to follow the walls of the reducing cylindrical volume causing the local pressure to drop. This is confirmed by examining the images corresponding to points A and B in Fig. 14.3.

At point C, we see a rapid spike in pressure spike, taking approximately 300 μs rise from the minimum pressure to the maximum pressure. This spike corresponds to the walls of the cylinders contacting each other and arresting their movement, as seen in the matched image in Fig. 14.3. When the walls suddenly stop, so must the fluid accelerated during the previous stage of the collapse, and this rapid change in momentum results in the release of a pressure wave. Following the pressure spike at time C, the pressure drops back down to roughly hydrostatic as the buckled shape spreads axially along the cylinder, causing catastrophic damage to the specimen. In these images, a great deal of damage is clearly visible. The majority of this damage is in matrix cracking and delamination, manifesting in the “ribboning” seen in the high speed images. Upon further post-mortem investigation of the specimens, it is also clear that a good deal of fiber pull-out is present. These features are important to note, as they are energy intensive damage processes which affect the speed of the collapse and thereby the local pressure history.

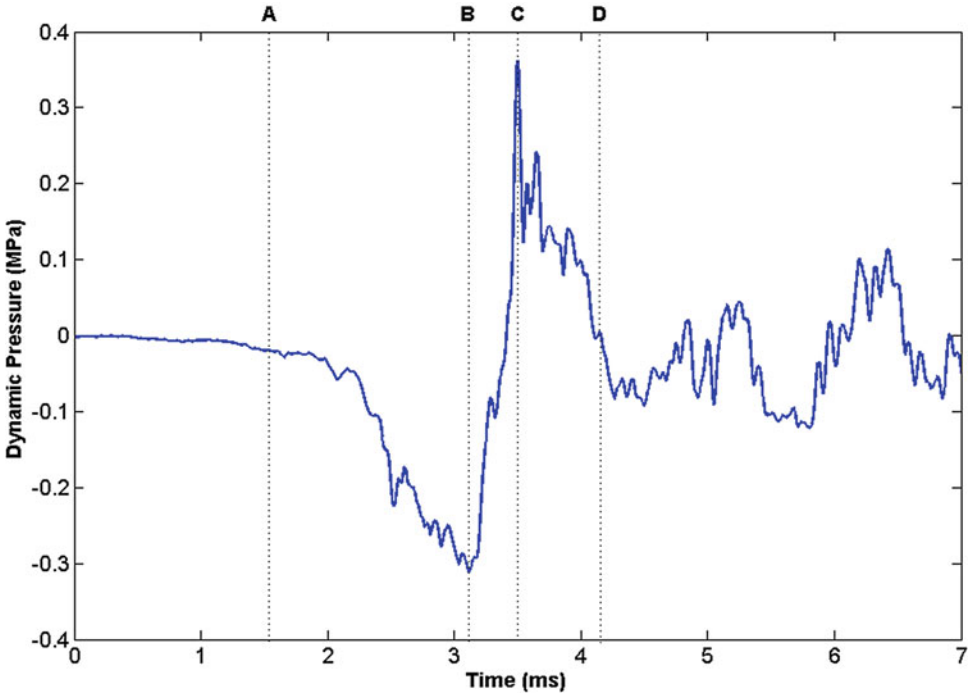

Fig. 14.2 Typical dynamic pressure trace about midspan of glass/PE tubes

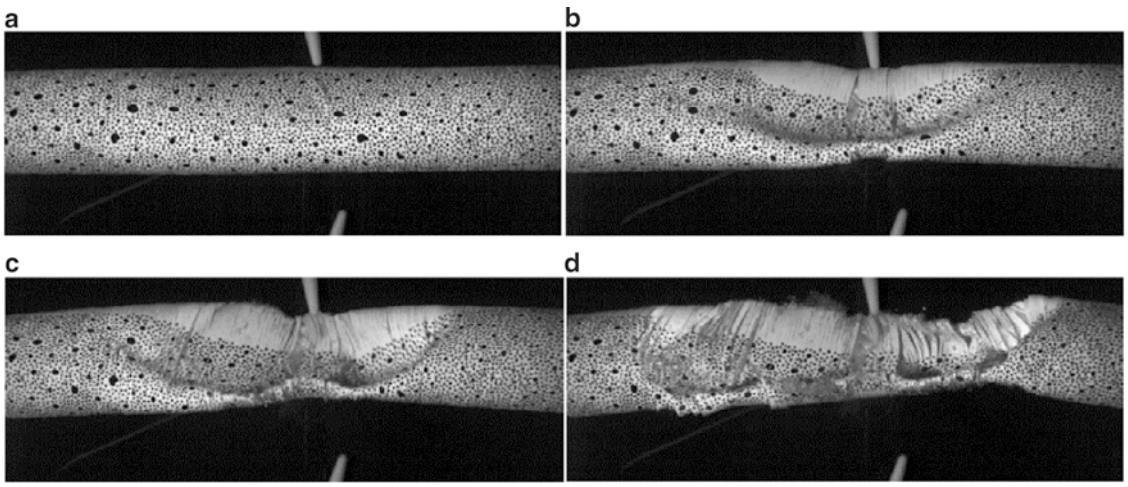

Fig. 14.3 High speed images of implosion event for glass/PE tube

Figure 14.4 shows a typical pressure history about the midspan of carbon/epoxy tubes. At first glance, the key points of this trace resemble that of the glass fiber tubes: the local pressure begins to drop gradually at point A and falls to a minimum at point B. The pressure then rises to a sharp peak at point C, followed by a broader region of lower overpressure until finally returning to hydrostatic pressure at point D.

However, we can notice two major differences in this pressure trace: a much more peaky underpressure region, and a much sharper and greater pressure spike. The small peaks in the underpressure region are due to localized catastrophic material failures coupled with the collapse of cavitation bubbles on the specimen surface. The collapse of these small bubbles release pressure pulses, adding some noise to the data in this region.

From the images in Fig. 14.5 we can see that from point A to point B, the structure deforms with very little visible damage. Similarly, the pressure trace this region shows a fairly smooth drop in local pressure. At point B, pressure is seen to drop suddenly as the first cracks appear along the length axis of the specimen. Between points B and C, through-thickness

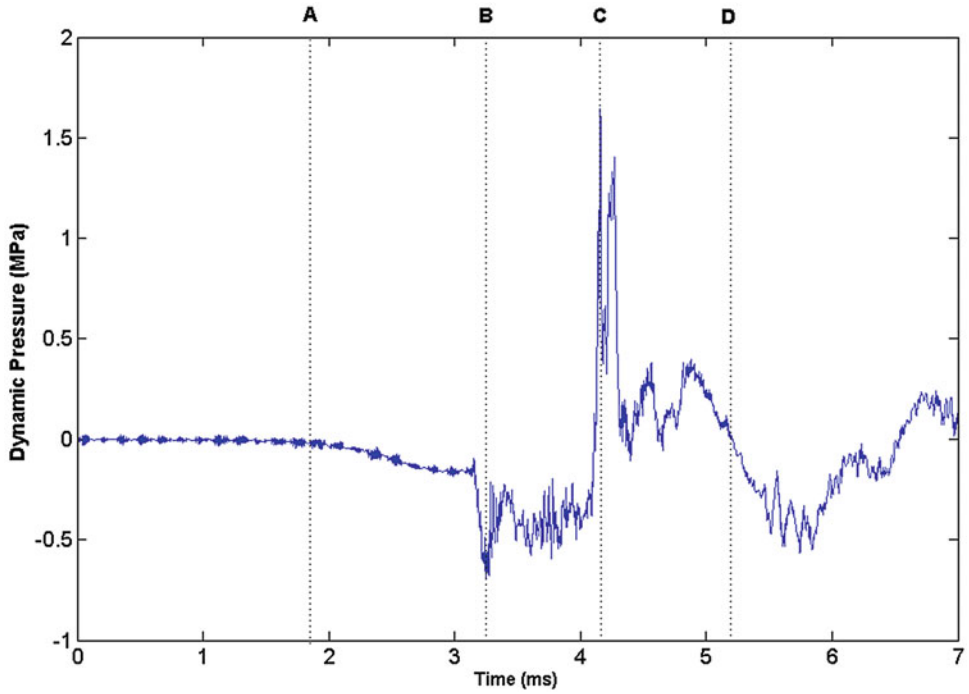

Fig. 14.4 Typical dynamic pressure trace about midspan of carbon/epoxy tubes

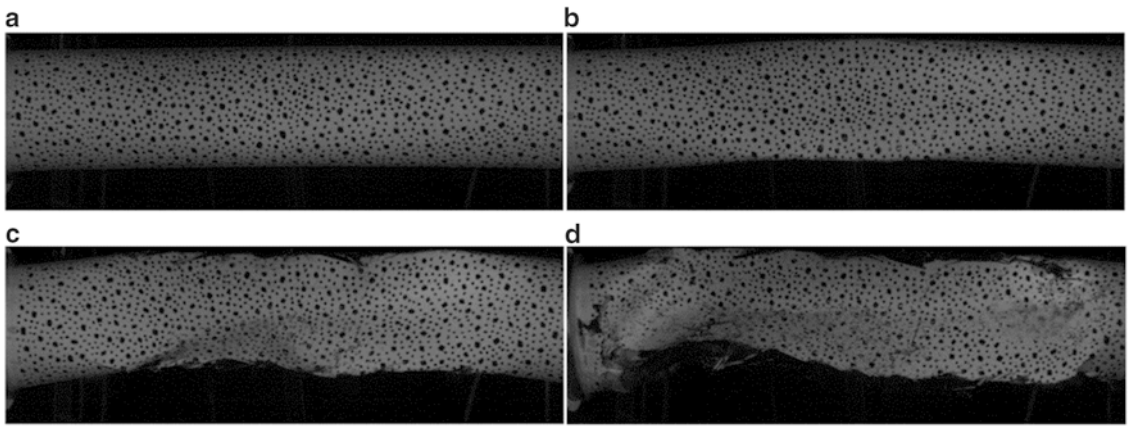

Fig. 14.5 High speed images of implosion event for carbon/epoxy tube

longitudinal cracks continue to progress very rapidly through the length of the specimen causing it to accelerate swiftly through the completion of collapse. After point C, the cylinder wall contact propagates through the length of the cylinder, resulting in the positive pressure region between C and D.

To compare these pressure traces more quantitatively, the minimum and maximum pressures are determined as a percentage of hydrostatic pressure, and the specific impulse of the under and overpressure regions are calculated. The specific impulse is defined as the area under the pressure curve for the time interval of interest. These quantities are compared in Fig. 14.6. Here it is found that carbon/epoxy tubes reach a lower minimum pressure, a higher maximum pressure, and deliver a much greater impulse in the pressure pulse emitted upon collapse.

The cause of this increase in pressure and impulse is a result of the increased speed of collapse observed in the high-speed imaging. Due to the catastrophic nature of the collapse of carbon/epoxy tubes, the specimens lose structural stability quite severely early in the implosion event, allowing them to fail at a higher rate. DIC is used to confirm and quantify this difference in collapse speed. The DIC system is first calibrated to collect accurate displacements on the surface of the submerged specimens. The accuracy is then confirmed for each specimen by comparing the outer radius of the specimen calculated by the software to its true value. A finite difference scheme is applied to the measured displacements to calculate

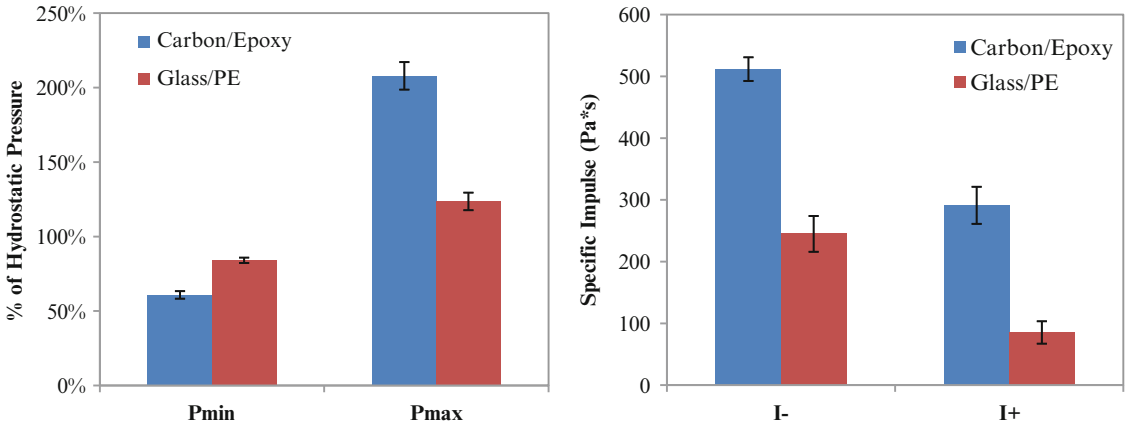

Fig. 14.6 Under/overpressure values (*left*) and calculated specific impulses (*right*) for different material systems

velocities of deformation. Collapse velocities are measured at the midspan of each specimen and the maximum values are used for comparison. Using this method, the initial velocities of the carbon/epoxy tubes are found to be significantly greater than those of glass/PE specimens, corroborating with previous observations.

Finite element analysis is performed using the commercially available ABAQUS software package (Dassault Systèmes Americas Corp., Waltham, MA) to confirm experimental observations and better understand the physics of the collapse process. Both linearized buckling analyses and non-linear Rik's method analyses are performed on the composite structures. For each type of specimen tested, these analyses accurately reproduce the observed critical collapse pressure and mode shapes of the implodable volumes, and aid in the understanding of the progression of their failure.

14.5 Conclusions

As a result of this study, the failure, damage progression, and pressure pulse released during the hydrostatic collapse of filament wound composite tubes is characterized. It is concluded that upon implosion, glass/PE filament wound tubes generate pressure waves with significantly reduced damage potential as compared with carbon/epoxy tubes of the same make. As seen in the collapse images, these tubes contain more energy intensive damage processes, such as delamination and fiber pull-out, causing less of the potential hydrostatic energy available to be transferred into the pressure pulse. The increased energy cost of deformation is also reflected in the speed of collapse, which for glass/PE tubes is roughly half that of carbon/epoxy tubes.

Another important finding is the difference between the negative impulse and positive impulse of the pressure history. In previous work by Turner [7] and Farhat [8], the negative and positive impulses of imploding glass and metallic volumes are found to be roughly equal. However in both carbon and glass fiber composites studied here, the positive impulse is significantly lower than the negative impulse. This shows that the complex damage and failure mechanisms present in both of these materials serve to dissipate much of the energy that would otherwise be released in the form of the pressure pulse. This in turn makes filament wound composite tubes a more attractive option when considering the potential of the material to damage nearby structures should an implosion occur.

Acknowledgements The authors kindly acknowledge the financial support provided by Dr. Yapa D. S. Rajapakse, under the Office of Naval Research (ONR) Grant No. N00014-10-1-0662, as well as Sachin Gupta, Craig Tilton, and Christopher Shillings for their invaluable help in conducting experiments.

References

1. Mouritz AP, Gellert E, Burchill P, Challis K (2001) Review of advanced composite structures for naval ships and submarines. Compos Struct 53(1):21–42
2. Accident grounds neutrino lab—physicsworld.com [WWW document], n.d. http://physicsworld.com/cws/article/news/2001/nov/15/accident-grounds-neutrino-lab. Accessed 2 Oct 2014

3. Ling J, Bishai M, Diwan M, Dolph J, Kettell S, Sexton K, Sharma R, Simos N, Stewart J, Tanaka H, Viren B, Arnold D, Tabor P, Turner S, Benson T, Wahl D, Wendt C, Hahn A, Kaducak M, Mantsch P, Sundaram SK (2013) Implosion chain reaction mitigation in underwater assemblies of photomultiplier tubes. Nucl Instrum Methods Phys Res Sect A Accel Spectrometers Detect Assoc Equip 729:491–499
4. Orr M, Schoenberg M (1976) Acoustic signatures from deep water implosions of spherical cavities. J Acoust Soc Am 59:1155–1159
5. Harben PE, Boro C (2001) Implosion source development and diego garcia reflections. Presented at the 23rd Department of Defense/ Department of Energy Seismic Research Review, Jackson Hole, Wyoming
6. Turner SE (2007) Underwater implosion of glass spheres. J Acoust Soc Am 121:844–852
7. Turner SE (2012) Underwater implosion of cylindrical metal tubes. J Appl Mech 80(1):011013
8. Farhat C, Wang CG, Main A, Kyriakides S, Lee LH, Ravi-Chandar K, Belytschko T (2013) Dynamic implosion of underwater cylindrical shells: experiments and computations. Int J Solids Struct 50(19):2943–2961
9. Moon CJ, In-Hoon K, Bae-Hyeon C, Jin-Hwe K, Choi JH (2010) Buckling of filament-wound composite cylinders subjected to hydrostatic pressure for underwater vehicle applications. Compos Struct 92(9):2241–2251
10. Ross CTF, Little APF, Haidar Y, Waheeb AA (2011) Buckling of carbon/glass composite tubes under uniform external hydrostatic pressure. Strain 47:156–174
11. Smith PT, Ross CTF, Little APF (2009) Collapse of composite tubes under uniform external hydrostatic pressure. J Phys Conf Ser 181:156–157
12. Hernández-Moreno H, Douchin B, Collombet F, Choqueuse D, Davies P (2008) Influence of winding pattern on the mechanical behavior of filament wound composite cylinders under external pressure. Compos Sci Technol 68(3–4):1015–1024
13. Hur SH, Son HJ, Kweon JH, Choi JH (2008) Postbuckling of composite cylinders under external hydrostatic pressure. Compos Struct 86 (1–3):114–124
14. Yang C, Pang SS, Zhao Y (1997) Buckling analysis of thick-walled composite pipe under external pressure. J Compos Mater 31(4):409–426
15. Rasheed HA, Yousif OH (2005) Stability of anisotropic laminated rings and long cylinders subjected to external hydrostatic pressure. J Aerosp Eng 18(3):129
16. Koudela KL, Strait LH (1993) Simplified methodology for prediction of critical buckling pressure for smooth-bore composite cylindrical shells. J Reinf Plast Compos 12(5):570–583

Chapter 15
Experimental Investigation of Bend-Twist Coupled Cylindrical Shafts

S. Rohde, P. Ifju, and B. Sankar

Abstract A new and unique way of orienting carbon fiber lamina in cylindrical shafts results in bend-twist coupling. A beam is said to possess bend-twist coupling when a pure bending moment applied to the beam results in simultaneous bending and twisting. This effect is normally associated with asymmetric cross-sections (such as c-shaped sections) but can result from a symmetric cross-section if the beam is anisotropic. In this case we study the bend-twist coupling resulting from a cylindrical shaft fabricated using a unique, non-obvious anisotropic lay-up. This research covers the design and manufacturing of these carbon fiber shafts to maximize the bend-twist coupling while simultaneously achieving acceptable torsional and flexural rigidity. Once constructed, the composite shafts are tested using DIC to measure the degree of rotation and deflection given an applied bending and twisting moment. The results are used to determine the shear center, degree of bend-twist coupling, torsional rigidity, and flexural rigidity as well as to verify the Finite Element Models. These models are used to predict the success of potential designs and to provide greater understanding of the phenomenon. Closed-form solutions provide a third means of verification, analysis, and optimization.

Keywords Bend-twist coupling • Carbon fiber • Digital image correlation • Extension-shear coupling • Shear center

15.1 Introduction

The most familiar example of bend-twist coupling is that of a channel shaped cantilever beam with an asymmetric cross-section such as Fig. 15.1. When a point load is applied through the geometric centroid at the tip of the beam, it experiences twisting as well as bending. The twisting, which is often surprising to viewers, is caused by unbalanced shear flows in the asymmetric cross section. The amount of twisting that will result can be determined from the shear center which acts in the same manner to moment arms as the centroid does in symmetrically shaped cross-sections.

The kind of bend-twist coupling that is the topic of this paper does not result from shear flows. While, the terminology of shear center and bend-twist coupling are borrowed from the more typical kind discussed above, the phenomena is fundamentally different here [1, 2]. This coupling of bending and twisting results from the way that anisotropic materials carry loads differently from that of isotropic materials. In anisotropic plates shear strain can result from pure extension. The way that these loads are connected is expressed through the ABD matrix in classical laminate plate theory. Every unique design of anisotropic plates produces its own unique ABD matrix. This matrix, shown in Eq. 15.1, maps the forces and moments applied on an anisotropic plate to the extension, shear, and curvature that result from them.

S. Rohde (✉) • P. Ifju • B. Sankar
University of Florida, New Engineering Building 235, 131, and 137, 1064 Center Dr., Gainesville, FL 32611, USA
e-mail: srohde719@gmail.com

G. Tandon (ed.), *Composite, Hybrid, and Multifunctional Materials, Volume 4: Proceedings of the 2014 Annual Conference on Experimental and Applied Mechanics*, Conference Proceedings of the Society for Experimental Mechanics Series,
DOI 10.1007/978-3-319-06992-0_15,

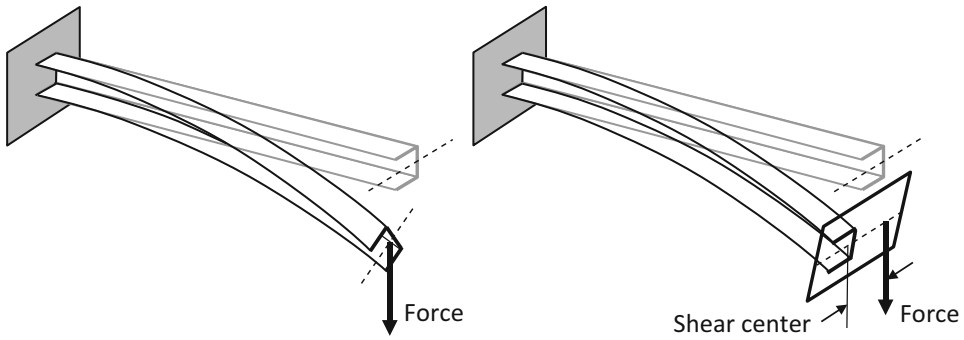

Fig. 15.1 For isotropic beams the shear center results from the sectional geometry and indicates the point at which a point load causes bending without twisting

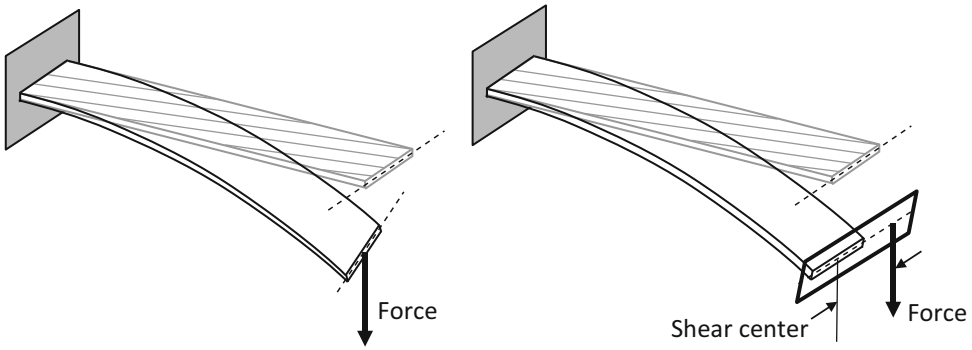

Fig. 15.2 Anisotropic plates can experience off-axis shear centers by carrying the loads asymmetrically

$$\begin{bmatrix} N_x \\ N_y \\ N_{xy} \\ M_x \\ M_y \\ M_{xy} \end{bmatrix} = \begin{bmatrix} A_{11} & A_{12} & A_{16} & B_{11} & B_{12} & B_{16} \\ A_{12} & A_{22} & A_{26} & B_{12} & B_{22} & B_{26} \\ A_{16} & A_{26} & A_{66} & B_{16} & B_{26} & B_{66} \\ B_{11} & B_{12} & B_{16} & D_{11} & D_{12} & D_{16} \\ B_{12} & B_{22} & B_{26} & D_{12} & D_{22} & D_{26} \\ B_{16} & B_{26} & B_{66} & D_{16} & D_{26} & D_{66} \end{bmatrix} \begin{bmatrix} \varepsilon_x^0 \\ \varepsilon_y^0 \\ \varepsilon_{xy}^0 \\ \kappa_x^0 \\ \kappa_y^0 \\ \kappa_{xy}^0 \end{bmatrix} \tag{15.1}$$

In most cases negligible values for the A_{16} and A_{26} terms are desired. Most lay-ups are designed to achieve this result. This prevents residual stresses and other unintended consequences. This also means that tension causes extension and shear causes shear strain with no "cross-talking" between the two, but here the goal has been to create a lay-up design that will maximize A_{16} and A_{26}. For simplicity, choosing the x-axis to run along the beam results in only A_{16} being of concern. The relevant value is now only A_{16} which causes in-plane shear strain, ε_{xy}^0, to result from the axial normal force, N_x. The proper way to think of this is illustrated in Figs. 15.1, 15.2, and 15.3 which demonstrate how bend-twist coupling in a cylinder can result from extension-shear coupling.

Although the term bend-twist coupling is used, the relevant coupling is between tension and shear. Since the large values of tension and compression are most easily obtained through bending and the shear strain most obviously observed as twisting: the term bend-twist coupling is often used as this is what is obvious on the macro level. In these experiments the anisotropic material is carbon fiber. Layers of unidirectional carbon fiber are wrapped around a cylindrical mandrel in a unique, non-obvious design pattern which results in a large value for A_{16}. This couples the tension and shear forces.

The question remains as to why choose a cylindrical design. A boxed or even flat plate would experience similar bend twist coupling, but the cylinder provides a more stable and symmetric design. It is capable of being rotated 360 and experiencing a sinusoidal change in its horizontal shear center. The cylindrical design is more stable and avoids the buckling modes that may affect other designs.

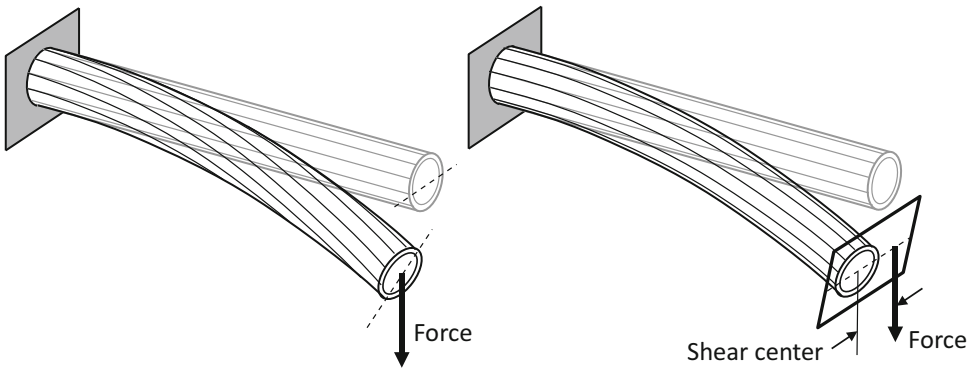

Fig. 15.3 The concept of off-axis shear centers is extended to composite cylinders

15.2 Manufacturing

The mandrel is 0.5″ in diameter. To prevent the carbon fiber epoxy from sticking to it, the mandrel is wrapped in Teflon. The wrapping is done in a spiral pattern using an inch wide roll of Teflon. This provides two or three layers between the steel mandrel and the carbon fiber. Without the Teflon, the epoxy would adhere to the steel mandrel and the shaft could not be removed. The carbon fiber is cut from larger sheets into rectangular strips. Great care is taken to ensure the fiber orientations match those of the intended design. The layers are then wrapped around the mandrel one at a time. Here care is again taken to keep the fibers properly oriented. Once all layers have been applied, a shrink wrap is wrapped around the mandrel from the outside. The shrink wrap will shrink about 30 % during the curing process. This applies the necessary pressure to ensure that the epoxy can properly harden. The shrink wrap is applied once in one direction and then a second time in the other direction. This is intended to cancel out any directional effects that may result from wrapping the spiral in one particular direction. After all layers have been added a line is marked to indicate the orientation of the layers. This line acts as a point of reference for the testing and indicates the point of maximum shear center when orientated horizontally (Fig. 15.4).

The major manufacturing difficulty is in removing the shaft from the mandrel, because the mandrel is not tapered, friction forces must be combated at all points until the entire shaft is removed. Multiple techniques have been attempted to facilitate this removal. These include: slowly applying torque to push the shaft off with an internal thread and nut, hammering the inner mandrel out, heating the set and then hammering the mandrel out, pulling the shaft with a come-along winch, removing the mandrel in pieces. All of these methods either failed to budge the shaft or resulted in large compressive forces that destroyed the carbon fiber shaft.

Throughout industry most instances of carbon fiber cylinders cured on a mandrel are more easily removed because they are of tapered design, an example being fishing rods. The taper allows for much easier removal of the shafts as only a single impulse is needed to dislodge the shaft instead of the continuous force that is needed to slide off the non-tapered version. However, for the purpose of research, the non-tapered design is needed. A constant cross-section prevents lengthwise changes in parameters such as the diameter which might affect the bend-twist coupling and shear center.

The current manufacturing process splits the mandrel into three parts longitudinally. They are stable enough to hold the mandrel in shape during the lay-up and curing process. After curing, a drift pin is used to slowly remove the inner piece. Once removed, the two outer sections of the mandrel collapse inward and the shaft can be easily removed. The Teflon is peeled from the inside of the carbon fiber and the shaft is cut to ensure consistent length. The current dimensions of the cylinders are 18 in. long with an inner radius of 0.5″ and a thickness of a few millimeters.

15.3 Testing

The fabricated carbon fiber shaft is firmly clamped in a vice. The shaft is orientated horizontally using a level. The portion of the shaft clamped in the vice has a short steel insert to prevent it from being crushed under pressure in the vice. The tip of the cantilever has a flat round disc of 1 in. diameter adhered with epoxy to the front. This disc has been speckled for digital image correlation. This is how the tip deflection and rotation are recorded.

A device was machined from aluminum to provide the necessary loading conditions. The loading conditions require a constant downward point load and a torque that can be adjusted linearly. The point load is provided by a hanging weight.

Fig. 15.4 The steel mandrel wrapped in non-stick Teflon. Beneath that is a completed carbon fiber shaft 18⅓″ in length

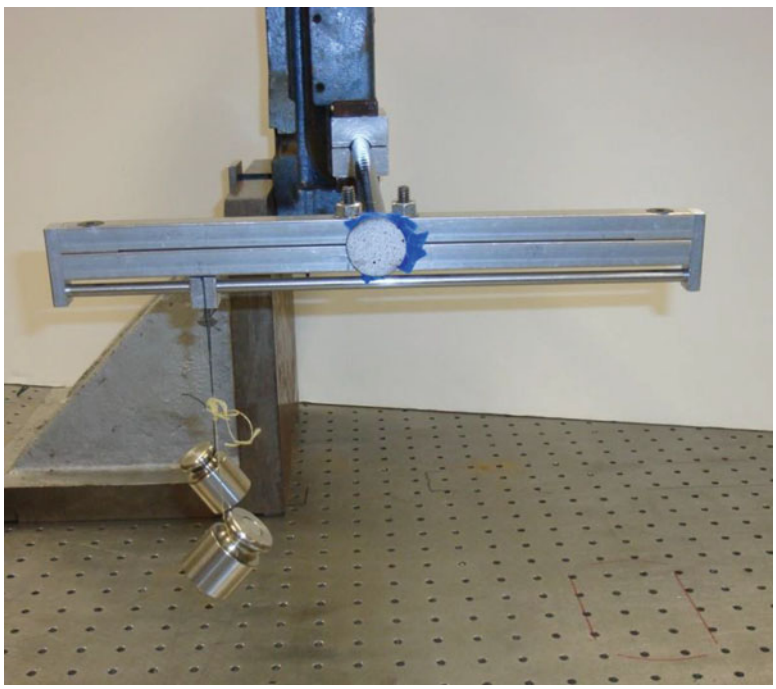

Fig. 15.5 The apparatus for applying a torque as a function of the moment arm. The weight can slide 70 mm either way

The variable torque was adjusted using that same constant load with different length moment arms. This has the secondary effect of clearly illustrating the location of the shear center. At the shear center the point load is applied and pure bending with no torsion results. This was achieved by hanging a constant weight of 300.5 g from the apparatus and then sliding this weight along the bar to linearly adjust the torque applied. A digital caliper was used to increase the moment arm by 1 cm intervals and ensure accuracy (Figs. 15.5, 15.6, and 15.7).

After the loading conditions were adjusted, an image was taken using the digital image correlation set up that had been created. This was then repeated with the entire shaft being rotated by 90°. Rotations of exactly 90° could not be guaranteed but are easily measured by how much in-plane rotation has occurred since the original reference image was taken at 0°. To determine the degree of bend-twist coupling or the location of the shear center a minimum of two points are required where each point indicates the length of the moment arm as the x-value and the corresponding in-plane rotation as the y-value. The point at which the line crosses the x-axis (zero rotation occurs) indicates the shear center. The slope of this line is a measure of the shaft's torsional rigidity. The length of the shear center relative to the radius of the shaft is a measure of the bend-twist coupling.

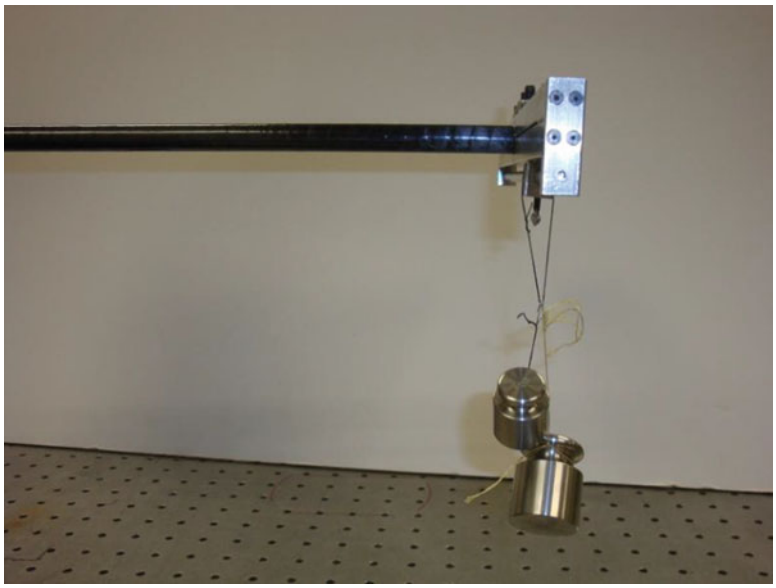

Fig. 15.6 The side view

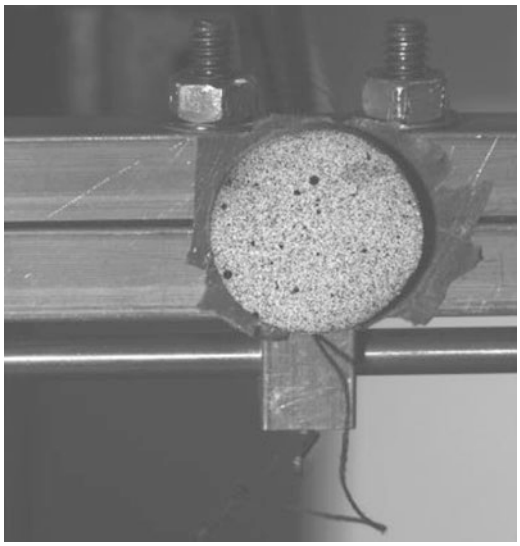

Fig. 15.7 The speckled disc used by the cameras to determine tip rotation and deflection

15.4 Digital Image Correlation

Care was taken during calibration because of the large amount of out of plane deflection that occurred during testing. Angles of rotations were calculated using an in-plane rotation calculator. The values for vertical deflection and rotation were constant across the speckled disc. To remove any noise, the values to be used in the final calculations were averaged over the speckled disc.

It should also be noted that the weight of the slide apparatus should have no measurable effect on the results. This is because the reference image is taken after the apparatus is attached but before the weight is hung. This causes a point load to be applied at the center of gravity of the apparatus which is through the geometric centroid of the beam cross section. Since this load is not applied through the shear center, it results in bending as well as twisting. The reference image is then taken after this initial deflection and rotation so that the effects of the apparatus can be ignored. In other words the principle of superposition is used to differentiate between the deflection and rotation caused by the weight of the apparatus itself from the deflection and rotation caused by the hanging weight. If the twisting were not a linear function of the bending then this assumption of superposition would not be valid. For these small deflections and rotations the linearity assumption is acceptable.

15.5 Finite Element Model

The finite element software ABAQUS was used to model the shaft under the same loading conditions. The shaft was modeled as an orthotropic shell element. What resulted was an accurate prediction of the shear center and a slight error in the predicted torsional rigidity. The most likely cause of this is using inaccurate material properties for the carbon fiber. There can be a large amount of variance in the E_1 and E_2 for carbon fiber sheets across various products. This ratio between E_1 and E_2 appears to have a large affect on the degree of bend-twist coupling as well as the flexural and torsional rigidities. This is the most likely explanation for why the shear center was predicted so well but the torsional rigidity was not.

The FEM model was important in determining the optimum fiber orientations to maximize the A_{16} term. A combination of Matlab, python scripts, and EXCEL were used to systematically explore the design space and determine the best design for the carbon fiber shaft to maximize the amount of bend-twist coupling while still maintaining certain acceptable levels of flexural and torsional rigidity. What quickly becomes apparent is that the optimum design is heavily determined by the relative E_1 and E_2, and since these can vary between carbon fiber products it becomes very important to accurately determine these properties before using the FEM model.

15.6 Closed-Form

A closed-form analytical solution of the bend-twist coupling is provided here as a third way to consider the results. The assumption is made that plane sections remain plane and that they remain normal to the tube axis. This should be accurate for the thin-walled and long tubes discussed here. The derivation assumes that the plate undergoes plane stress with no hoop stress such that:

$$\begin{Bmatrix} \varepsilon_{xx} \\ \gamma_{xs} \end{Bmatrix} = \begin{bmatrix} \frac{1}{E_x} & \frac{\eta_{xs,x}}{G_{xs}} \\ \frac{\eta_{x,xs}}{E_x} & \frac{1}{G_{xs}} \end{bmatrix} \begin{Bmatrix} \sigma_{xx} \\ \tau_{xs} \end{Bmatrix} \tag{15.2}$$

The $\eta_{xs,x}$ term is related to the A_{16} term discussed above. Ultimately the shear center is determined to be:

$$\frac{e_y}{L} = \frac{2\eta^{(1)}_{xs,x}}{\pi\left(1 + \left(\frac{8}{\pi^2} - 1\right)\eta^{(1)}_{x,xs}\eta^{(1)}_{xs,x}\right)} \tag{15.3}$$

15.7 Results

See Fig. 15.8.

15.8 Conclusion

A shear center that was 5.2 times the radius was achieved. Higher values could most likely be obtained if the lamina was altered in a way that increased bend-twist coupling at the expense of torsional and flexural rigidity. In Fig. 15.9 it is shown how the shear center changes sinusoidally as the beam is reclamped in the vice at 90° intervals. This is to be expected. In future tests the shaft can simply be oriented at 0° or 180° to achieve the maximum shear center and degree of bend-twist coupling.

More research needs to be done to see how the length of the beam affects the location of the shear center. Both FEA models and the closed-form equation indicate that the location of the shear center increases as the length of the beam increases. This length dependence differs from the isotropic version of shear center which is a sectional property.

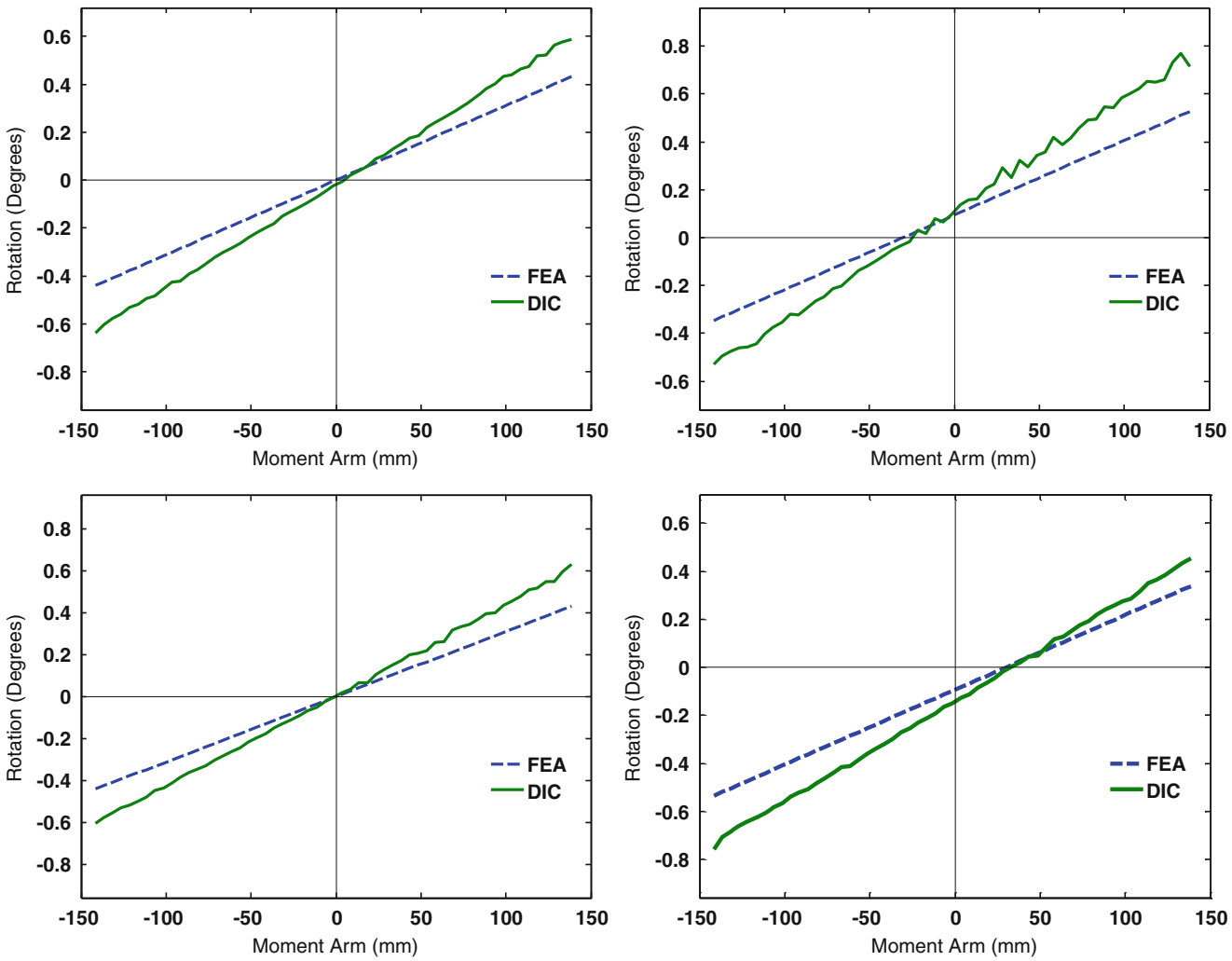

Fig. 15.8 From top left clock-wise 90°, 180°, 270°, and 0°. These compare the amount of in-plane rotation predicted by FEA to that measured during the experiment. The shear center is indicated by where the x-axis is crossed. Only the 180° and 270° orientations should have non-zero shear centers

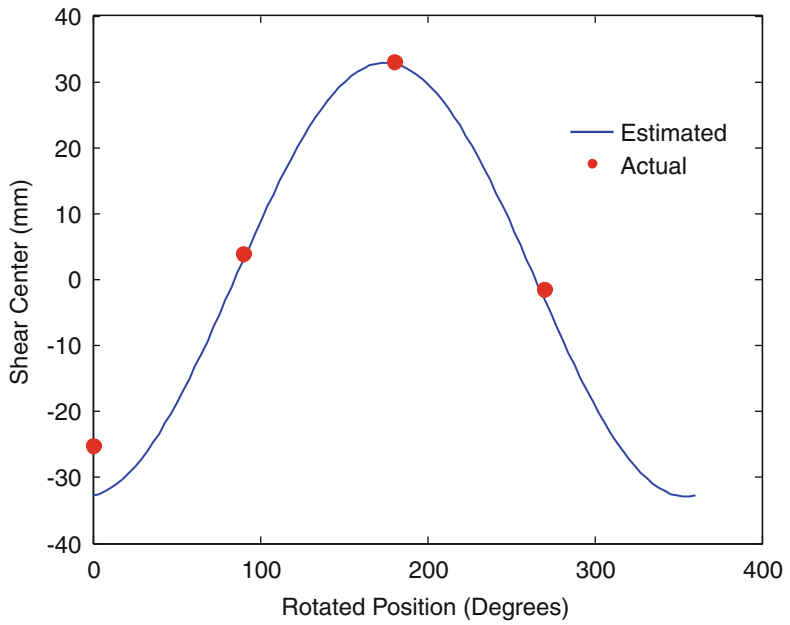

Fig. 15.9 The measured shear center for the four cases with a sinusoidal best fit

The slope discrepancy between the FEA predictions and those measured in DIC indicate that improvements in the modulus values are also required to acquire a better measure of torsional rigidity.

With the construction of a new mandrel that splits longitudinally more shafts can be constructed more easily. The research will proceed to new lamina designs. These new designs should offer new combinations of bend-twist coupling, flexural rigidity, and torsional rigidity. More shafts will allow for uncertainties in fabrication and testing to be better estimated and for greater verification of the FEA model and analytical equations.

References

1. Kosmatka JB (1992) Extension-bend-twist coupling behavior of nonhomogeneous anisotropicbeams with initial twist. AIAA J 30(2):519–527
2. Liu Z, Young YL (2009) Utilization of bend-twist coupling for performance enhancement of composite marine propellers. J Fluid Struct 25(6):1102–1116

Chapter 16
Processing and Opto-mechanical Characterization of Transparent Glass-Filled Epoxy Particulate Composites

Austin B. Branch and Hareesh V. Tippur

Abstract A transparent glass-filled epoxy composite was developed by matching the refractive index of the filler and the matrix. This material was processed at varying volume fractions (V_f) from 0 to 15 % of filler with transparency being maintained at each V_f. Initial investigation included quasi-static three-point bending to determine the critical SIF (K_{Icr}) values. Improvement over the neat epoxy was seen in each case with a maximum improvement of approximately 30 %. Furthermore, this material was observed to exhibit birefringent properties, thus making mechanical characterization through photoelastic methods feasible. The samples were loaded using a symmetric four-point bending set up and isochromatics were observed using a dark-field polariscope. The stress intensity factors for each sample were evaluated at various loads and compared to those determined analytically. Experimental measurements closely matched analytically determined ones, thus validating the use of this method. This *work-in-progress* includes investigating the fracture behavior of these composites under low and high strain rate conditions.

Keywords Optical transparency • Glass-filled epoxy • Photoelasticity • Fracture • High-strain rate loading

16.1 Introduction

Optically transparent materials have a wide range of applications in areas such as face shields, ground vehicle and aircraft windows, and bullet resistant enclosures. Glass, the standard material used for applications requiring transparency, is often deficient in providing low weight, high mechanical strength and toughness. Hence, the development of polymer-based transparent composites has the potential to offer complementary material systems for such applications at low cost.

Particulate composites are made transparent primarily through two methods. One method is to reduce the size of the reinforcement material below the wavelength of light. Practically, this process requires a composite with a very low volume fraction of reinforcement which may not allow for optimal strength and stiffness. Furthermore, agglomeration of nanofillers could be a potential difficulty to overcome. The other, more common method is to match the refractive indices of the constituents, namely transparent fillers with that of the matrix. This method also comes with its own difficulties. When matching indices of refraction to obtain transparency, the indices must be matched to approximately the third decimal place. The high precision required in index matching significantly limits the number of materials with which the matrix or the reinforcement constituent can be paired. Secondly, the transmittance of a composite is also dependent on filler volume fraction.

16.2 Material Processing

A transparent glass-filled epoxy composite was developed based on the principle of refractive index matching (Fig. 16.1). Rod shaped E-glass milled glass fibers were used as filler and were dispersed into a low viscosity epoxy system and cured at room temperature. Samples were processed with 0, 5, 10 and 15 % volume fraction (V_f) of filler. In Fig. 16.2, the logo was

A.B. Branch • H.V. Tippur (✉)
Department of Mechanical Engineering, Auburn University, Auburn, AL 36849, USA
e-mail: htippur@eng.auburn.edu

G. Tandon (ed.), *Composite, Hybrid, and Multifunctional Materials, Volume 4: Proceedings of the 2014 Annual Conference on Experimental and Applied Mechanics*, Conference Proceedings of the Society for Experimental Mechanics Series,
DOI 10.1007/978-3-319-06992-0_16,

Fig. 16.1 10% V_f glass-filled sample

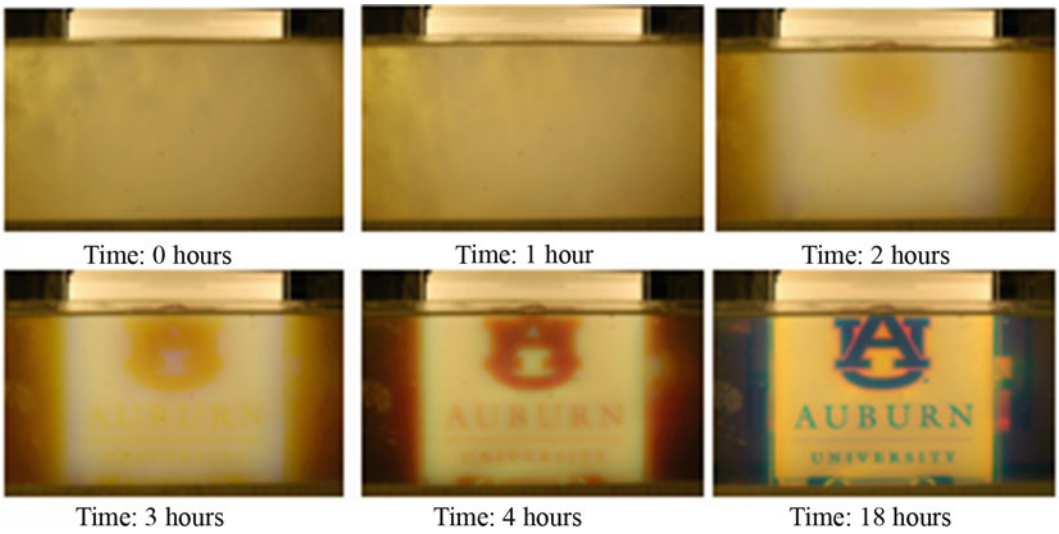

Fig. 16.2 Optical transparency evolution of glass-fiber epoxy composite (10 % V_f)

placed 4 in. behind a 6.5 mm thick 10 % V_f sample and the optical transparency evolution of the composite can be seen throughout the curing process. As epoxy cures, its refractive index begins to match with that of the glass fiber, resulting in a transparent composite.

16.3 Quasi-Static Crack-Initiation Toughness Investigation

In order to gain an initial understanding of this material's failure characteristics, quasi-static symmetric three-point bend fracture tests were performed to determine the crack-initiation toughness (K_{Icr}) of each sample compared to the neat epoxy. A schematic of the experimental setup can be seen below in Fig. 16.3.

The sheets of each V_f (0, 5, 10 and 15 %) were machined into specimens having the dimensions of 40 mm × 10 mm × 4.3 mm. Additionally, a notch of the length 2.5 mm was introduced at the mid-span of each specimen with a diamond impregnated circular saw and was then sharpened with a razor blade. Each specimen was loaded at a rate of 0.25 mm/min until fracture and the failure load (P_{max}) was recorded. The K_{Icr} values were computed using Eq. 16.1 and the results are shown below in Table 16.1:

$$K_{Icr} = \frac{\frac{P_{max}}{B\sqrt{W}}\left(3\frac{s}{W}\sqrt{\frac{a}{W}}\right)}{2\left(1+2\frac{a}{W}\right)\left(1-\frac{a}{W}\right)^{1.5}}\left[1.99-\frac{a}{W}\left(1-\frac{a}{W}\right)\left\{2.15-3.93\left(\frac{a}{W}\right)+2.7\left(\frac{a}{W}\right)^2\right\}\right] \tag{16.1}$$

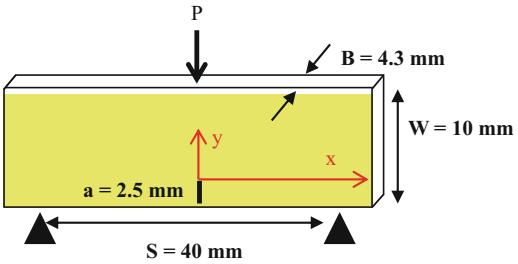

Fig. 16.3 Symmetric three-point bend fracture test schematic

Table 16.1 Crack-initiation toughness results

V_f (%)	K_{Icr} (MPa$\sqrt{m}$)	% Increase
0	2.24 ± 0.075	–
5	2.35 ± 0.017	4.9
10	2.87 ± 0.02	28.1
15	2.85 ± 0.01	27.2

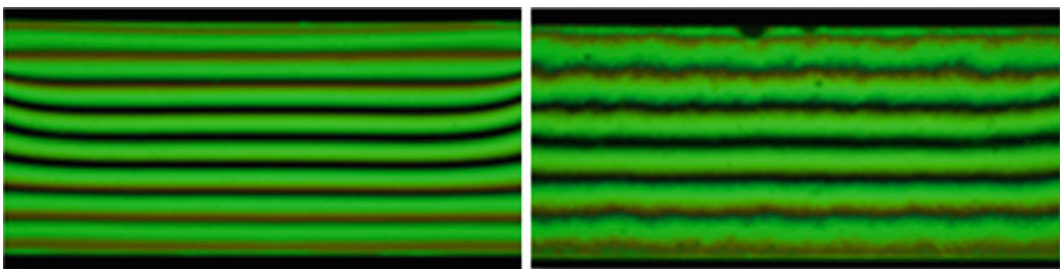

Fig. 16.4 Recorded fringes for 0 % (left) and 10 % (right) glass-filled epoxy

Table 16.2 Stress-optic constants

V_f (%)	F_σ (kN/m)
0	19.0 ± 0.3
5	22.9 ± 0.2
10	28.4 ± 0.4
15	38.5 ± 0.2

16.4 Opto-mechanical Characterization

Upon initial investigation of the samples, these transparent composites were found to exhibit birefringent properties, thus making it feasible to mechanically study the material using photoelasticity. First, the stress optic constant (F_σ) for each material composition was determined using a standard dark-field circular polariscope. Each sample was subjected to symmetric four-point bending and the resulting fringes were recorded using time-lapse photography. Shown in Fig. 16.4 are two typical fringes for a neat and 10 % V_f sample at a 600 N load within the pure bending zone of the specimen. By analyzing these isochromatics in cojunctions with the elementary beam theory, the stress-optic constant F_σ was determined for different glass-filled epoxies. The resulting F_σ values are shown in Table 16.2:

With the stress-optic constant of each material known, it was then possible to evaluate the fracture performance of these transparent composites. As a first step, edge cracked four-point bend samples were examined in a standard plane polariscope and isochromatics were recorded in the region of interest. An example of the same for 5 % V_f case, is shown in Fig. 16.5. Very good crack tip fringe discernibility is evident. To determine the K_I values, the classical Smith and Schroedl method [1] was used due to its simplicity. The measurements were examined relative to the boundary collocation results [2] and found to be very accurate as shown in Table 16.3:

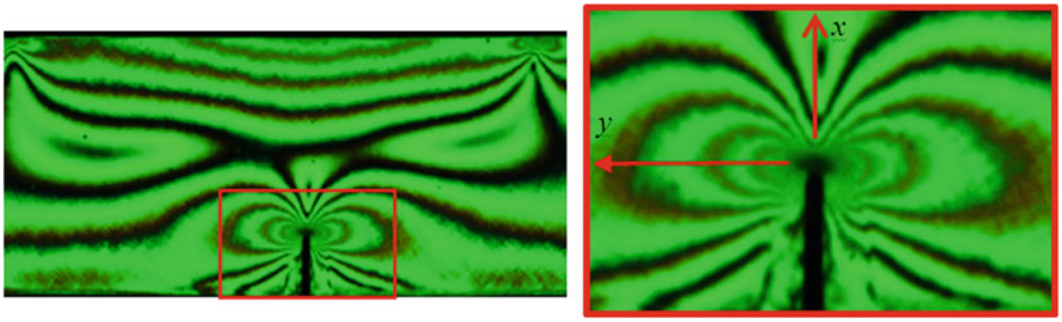

Fig. 16.5 Isochromatic fringes for 5 % V_f sample

Table 16.3 Measured K_I results and comparison with theory

Volume fraction (%)	Load[a] (N)	K_I experimental (MPa√m)	K_I theoretical (MPa√m)	% Difference
0	447	1.54	1.52	1.40
5	453	2.17	2.168	0.23
10	511	1.70	1.705	0.55
15	528	1.67	1.76	5.02

[a]*Note*: 5 % V_f sample was of different dimensions compared to the other samples, hence a different K_I value for a similar applied load value for 0, 10 and 15 %

16.5 Planned Work: Dynamic Photoelastic Investigation

Investigation of these material's properties under dynamic loading conditions is currently underway. Dynamic loading of the specimen will achieved through the use of a striker fired from a gas-gun impacting a long bar and creating a compressive stress wave which is then transmitted to the sample. A dark-field polariscope will be used to create isochromatic fringes. The fringe evolution during the loading process will be recorded using high-speed photography. These fringes will be analyzed to determine the stress intensity factor histories throughout loading to study the dynamic fracture characteristics of these novel transparent composites.

16.6 Summary

A method of processing optically transparent composites comprised of milled E-glass fibers dispersed in epoxy has been created. Static K_{Icr} values were determined using a symmetric three-point bend setup to gain an initial understanding the material properties. The resulting K_{Icr} values showed nearly a 30 % improvement in the 10 and 15 % samples compared to neat epoxy. Furthermore, the material exhibited good birefringent properties in the filler volume fraction range of 0–15 %. The experimentally determined stress intensity factors using 2D photoelasticity were found to be accurate when compared to the theoretical values. The work-in-progress includes investigating the fracture behavior of these composites under low and high strain rate conditions.

References

1. Dally JW, Riley WF (2005) Experimental stress analysis, 4th edn. College House Enterprises, Knoxville, TN
2. Tada H, Paris PC, Irwin GR (2000) The stress analysis of cracks handbook. ASME, New York

Chapter 17
Study of Influence of SiC and Al_2O_3 as Reinforcement Elements in Elastomeric Matrix Composites

D. Zaimova, E. Bayraktar, I. Miskioglu, D. Katundi, and N. Dishovsky

Abstract Rubber is an important polymer type that is widely used due to its high and reversible deformability. Since the modulus and strength of neat rubber are low, an additional reinforcing phase is necessary for the use of rubber materials in practical applications. Rubber is generally reinforced with fibers, carbon black (CB), and silicates. In our study we also use carbon black as filler reinforcement but in order to increase the mechanical properties even more we have added different particles (SiC and Al_2O_3) in rubber based composites. In the frame of the common research project, NR/BR based composites with different curing systems were characterized with respect to their curing characteristics and mechanical properties. The cure characteristics of the rubber compounds were studied by using the Monsanto MDR 2000 rheometer. Microindentation test was used for studying the viscoelastic behaviour of the compounds. Addition of different reinforcing particles can improve certain properties of rubber blends, such as stiffness, vulcanisation rate and crosslink density.

Keywords Elastomeric composite • Reinforcement • Silicon carbide • Alumina • Crosslink density

17.1 Introduction

Scrap tires can be utilized in a variety of engineering applications, especially as insulating material in the building market. In fact, European energy regulation actually considers a high standard of thermal protection in buildings with reasonable energy consumption hence lower operational costs [1]. Other most important areas such as aerospace and microelectronics industries have very high demand for high performance (ductile and high toughness) structural adhesive systems like epoxy and/or elastomer reinforced composites. Mainly for the microelectronics industry, the curing of such thermosetting systems have become the critical step of the whole production process [2, 3]. Although the rubber waste accounts only 2 % of the total amount of solid waste, increase in the production of scraps is turning it into an inclusive industrial waste problem. In Europe, the annual cost for management of waste rubber tires is estimated at €600 million. Today, "The World Rubber" Industry announces that countries of the European Union generate 3,300,000 tons of waste rubber tires per year. Additionally, the main component of these waste rubber tires is styrene–butadiene rubber (SBR) and, in spite of the different uses for recycling it, the research for new applications is still needed because of supply of waste rubber tires is increasing at a fast rate annually [4–6].

D. Zaimova (✉)
UCTM, University of Chemical Technology and Metallurgy, Sofia, Bulgaria

School of Mechanical and Manufacturing Engineering, Supmeca-Paris, Saint-Ouen, France
e-mail: diana.zaimova@gmail.com

E. Bayraktar (✉) • D. Katundi
School of Mechanical and Manufacturing Engineering, Supmeca-Paris, Saint-Ouen, France
e-mail: bayraktar@supmeca.fr

I. Miskioglu
ME-EM Department, Michigan Technological University, Houghton, MI, USA

N. Dishovsky
UCTM, University of Chemical Technology and Metallurgy, Sofia, Bulgaria

G. Tandon (ed.), *Composite, Hybrid, and Multifunctional Materials, Volume 4: Proceedings of the 2014 Annual Conference on Experimental and Applied Mechanics*, Conference Proceedings of the Society for Experimental Mechanics Series,
DOI 10.1007/978-3-319-06992-0_17,

In recent years, the rubber waste was used mainly in asphalt roads, in asphalt–concrete mixtures, floor mats as an aggregate replacement. The rubber for tire manufacturing must have high elasticity and frictional properties as well as the high load bearing capacity. Additionally, these materials are commonly used for long term applications at ambient or at moderately elevated temperatures. Potentially e service life of these materials can be improved by creating new elastomeric based composites by changing their traditional composition. Conforming to these needs, elastomers (rubbers) should be used by simple processing with various materials under different conditions by addition of new alloying elements [7–11]. This paper is an attempt to address to formulate waste elastomers (SBR-rubbers) composites with different proportions of filler particles and epoxy resin reinforcements by using of the simple curing methods. For this reason, physical–thermal–mechanical properties of cured samples should be evaluated and analyzed in order to improve the resistance of these types of composites. Naturally, the main objective of our current research is to determine the ductility and toughness of waste elastomer (SBR rubber) matrix composites containing SiC, B, Al_2O_3, and glass powder as reinforcements. This paper contains partial preliminary experimental results of the research project for French aeronautic industry going on at LISMMA-Paris. As the first stage preliminary study, certain dynamic and static properties, scratch test, hardness—Shore-A, thermal analysis, DMTA, microindentation, etc.) were investigated. Scanning electron microscopy (SEM) was used to study the microstructure of these composites.

17.2 Experimental Conditions

In this study, very fine waste elastomer (SBR-rubber) powder was used as a matrix reinforced with SiC, B, Al_2O_3, fine epoxy and glass powder. All the composites were fabricated by mixing for 4 h and then placed in an ultrasonic dispersion for 1 h. The specimens were then manufactured by hot mounting of the powder compositions under 20 kN pressure at a temperature of 180 ºC for 10 and 15 min heating time after which there was 15 min of cooling time. Four compounds were designed and identified according to their composition and heating times (SiC-10, B-10 and SiC-15, B-15). The specimens were post-cured in an isothermal oven for 24 h at 80 ºC. The general compositions of the specimens are given in Table 17.1.

The hardness of each specimen using—"Shore A" scale were measured per ASTM D 2240-05 Five measurements were taken for each specimen and averaged. The load was applied for 60 s per measurement Some of the specimens were subjected to a special aging process over 40 days by exposure to ultra-violet radiation at a temperature of 50 °C (UV lamps with 365 nm wavelength). This test was done according to ASTM D750-06.

Elastoplastic behaviour of the composites was studied with a CSM Micro-Indentation Tester. Nine tests were performed with a Vickers diamond indenter for each composition and then averaged. The samples' thickness was approximately 5 mm. The maximum indentation load (F_{max}) was 250 mN, the load–unload rate was 500 mN/min. The load was held at maximum for 50 s. The indentation hardness (H_{IT}), indentation modulus (E_{IT}) and Vickers hardness (HV) were determined by using the Oliver and Pharr method [12, 13].

Dynamic Mechanical Thermal Analysis (DMTA) was carried out on the Dynamic Mechanical Analyzer MK III system (Rheometric Scientific). As a mode of deformation, single cantilever beam was used at a heating rate of 2 °C/min, a frequency of 5 Hz and deformation 64 μm in the temperature range from –80 to 80 °C.

Scratch tests have been carried out on two basic compositions by using a LISMMA-Paris Micro-Scratch Tester with a Vickers diamond indenter. Test conditions were set as 240 g normal load at a frequency of 10 Hz for 5,000, 10,000 and 15,000 cycles. Tangential and normal forces were recorded by the software of LISMMA during the test from which hence coefficient of friction could be determined. After the test, damaged zone were investigated by a 3D optical roughnessmeter to characterize damage occurred during the scratch test.

Table 17.1 Composition of the waste elastomeric based composite compounds

	Components (wt %)					
Composition	Rubber	Al_2O_3	SiC	Epoxy	Boron	Glass powder
SiC-10	100	20	5	25	–	5
SiC-15	100	20	5	25	–	5
B-10	100	20	5	25	2	5
B-15	100	20	5	25	2	5

17.3 Results and Discussion

17.3.1 Dynamic Mechanical Thermal Analysis (DMTA)

The storage modulus (E′) and loss factor (Tan Delta) for all the compounds were studied in the temperature interval from −80 to +80 °C. In general way, there were no significant differences in the range –80 to –40 °C in the storage modulus (E′) and the loss factor (Tan Delta) (Fig. 17.1) between the four compounds. The graphs for the compounds SiC-10 and SiC-15 are presented because the response of SiC-10 was observed to be slightly higher than SiC-15. The decrease of storage modulus (E′) with the increasing temperature, in other words, the transition from the glassy to the high elastic state occurs at about –25 °C. In the interval from –40 to –80 °C, the increase in storage modulus (E′) can be attributed to the limited mobility of rubber molecules. Both of the curves presented for (E′) in Fig. 17.1 are similar meaning the reinforcing effect of the filler is the same for all four compounds (considering all of the compounds tested here).

The loss factor is the ratio between the dynamic loss modulus (E″) and the dynamic storage modulus (E′) (Tan Delta = E″/E′). It represents the mobility of the molecular chains and polymer's phase transitions. It is accepted that the higher the Tan Delta is the greater the mechanical losses; these losses are related to higher energy input required for the motion of the molecular chains of the polymer as the glass transition is being approached [3, 14–16]. The peak of the Tan Delta versus temperature curve can be used to identify the T_g of the rubber based composite materials.

It is observed that T_g of the studied compounds does not change considerably (within the limits of 3–4 °C). The magnitude of the peak is also almost the same. The results for Tan Delta suggest that despite the difference in crosslink density and the different vulcanization mechanism the interactions between rubber–rubber and rubber–filler are similar for all the compounds.

17.3.2 Microindentation Analysis

The microindentation test is a relatively simple tool with which valuable information about the morphology and mechanical properties of polymeric materials can be obtained. The indentation method has been also successfully employed to investigate the glass transition temperature of polymers [17]. It has proved to be a helpful tool for micromechanical and microstructural investigation of polymers [18, 19]. Microindentation differs from classical measurement of hardness, where the impressions are generated and then imaged with a microscope. Load and associated penetration depths are recorded simultaneously during both loading and unloading stages A typical load–displacement diagram and the microindenter used in this research are shown in Fig. 17.2.

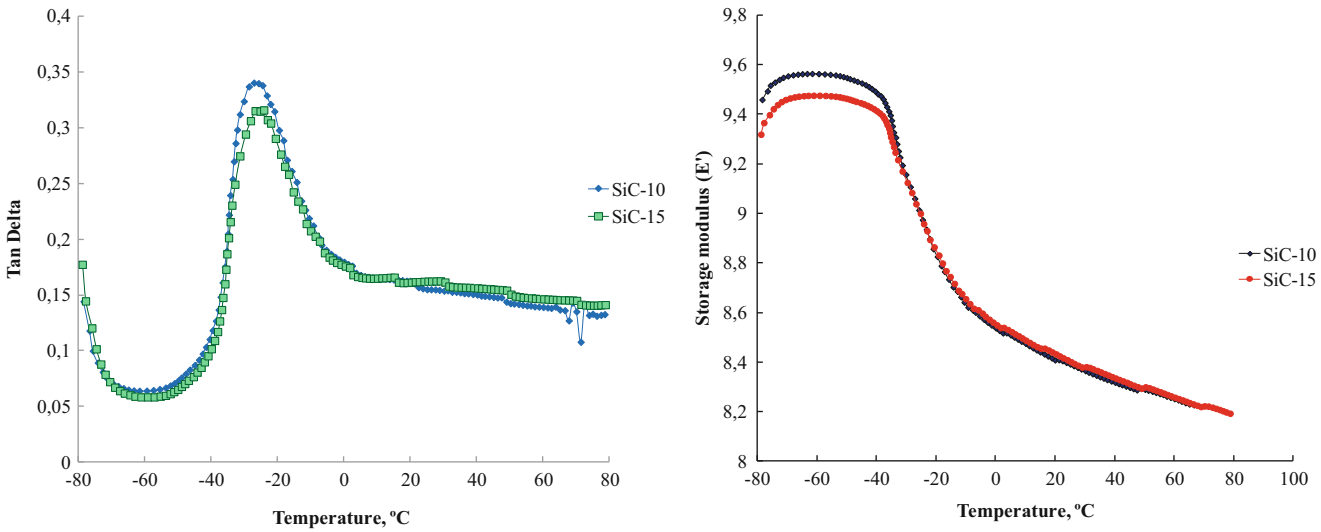

Fig. 17.1 Tan Delta (*left*) and storage modulus (*right*) as a function of the temperature for the compounds SiC-10 and SiC-15 under normal conditions

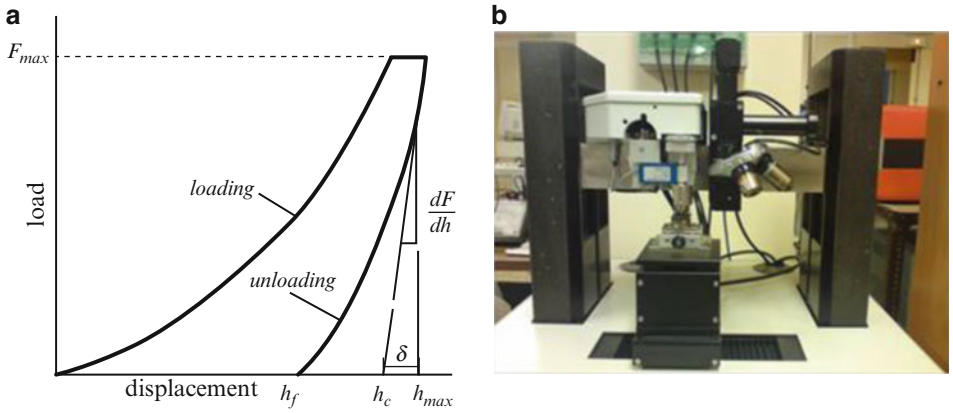

Fig. 17.2 Schematic representation of the force–depth curve for micro indentation procedure (**a**) and measurement device (**b**)

The Oliver and Pharr method (Power Law method) [12] recognizes the fact that the first portion of unloading curve may not be linear, and can be described by a simple power law relationship as follows:

$$F = k\left(h - h_p\right)^m \tag{17.1}$$

where k is a constant and m is an exponent which depends on indenter geometry. A power law function is used to describe the upper part of the unloading data.

$$F = F_{max}\left(\frac{h - h_p}{h_m - h_p}\right)^m \tag{17.2}$$

where the constants m and h_p are determined by a least of square fitting procedure. The contact stiffness $S = (1/C)$ is given by the derivative at peak load:

$$S = \left(\frac{dF}{dh}\right)_{max} = mF_{max}\left[\frac{\left(h_m - h_p\right)^{m-1}}{\left(h_m - h_p\right)^m}\right] = mF_{max}\left(h_m - h_p\right)^{-1} \tag{17.3}$$

and the tangent depth, h_r, is thus given by:

$$h_r = h_m - \frac{F_{max}}{S} \tag{17.4}$$

The contact depth, h_c, is then:

$$h_c = h_m - \varepsilon(h_m - h_r) \tag{17.5}$$

where ε now depends on the power law exponent m.

The tangent is found by differentiating the unloading curve and evaluating at maximum load (F_{max}). The intercept of this tangent with the displacement axis yields h_r. Four compositions (SiC-10/15 and B-10/15) based on waste rubber matrix reinforced essentially with SiC, B, Al_2O_3, fine epoxy resin powder and glass powder, were investigated by microindentation test. As indicated in former section, all of the parameters such as the indentation hardness (H_{IT}), indentation modulus (E_{IT}) and Stiffness (S) were determined by using the Oliver and Pharr method transformed in the following relations:

$$A_p = f(h) \tag{17.6}$$

where A_p is projected contact area

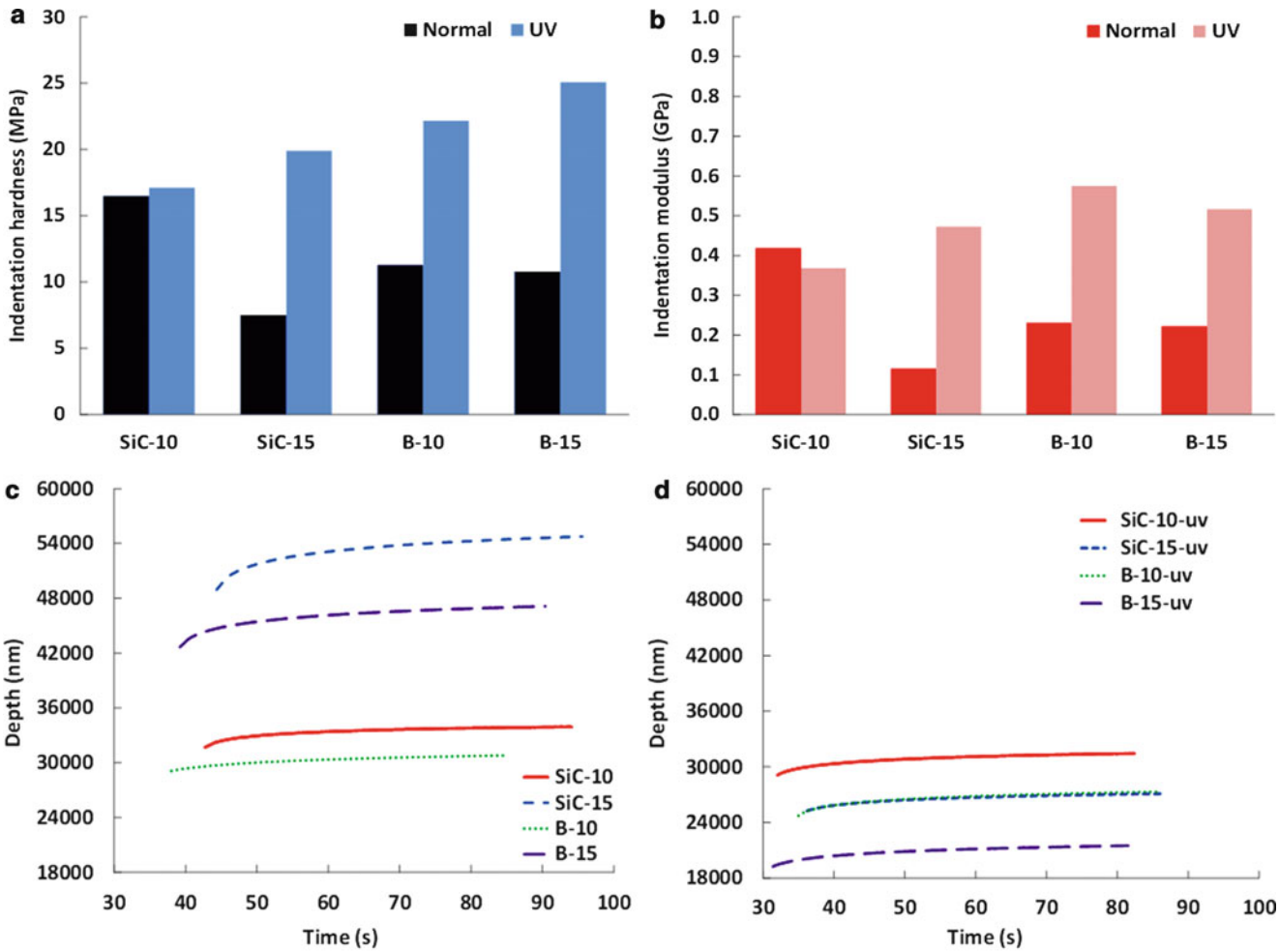

Fig. 17.3 (**a**) Comparison of indentation hardness (H_{IT}), (**b**) comparison of indentation modulus (E_{IT}), (**c**) comparison of microindentation depth at maximum load as a function of time for the compound treated under normal conditions and (**d**) UV aged treated specimens

$$\boldsymbol{H_{IT}} = \frac{F_{max}}{A_p(h_c)} \quad \text{and} \tag{17.7}$$

$$\boldsymbol{E_{IT}} = \frac{1-\nu_s^2}{\dfrac{1}{E_r} - \dfrac{1-\nu_i^2}{E_i}} \quad \text{and also} \tag{17.8}$$

$$\boldsymbol{E_r} = \frac{\sqrt{\pi}S}{2\beta\sqrt{A_p(h_c)}} \tag{17.9}$$

In this test, indenter and sample characteristic were defined as E_i—elastic modulus of the indenter (1,141GPa) with ν_i—Poisson's ratio of the indenter (0.07); E_r—reduced modulus of the indentation contact; ν_s—Poisson's ratio of the sample (0.35).

The results for the indentation hardness, modulus and variation of indentation depth at maximum load for the normal and UV aged specimens with time of the four compositions are presented in Fig. 17.3. Fig. 17.3a, b show that longer heating time during the manufacture of the specimens resulted in a decrease in both modulus and hardness for the SiC specimens but had no effect on the B specimens (Fig. 17.3a, b). The effect of UV aging is also clear that all four compounds exhibited higher hardness and modulus after aging. Also, Fig. 17.3c, d show that the deformation response of the UV aged specimens is much less than the normal specimens which is consistent with the modulus and hardness results.

Fig. 17.4 Scratch test measurement system designed by LISMMA

The viscoelastic properties of polymers are markedly dependent on the type of crosslinks, the degree of crosslinking and interaction between matrix and fillers. Crosslinking can raise the glass-transition temperature (T_g) of a polymer by introducing constraints on the molecular motions of the polymer chains. Low degrees of crosslinking in normal vulcanized rubbers act in a similar way to entanglements and raise the T_g only slightly above that of the crosslinked polymer. Sulphur also have a large influence on the viscoelastic properties. In this paper, we have compared all of the waste elastomeric based composite specimens reinforced with filler particles and epoxy resin designed here by testing extensively using micro indentation and compared to evaluate the viscoelastic behaviour of these composites (Fig. 17.3a–d).

When the viscoelastic behaviour of these four compounds is compared, Fig. 17.3c depicts that samples with compounds "SiC-10" and "B-10" have higher resistance to viscoelastic deformation than the two other compounds due to improved chain mobility (moderately due to subdivision and more relaxation after loading) under normal conditions. As for the UV treated specimens, all compounds exhibited less deformation than the normal specimens, however the ranking of the compounds with respect to deformation changed, i.e., for normal specimens, SiC-15 deformed the most, for UV treated largest deformation was observed in SiC-10. Interestingly, UV treated SiC-15 deformed the least.

After UV aging three of the compounds (SiC-15, B-10, B-15) have shown a moderate improvement in both of the mechanical properties measured [16, 20] as well as the resistance to viscoelastic deformation. These results are partially supported by supplementary "Hardness – Shore-A" tests that are not reported in this paper due to the confidentiality agreement with our industrial partners. Similar researches have also been reported in literature [2, 3, 13, 16, 21, 22]. Additional tests will be carried out in the frame of the research project going on and they will be used for modelling the viscoelastic behaviour of the elastomeric composites.

17.3.3 Damage Analysis by Means of Scratch Test and 3D Optical Roughness Meter

Scratch tests results give a basic idea on the tribological behaviour of the waste elastomer based composites designed in the current research. After the scratch test, damage zone was investigated by a 3D optical roughnessmeter to assess damage in terms of, scratch depth, average scratch roughness. Figure 17.4 shows scratch test system designed by LISMMA-Paris. All of the data discussed here are controlled with special scratch test software-LISMMA.

In the scratch test the contact between the slipping diamond indenter and the surface of the composite material during scratch test is analyzed. The normal and tangential forces on indenter are recorded and the tangential stress on the surface and the interfacial stresses can be obtained. Further detailed results and discussion of the scratch test with Finite Element Analysis (FEM) will be published in an upcoming paper [16].

In reality, because of the high shear stress at the interfaces the interfacial shear stress may be the main reason for damage of the matrix and reinforced filler interfaces [2, 21]. As well known, when the indenter is slipping, tangential tensile stress is caused on the surface behind the indenter, while in front of the indenter the tangential stress is compressive.

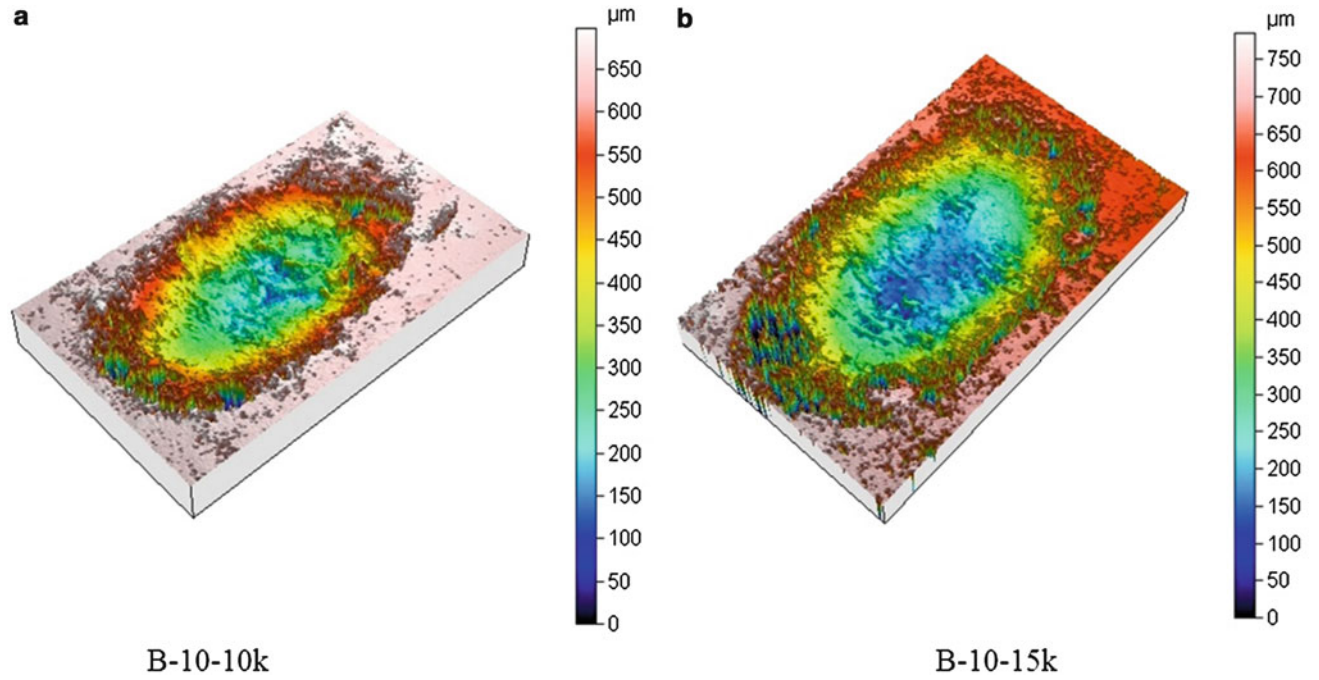

Fig. 17.5 (**a**) Damage traces obtained in the direction of width and length for the specimen B-10 for 10,000 cycles, and (**b**) for 15,000 cycles

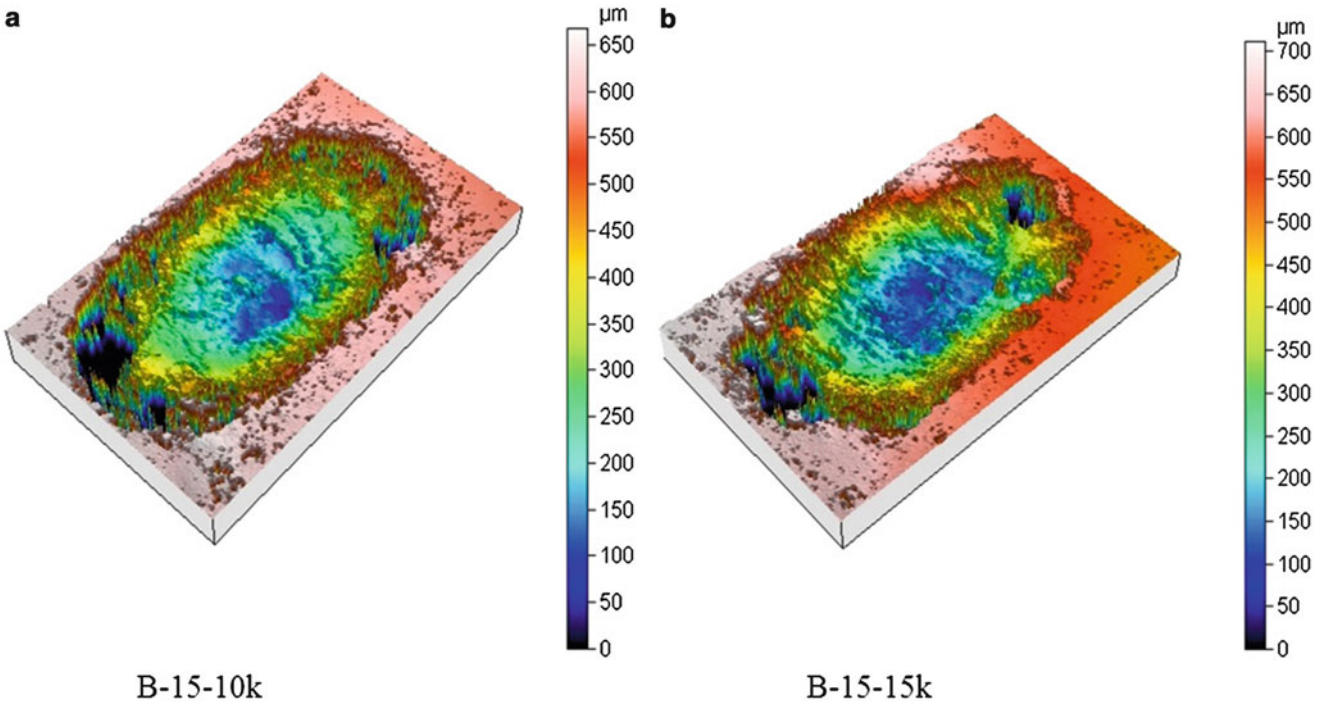

Fig. 17.6 (**a**) Damage traces obtained in the direction of width and length for the specimen B-15 for 10,000 cycles, and (**b**) for 15,000 cycles

In the frame of the current research, the resistance to scratch deformation (damage) is evaluated in terms of scratch depth, and average scratch roughness subsequent to scratching. A 3D optical roughnessmeter was used to identify the damage zone subsequent to scratching carried out with the test conditions set as 240 g normal load at10 Hz 5,000, 10,000 and 15,000 cycles.

To simplify the evaluation, only two test conditions (10,000 and 15,000 number of cycles for all of the composition are presented here. Figures 17.5, 17.6, 17.7, and 17.8 depict scratch damaged zone and characteristic parameters obtained by 3D optical roughnessmeter after the test conditions carried up to 10,000 and 15,000 number of cycles respectively.

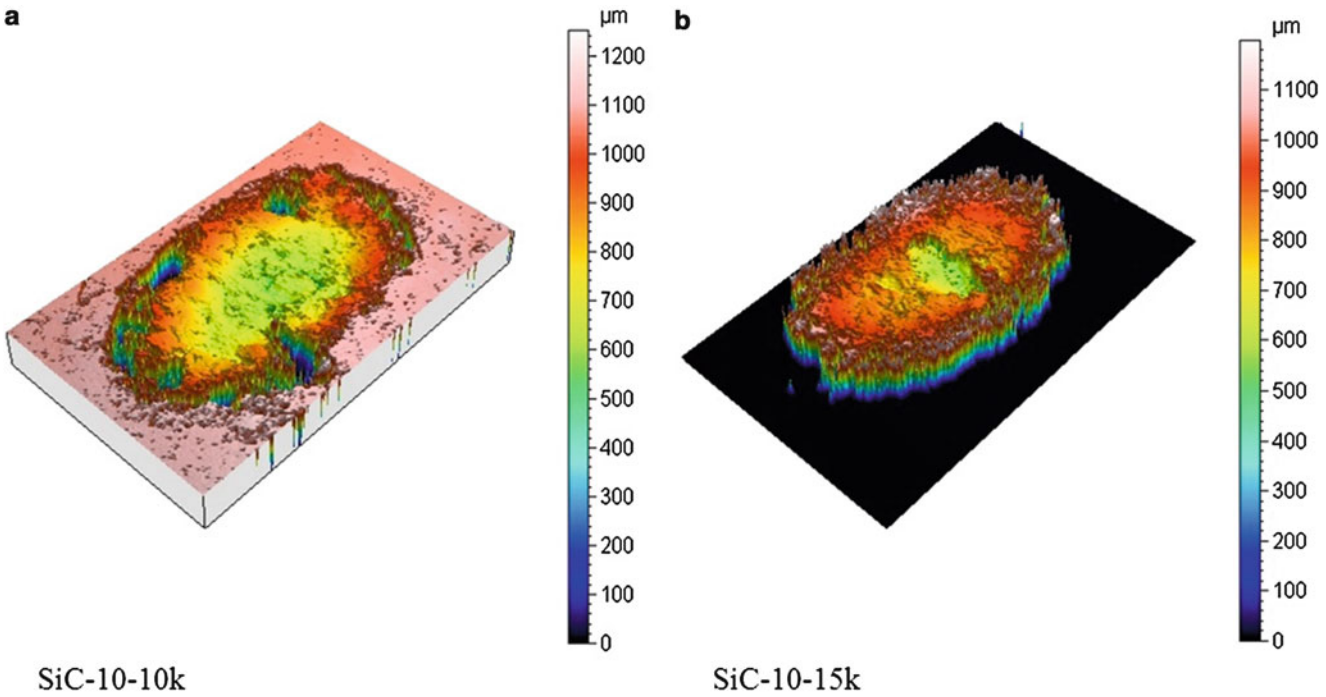

Fig. 17.7 (**a**) Damage traces obtained in the direction of width and length for the specimen SiC-10 for 10,000 cycles, and (**b**) for 15,000 cycles

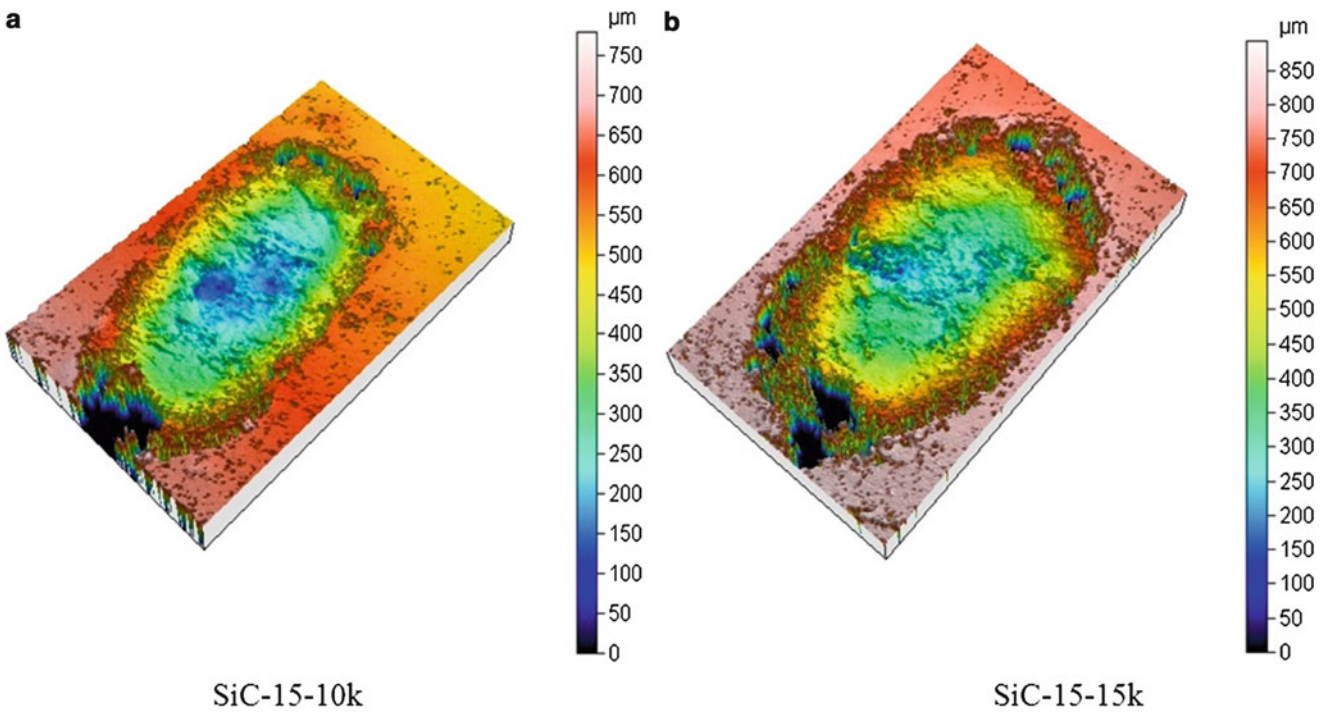

Fig. 17.8 (**a**) Damage traces obtained in the direction of width and length for the specimen SiC-15 for 10,000 cycles, and (**b**) for 15,000 cycles

Additionally, the filler particle size at a constant weight fraction has a significant influence on the scratch resistance of the composites. This is also confirmed with micro indentation tests. It means that certain fillers play an important role for the scratch resistance that they were used as reinforcement elements here (the size of Al_2O_3 was under the 1 μm, Boron, 2 μm, SiC 2 μm and waste rubber powder used as a matrix was variable between 5 and 10 μm and also fine glass powder was added

Table 17.2 Friction coefficient after scratch test carried for the designed compositions

Number of cycles	SiC-10	SiC-15	B-10	B-15
5 k (5,000)	074	0.71	0.94	0.94
10 k (10,000)	0.81	0.80	0.90	0.87
15 k (15,000)	0.76	0.90	0.84	0.88

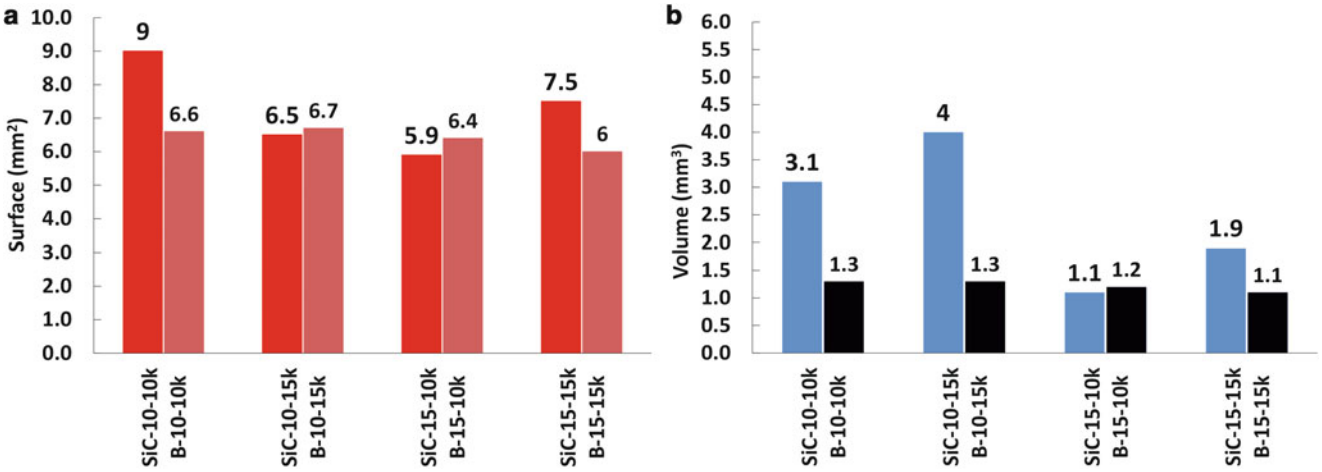

Fig. 17.9 (**a**) Volume, (**b**) surface of the damage trace after scratch calculated from roughness test results for all compounds for certain number of cycles

with a powder diameter was ~1 μm). Most probably, here Al_2O_3 and SiC can play fulfillment scratch resistance. For additional information, coefficient of friction for each compound determined after the scratch test were summarized in Table 17.2. The scratch test conditions reveal that the compositions heated 15 min during molding and compacting have shown higher increment in the scratch resistance values when compared to the other composition heated 10 min during molding and compacting.

In Fig. 17.9 the volume and surface of the damage trace after scratch calculated from roughness test results are given. It is hard to find relation between the composition and compacting conditions concerning the surface of the damage trace. However, based on Fig. 17.9a, it seems that addition of boron to the compound resulted in less damage. Also, for the same compound, samples with increased heating time exhibited less damage. In addition the number of cycles doesn't play a role for any of the four compounds (SiC-10, SiC-15, B-10, B-15) concerning volume and surface of the damage trace.

As indicated in the former section, these results are only preliminary results of the actual research project that is going on. For final and detail evaluation, more comprehensive study and more intensive experimental test should be carried out.

17.4 Conclusion

The preliminary results of the current research show that damage of waste elastomeric matrix composites reinforced with epoxy and fine filler particles can be used in front door applications considerably by adding fine filler-size reinforcements (Al_2O_3, SiC, etc.). They can increase the modulus, but can decrease the strain-to-failure. However, the role of the fine waste rubber powder satisfies the toughness characteristics.

Under test conditions given here, the specimens produced from four compounds have shown more reliable results at some levels of loading results in a tougher composite than the traditional elastomeric based composites (less damage by UV aging and scratch resistance). In detail evaluation with the elastic indentation load–depth model at the maximum indentation load describes the indentation depth versus time curves quite well for the four compounds reinforced with particles of waste elastomeric based composites.

Based on the material processing, mechanical characteristics and viscoelastic behaviour, optimum composition between these four compounds after that an optimistic choice will be useful to classify according to different properties for different industrial applications for a detail suggestion after final results of the actual research project.

References

1. The European Parliament and the Council of the European Union. Council Directive of 2002/91/EC: the energy performance of buildings, issued in 2012
2. Ouali N, Oppici A-C (2012) Elastomer toughend epoxy based composites. AMPT-Wollonong-Sydney, NSW-Austraila
3. Zaimova D, Bayraktar E, Katundi D, Dishovsky N (2012) Elastomeric matrix composites: effect of processing conditions on the physical, mechanical and viscoelastic properties. JAMME 50(2):81–91
4. Papadopoulos AM (2005) State of the art in thermal insulation materials and aims for future developments. Energy Build 37:77–86
5. Turgut P, Yesilata B (2008) Physico-mechanical and thermal performances of newly developed rubber-added bricks. Energy Build 40:679–688
6. Kaynak C, Sipahi-Saglam E, Akovali G (2001) A fractographic study on toughening of epoxy resin using ground tyre rubber. Polymer 42:4393–4399
7. Yesilata B, Turgut P (2007) A simple dynamic measurement technique for comparing thermal insulation performances of anisotropic building materials. Energy Build 39:1027–1034
8. Bessri K, Montembault F, Bayraktar E, Bathias C (2010) Understanding of mechanical behaviour and damage mechanism in elastomers using X-ray computed tomography at several scales. IJTS 14:29–40
9. Bayraktar E, Antholovich S, Bathias C (2006) Multiscale observation of fatigue behaviour of elastomeric matrix and metal matrix composites by X-ray tomography. IJF 28:1322–1333
10. Bayraktar E, Isac N, Bessri K, Bathias C (2008) Damage mechanisms in natural (NR) and synthetic rubber (SBR): nucleation, growth and instability of the cavitations. IJFSM 31(1):1–13
11. Luong R, Isac N, Bayraktar E (2007) Damage initiation mechanisms of rubber. JAMME 28(1):19–26
12. Oliver WC, Pharr GM (1992) An improved technique for determining hardness and elastic modulus using load and displacement sensing indentation experiments. J Mater Res 7:1564–1583
13. Ania F, Martinez-Salazar J, Baltar' Calleja FJ (1989) Microindentation tests in materials. J Mater Sci 24:2934–2939
14. Zaimova D, Bayraktar E, Dishovsky N (2011) State of cure evaluation by different experimental methods in thick rubber parts. JAMME 44 (1):161–167
15. Botelho DS, Bayraktar E (2009) Experimental and numerical study of damage initiation mechanism in elastomeric composites-double cantilever beam specimens-DCB. JAMME 36(1):65–71
16. Zaimova D, Bayraktar E, Katundi D, Dishovsky N (2012) Damage analysis of elastomeric based composites. AMPT-Wollonong-Sydney, NSW-Austraila
17. Hamed GR, Al-Sheneper AA (2003) Effect of carbon black concentration on cut growth in NR vulcanizates. Rubber Chem Technol 76:436–460
18. Kohl JG, Singer IL (1999) Pull-off behavior of epoxy bonded to silicone duplex coatings. Prog Org Coat 36:15–20
19. Brady RF, Singer IL (2000) Mechanical factors favoring release from fouling release coatings. Biofouling 15:73–82
20. Bhowmick AK, White JR (2002) Thermal, UV- and sunlight ageing of thermoplastic elastomeric natural rubber–polyethylene blends. J Mater Sci 37(23):5141–5151
21. Dasari A, Misra RDK, Rohrmann J (2004) Scratch deformation characteristics of micrometric wollastonite-reinforced ethylene–propylene copolymer composites. Polym Eng Sci 44(9):1738–1748
22. Nasrat LS (2007) An investigation into the electrical properties of rubber blends. In: Electrical insulation conference and electrical manufacturing expo, 22–24 Oct 2007, Nashville, pp 146–149

Chapter 18
Manufacturing of New Elastomeric Composites: Mechanical Properties, Chemical and Physical Analysis

D. Zaimova, E. Bayraktar, I. Miskioglu, D. Katundi, and N. Dishovsky

Abstract Filler-reinforced vulcanized rubber and its blends are frequently used for engineering applications for over a century. Traditional applications include tires, seals, bushings, and engine mounts. The rubbers for tire manufacturing must have high elasticity and frictional properties as well as the high load bearing capacity. Conforming to these needs, rubbers are vulcanized by various materials such as sulphur, carbon black, accelerators, and retardants in different conditions. The reactivity of sulphur vulcanization and physical properties of the final product are affected by the chemical structure, molecular weight, and conformation of the base elastomers. The aim of this study is to investigate the influence of accelerator-vulcanizing agent system and the vulcanization temperature on the mechanical and aging properties of vulcanizates based on Natural rubber/Polybutadiene rubber (NR/BR) compounds. This preliminary study will allow optimizing the composition for improving the mechanical properties and understanding the damage behavior.

NR/BR based composites with different vulcanization temperatures and curing systems were characterized. The mechanical properties investigated were tensile strength, elongation at break, tensile modulus at 100 % (M_{100}) and at 300 % (M_{300}) deformation. Hardness (Shore A) and molecular mass of the samples were also determined. Scanning electron microscopy was used to study the microstructure of the fracture surfaces.

Keywords Elastomer composites • Mechanical properties • Chemical–physical analysis • SEM study

18.1 Introduction

Filler-reinforced vulcanized rubber and its blends are frequently-used for engineering applications for over a century [1]. Traditional applications include tires, seals, bushings, and engine mounts. The rubbers for tire manufacturing must have high elasticity and frictional properties as well as high load bearing capacity. Conforming to these needs, rubbers are vulcanized by various materials such as sulphur, carbon black, accelerators, and retardants in different conditions. The reactivity of sulphur vulcanization and physical properties of the final product are affected by the chemical structure, molecular weight, and conformation of the base elastomers [2].

The sulphur vulcanization with unsaturated rubbers occurs through complicated radical substitution in the form of mono-, di-, or polysulphide bridges and sulphur containing intracyclization of the polymer molecules. The cross-link density and

D. Zaimova (✉)
UCTM, University of Chemical Technology and Metallurgy, Sofia, Bulgaria

School of Mechanical and Manufacturing Engineering, Supmeca-Paris, Saint-Ouen, France
e-mail: diana.zaimova@gmail.com

E. Bayraktar (✉) • D. Katundi
School of Mechanical and Manufacturing Engineering, Supmeca-Paris, Saint-Ouen, France
e-mail: bayraktar@supmeca.fr

I. Miskioglu
ME-EM Department, Michigan Technological University, Houghton, MI, USA

N. Dishovsky
UCTM, University of Chemical Technology and Metallurgy, Sofia, Bulgaria

G. Tandon (ed.), *Composite, Hybrid, and Multifunctional Materials, Volume 4: Proceedings of the 2014 Annual Conference on Experimental and Applied Mechanics*, Conference Proceedings of the Society for Experimental Mechanics Series,
DOI 10.1007/978-3-319-06992-0_18,

distribution affect the physical properties and stability of rubber on aging. They depend not only on type and ratio of accelerator to sulphur, but also on the reaction temperature and time [3]. The vulcanization rate of rubber is closely related to the productivity of tire manufacture, and it is desirable to increase the rate by raising temperature. However, at higher temperature, the sulphur cross-links are less effective and the physical properties are sacrificed due to dissociation of sulphur bonds and rubber chains [4]. The vulcanization reactivity may be controlled by additional amounts of sulphur and accelerator instead of increasing temperature. Although the addition of sulphur increases cross-link density and ratio of polysulphide linkage, it may decrease the stability, especially on aging [5].

By increasing the accelerators, the effectiveness of sulphur vulcanization with mono- and disulphide linkage is improved to give stability on aging, but dynamic properties may degrade [6]. The optimum conditions must be chosen to obtain the best properties for products and productivity. For this reason the aim of this study is to investigate the influence of accelerator-vulcanizing agent system and the vulcanization temperature on the mechanical and aging properties of vulcanizates based on Natural rubber/Polybutadiene rubber (NR/BR) compounds.

The present study will allow optimizing the composition for improving the mechanical properties and understanding the damage behavior. NR/BR based composites with different vulcanization temperatures and curing systems were characterized with respect to their curing characteristics (for 140 and 160 °C) and mechanical properties. The cure characteristics of the rubber compounds were studied by using the Monsanto MDR 2000 rheometer. The mechanical properties investigated were tensile strength, elongation at break, tensile modulus at 100 % (M_{100}) and at 300 % (M_{300}) deformation. The hardness (Shore A) and molecular mass of the samples were also determined. Scanning electron microscopy was used to study the microstructure of the fracture surfaces. In this paper partial results of the applied project supported by French-Bulgarian research cooperation are presented. The exact composition of the blends used in this study is proprietary, hence will not be discussed in this paper.

18.2 Experimental Conditions

The two compounds were mixed in laboratory using two rolling mixer. The moulding conditions were determined from torque data using moving die rheometer MDR 2000 (Alpha Technologies) for temperatures 140 and 160 °C. At the end, four compounds (A, B, C, D) based on sulphur vulcanized.

Natural rubber/Polybutadiene rubber blends were prepared containing certain fillers and/or reinforcements in order to investigate their deformation behaviour. Two ratios of accelerator to sulphur were used for preparation of the compounds also known as conventional vulcanization system (CV), where the quantity of sulphur is more and efficient vulcanization system (EV), where the quantity of accelerator is more. Compounds A and B are vulcanized using conventional vulcanization system (CV) and vulcanization temperatures 140 °C and 160 °C respectively. Compounds C and D are vulcanized using efficient vulcanization system (EV) respectively at 140 °C and 160 °C.

Cured sheets were prepared by compression moulding. The moulding took place at 140 and 160 °C and pressure 100 kg/cm^2. The behaviour of these compounds in detrimental environmental conditions was tested by means of swelling experiments that all of the swelling tests were carried out with the molded samples soaking them in toluene at room temperature. After these tests, the crosslink densities for each compound were calculated according to the molecular mass between two crosslinks. All of the crosslink densities were calculated according to Fory–Rehner relation [7]:

$$\frac{1}{2M_c} = \frac{1}{2\rho V_0}\left[\frac{ln(1-V_r)+V_r+\mu V_r^2}{V_r^{1/3}-\frac{1}{2}V_r}\right] \tag{18.1}$$

$$\nu = \frac{1}{2M_c} \tag{18.2}$$

where M_c is the molecular mass between crosslinks; ρ is the Density of the rubber; V_0 is the molar volume of the solvent; V_r is the volume fraction of the swollen rubber; μ is the interaction parameter between the rubber sample and the solvent; ν is the Crosslink density.

The nominal thickness of the sheets was set at 2 mm. The measurements of mechanical properties before and after aging were carried out in accordance with ASTM D 412a$^{\varepsilon 2}$ (2010). The aging test was performed in air flow oven at 70 °C for 21 days. Second type of aging was performed in ultraviolet box for 21 days. The samples were cut from the moulded sheets in dumbbell shape. The sample length and thickness were measured. Tensile tests were performed on an Instron (model 4507).

A minimum of three specimens was tested for each compound. Testing was done at room temperature with a cross head speed of 500 mm/min^{-1}.

Hardness values (Shore A) were measured according to the standard ASTM D 2240-05 (2010). Dynamic Mechanical Thermal Analysis (DMTA) was carried out on the Dynamic Mechanical Analyzer MK III system (Rheometric Scientific). As a mode of deformation, single cantilever bending was used at a heating rate of 2 °C/min, a frequency of 5 Hz and deformation 64 μm in temperature range from –80 to 80 °C.

CSM Micro Indentation Tester with a Vickers diamond indenter was used. Nine tests were performed for each composition and then averaged. The samples' thickness was approximately 2 mm. The maximum indentation load (F_{max}) was 250 mN, the rate for loading–unloading was 500 mN/min. The load was held at maximum for 50 s. The indentation hardness (H_{IT}) was determined by using the Oliver and Pharr method.

18.3 Results and Discussion

18.3.1 Vulcanization Characteristics

The rheometer, a convenient instrument to evaluate the effects of carbon black–rubber interactions on rate of cure and cross-linking, was employed for the purpose of characterizing critical parameters related to the vulcanization process. Table 18.1 shows the vulcanization characteristics of the four compounds used in this study.

The minimum torque (M_L) in a rheograph measures the viscosity of the vulcanizates, and the maximum torque (M_H) is generally correlated with the stiffness and crosslink density. It is well known that the difference between maximum (M_H) and minimum (M_L) torque is a rough measure of the crosslink density of the samples and usually known as ΔM. From the table it is noticed that the highest value of ΔM is for compound A. Hence the crosslink density is larger for compound "A" compared with the other three compounds. This is also confirmed by the results for the crosslink density obtained by the equilibrium swelling (Fig. 18.1). The highest crosslink density is registered for compound "A". But the carbon black particles whose surfaces are covered by entangled rubber chains can be considered as physical crosslinks. The physical crosslinking hinders the mobility of rubber chains and restrains the deformation of rubber therefore increases the torque. However, swelling cannot detect the type of the crosslinks although the high maximum torque for compound "A" can be considered also as a sign for higher number of physical crosslinks.

Table 18.1 Vulcanization characteristics of four compounds studied in this research

Blend No. / Characteristic	A	B	C	D
ML, dNm	2.98	2.71	2.73	2.53
MH, dNm	36.46	33.97	32.27	31.67
ΔM = (MH – ML)	33.48	31.26	29.54	29.14
T_{90}, min:s	17:22	4:47	17:24	5:43
T_{s2}, min:s	6:18	1:23	9:34	2:41
V, %min	9	31	13	33

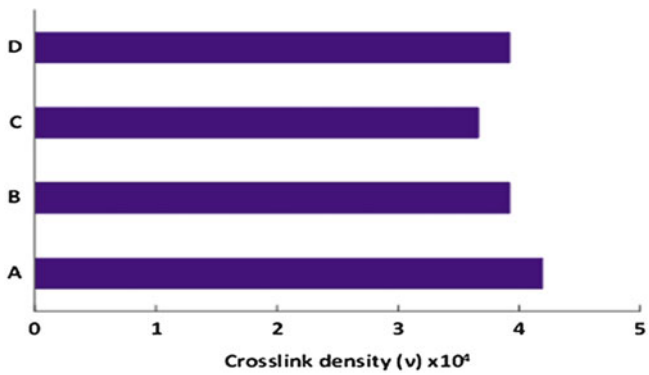

Fig. 18.1 Crosslink density determined by swelling

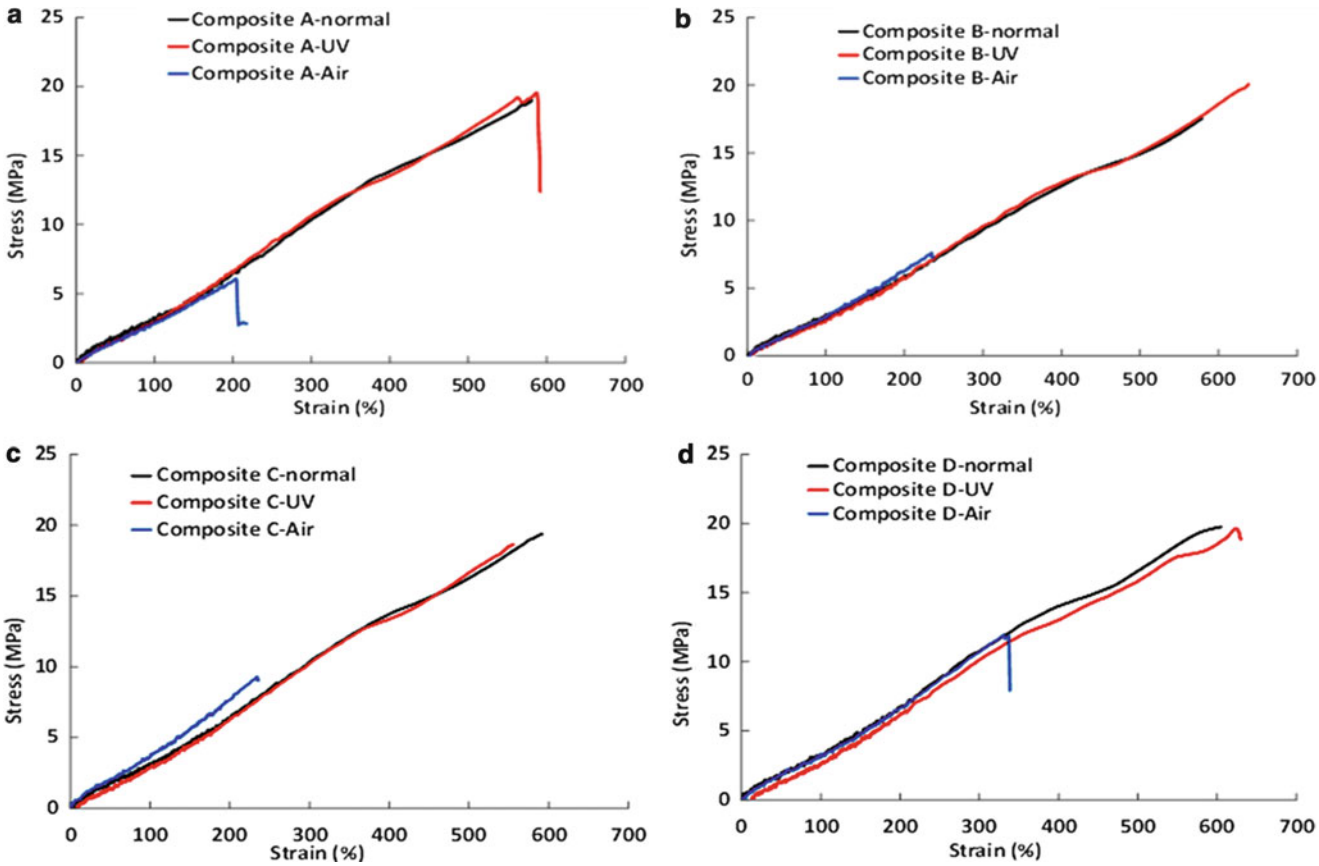

Fig. 18.2 Stress–strain curve for (**a**) compound A, (**b**) compound B, (**c**) compound C, and (**d**) compound D

The scorch time (Ts_2) is the time required for the minimum torque value to increase by two units and measures the premature vulcanization of the material. What makes an impression is that the CV system exhibited shorter Ts_2 values than the EV therefore more crosslinks are formed in shorter time.

These results are expected because the greater quantity of the accelerator (in compounds "C" and "D") should provide higher values for Ts_2. It is possible this anomaly to be due to the nature of sulphenamide class accelerators (delayed action in the beginning of vulcanization) and on the other hand the higher content of sulfur in compound "A" and "B". But the overall rate (V) of vulcanization is slightly in favour of the compound cured with EV.

18.3.2 Mechanical Properties Before Aging

Tensile properties are commonly used to measure the degradation behavior of elastomers. Fig. 18.2 illustrates the typical stress–strain curves of compounds A, B, C and D.

As shown in Fig. 18.3a, b all compounds show similar values of modulus at 100 % (M_{100}) and modulus at 300 % (M_{300}) deformation. Although the compounds vulcanized with CV (A and B) give slightly better results than those vulcanized with EV (D and C). These results are showing that compounds D and C poses better stiffness in low deformation than the other two. This is probably due to the different nature of the network structure obtained during vulcanization. The higher number of mono-sulphidic and C–C bonds, typical for EV, are characterized with higher strength especially under low deformation explains this phenomenon. Obviously the temperature of vulcanization does not affect significantly on M_{100} and M_{300}.

On the other hand the tendency is not the same for tensile strength (Fig. 18.3c) and the elongation at break (Fig. 18.3d). The higher values are for the compound vulcanized with CV. All compounds have the ability to exhibit crystallization under stress thanks to NR but according to literature the superior number of di- and poly- sulphidic linkages (result from CV) improves the elasticity of the compound which explains the higher values of elongation at break. In addition CV gives more homogeneous structure which plays positive role for the strength of vulcanizates. Once more the temperature of vulcanization does not play significant role for the tensile strength and elongation at break.

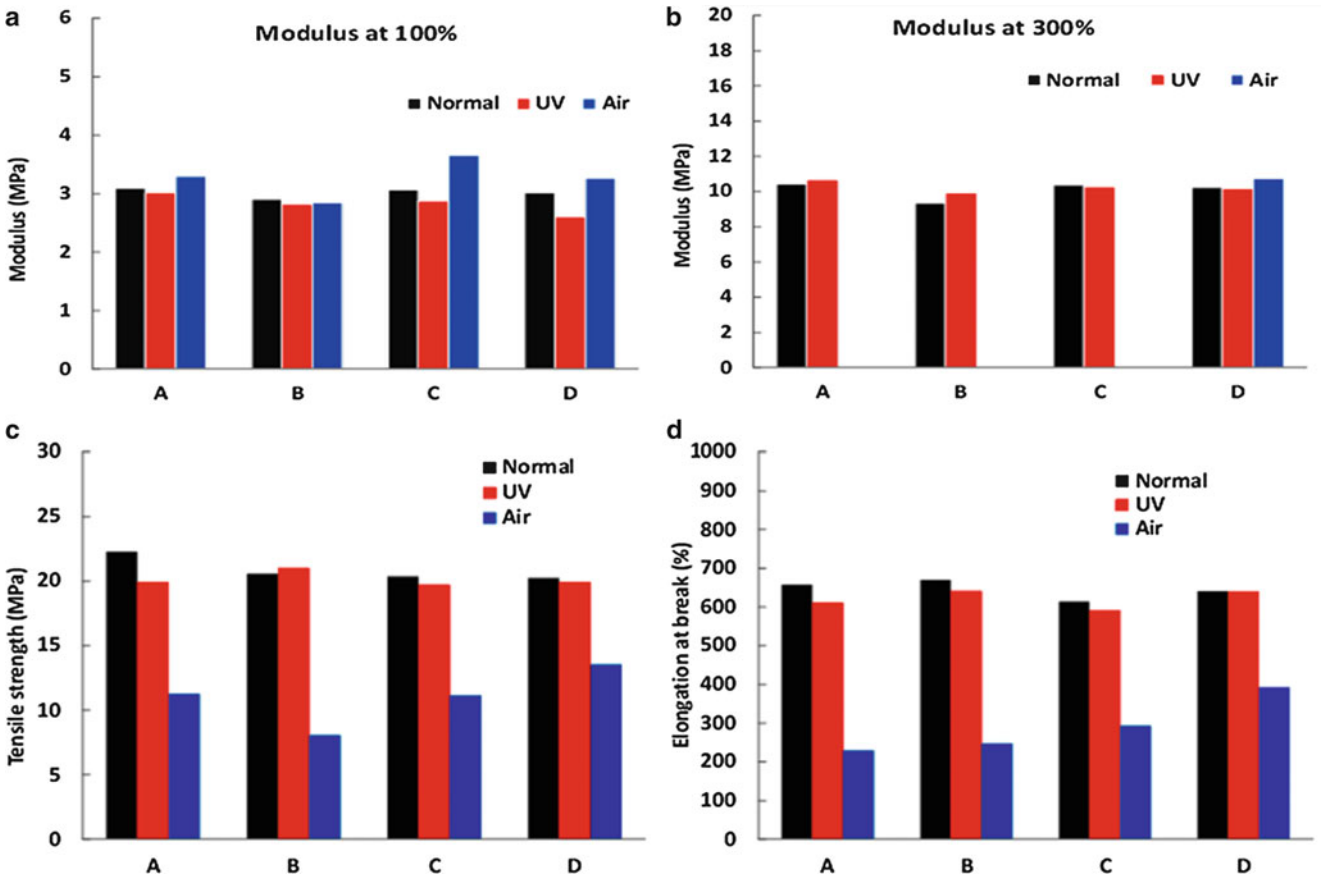

Fig. 18.3 Comparison of (**a**) M_{100}, (**b**) M_{300}, (**c**) tensile strength, (**d**) elongation at break for compounds A, B, C, D in normal and aging conditions

18.3.3 Mechanical Properties After Aging

The mechanical properties of the compounds after aging are also investigated. In Fig. 18.2 the stress–strain curves before and after 21 days aging (in air oven and under UV light) are compared. It can be seen that UV light does not affect significantly the mechanical properties of the studied compounds. The same relation is observed for M_{100}, M_{300}, tensile strength and elongation at break.

These results can be explained with the ability of rubber compound to form additional crosslinks under the influence of temperature and UV light. Although the overcrosslinking makes the vulcanizate brittle and reduces its elasticity apparently the period of exposure was not sufficient to create overcrosslinked vulcanizates. Probably the number of crosslinks created during UV aging compensates the number of the chains destroyed by aging. The thermal aging however (21days in air oven at 70 °C) causes more severe damage on the studied compounds. Under low level of deformation (100 %) thermal aging has positive effect.

At this stage, crosslink scissions and the formation of new crosslinks into the networks affected these properties. But under high stress and deformation the process of destruction of the crosslinks is much more significant and leads to failure of the specimen.

Concerning the type of vulcanization system the values of all mechanical properties shown in Fig. 18.3 of the four studied compounds (A, B, C, and D) presenting the resistance to UV aging are similar. The CV system vulcanizates (C and D) has a high content of polysulphide linkages with low bond strength. By contrast, monosulphide linkages have relatively strong bond strength and are dominant in the EV system vulcanizates [8]. As a result, the CV system exhibits a weaker thermal aging resistance than polysulphide crosslinks. For all compounds the extended period of heating, the excessive main chain scission and/or modification resulted in a reduced tendency to crystallize at high elongation. It is observed that the effect of the temperature of vulcanization is not significant for aging resistance.

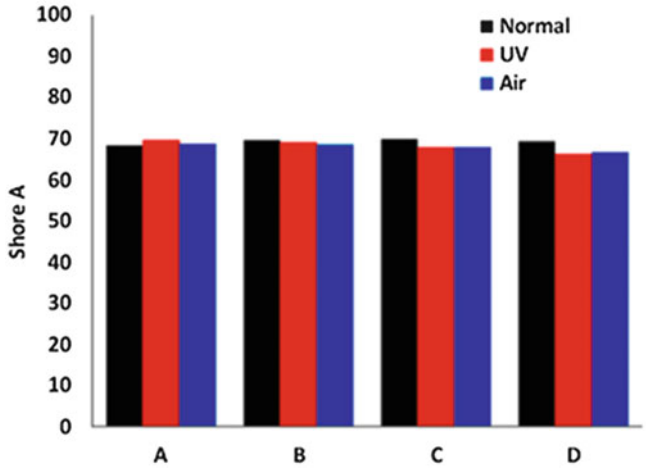

Fig. 18.4 Comparison hardness (Shore A) for compounds A, B, C, D in normal and aging conditions

18.3.4 Hardness-Shore "A" Test Evaluation

The hardness (Shore A) is presented in Fig. 18.4. The hardness is relatively high for NR compound but this is probably due to the presence of BR in the mixture. The results do not show any dependence on the vulcanization system or vulcanization temperature. For most of the compounds UV and thermal aging leads to reduction in the hardness values. However there is almost no difference between the effect of UV aging and thermal aging although it was observed one for the mechanical properties.

18.3.5 Dynamic Mechanical Thermal Analysis (DMTA)

The dependences of storage modulus (E′) and dynamic mechanical loss angle tangent (Tan Delta) on the temperature of vulcanization and vulcanization system were studied in the temperature interval from −80 to +80 °C.

As shown in Fig. 18.5, in the range of −80 to −40 °C there are no considerable changes that occurred in the storage modulus (E′). There is a slight difference of the maximum values among compounds B, C and D. What makes an impression is that the maximum of storage modulus for compound A is considerably lower compared to the other three compounds. The decrease of storage modulus (E′) with the increasing temperature, in other words, the transition from the glassy to the high elastic state occurs at about −49 °C. In the interval from –40 to 80 °C, when the vulcanizates are in high elastic state, the increase in storage modulus (E′) can be related to the limited mobility of rubber molecules, being immobilized by the carbon black surface. According to [9], this effect may be used as a measure of the filler reinforcing activity, because the greater reinforcing activity of the filler, the lesser the mobility and the higher storage modulus (E′) values are. All the curves presented for (E′) in Fig. 18.5 are similar meaning the reinforcing effect of the filler is the same for all four compounds.

The loss factor of rubber materials is related to the energy lost due to energy dissipation as heat under an oscillating force.

The mechanical loss angle tangent is the ratio between the dynamic loss modulus (E″) and the dynamic storage modulus (E′) (Tan Delta = E″/E′). It represents naturally the macromolecules mobility of the chains and polymers phase transitions [10–15].

It is accepted that the higher the Tan Delta is the greater the mechanical losses; these losses are related to high energy input required for the motion of the molecular chains of the polymer as the transition is being approached [16–22]. The position of the tan delta peak in the loss factor versus temperature curve can be used to identify the T_g of the rubber materials.

It is observed that T_g of the studied compounds does not change considerably (within the limits of 2–3 °C). The intensity of the peak is also similar. Obviously the vulcanization system and vulcanization temperature does not play role in this particular case. This is not in accordance with our previous results, where only the temperature does not play a role for tan delta and storage modulus. The results for tan delta suggest that despite the difference in crosslink density and the different vulcanization mechanism the interactions rubber–rubber and rubber–filler are similar for all the compounds.

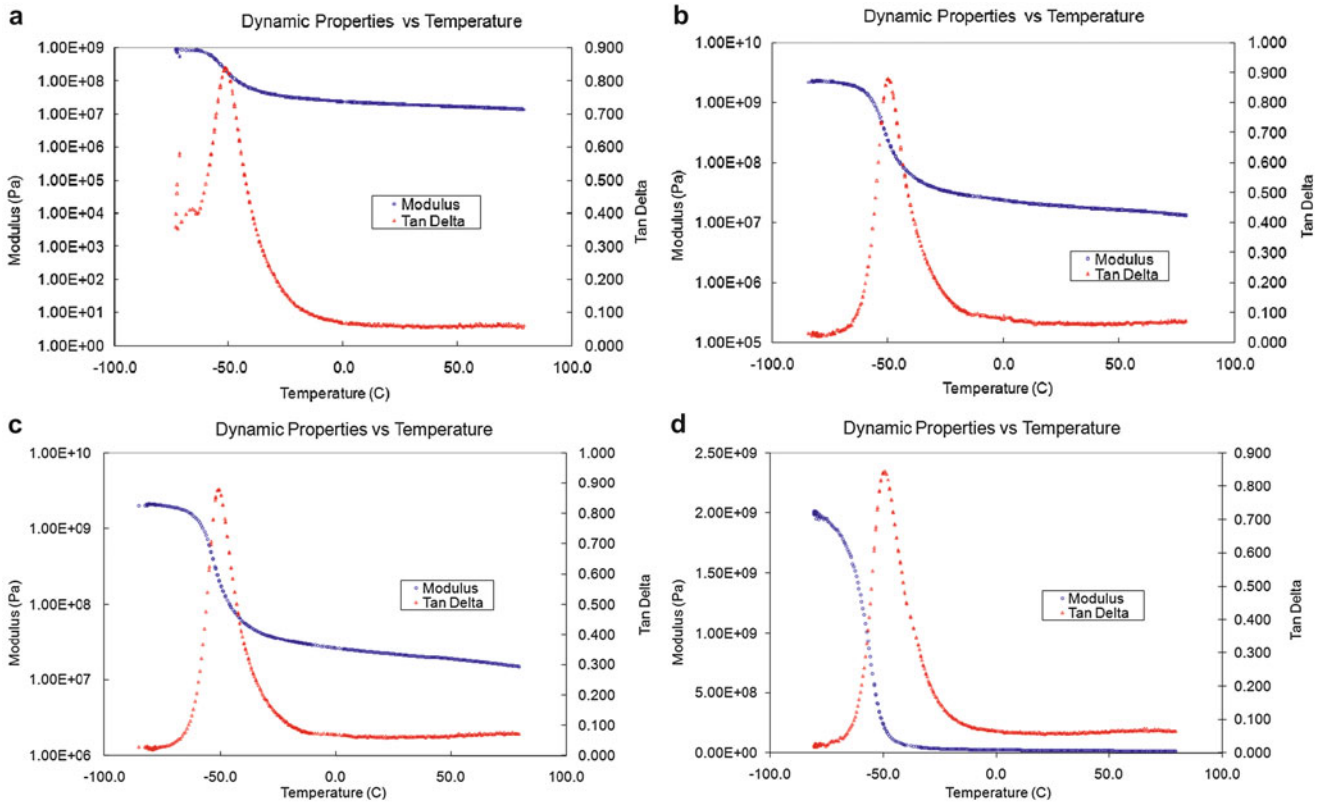

Fig. 18.5 Storage modulus and Tan Delta as a function of the temperature (**a**) compound A, (**b**) compound B, (**c**) compound C, (**d**) compound D

18.3.6 Microindentation Analysis

The micro indentation test has become a popular technique due to its simplicity and to the fact that it provides valuable information about the morphology and mechanical properties of polymeric materials. Additionally, the indentation method has been successfully employed to investigate the glass transition temperature of polymers [23]. In a special study, micro indentation has emerged as a promising tool for micromechanical and microstructural investigation of polymer blends [24, 25]. First of all, micro indentation differs from classical measurement of hardness, where the impressions are generated and then imaged with a microscope. In a micro indentation test load and associated penetration depths are recorded simultaneously during both loading and unloading, producing a force–displacement diagram as shown schematically in Fig. 18.6a.

The viscoelastic properties of polymers are markedly dependent on the type of crosslinks and the degree of crosslinking. Crosslinking can raise the glass-transition temperature (T_g) of a polymer by introducing constraints on the molecular motions of the chain.

Low degrees of crosslinking in normal vulcanized rubbers act in a similar way to entanglements and raise the T_g only slightly above that of the crosslinked polymer. The effect of crosslinking is the most important and best understood in elastomers. Sulphur crosslinking of NR produces a variety of crosslinking types and crosslink lengths [25–32].

It is well known that polysulfide linkages predominate with conventional sulphur vulcanization system whereas mono-sulfide and disulfide crosslinks are formed with an efficient vulcanization system, which has a higher accelerator/sulphur ratio. Sulphur also introduces main chain modifications either in the form of pendant groups or as cyclic sulfide linkages that have a large influence on the viscoelastic properties [26–34].

Networks containing high proportions of polysulfide crosslinks display different mechanical properties from those containing mono-sulfides crosslinks. It is shown in the literature that the increase in the accelerator level only resulted in small changes of the T_g and that the rubbery tensile modulus was dependent on the crosslink density but almost independent of the crosslink type [25–31].

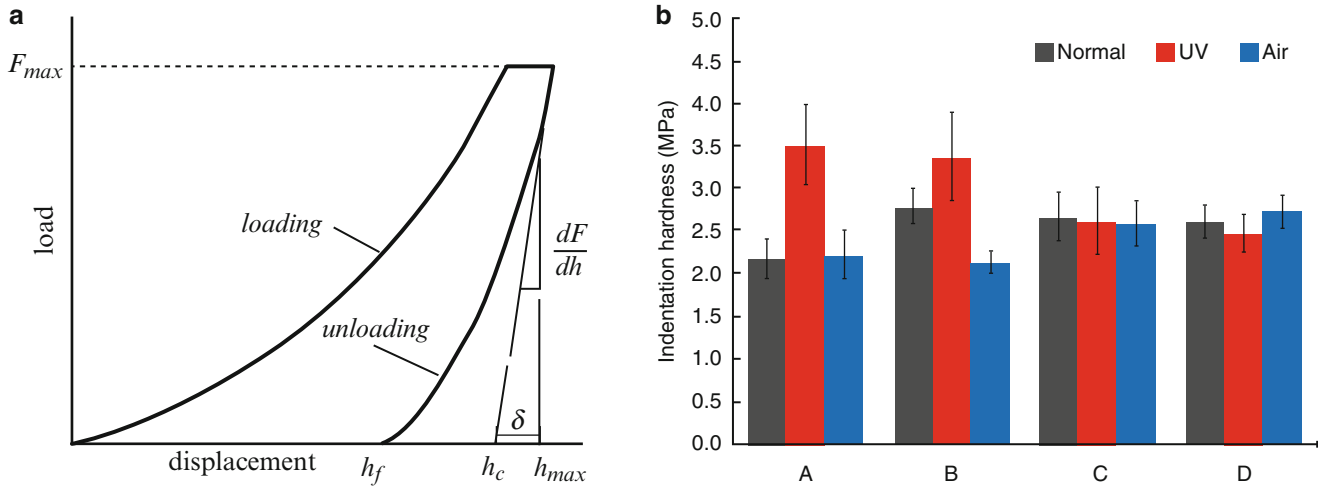

Fig. 18.6 (**a**) Schematic representation of the force–depth curve for micro indentation procedure and (**b**) comparison of indentation hardness for compounds A, B, C, D in normal and aging conditions

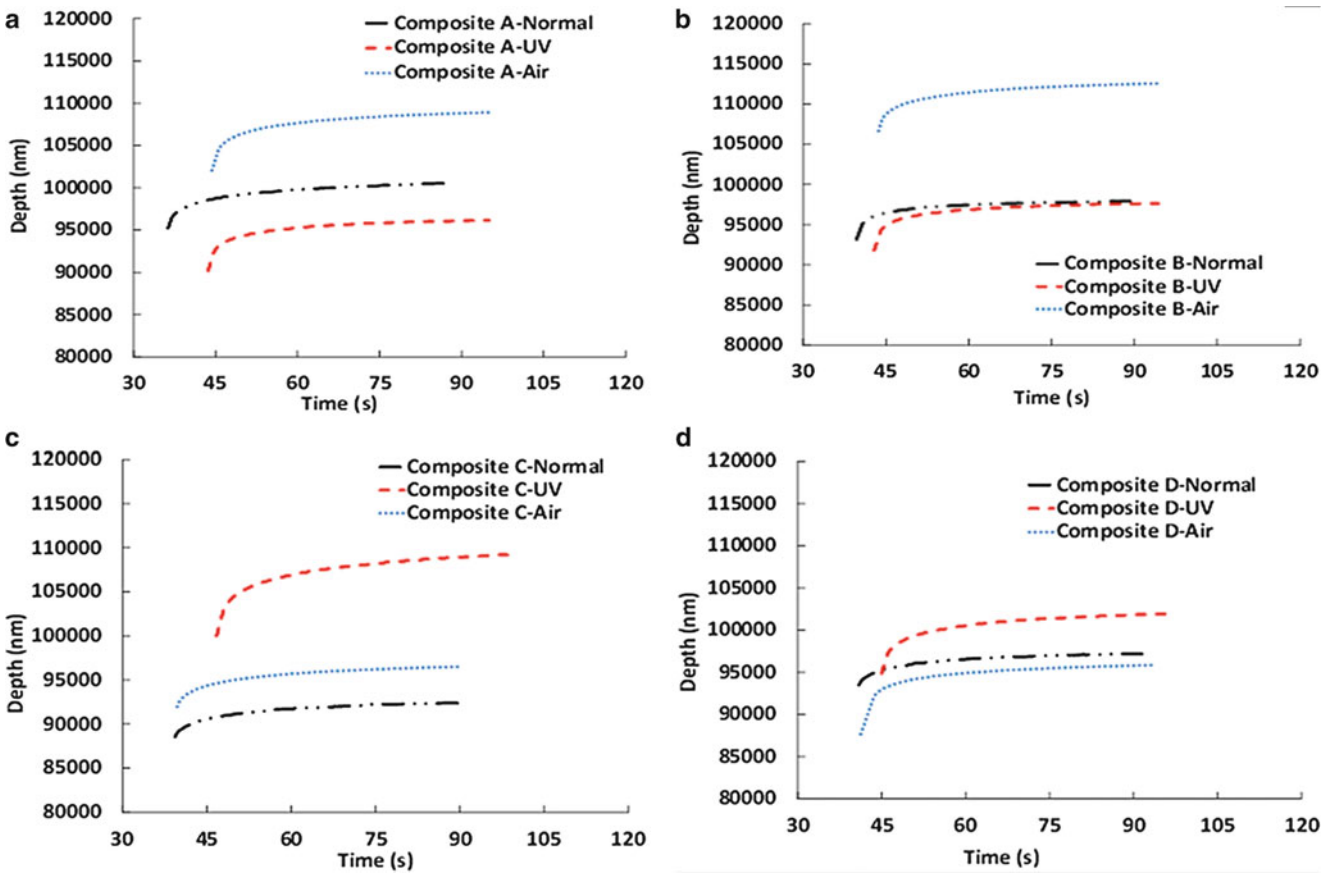

Fig. 18.7 Comparison of microindentation depth at maximum load as a function of time (**a**) compound A, (**b**) compound B, (**c**) compound C and (**d**) compound D

Normal and aged (air flowing and UV) specimens of the elastomer based composites manufactured were tested by micro indentation device and their hardness and viscoelastic responses were compared Fig. 18.6b shows the comparison of indentation hardness for compounds A, B, C, D in normal and aging conditions (air flowing and UV).

Figure 18.7 shows microindentation depth at maximum load as a function of time for the compounds "A", "B", "C" and "D" respectively under normal and aging conditions. It is revealed that samples with compound "C" have a higher

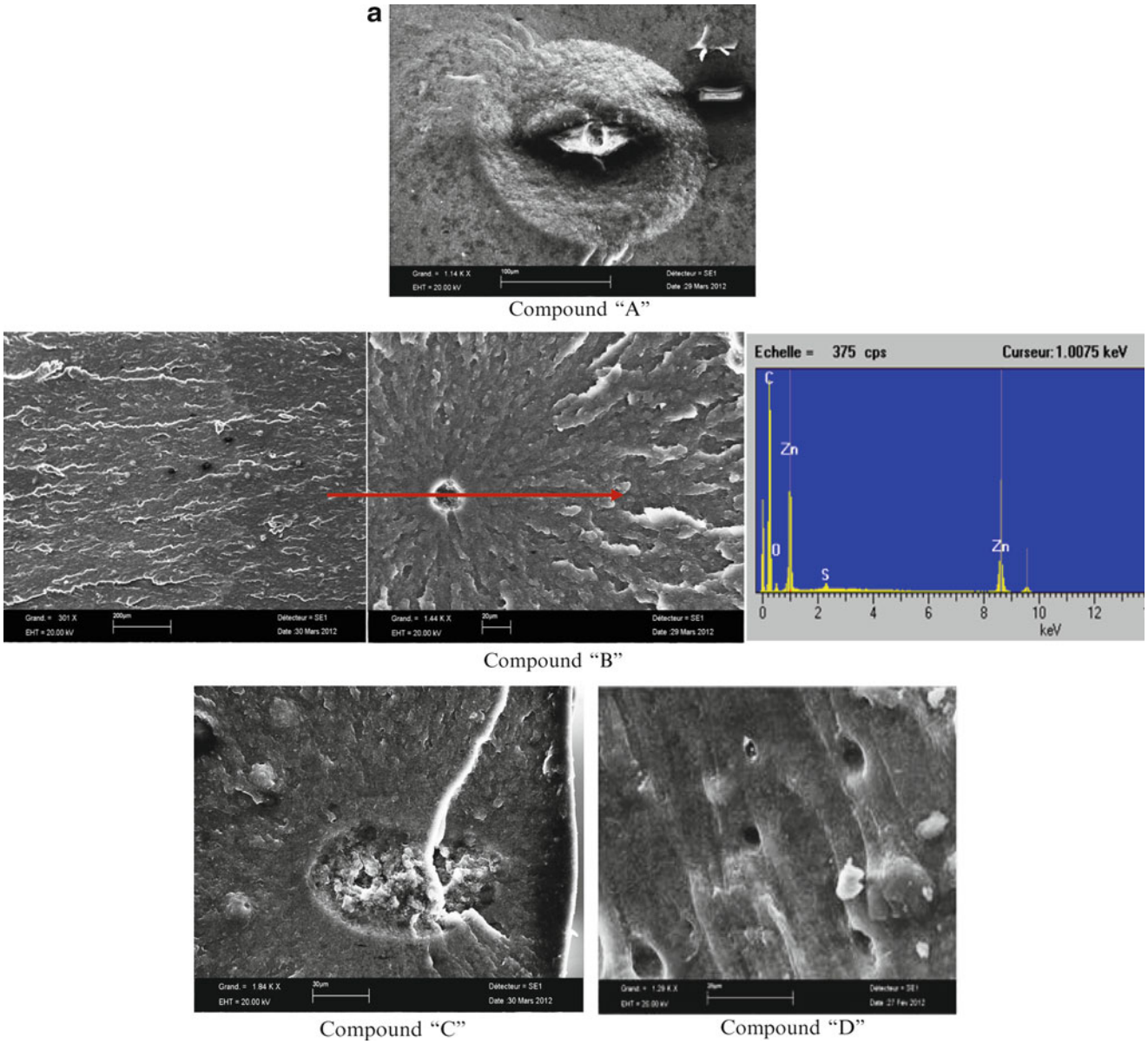

Fig. 18.8 Typical Scanning Electron Microscopy (SEM) fracture surface images, at low and high magnifications (**a–c**): (**a**) compound "A", compound "B, compound "C" and compound "D", (**b**) compound "C", cartography (*left column*) and tongue formation at the fracture surface (*right column*), (**c**) compound "B" after thermal-airflow aging (*left column*) and compound "D" after thermal-airflow aging (*right*)

viscoelastic deformation in normal conditions than the corresponding samples with compounds "A", "B" and "D" due to improved chain mobility (moderately due to subdivision) and allow more relaxation after loading.

In the same way, air flowing (thermal) aging condition influences very strongly the structure of the compounds "A" and "B" and interesting results were observed in case of aging effect by UV on the compounds of "C" and "D" as indicated in Fig. 18.7c, d. All of these results will be used for modelling the viscoelastic behaviour of the elastomeric composites that will be presented in an upcoming paper.

18.3.7 Damage and Fracture Surface Analysis by Means of Scanning Electron Microscopy

As well indicated in the former sections, fracture surfaces analysis of tensile specimens observed by means of the Scanning Electron Microscopy (SEM) should give more realistic information to understand the damage behaviour of these four

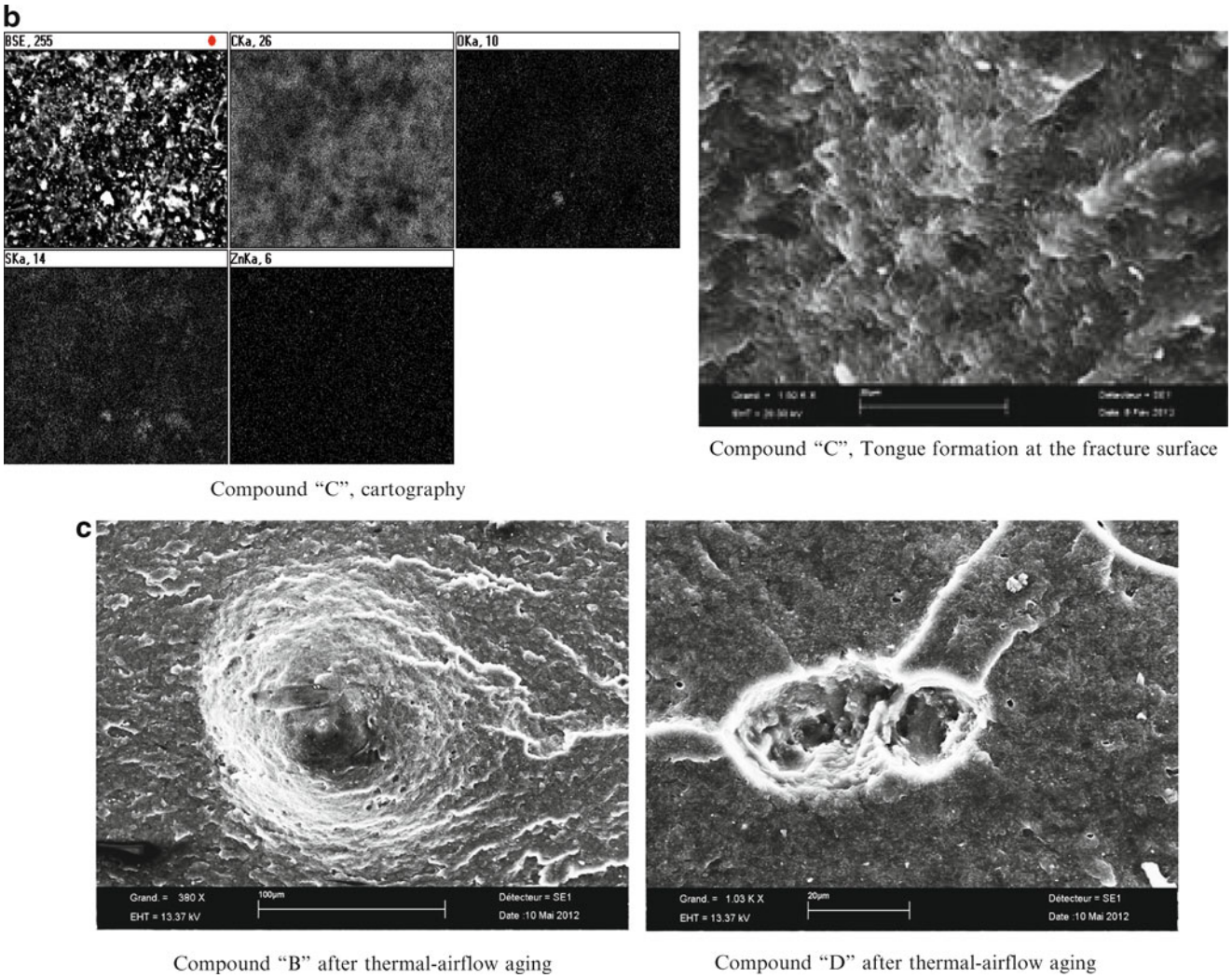

Fig. 18.8 (continued)

compounds. Because these observations show that the fracture energy and stability are exceedingly reliant on the composition and morphology of these new elastomeric composites.

Fracture surfaces are shown in Fig. 18.8a–c as low and high magnification. In reality, elastomeric composites do not exhibit the same fracture type as metallic materials. At high magnifications, it is always possible to see tearing deformation lines in films and deformed fibrils, occasionally one may see on each specimen. Elliptical cap, steps and striped patterns can also be observed. These microstructures that are located in narrow stressed layers of the fracture surface give obvious information about the initiation peak and propagation and fracture directions. Typically, these entire compounds show similar crack initiation zone called "cavitations" very similar to the "fish eye formation". It means that the failure initiates from a particle ("EDS" analysis gives basically a small metallic and/or metallic oxide such as Zn) and propagates around these particles by forming a circle shape after that, at the final stage, a catastrophic failure occurs very rapidly by showing regular tearing lines at the fracture surface (very similar to the failure bands due to the tearing crossing over heterogeneities).

Typical tongue formation at the fracture surfaces were observed in entire compounds (an example is given here Fig. 18.8b with cartography of the compound "C". This phenomenon is due to the behaviour of the natural rubber during the deformation. This behaviour can be observed very often in entire compounds from elastomeric composites. Similar results carried out on the four compounds designed here can be found in the literature [6, 7, 13].

18.4 Conclusion

In the frame of the common research project going on, the processing, mechanical and viscoelastic parameters of new elastomeric composites containing basically the mixture of NR-BR vulcanizates with different addition-reinforcements have been studied and basic results were discussed in comparison of the compounds each other. Essentially, swelling test is a very interesting evaluation way for these compounds, giving detailed information about crosslinking density. The physical crosslinking hinders the mobility of rubber chains and restrains the deformation of rubber therefore increases the torque.

Fracture surfaces carried out by SEM analysis show similar crack initiation zone called "cavitations" very similar to the "fish eye formation". It means that the failure initiates from a particle and propagates around these particles by forming a circle shape after that, at the final stage, a catastrophic failure occurs and regular tearing lines are observed at the fracture surface. Typical tongue formation at the fracture surfaces were observed in entire compounds due to the natural rubber behaviour. All of this comprehensive study gives the same tendency among the two basic mixtures. Based on the processing, mechanical characteristics and viscoelastic behaviour, optimum composition between four compounds studied here, optimistic choice can be classified different properties for different industrial applications that will be useful to make a detail suggestion after final results of the research project that is going on.

References

1. Morawetz H (2000) History of rubber research. Rubber Chem Technol 73:405–426
2. Smith FB (1961) Response of elastomers to high temperature cure. Rubber Chem Technol 34:571–585
3. Nasiar M, Teh GK (1988) The effect of various types of cross-links on the physical properties of natural rubber. Eur Polym J 24:733–736
4. Bhowmick AK, Mukhopadhyay R, De SK (1979) High temperature vulcanization of elastomers. Rubber Chem Technol 52:725–734
5. Studebaker ML, Beatty JR (1972) The oxidative hardening of SBR. Rubber Chem Technol 45:450–466
6. Bayraktar E, Bessri K, Bathias C (2008) Deformation behaviour of elastomeric matrix composites under static loading conditions. Eng Fract Mech 75(9):695–706
7. Luong R, Isac N, Bayraktar E (2007) Damage initiation mechanisms of rubber. J Arch Mater Sci Eng 28(1):19–26
8. Morrison NJ (1984) The reaction of cross-link precursors in natural rubber. Rubber Chem Technol 57:86–96
9. Zaper AM, Koeing JL (1987) Solid state C-13 NMR studies of vulcanized elastomers, accelerated sulphur vulcanization of natural rubber. Rubber Chem Technol 60:278–297
10. Gonzalez L, Rodriguez A, Valentin JL, Marcos-Fernandez A, Posadas P, Kunstst KG (2005) Conventional and efficient crosslinking of natural rubber. Kaut Gummi Kunstst 58:638–643
11. Bessri JK, Montembault F, Bayraktar E, Bathias C (2010) Understanding of mechanical behaviour and damage mechanism in elastomers using X-ray computed tomography at several scales. Int J Tomogr Stat 14:29–40
12. Ramier C, Gauthier L, Chazeau L, Stelandre L, Guy L (2007) Payne effect in silica-filled styrene–butadiene rubber: influence of surface treatment. J Polym Sci B 45(3):286–298
13. Bayraktar E, Isac N, Bessri K, Bathias C (2008) Damage mechanisms in natural (NR) and synthetic rubber (SBR): nucleation, growth and instability of the cavitations. Int J Fatigue Fract Struct Mater 31(1):1–13
14. Zulkifli R, Fatt LK, Azhari CH, Sahari J (2002) Interlaminar fracture properties of fibre reinforced natural rubber/polypropylene composites. J Mater Process Technol 128(1–3):33–37
15. Brydson JA (1988) Natural rubber in: rubber materials and their compounds. Elsevier Science, New York
16. Botelho DS, Bayraktar E (2009) Experimental and numerical study of damage initiation mechanism in elastomeric composites—double cantilever beam specimens-DCB. J Achiev Mater Manuf Eng 36(1):65–71
17. Varghese S, Karger - Kocsis J, Gatos KG (2003) Melt compounded epoxidized of natural rubber/layered silicate nanocomposites; structure–-properties relationships. Polymer 44(14):3977–3983
18. Botelho DS, Isac N, Bayraktar E (2007) Modeling of damage initiation mechanism in rubber sheet composites under the static loading. Int J Achiev Mater Manuf Eng 22(2):55–59
19. Sombatsompop N (1999) Dynamic mechanical properties of SBR and EPDM vulcanizates filled with cryogenically pulverized flexible polyurethane foam particles. J Appl Polym Sci 74(5):1129–1140
20. Bayraktar E, Antholovich S, Bathias C (2006) Multiscale observation of fatigue behaviour of elastomeric matrix and metal matrix composites by X-ray tomography. Int J Fatigue 28:1322–1333
21. Al-Hartomy OA, Al-Ghamdi A, Dishovsky N, Ivanov M, Mihaylov M, El-Tantawy F (2011) Influence of carbon black structure and specific surface area on the mechanical and dielectric properties of filled rubber composites. Int J Polym Sci ID521985:1–8
22. Zaimova D, Bayraktar E, Dishovsky N (2011) State of cure evaluation by different experimental methods in thick rubber parts. J Achiev Mater Manuf Eng 44(2):161–167
23. Hamed GR, Al-Sheneper AA (2003) Effect of carbon black concentration on cut growth in NR vulcanizates. Rubber Chem Technol 76:436
24. Kohl JG, Singer IL (1999) Pull-off behavior of epoxy bonded to silicone duplex coatings. Prog Org Coat 36:15–20
25. Brady RF, Singer IL (2000) Mechanical factors favoring release from fouling release coatings. Biofouling 15:73–82
26. Oliver WC, Pharr GM (1992) An improved technique for determining hardness and elastic modulus using load and displacement sensing indentation experiments. J Mater Res 7:1564–1583

27. Hofmann W (1988) Natural rubber; rubber technology handbook. Hanser, New York
28. Nielsen LE, Landel LE (1994) Mechanical properties of polymers and composites, 2nd edn. Marcel Dekker, New York
29. Chapman AV, Porter M (1988) In: Roberts AD (ed) Natural rubber science and technology. Oxford Scientific Publications, New York (Chapter 12)
30. Singer IL, Kohl JG, Patterson M (2000) Mechanical aspects of silicone coatings for hard foulant control. Biofouling 16:301–309
31. Kohl JG, Singer IL, Griffith JR (2000) Evaluating the durability of silicone duplex coatings using a scratch tester. Rubber Chem Technol 73:607–618
32. Kohl JG, Singer IL, Schwarzer N, Yu VY (2006) Effect of bond coat modulus on the durability of silicone duplex coatings. Prog Org Coat 56:220–226
33. Ngan AHW, Wang HT, Tang B, Sze KY (2005) Correcting power-law viscoelastic effects in elastic modulus measurement using depth-sensing indentation. Int J Solids Struct 42:1831–1846
34. Fischer-Cripps AC (2004) A simple phenomenological approach to nanoindentation creep. Mater Sci Eng A 385:74–82

Chapter 19
The Effect of Particles Size on the Thermal Conductivity of Polymer Nanocomposite

Addis Tessema and Addis Kidane

Abstract The variation in thermal conductivity of polymer nanocomposite with different particle sizes and volume fractions have been investigated. Particle reinforced nano-composites with two different particle sizes and the volume ratio of each size ranging from 0 to 50 % is considered. The test is conducted using a unidirectional/linear heat transfer device that has six thermocouples to monitor the temperature flow through and across the cross section of the specimen. In addition, based on Lewis-Nielson and modified effective medium approximation, a three phase analytical model is proposed to determine the thermal conductivity of different nanocomposites. It is observed that the thermal conductivity linearly increases as the volume fraction of the particles increases. On the other hand, though the particle size has an effect on the thermal conductivity of the nanocomposites, the effect is minimal compared with the volume fraction. The analytical model has been applied to different batches of specimens, and the results from the experiment and analytical model are compared.

Keywords Nanocomposite • Thermal conductivity • Kapitaz resistance • Interface layer • Surface functionalizing

19.1 Introduction

Polymers are playing a crucial role in modern material technology; they can be applied in a wide variety of applications from the electronics industry, chemical, power generation, and automotive up to aerospace industries [1–3]. There have been great efforts to improve the physical, chemical and mechanical properties of polymers by inclusion of different fillers. Carbon nanotubes, Graphenes, Glass fibers, Ceramic nanoparticles and Aluminum nanoparticles are some of the fillers used as reinforcement in nano-composites [4]. Even though nanoparticle reinforced polymer composites have proven to have many advantages, their analysis is more complicated relative to the plain polymer due to the non-uniform distribution of reinforcement and variation in properties from matrix to filler.

The thermal conductivity of nano-composites plays a vital role in the overall system performance, especially in the electronic, chemical and power generation industries where these materials are used either as a thermal conductor or insulator [3]. Studies have indicated that effective thermal conductivity of nanocomposites is influenced by the thermal property of the constituents, K_{matrix} and K_{filler}, thickness of the interface layer (t_i), uniformity of filler distribution, filler geometry/aspect ratio and filler volume fraction [1, 4–8]. Out of the listed parameters, the thickness of the interface layer (t_i) is difficult to manage. To date, there have been great efforts in surface modifications techniques that are hoped to reduce or eliminate the interface layer thickness.

On the other hand, functionalizing the surface of nano fillers has improved the dispersion of fillers and the interface layer between the filler and the matrix. The main focus of this paper is to investigate the effect of particle size and functionalization on the thermal conductivity of polymer nanocomposites at different temperatures and filler volume fractions.

A. Tessema (✉) • A. Kidane
Mechanical Engineering Department, University of South Carolina, 300 Main Street, Columbia, SC 29208, USA
e-mail: addisng@gmail.com; atessema@email.sc.edu

G. Tandon (ed.), *Composite, Hybrid, and Multifunctional Materials, Volume 4: Proceedings of the 2014 Annual Conference on Experimental and Applied Mechanics*, Conference Proceedings of the Society for Experimental Mechanics Series,
DOI 10.1007/978-3-319-06992-0_19,

19.2 Material and Specimen Geometry

In the current study nano-composites made of Poly(2-vinyl pyridine) (97k) polymer and SiO_2 particle is considered. The particles are first treated with two different solutions, Methyl Ethyl Ketone (MEK) and Pyridine (PYR), and their effect on the thermal conductivity of the composites has been investigated. The fabrication process can be obtained elsewhere [9], and here it is presented briefly. First, polystyrene chains are attached to the surface of the spherical silica nanoparticles (diameter of 14 and 50 nm). The functionalized particles are mixed with a monodisperse polystyrene matrix with different volume ratios. Then the mixture is casted in an 8 mm diameter cylindrical mold and let cured in room temperature. Through this process, nano-composites containing of 14 and 50 nm diameters SiO_2 and different volume fractions (10, 20, 30, 40, 45 and 50 %) are fabricated. Typical SEM images of the nano-composites made with two different methods are shown in Fig. 19.1, from the figure it is clear that the particles functionalized with Methyl Ethyl Ketone are well dispersed.

19.3 Experimental Method

A unidirectional/linear heat transfer apparatus is used to measure the thermal conductivity of the nano-composites described above. The apparatus mainly consists of a heat source, heat sink, two conductive brass rods, and eight thermocouples to monitor the temperature flow through and across the cross section of the specimen. This apparatus is arranged so that, the electric heat source, is directly connected to a brass bar in one end and a heat sink, continuously running tap water, is connected to the other brass bar. The specimen is sandwiched between these two 8 mm diameter brass rods above and below. The sectioned schematic diagram of the experiment set up is shown in Fig. 19.2. Where T1–T8 are the thermocouples to measure the in situ temperatures, HSo is the heat source, HSi is the heat sink and IM is the intermediate module. To insure a unidirectional heat transfer, the entire system is insulated using a Teflon jacket.

During the experiment, the temperature is varied by manually adjusting the voltage input into the system. The specimens are tested at three different temperatures, and the effect of temperature on the thermal conductivity is investigated. Using the steady state linear heat equation given in Eq. 19.1, the thermal conductivity of the specimen (K_e) can be calculated from the known thermal conductivity of brass rod, K_{Brass}, and the temperatures measured.

$$K_e = K_{Brass} * \left(\frac{\Delta X_{Speci}}{\Delta X_{Brass}}\right) * \left(\frac{T_L - T_5}{T_H - T_L}\right) \tag{19.1}$$

where K_{Brass} is thermal conductivity of the brass, ΔX_{Speci} is thickness of the specimen; ΔX_{Brass} is the distance between the position of the thermocouple and the tip of the brass conductor, which is in contact with the specimen. T_L is the temperature at the lower surface of the specimen, and T_H is the temperature at the top surface of the specimen.

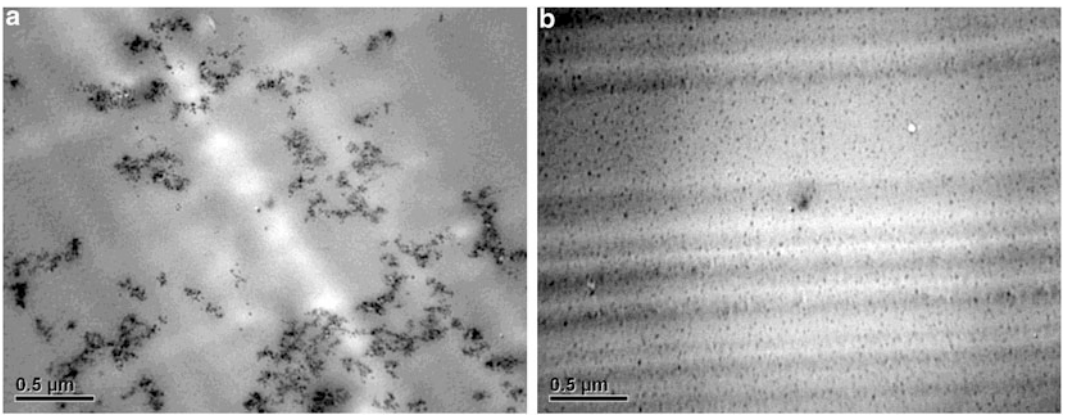

Fig. 19.1 SEM image of nanocomposites prepared (**a**) pyridine and (**b**) methyl ethyl ketone (prepared by Prof. Sanat Kumar group)

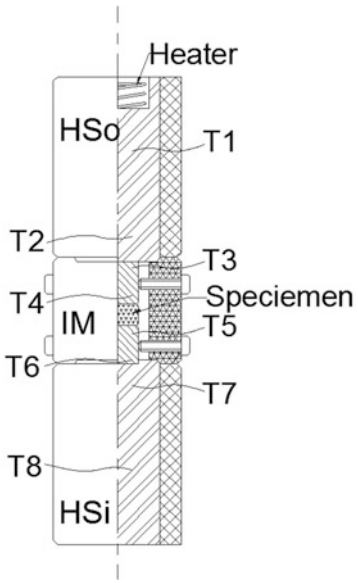

Fig. 19.2 Schematic diagram of unidirectional/linear heat transfer apparatus

19.4 Analytical Method

Different analytical and semi empirical schemes have been developed to estimate the thermal conductivity of composite materials [4, 7, 8]. Among those, the Lewis-Nielson (L-N) [4], Maxwell Eucken-EMA (ME-EMA) [8], and Hamilton and Cheng-Vachon model [5] are widely used. Most of the models consider the geometry of the filler, the volume fraction of the filler, the thermal conductivity of both the matrix and the filler, and thermal resistance at the junction between the filler and the matrix (Kapitaz Resistance). In the current study the Lewis-Nielson model is used. The detail analysis of the model can be found elsewhere [4], and here it is briefly described below.

19.4.1 Lewis-Nielson (LN) Model

The Lewis-Nielson (LN) model is adopted from the Halpin-Tsai (HT) mechanical model. It has a semi-empirical equation, which considers the effect of particle size, particle shape (aspect ratio), the volume fraction of the particle and the critical or maximum packing of particles. The effective thermal conductive of the composite can be shown as Eq. 19.2:

$$K_e = K_m * \left(\frac{\left(1 + \varepsilon^* \eta^* \varphi_{cp}\right)}{\left(1 - \phi^* \eta^* \varphi_{cp}\right)} \right) \tag{19.2}$$

Where, $\phi = 1 + \left[\frac{(1 - \varphi_m)}{(\varphi_m{}^2)} \right] \varphi_{cp}$ and $\eta = \left[\frac{\left(K_f - K_m\right)}{\left(K_f + K_m * \varepsilon\right)} \right]$ and K_m = thermal conductivity of the matrix, K_f = thermal conductivity of the particle and the interface layer, and is given as

$$K_f = 1 \Big/ \left[\left[\frac{\varphi_p}{K_f \left(\varphi_p + V_l\right)} \right] + \left[\frac{\varphi_l}{K_m \left(\varphi_p + \varphi_l\right)} \right] \right] \tag{19.3}$$

and φ_p is the volume fraction of the particle and φ_l is the volume fraction of the interface layer, and they are related as

$$\varphi_l = \varphi_p \left[\frac{\left(r_p + t\right)^3}{\left(r_p\right)^3} - 1 \right] \text{ and } \varphi_{cp} = \varphi_p * \delta \tag{19.4}$$

where $\delta = \left(1 + {}^{t}/_{r_p}\right)^3$, r_p is the radius of the particle, φ_{cp} is the combined volume fraction of the particle and the interface layer. And $\varepsilon = 1.5$ (aspect ratio factor) and $\varphi_m = 0.637$ (maximum packing) for the spherical particle.

19.5 Result and Discussion

The effective thermal conductivity of the polymers as a function of temperature, volume fraction and particle size is presented below.

19.5.1 Effect of Surface Functionalization

The results from tests made on the 50 nm particle for both made the Methyl Ethyl Ketone (MEK) and Pyridine (PYR) functionalized specimens as a function of the volume fraction are shown in Fig. 19.3. It is clearly seen that for the same particle size and volume fraction, the specimen made with MEK surface functionalization has higher thermal conductivity than that made with PYR. As shown previously in Fig. 19.1, the surface functionalization improved the particle dispersion and may have also had an influence on the interface layer between the two constituents.

To investigate the effect of particle size on the thermal conductivity of nanocomposites, the experimental and numerical results for specimens made with different size (i.e. 14 and 50 nm) particles and different volume fraction are presented in Fig. 19.4. Both the numerical and experimental studies show that specimens with smaller particle size (14 nm) have higher thermal conductivity than specimen with larger particle (50 nm). Note that the two particles are spherical and hence they have a similar aspect ratio. The effect could be due to the fact that the smaller the particle size, the larger the contact surface area per volume of the particle, which will increase the thermal conductivity of the nanocomposites.

One more thing noted in Fig. 19.4 is that with disrespect to the particle's size and functionalization method, the thermal conductivity of the composites increase monotonically with the increase in the volume fraction of the particle.

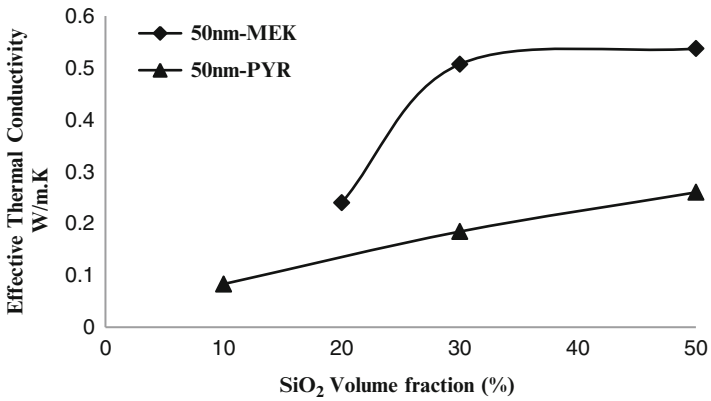

Fig. 19.3 Variation of effective thermal conductivity as a function of particle volume fraction for functionalized and non-functionalized specimen

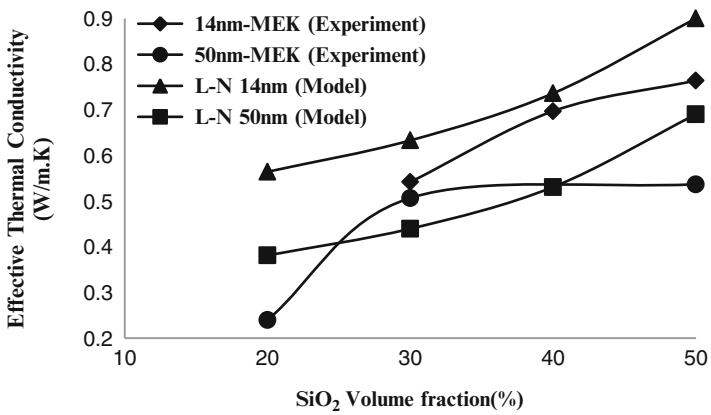

Fig. 19.4 Variation of effective thermal conductivity as a function of particles volume fraction for different particle size (comparison numerical and experimental)

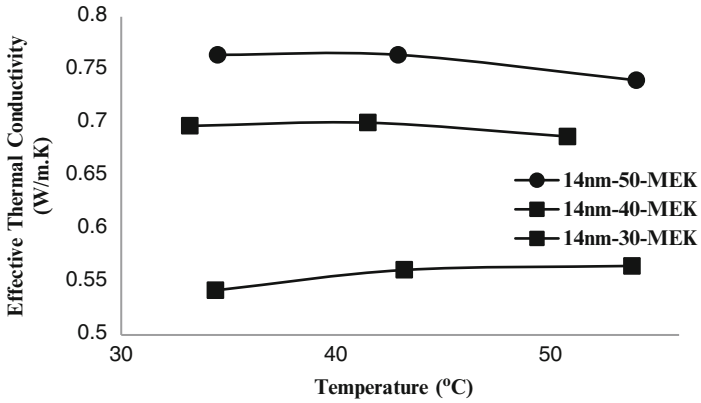

Fig. 19.5 Variation of thermal conductivity as a function of temperature for three different volume fraction (30, 40 and 50 %) 14 nm particle nanocomposites

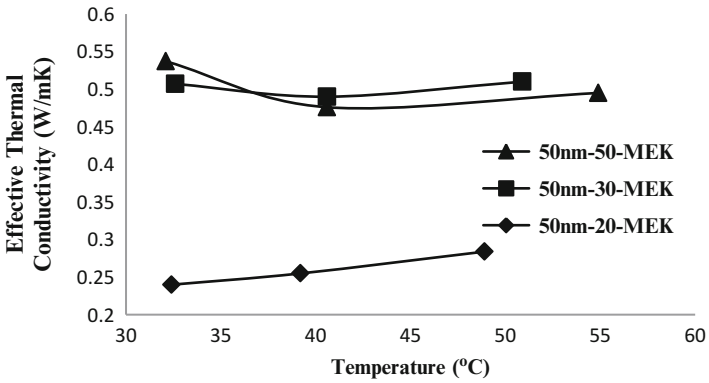

Fig. 19.6 Variation of thermal conductivity with temperature (T) for functionalized 50 nm composites

19.5.2 Variation of Thermal Conductivity with Temperature

In most materials, it is obvious that the thermal conductivity is highly influenced by the working temperature. Therefore surface functionalized specimens were tested at different temperature to determine how the variation in temperature could influence the composite system. Figure 19.5 shows the variation of thermal conductivity as a function of temperature for three different volume fractions (30, 40 and 50 %) of 14 nm particle filled nanocomposites.

As shown in Fig. 19.5, for the low volume fraction (30 %), the thermal conductivity increases as the temperature increases. This is expected because an increase in temperature will increase the thermal conductivity of the polymer and the particle. Note in the lower volume fraction, the polymer is the dominant factor, and the thermal conductivity remains at a low value. However, a different trend is observed in the case of the higher volume fraction: for example, for (50 %) composites where the thermal conductivity decreases as the temperature increases and for (40 %) composites where the thermal conductivity first increases and then decrease as the temperature increases. The reason behind the decrease in thermal conductivity for composites with higher volume fractions is not clear; however, it could be associated with a presence of voids or porosity within the composite. The possibility of voids and porosity in composites is high in the case of higher volume fractions. During high temperatures due to the expansion of the composites, the void size could increase and result in a lowering of the thermal conductivity.

A similar trend was observed for the case of higher particle size as shown in Fig. 19.6. The thermal conductivity of the composites increases with temperature at lower volume fractions and decreases with temperature at higher volume fractions. However, unlike the small particle size (14 nm) in the case of composites with larger particle size (50 nm), the thermal conductivity decreases with temperature at a volume fraction of 30 %. It is interesting to note that, in the case of larger particle size the reduction in thermal conductivity is observed at lower volume fractions. One can expect more porosity in nanocomposites with larger particle size than the smaller particle size and this could result in the reduction of thermal conductivity as the porosity enlarges with the temperature. However, additional study is required to understand the reasons in greater detail.

19.6 Conclusion

The thermal conductivity of particle reinforced polymer nanocomposites is investigated both analytically and experimentally. The effect of particle functionalization, particle size, volume fraction, and temperature on the effective thermal conductivity of the nanocomposites is investigated. Both the experimental and the analytical model agreed. Based on the experimental and analytical studies, the findings are summarized below.

- Functionalizing particles have improved both interfacial bonding and uniform distribution of the particles in the matrix.
- The thermal conductivity of the nanocomposites increases with the particle volume fractions.
- The thermal conductivity of the nanocomposites decreases with the particle size at the same volume fraction.
- The thermal conductivity of the nanocomposites increases with the temperature at lower volume fractions and decreases with the temperature at higher volume fraction.
- The thermal conductivity of the nanocomposites decreases with the particle size at the same volume fraction.

Acknowledgments The financial support of the National Science Foundation under Grant No. EEC-1342379 is gratefully acknowledged. The materials have been fabricated by Prof. Sanat Kumar's group at Columbia University and are also gratefully acknowledged.

References

1. Weindenfeller B, Hofer M, Schilling FR (2004) Thermal conductivity, thermal diffusivity and specific heat capacity of particle filled polypropylene. Compos Part A Appl Sci Manuf 35:423–429
2. Naik NK, Asmelash A, Kavala VR, Veerraju C (2007) Interlaminar shear properties of polymer matrix composites: strain rate effect. Mech Mater 39:1043–1052
3. Kidane A (2013) On the failure and fracture of polymer foam containing discontinuities. ISRN Mater Sci 2013:1–9
4. Kochetov R, Korobko AV, Andritsch T, Morshuis PHF, Picken SJ (2011) Modeling of thermal conductivity in polymer nanocomposites and the impact of the interface between filler and matrix. J Phys Appl Phys 44:395401
5. Carson JK (2011) Measurement and modeling of the thermal conductivity of dispersed aluminum composites. Int Commun Heat Mass Transf 38:1024–1028
6. Lu TJ, Hutchison JW (1994) Effect of matrix cracking and interface sliding on the thermal expansion of fiber-reinforced composites. Composite 26:403–414
7. Nan C-W, Birringer R, Clarke DR, Gleiter H (1997) Effective thermal conductivity of particulate composites with interfacial thermal resistance. J Appl Phys 81:6692
8. Nielsen LE (1974) The thermal and electrical conductivity of two-phase systems. Ind Eng Chem Fundam 13:17–20
9. Moll JF, Akcora P, Rungta A, Gong S, Colby RH, Benicewicz BC, Kumar SK (2011) Mechanical reinforcement in polymer melts filled with polymer grafted nanoparticles. Macromolecules 44(18):7473–7477

Chapter 20
Curing Induced Shrinkage: Measurement and Effect of Micro-/Nano-Modified Resins on Tensile Strengths

Anton Khomenko, Ermias G. Koricho, and Mahmoodul Haq

Abstract Fiber reinforced composites are widely used in automotive, aerospace and marine applications because of their light weight, low costs and excellent chemical resistance properties. Physical and chemical behavior of these composites is dependent on their matrix properties. The curing process of resins/matrix can introduce considerable shrinkage, which based on the component and its boundary conditions can detriment the strength of these materials and resulting components. One way to control the curing-induced effects is reinforcement of the resins with micro- and nano-fillers. In this work, the effect of various micro- and nano-fillers (3M™ Glass Bubbles iM16K and Cloisite® 30B nanoclay) in epoxy resin (SC-15) on curing-induced shrinkage and resulting tensile strengths was evaluated. Additionally, volumetric shrinkage (un-restrained) and curing-induced strains (ASTM D638 tensile tests) were measured by AccuPyc™ II 1340 pycnometer and fiber Bragg-grating (FBG) sensors respectively. A special technique was developed to correct the pycnometer measurement technique and make them independent on the testing chamber temperature. Results revealed that the morphology of the fillers (platelets/spherical) and their concentration significantly influence the curing-induced strains and associated shrinkage. Although such observations were expected, detailed quantification on the volumetric shrinkage and its effect on structural components made of such resins are not well documented. Overall, the study uses a novel technique to correct the pycnometer measurement technique and provides the groundwork for understanding the influence of the type and content of the fillers on the curing-induced shrinkage process. This will provide improved dimensional stability and reduce curing-induced residual stresses on resulting composites.

Keywords Curing-induced shrinkage • SC-15 epoxy resin • Nano-modification • Pycnometer • Fiber Bragg-grating sensor

20.1 Introduction

Composites are being increasingly used in aerospace, marine, and automotive sectors because of their light weight, high corrosion resistance, and excellent mechanical properties at elevated temperatures. However, during isothermal curing of epoxy resins, the polymerization of the three-dimensional network involves densification and hence a decrease in the resin volume [1, 2].

When the resin cures in geometrically constrained environment, such as between plates separated by a fixed spacer, or within the interstices present between consolidated fibers in the case of composite material processing, residual stresses are developed within the resin. These stresses may exceed the intrinsic strength of the resin at a given time, which depends on its degree of conversion. As a result it may cause early composite failure due to warpage, void formation, stress cracking, delamination and poor fiber-matrix adhesion [3].

One way to avoid structural defects due to curing-induced shrinkage is to use epoxy resins in combination with stiffer reinforcements [3]. It was demonstrated that addition of low concentrations of nanoparticles into polymers is a great solution to improve their mechanical performances without compromising on density, toughness or manufacturing process [4]. Therefore it is essential to study the influence of micro- and nano-modification of epoxy resin on the curing-induced

A. Khomenko (✉) • E.G. Koricho • M. Haq
Composite Vehicle Research Center, Michigan State University, 2727 Alliance Drive, Lansing, MI 48910, USA
e-mail: khomenka@msu.edu; haqmahmo@egr.msu.edu

G. Tandon (ed.), *Composite, Hybrid, and Multifunctional Materials, Volume 4: Proceedings of the 2014 Annual Conference on Experimental and Applied Mechanics*, Conference Proceedings of the Society for Experimental Mechanics Series,
DOI 10.1007/978-3-319-06992-0_20,

shrinkage and residual stresses in order to improve dimensional stability and reduce curing-induced residual stress of resulting composite structures.

One of the promising fillers for improvement of the dimensional stability in composite part productions is microsphere glass bubbles. Initially, glass bubbles were designed to decrease the weight, improve impact strength and decrease the mold cycle times for composite structures [5]. Moreover, composites made of glass bubbles/epoxy resin mix were found to resist corrosion and high pressure while low density of glass bubbles produced buoyancy. Combined together these properties make such composites ideal for marine/sub-sea applications [6]. Furthermore, adding the glass bubbles in epoxy resin reduces the permittivity which makes these composites appealing for electrical applications [7]. On the other hand, nanoclay has gained considerable attention for enhancing the mechanical, thermal, and chemical properties of composite materials. Cloisite® 30B nanoclay is known to slightly increase tensile strength of epoxy resin [8], substantially improve residual strength of composite after the impact [4] and significantly reduce water uptake [9]. However, mechanical properties of resulting composites start to deteriorate with the increase of the filler content over certain threshold [7, 8]. Moreover, with the increase in nanoclay, concentration, the resin flow speed significantly decreases, therefore strongly affects the wetting process of laminates in composite manufacturing [8].

In this work, micro- and nano-filler were used as additives to epoxy resin, i.e. 3M™ Glass Bubbles iM16K and Cloisite® 30B nanoclay respectively. Varying filler content was considered as a main parameter in study of its effects on the resin shrinkage and residual strains. Volumetric measurements were made with pycnometer and the residual strains were measured using embedded FBG. A special technique was developed to adjust volumetric measurements provided by the pycnometer equipment. After comparison of linear and volumetric shrinkage of pristine, micro- and nano-modified resins, the tensile properties of these resins after the curing were also compared. This study shows that pycnometer along with the proposed measurement technique can be used for precise volumetric measurements regardless of the testing chamber temperature. This provides the foundation for understanding curing-induced effects on strengths of micro- and nano-modified resins and resulting composite structures.

20.2 Specimen Preparation

20.2.1 Processing of Micro- and Nano-fillers in Epoxy Resin

The resin used was two part toughened epoxy, namely SC-15 obtained from Applied Poleramic. The micro- and nano-fillers used included: Cloisite® 30B (Southern Clay Products, Inc., TX), and 3M™ Glass Bubbles iM16K (3M Center, MN). As mentioned earlier, high fillers contents in epoxies can deteriorate resulting composites mechanical properties, hence relatively lower weight contents were selected in this work: 0.5, 1, 2, 3 and 5 wt%.

Initially, part A of SC-15 epoxy was mixed with desired concentration of filler and the resulting compound was sonicated (Vibra-Cell™ sonicator) for around 30 min until the total applied energy was 30 kJ. Intermittent sonicating energy (10 s energy: 5 s pause) was applied to control the rise in temperature of compound. Once 30 kJ was applied, the resulting mixture was cooled at room temperature for 10 min, followed by mixing of part B of SC-15 epoxy. The solution was mixed thoroughly, degassed and cured in a convection oven at 60 °C for 2 h followed by post curing at 94 °C for 4 h.

20.2.2 Experimental Sample Preparation

The samples for volumetric measurements were prepared by placing pristine and modified epoxy systems in 2.5 cm^3 disposable aluminum cups (see Fig. 20.1). The initial mass of epoxy resin was recorded and monitored between consecutive volumetric measurements.

The samples for residual strain measurements were prepared according to ASTM D638 standard with FBG sensor longitudinally embedded in the center. The mold was modified in order to keep FBG sensor elevated and in the center of the specimen. Two cases were studied: pristine SC-15 epoxy resin and SC-15 resin with 5 wt% of 3M™ Glass Bubbles iM16K. The specimen before and after the curing are shown in Fig. 20.2a, b respectively.

Fig. 20.1 Micro- and nano-modified epoxy resin samples prepared for volumetric measurements

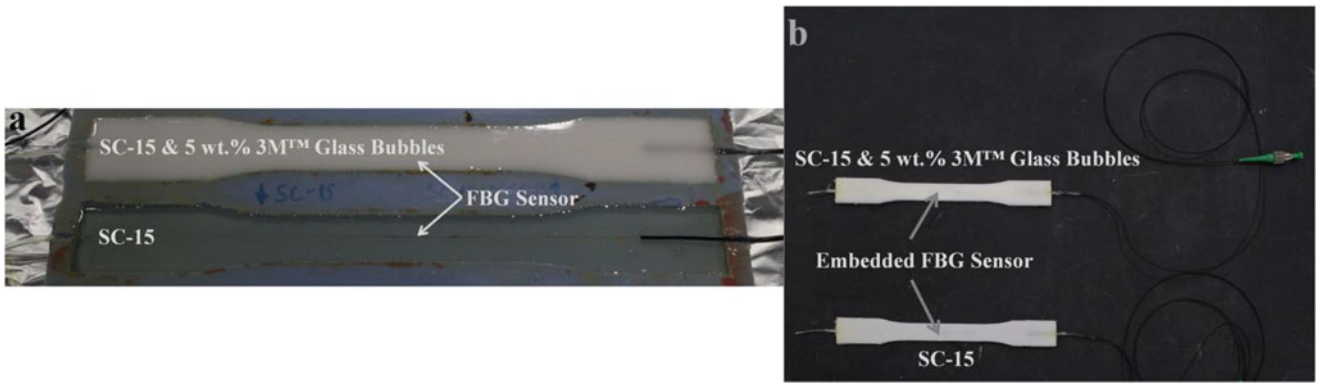

Fig. 20.2 SC-15 and SC-15 with 5 wt% of 3M™ Glass Bubbles epoxy resin (**a**) before the curing, (**b**) after the curing

20.3 Experimental Tools and Methodology

20.3.1 Volumetric Shrinkage Measurements Using Pycnometer

Volumetric measurements of micro- and nano-modified epoxy resin before and after the curing were made with AccuPyc™ II 1340 pycnometer provided by Micromeritics. The AccuPyc works by measuring the amount of displaced gas at a constant chamber temperature: the pressure changes observed upon filling the sample chamber and then discharging it into a second empty chamber allows computation of the sample volume. The instrument automatically purges water and volatiles from the sample and then repeats the analysis until successive measurements converge upon a consistent result [3, 10]. However, it was found that the chamber temperature changes depending on sample type (epoxies are usually exothermic), thereby the volumetric measurements made with pycnometer become un-reliable, and further research is needed to identify apparatus or measurement methodology-induced errors [3]. In this work, a special technique was developed (based on experimental observations) to overcome this problem and correct the data to the true values by making volumetric measurements independent on the testing chamber temperature.

To verify the mass conservation during the curing process, the mass of the each resin sample was measured before and after the curing process, followed by volumetric measurements. As it was expected, the mass of resin samples was found to be constant. Afterwards volumetric measurements were adjusted according to the developed technique, the curing-induced shrinkage was obtained.

20.3.2 Linear Shrinkage Measurements Using FBG

Residual strains caused by curing-induced shrinkage were measured with FBG sensors embedded in micro- and nano-modified epoxy resin. FBG is a sandwich-like distributed reflector with periodically changed refractive index that is embedded into the optical fiber [11]. Such a structure acts as an optical filter that transmits the entire spectrum of the light source and reflects back the resonant, Bragg wavelength. Bragg wavelength is given by the following Eq. 20.1:

$$\lambda_B = 2n_{eff}\Lambda, \tag{20.1}$$

where n_{eff} is the effective refractive index of the core and Λ is the period of Bragg-grating. The spectrum bandwidth of back reflected radiation also depends on the effective refractive index of the fiber core and Bragg-grating period. As one can see the perturbation of Bragg-grating period results in the shift of Bragg wavelength: the strain response arises due to both the physical elongation of the sensor and the change in fiber effective refractive index due to photoelastic effects, whereas the thermal response arises due to the inherent thermal expansion of the fiber material and the temperature dependence of the refractive index.

Wavelength-encoded nature of the FBG output provides a built-in self-referencing capability for the sensor. Since the wavelength is an absolute parameter, the output does not depend directly on the total light levels, losses in the connecting fibers and couplers, or source power. Moreover, the fiber and sensor have relatively small dimensions; therefore embedding of FBG sensor does not affect the intrinsic properties of the host. These advantages of FBG sensors along with its immunity to electromagnetic interference, lightweight, and high sensitivity make it very appealing for many areas of NDE applications, such as internal strain measurements during epoxy resin curing [12].

Spectral responses, i.e. Bragg wavelength and Full Width at Half Maximum (FWHM) of FBG sensors embedded in SC-15 epoxy resin and SC-15 with 5 % of 3M™ Glass Bubbles iM16K before and after the resin curing were recorded in PC using Micron Optics Optical Sensing Interrogator sm125-700. Thereafter, associated curing-induced residual strains were calculated and compared to volumetric shrinkage of the resin.

20.4 Experimental Results and Discussion

20.4.1 Volumetric Shrinkage of Pristine, Micro- and Nano-Modified Epoxy Resin

In the first set of experiments, volumetric shrinkage of pristine, micro- and nano-modified resins with filler concentration of 0.5, 1, 2, 3, and 5 wt% was measured. In order to understand the influence of the filler, the measured volumetric shrinkage was compared to "computed" shrinkage. The computed shrinkage takes into account only the volumetric changes and ignores all filler-induced effects. The difference of the computed and measured volumetric shrinkage is considered as "filler influence". The term filler influence has been coined to summarize the total contribution of the filler properties that include the following, but not limited to: filler morphology, aspect ratios, chemical modifications, etc. Individual contributions from each of these factors is beyond the scope of the work. Ideally, the difference between the computed and measured shrinkages is an indication of filler efficiency in reducing the shrinkage for the particular concentration.

Figure 20.3 shows the measured and computed volumetric shrinkage of SC-15 epoxy resin modified with Cloisite® 30B nanoclay. As it can be seen from Fig. 20.3, the volumetric shrinkage follows a general trend of reducing shrinkage with increasing concentration (as also observed in computed shrinkage). Nevertheless, the maximum "filler influence" of Cloisite® 30B on resin shrinkage (0.128 %) was found to be at 3 wt% filler content. This indicates that the optimal Cloisite® 30B nanoclay concentration that reduces epoxy resin volumetric shrinkage was 3 wt%.

Figure 20.4 shows the measured and computed volumetric shrinkage of SC-15 epoxy resin modified with 3M™ Glass Bubbles. Unlike Cloisite® 30B modified resin, the effect of glass bubbles concentration on resin shrinkage was fairly

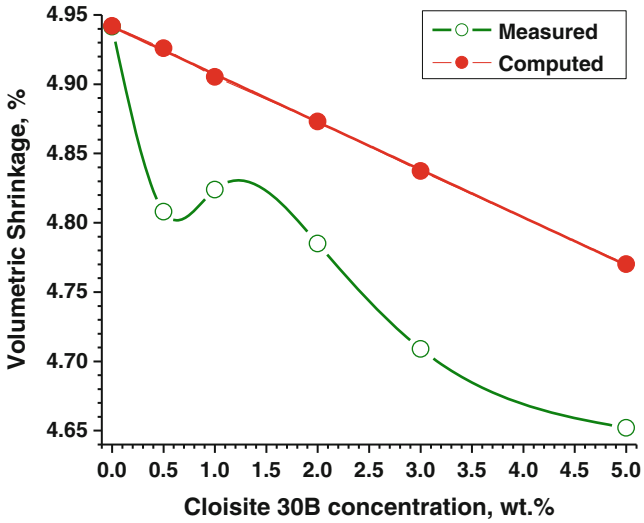

Fig. 20.3 Measured and computed volumetric shrinkage of Cloisite® 30B nanoclay modified SC-15 epoxy resin

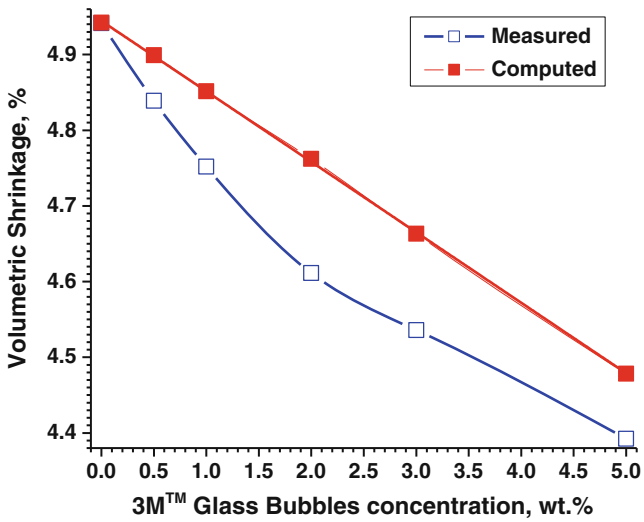

Fig. 20.4 Measured and calculated volumetric shrinkage of 3M™ Glass Bubbles iM16K modified SC-15 epoxy resin

monotonic with the maximum "filler influence" (0.151 %) located at 2 wt% filler content. This implies that 2 wt% concentration produced the optimal shrinkage in epoxy resin. As explained earlier, higher concentrations can further reduce shrinkage, but the maximum filler efficiency in reducing the shrinkage was obtained by comparing the computed and measured shrinkages. Additionally, the higher filler contents can deteriorate material properties while reducing workability.

Figure 20.5 illustrates comparison of measured volumetric shrinkage for SC-15 resins modified with Cloisite 30B® and glass bubbles.

If the density of the pristine resin and mass content of the filler are known and there is no chemical reaction between the filler and the resin, the density of the filler inside the modified resin can be calculated according to the Eq. 20.2:

$$\rho_{\text{filler}} = \frac{nm}{V - (1-n)\frac{m}{\rho_{\text{resin}}}}, \tag{20.2}$$

where ρ_{resin} is the density of pristine resin, m and V are the mass and volume modified resin respectively, n is the concentration of the filler. Using Eq. 20.2 the density of Cloisite® 30B and 3M™ Glass Bubbles in SC-15 epoxy resin was calculated and compared to the nominal density. In case of 3M™ Glass Bubbles, the calculated density was in good correspondence with nominal density: 0.58 ± 0.03 and 0.46 ± 0.03 g/cm^3 respectively [5]. This implies that glass bubbles are well embedded in the epoxy resin. However, in case of Cloisite® 30B, the calculated density was considerably lower than

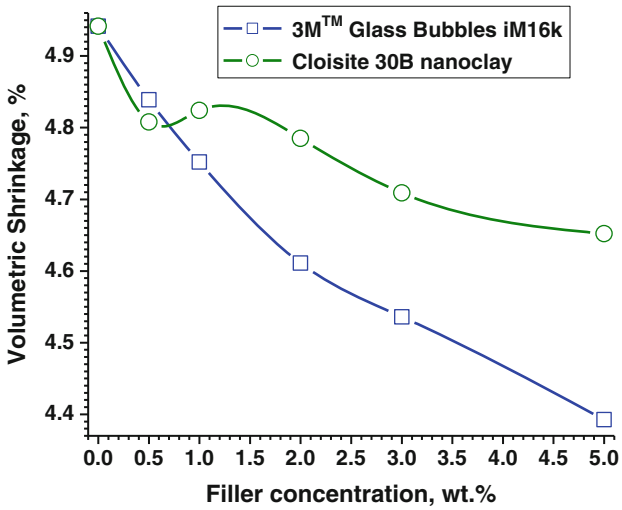

Fig. 20.5 Comparison of measured volumetric shrinkage for Cloisite® 30B nanoclay and 3M™ Glass Bubbles iM16K modified SC-15 epoxy resin

nominal density: 1.57 ± 0.08 and 1.98 g/cm^3 respectively [13]. It is suggested that due to the morphology of the particle (platelet), Cloisite® 30B tends to increase its volume inside the modified epoxy resin by creating buffer zone around the particle. This may be due to the polymer penetration into the galleries of intercalated particles [14].

20.4.2 Residual Strains and Tensile Properties of Pristine and Micro-glass Bubble Modified Epoxy Resin

In the second set of experiments curing-induced strains for pristine and glass bubbles (5 wt%) reinforced SC-15 epoxy were measured. The FWHM of the Bragg wavelength was monitored before and after the resin curing process and was found to remain constant (0.35 nm). This implies the uniform curing-induced shrinkage of both pristine and micro-modified SC-15 resins [11]. Curing-induced strains were found to be 2,661 and 2,061 με for pristine and 5 wt% glass bubbles reinforced SC-15 respectively. Isotropic volumetric shrinkage can be related to linear shrinkage strains using Eq. 20.3:

$$V_{\text{iso}}^{\%} = \frac{\Delta V}{V} = 3\varepsilon - 3\varepsilon^2 + \varepsilon^3, \tag{20.3}$$

where $V_{\text{iso}}^{\%}$ is the isotropic volumetric shrinkage, ε is the linear shrinkage strain. Calculated from Eq. 20.3, isotropic shrinkage for unmodified and 5 wt% glass bubbles reinforced SC-15 was 0.80 % and 0.62 % respectively. However, volumetric shrinkage measured with pycnometer was significantly higher: 4.92 and 4.39 % for SC-15 and 5 wt% glass bubbles reinforced SC-15 respectively. One of the main reasons for discrepancy of volumetric shrinkage measured by pycnometer and FBG is geometry profile. In case of pycnometer volumetric shrinkage was measured for the specimen confined in cylindrical cup, whereas FBG was measuring linear shrinkage for flat, long and thin cross-section specimen, according to ASTM D638. Thus geometry profile plays the key role for linear shrinkage measurements and volumetric shrinkage of epoxy resins cannot be explained directly by means of linear shrinkage.

Finally, the tensile properties of SC-15 and SC-15 micro-modified with 5 wt% of 3M™ Glass Bubbles iM16K epoxy resin samples were compared. According to ASTM D638 the specimens were subjected to monotonic tensile loading with a loading rate of 2 mm/min. As expected, the ultimate tensile stress of 5 wt% glass bubbles reinforced SC-15 was lower than pristine SC-15, 45.7 MPa vs. 58.2 MPa respectively. However, Young's modulus of glass bubbles modified (5 wt%) samples increased significantly: 2.45 GPa compared to 1.24 GPa for pristine SC-15 resin. Therefore, substantial increase in material stiffness with slight reduction in tensile strength is possible by proper micro-modification of the resin. Furthermore, the study used only a single concentration (5 wt%) to evaluated the effect on mechanical properties. Further studies including varying concentrations, sample geometries and boundary conditions that replicate various bonded joints should be studied in detail to fully evaluate the effect of the filler and its role in reducing shrinkage-associated properties.

20.5 Conclusions

The effect of various micro- and nano-fillers (iM16K 3M™ Glass Bubbles and Cloisite® 30B nanoclay) with different weight contents in epoxy resin (SC-15) on polymerization shrinkage was studied. A special technique was developed to overcome the pycnometer measurement methodology and to obtain the true values. This was done by making volumetric measurements independent on the testing chamber temperature. It was found that in case of nanoclay the dependence of the filler content on the resin shrinkage was significant and non-linear, while 3M™ Glass Bubbles iM16K showed relatively monotonic behavior. Optimum filler mass content providing minimum resin shrinkage was found to be 2 and 3 wt% for 3M™ Glass Bubbles iM16K and Cloisite® 30B nanoclay respectively. Comparison of linear shrinkage (curing-induced strains) to volumetric shrinkage revealed that geometry profile plays a key role in case of linear shrinkage. Therefore volumetric shrinkage of epoxy resins cannot be explained directly by means of linear shrinkage. It was found, that substantial increase in material stiffness with small reduction in tensile strength can be achieved through micro-glass bubbles reinforcement of the resin. Overall, the study uses novel technique to correct pycnometer methodology and lays the groundwork for understanding the influence of the type and content of the fillers on the curing-induced shrinkage process. That in turn will allow improved dimensional stability and reduce curing-induced residual stress of resulting composite structures.

Acknowledgements This work was supported by US Army under TACOM/MSU Cooperative Agreement No. W56HZV-07-2-0007. The authors acknowledge Mr. Paul Kester and Micromeritics for the provision of demo-equipment (AccuPyc™ II 1340 pycnometer). The authors also acknowledge the in-kind material contribution by Southern Clay Products Inc., TX and 3M Center, MN.

References

1. Eom Y, Boogh L, Michaud V, Sunderland P, Mason J-A (2001) Stress-initiated void formation during cure of a three-dimensionally constrained thermoset resin. Polym Eng Sci 41(3):492–503
2. Msallem YA, Jacquemin F, Poitou A (2010) Residual stresses formation during the manufacturing process of epoxy matrix composites: resin yield stress and anisotropic chemical shrinkage. Int J Mater Forming 3(2 Supplement):1363–1372
3. Shah DU, Schubel PJ (2010) Evaluation of cure shrinkage measurement techniques for thermosetting resins. Polym Test 29(6):629–639
4. Reis PNB, Ferreira JAM, Zhang ZY, Benameur T, Richardson MOW (2014) Impact strength of composites with nano-enhanced resin after fire exposure. Compos Part B Eng 56:290–295
5. Yalcin B, Amos SE, Williams MJ, Gunes IS, Ista TK, Friedrich S, Doering M, Yamabe T (2013) 3M™ glass bubbles iM16K for reinforced thermoplastics. 3M Technical paper
6. Lin W-H, Jen M-HR (1998) Manufacturing and mechanical properties of glass bubbles/epoxy particulate composite. J Compos Mater 32 (15):1356–1390
7. Chen J, Meng D, Feng Y, Li N, Krivda A, Greuter F, Rocks J.F (2013) Epoxy composites with glass bubbles for electrical application. In: Proceedings of electrical insulation conference (EIC), 2013 IEEE, pp 20–24
8. Kanny K, Mohan TP (2014) Resin infusion analysis of nanoclay filled glass fiber laminates. Compos Part B Eng 58:328–334
9. Alamri H, Low IM (2012) Effect of water absorption on the mechanical properties of nano-filler reinforced epoxy nanocomposites. Mater Des 42:214–222
10. http://www.micromeritics.com/product-showcase/AccuPyc-II-1340-Pycnometer/AccuPyc-II-1340-Density-Analyzer-Technique-Overview.aspx
11. Haq M, Khomenko A, Udpa L, Udpa S (2014) Fiber Bragg-grating sensor array for health monitoring of bonded composite lap-joints. Exp Mech Compos Hybrid Multifunct Mater 6:189–195, Ch. 22
12. Harsch M, Karger-Kocsis J, Herzog F, Fejős M (2011) Effect of cure regime on internal strain and stress development in a filled epoxy resin assessed by fiber Bragg-grating optical strain and normal force measurements. J Reinforced Plast Compos 30(17):1417–1427
13. www.matweb.com/search/datasheettext.aspx?matguid=1213e923b3544011850ad51fa523571c
14. Haq M, Burgueño R, Mohanty AK, Misra M (2009) Processing techniques for bio-based unsaturated-polyester/clay nanocomposites: tensile properties, efficiency & limits. Compos Part A Appl Sci Manuf 40(4):394–403

Chapter 21
Graphene Reinforced Silicon Carbide Nanocomposites: Processing and Properties

Arif Rahman, Ashish Singh, Sriharsha Karumuri, Sandip P. Harimkar, Kaan A. Kalkan, and Raman P. Singh

Abstract This study investigates the effect of graphene nanoplatelets on the microstructure and mechanical properties of silicon carbide (SiC). Graphene nanoplatelets are dispersed in a liquid preceramic polymer by ball milling. Pyrolysis of the graphene nanoplatelet–preceramic polymer slurry results in near-stoichiometric SiC–graphene nanoplatelet powder. This method leads to improved dispersion of graphene in the SiC matrix as compared to conventional mechanical blending of dry powders and thereby significantly influences the resulting mechanical properties. Subsequently, spark plasma sintering (SPS) is used to consolidate dense bulk SiC–graphene composites with varying graphene content up to a maximum of 5 wt%. X-ray diffraction (XRD) investigation reveal that inclusion of graphene restricts grain growth of SiC matrix during SPS processing. Fracture toughness of SiC-graphene composite is increased by 40 % with the inclusion of 2 wt% graphene nanoplatelets. However, for higher graphene content the change in fracture toughness is limited. Improvement in fracture toughness is due to crack bridging reinforcing mechanism provided by the graphene platelets. Finally, Raman spectroscopy is used to understand the effect of SPS processing on integrity of graphene nanoplatelets.

Keywords Graphene • Silicon carbide • Raman spectroscopy • Fracture toughness • Flexural strength

21.1 Introduction

Even though SiC has excellent mechanical properties, its application has been limited due to lower fracture toughness of the material [1–3]. To induce crack resistance in SiC, fillers such as whiskers, particulate or carbon fibers have been studied over the years [4–7]. Reinforcing SiC with carbon fibers not only overcome low toughness issue but also the high flaw sensitivity of monolithic SiC ceramics [4]. It has been reported that the interfacial bonding between carbon fiber and SiC dominates the mechanical properties of the composite [8]. Fiber debonding and pullouts mechanisms, which occur at the fiber-matrix interface when the interface is neither very strong nor weak, increases the toughness of carbon fiber reinforced SiC. Various processing techniques such as Chemical Vapor Infiltration (CVI), Liquid Polymer Infiltration (LPI), and Melt Infiltration (MI) have been used to fabricate SiC/C composites. However, these methods are often associated with high processing cost and time consuming. Furthermore, oxidation of carbon fiber during processing is detrimental to properties of the composite. As an alternative, short carbon fiber reinforced SiC composite have been fabricated due to its ease of processability using spark plasma sintering. However, sintering additives have been used during sintering process in order to aid densification [4, 5]. Similar studies on carbon-fiber reinforced SiC is also studied by Tang et al. where volume percentage of C fiber was varied and the composite was processed using hot pressing [7]. Even tough carbon fiber-SiC composites have been well studied for quite some time now, none of these studies reported significant improvement in fracture toughness for SiC ceramics. Note that the SiC ceramic matrices in most of these investigations had micro-grained structure (grain size significantly greater than 500 nm) with diameters of carbon fibers in the range of 5–25 μm.

A. Rahman • A. Singh • S. Karumuri • S.P. Harimkar • K.A. Kalkan • R.P. Singh (✉)
School of Mechanical and Aerospace Engineering, Oklahoma State University, Stillwater, OK 74078, USA
e-mail: raman.singh@okstate.edu

G. Tandon (ed.), *Composite, Hybrid, and Multifunctional Materials, Volume 4: Proceedings of the 2014 Annual Conference on Experimental and Applied Mechanics*, Conference Proceedings of the Society for Experimental Mechanics Series,
DOI 10.1007/978-3-319-06992-0_21,

Recently, carbon nanotubes (CNTs) are attracting significant attention as potential toughening agents in micro-grained ceramics due to its excellent properties, such as low density, high aspect ratio (1000–10000), tensile strength (150 GPa), and an elastic modulus of 1 TPa [9]. Initial investigations on toughness of CNT/ceramic composites indicated little or no improvement in fracture toughness due to difficulties such as dispersion of CNT in matrix, and methods used for determining fracture toughness that failed to uncover the actual failure mechanism. Zhan et al. have observed three fold increase in fracture toughness for 10 vol% CNT-Al_2O_3 compared to pure alumina [10]. Recently, CNT reinforced ceramics composites were processed using powder metallurgy routes where dispersion of CNT in the matrix were achieved by ball milling using high energy ball mills. It should be noted that conventional hot pressing was avoided while compacting these materials as hot pressing might damage CNTs and degrade their properties [10]. It was observed that conventional sintering techniques like hot pressing were not helpful in compacting these composites as sintering this composites at higher temperatures for longer time results in damaging of CNTs. In a recent investigation, Ma et al. reported only incremental (10 %) increase in toughness for CNT reinforced SiC composites processed using conventional hot pressing [11]. While significant progress has been made towards using chemical, mechanical, and ultrasonic methods to enhance the dispersion of the CNTs in various matrices, the non-uniform distribution of CNTs is still a serious issue. High quality carbon nanotubes dispersed effectively in the ceramic matrix is very essential in order to carry loads and transfer stress which results in toughening of the ceramic.

Graphene is a one atom thick 2-D layer of sp^2 carbon arranged in a honeycomb lattice [12, 13]. It is considered the building block of different forms of carbon such as fullerene, carbon nanotube and graphite. While fullerene and carbon nanotube can be visualized as graphene rolled into spherical and cylindrical shape, graphite is basically graphene sheets stacked together to form a 3-D structure. Graphene or few layer of graphene possess a combination of unique set of electrical, optical, and mechanical properties. Specially, these properties provide a way to overcome the shortcomings of other materials that are currently being used or worked on. Mechanical properties of graphene has been much less investigated compared to its electronic and optical properties until recently. Like other allotropes of carbon (CNT), graphene also possess excellent mechanical properties. Recent investigation of suspended graphene sheet using AFM nanoindentation by Lee et al. revealed that graphene is the strongest material ever measured with elastic stiffness of $\sim$ 340 N/m and breaking strength of $\sim$ 42 N/m [14]. These values translates to 1.0 TPa Young's modulus and 130 GPa intrinsic strength for bulk graphite. Moreover, graphene can sustain more than 20 % local strain before fracture. In a separate study, it was shown that intrinsic strength of graphene film reduces slightly as the number layers is increased from single (130 GPa) layer to three layers (101 GPa) [15].

One of the possible ways to utilize these unique properties of graphene is to use it as nanofillers in nanocomposites. Even though graphene/polymer nanocomposite system is well studied for quite some time now, graphene/ceramic composite system has not been well understood. Most of the studies published so far indicate the possibility of improvement in properties due to addition of graphene in ceramic matrix. It has been reported that graphene nanosheet reinforced Al_2O_3 showed a percolation threshold of 3 vol%, however, for 15 vol% graphene nanosheet reinforcement electrical conductivity was increased to 5,709 S/m which is 170 % higher while compared with the result available for CNT reinforced Al_2O_3 [16]. This improvement in electrical conductivity was attributed to network like structure of graphene in the composite. It was also observed that graphene nanosheet restrained grain growth of Al_2O_3 in the composite during spark plasma sintering process [17]. Excellent improvement (53 %) in fracture toughness of alumina by graphene reinforcement has also been observed by Wang et al. [17]. This improvement in fracture toughness was mainly due to crack bridging and nanosheet pulling out. Liu et al. reported toughening of a multi-component system of ZrO_2-Al_2O_3 by graphene nanoplatelet [18]. Addition of graphene platelet increased fracture toughness by 40 % by various extrinsic toughening mechanisms. Walker et al. reported a remarkable 235 % increase in fracture toughness of Si_3N_4 by only addition of 1.5 vol% [19]. This increase in fracture toughness was attributed to proper processing of the composite and a new toughening mechanism (out of plane crack deflection) that was observed for these composites. In their work, dispersion of the graphene was achieved by colloidal processing and compaction was obtained by spark plasma sintering. Recently, graphene-Si_3N_4 system has also been studied for tribological properties [20]. It was found that at lower wt% addition graphene bonds strongly to the matrix and does not provide any wear resistance. However, 3 wt% graphene addition reduced wear rate by 60 % compared to monolithic Si_3N_4. In our previous work, we have observed strengthening of SiC matrix with graphene addition due to better dispersion [21].

In the current investigation, a novel approach is presented that combines the techniques of polymer precursor processing and spark plasma sintering (SPS). This process can yield bulk SiC with uniform dispersion of graphene nanoplatelets with the possibilities of retaining grain sizes down to the sub-500 nm range while still being able to fabricate net-shape dense forms. The aim of the study is to establish a novel processing technique to enable fabrication of fine-grained SiC reinforced with uniform graphene dispersion, investigate the microstructure and the mechanical properties as a function of graphene content.

21.2 Material Fabrication

As a first step amorphous–nanocrystalline SiC powder was prepared from a preceramic polymer, allylhydridopolycarbosilane (AHPCS) (Starfire Systems Inc., Malta, NY). The powder preparation process was started by heating the liquid polymer precursor to 650 °C, at 1 °C/min, under an inert atmosphere and then holding it at 650 °C for 10 min. This initiated the cross-linking of the polymer precursor. For complete conversion to amorphous–nanocrystalline SiC, the heating was continued till 1,400 °C, at 3 °C/min. The material was held at the final temperature for 1 h to ensure thermal equilibrium and complete processing. Finally, the material was cooled down to room temperature, at 5 °C/min.

Due to the release of hydrogen gas during the polymer to ceramic conversion, the final material contained large voids. This material was ground using a hand grinder until the particles passed through a colander of mesh size 12 followed by subsequent milling into fine powder ($\sim$ 0.5 μm) using a high energy ball mill (Pulverisette, Fritsch GmbH). Ball milling was performed using a ball-to-powder mass ratio of 5:1 with tungsten carbide (WC) balls as grinding media for 15 min with 750 rpm. Note that the starting powder was amorphous and the purpose of milling was to decrease the particle size without inducing any phase transformation. The amorphous/nanocrystalline powder was subsequently used in spark plasma sintering for processing bulk SiC.

Exfoliated graphene nanoplatelets, xGnP® -M-5 grade (99.5 % carbon) with an average diameter of 5 μm were obtained in dry powder from XG Sciences, Inc. (East Lansing, MI). Two sets of powder were prepared for this study. For preparing SiC-graphene powder mixture, controlled weight fraction (2 and 5 wt%) of graphene nanoplatelets was mixed with AHPCS polymer and ball milled using a planetary ball mill (PM-100, Retsch GmbH, Haan, Germany) for 30 min. Ball milling was performed using a ball-to-powder mass ratio of 10:1 with tungsten carbide (WC) balls as grinding media for 30 min with 300 rpm. Subsequently, this mixture was pyrolyzed using the similar procedure mentioned earlier. The pyrolyzed amorphous/nanocrystalline SiC reinforced with graphene nanoplatelets was carefully milled using parameters mentioned earlier such that uniform mixture without significant damage of graphene nanoplatelets can be achieved. It has been reported that controlled ball mill can aid in exfoliation of graphene nanoplates due to shear component of the applied stress [22]. SiC-graphene composite powder mixtures with varying levels of graphene reinforcements (2 and 5 wt%) was prepared for subsequent SPS densification.

Another set of powder was prepared for comparison. In this case, AHPCS was pyrolyzed first to prepare SiC powder. Then, 2 and 5 wt% graphene nanoplatelets were mixed with SiC powder (prepared from AHPCS) and ball milled in isopropanol as dispersing media using the parameters mentioned previously. For ease of identification, the first set of powder will be referred as AHPCS-2 wt% C, AHPCS-5 wt% C and the second set of powder will be referred as SiC-2 wt% C, SiC-5 wt% C. Note that these are essentially SiC-graphene composite powder prepared in different way.

Spark plasma sintering (SPS) was used to consolidate SiC and SiC-graphene powder using an SPS system (Model 10-3, Thermal Technology, LLC., Santa Rosa, California, USA). The DC pulse cycle for the system was 25 ms on and 5 ms off. The ball milled powder was loaded in a graphite die with an internal diameter of 20 and 10 mm of wall thickness. Graphite felt with a thickness of 4 mm was wrapped around the graphite die to avoid thermal loss during sintering. Temperature of the sample was monitored during sintering using an optical pyrometer through a hole of 2 mm diameter and 5 mm depth in the graphite die. Samples were sintered at 2,000 and 2,100 °C, using a heating rate of 150 °C/min under argon atmosphere. Sintering pressure of 70 MPa and a soak time of 10 min were employed for all the samples.

21.3 Experimental Procedure

Phase analysis of the sintered compacts was performed using Philips Norelco X-ray diffractometer operating with Cu Kα ($\lambda = 1.54178$ Å) radiation at 45 kV and 40 mA. The 2θ diffraction angle was varied between 10° and 90° at a step increment of 0.02° with a count time of 1 s. WITec alpha300 R Raman system with a 532 nm laser excitation was used for detailed investigations on fragmentation and exfoliation of graphene in the SPS sintered compacts. The buoyancy method was used for determining bulk density and porosity of the samples using a density measurement kit along with a high-resolution analytical balance following the ASTM C830–00 test method [23].

Vickers hardness of the polished samples were obtained using a microhardness tester (Tukon microhardness tester, Page–Wilson corporation, Bridgeport, Connecticut, USA) at a load of 49 N applied for 30 s. At least five readings were collected for each sample and an average value is reported. Fracture toughness was estimated by direct crack measurement (DCM) using the Anstis equation (Eq. 21.1) [24]

$$K_{IC} = A\left(\frac{E}{H}\right)^{\frac{1}{2}}\left(\frac{P}{C^{\frac{3}{2}}}\right) \tag{21.1}$$

where A is a geometric constant (0.016), E is the elastic modulus, H is the hardness value, P is the load, and C is the length of the radial crack from the center of the impression of the indent. In this method, toughness value is a function of radial crack length, elastic modulus and hardness. Since, elastic modulus can be a function of porosity, the following equation proposed by Snead et al. was used for calculating elastic modulus, E [25].

$$E = E_0 \exp(-CV_p) \tag{21.2}$$

Where $E_0 = 460$ GPa is the modulus of non-porous SiC, and $C = 3.57$ is a constant.

21.4 Experimental Results

21.4.1 Relative Density and Densification

Variation of relative density as a function of sintering temperature and graphene content is presented in Table 21.1. It is interesting to note that graphene content influence densification along with sintering temperature. Moreover, different dispersion routes also have effect on evolution of porosity in the bulk compact. Absolute density was calculated using rule of mixture as shown in equation (21.3).

$$\rho_c = \frac{1}{(W_f/\rho_f) + (W_m/\rho_m)} \tag{21.3}$$

Where, ρ_c = Density of the composite, W_f and W_m are weight fractions of graphene nanoplatelets and SiC, respectively, $\rho_f = 2.2$ g/cc is density of xGnP platelets and $\rho_m = 3.21$ g/cc is density of SiC.

From Table 21.1 it can be clearly seen that temperature plays an important role in densification with graphene addition. Specially in case of separate graphene addition in SiC matrix using IPA, even at 2,000 °C SPS temperature the relative densities are 85 % for 2 wt% C and 88 % for 5 wt% C addition. Moreover, open porosities are much higher compared to other samples. However, at 2,100 °C density improves for both samples. It is believed that addition of carbon during sintering of SiC activates the sintering process. Furthermore, carbon helps in eliminating the oxide impurities residing at the grain boundaries [26]. At higher sintering temperature the following reaction takes place when there is no excess carbon [27].

$$SiO_2 + nSiC = Si\uparrow + SiO\uparrow + CO\uparrow + (n-1)SiC$$

Table 21.1 Density and open porosity of graphene reinforced SiC samples at 2,000 and 2,100 °C sintering temperature

Sintering temperature (°C)	Sample	Density(g/cc)	Relative density (%)	Open porosity (%)
2,000	SiC	2.95±0.02	92	1.11
2,100	SiC	3.05±0.03	95	0.77
2,000	AHPCS-2 wt% C	2.92±0.09	92	1.70
2,100	AHPCS-2 wt% C	2.98±0.04	94	0.92
2,000	AHPCS-5 wt% C	2.87±0.05	92	4.27
2,100	AHPCS-5 wt% C	2.90±0.05	93	1.66
2,000	SiC-2 wt% C	2.70±0.05	85	11.83
2,100	SiC-2 wt% C	2.91±0.07	92	2.42
2,000	SiC-5 wt% C	2.77±0.03	88	8.73
2,100	SiC-5 wt% C	2.82±0.11	90	4.34

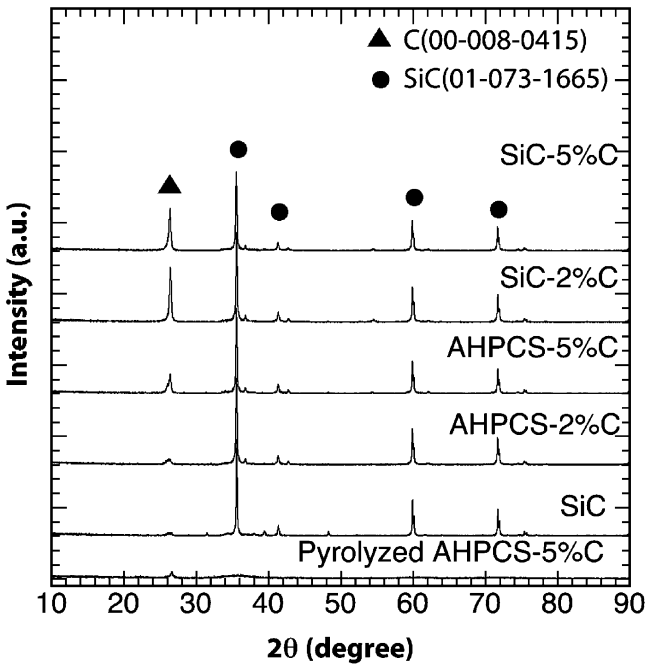

Fig. 21.1 XRD patterns from amorphous SiC-graphene powder and spark plasma sintered graphene-SiC compacts processed at 2,100 °C

Clearly, more volatile products are formed resulting in weight losses at higher sintering temperature. On the other hand, excess carbon leads to the following reaction [27].

$$SiO_2 + nSiC + 3C = CO\uparrow + (n+1)SiC$$

Hence, addition of C would reduce weight losses by reducing the production of volatile phases during sintering. However, addition of carbon can affect densification mechanisms, especially at higher weight fraction. It has been observed that higher weight fraction of only carbon addition can hinder mass transport mechanisms in sintering of SiC [28]. Stobierski et al. performed a systematic study on effect of carbon addition in sintering of SiC [27]. They have observed that addition of 3 wt% or more carbon can affect mass transport mechanism which in turn affects pore elimination process and hinders densification of SiC. Moreover, distribution of carbon content can affect the densification mechanism even at lower weight fraction. This effect is evident in case of SiC-graphene samples where the distribution of graphene is believed to be uneven due to processing technique. For SiC-2 wt% C and SiC-5 wt% C, the densification mechanism is affected due to non-uniform distribution of graphene and results in lower relative density. Increasing the sintering temperature to 2,100 °C, however, provides better densification for all the samples leading to relative density at or above 90 %.

21.4.2 Microstructural Evolution

For the current work, 5 wt% graphene-SiC powder prepared using polymer pyrolysis at 1,400 °C was characterized using X-ray diffraction (XRD). Figure 21.1 shows XRD patterns of starting amorphous/nanocrystalline powder as well as samples compacted using SPS technique. The XRD pattern of the initial graphene-SiC powder, obtained through pyrolysis at 1,400 °C, exhibited characteristic broad halo peaks with diffused intensity indicating an amorphous/nanocrystalline structure. Moreover, a peak at 26.4° for (002) plane of graphite indicates the presence of graphene after pyrolysis. Note that this peak was not observed for powder prepared using only AHPCS. SPS of amorphous/nanocrystalline powder at 2,100 °C resulted in crystallization of amorphous powder during sintering. Peaks at 36°, 42°, 60°, and 72° correspond to (111), (200), (220) and (311) planes of β-SiC (ICCD: 29–1129). It is postulated in literature that well exfoliation and dispersion of graphene platelets will result in either no peak or very small peak at 26.4° [29]. One can observe that for AHPCS-2 wt% C, the peak at 26.4 is very small compared to other samples. Even with AHPCS-5 wt% C the graphene peak intensity is much smaller compared to SiC-2 wt% C and SiC-5 wt% C. This indicates that using a separate solvent for dispersion results in non-uniform distribution.

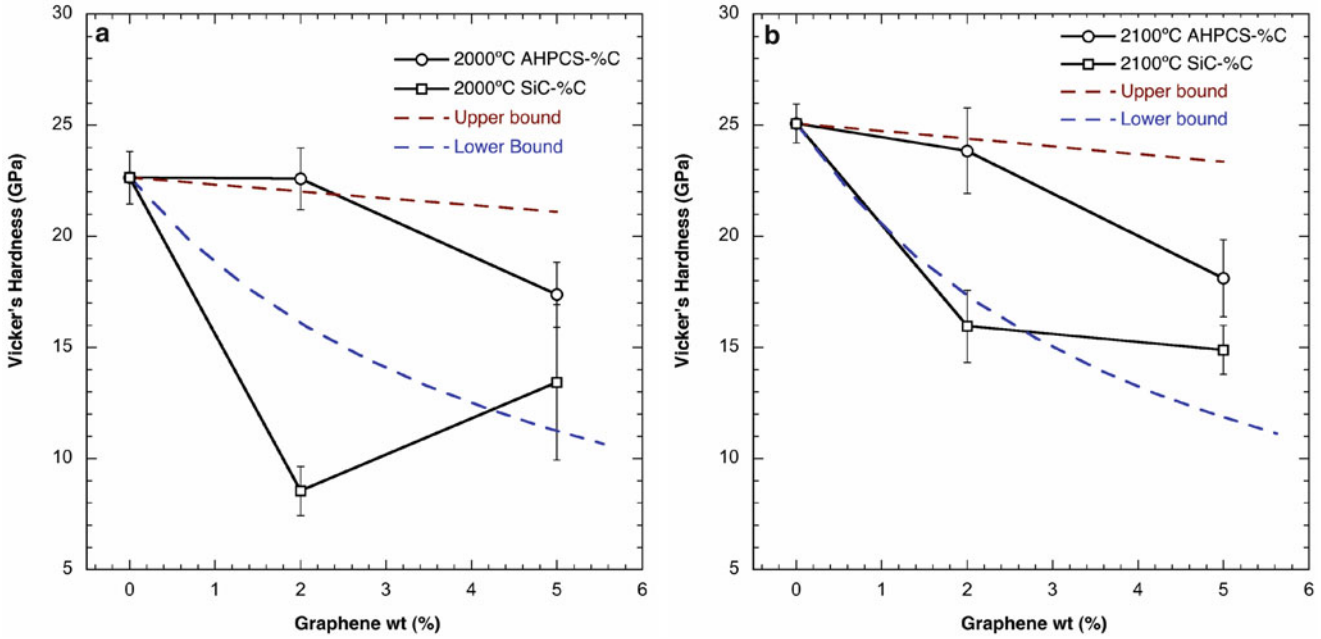

Fig. 21.2 Vickers hardness for (**a**) 2,000 °C samples and (**b**) 2,100 °C samples as a function of graphene weight fraction

Full pattern analysis was performed using XFIT program utilizing fundamental parameters (FP) approach [30]. Calculated average crystallite sizes were 540, 495, 301, 407, and 368 nm for SiC, AHPCS-2%C, AHPCS-5%C, SiC-2%C, and SiC-5%C samples sintered at 2,100 °C, respectively. It has been previously reported that addition of graphene restricts grain growth of ceramic matrix during sintering [31, 32]. Addition of carbon lowers dissociation pressure of SiC system rendering limited mass transport through the gas phase. As a result, surface diffusion mechanism is restricted leading to grain refinement [27]. Similar effect is observed in the current study. For the same sintering temperature, addition of 5 wt% C lead to 40% reduction in grain size.

21.4.3 Effect of Graphene Nanoplatelets on Hardness of Nanocomposites

Vickers hardness is plotted in Fig. 21.2 as a function of graphene weight fraction for graphene-SiC matrix sintered at 2,000 and 2,100 °C. From the figure, we can see that hardness varies as a function of graphene content. Moreover, this variation also depends on the processing route that was used. In literature, various allotropes of carbon such as fiber or nanotube are considered as a soft phase [33] and considered a reason for decrease in hardness of the composites. Recently, Kim reported the use of rule of mixture for estimating the hardness of a composite with a soft and a hard phase as shown below [34].

$$H_c^{up} = v_h H_h + v_s H_s \tag{21.4}$$

$$H_c^{low} = \frac{1}{v_h/H_h + v_s/H_s} \tag{21.5}$$

Where, H_h and H_s are hardness values of hard and soft phases, respectively. v_h and v_s are the volume fractions of hard and soft phases, respectively. The subscript 'up' is for upper bound and subscript 'low' is for lower bound of hardness of the composite. These equations are based on Reuss and Voigt model where Reuss model consider that all the elements of the composite bear equal stress (Eq. (21.5)) and Voigt model considers that all the elements undergo equal strain (Eq. (21.4)). If we consider SiC matrix to be hard phase and graphene nanoplatelets to be soft phase, then we can calculate the volume fraction by using

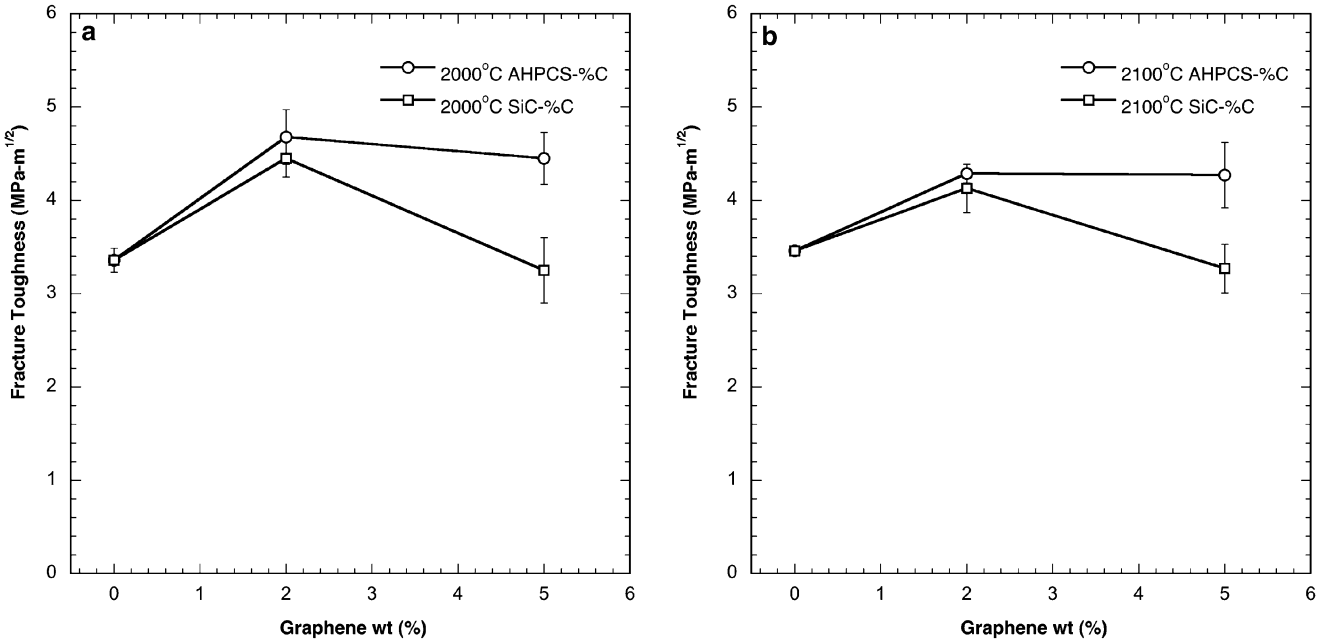

Fig. 21.3 Fracture toughness of (**a**) 2,000 °C samples and (**b**) 2,100 °C samples as a function of graphene weight fraction

$$v_s = \frac{\rho_c}{\rho_s} w_s \tag{21.6}$$

$$v_h = \frac{\rho_c}{\rho_h} w_h \tag{21.7}$$

Where ρ_c is density of the composite, ρ_s and ρ_h are densities of soft and hard phases, respectively. So, the volume fraction of graphene is, $v_s = 0.0292$ when $w_s = 0.02$ % and $v_s = 0.0729$ for $w_s = 0.05$. It should be noted that Reuss and Voigt models do not take porosity into account. Therefore, hardness of SiC was considered to be 22.64 and 25.08 GPa for 2,000 and 2,100 °C sintering temperature respectively. These values represent the hardness of these materials with almost similar porosity. For the soft phase, hardness of graphite was considered to be $H_s = 1.5$ GPa. Following equations (21.4) and (21.5) we found the upper and lower bound of the hardness of the composites as shown in Fig. 21.2.

It is postulated that uniform distribution of soft phase will lead to hardness close to upper bound whereas non-uniform dispersion of soft phase will lead to hardness value close to lower bound. From Fig. 21.2 we can see that for AHPCS-2 wt% C hardness values are almost similar to upper bound values for both 2,000 and 2,100 °C. However, for AHPCS-5 wt% C hardness values are slightly smaller than upper bound values for both 2,000 and 2,100 °C indicating some aggregation. On the contrary, for SiC-%C samples hardness values were close to or lower than lower bound hardness value. Specially, in case of SiC-2 wt% C sintered at 2,000 °C, the hardness value is almost half of lower bound hardness. This sample had much higher porosity ($\sim$ 15 %) compared to all the other samples sintered at 2,000 °C. Thus the reduction in hardness was a convoluted effect of non-uniform distribution of graphene nanoplatelets and higher residual porosity. This indicates agglomeration due to the processing technique can affect hardness adversely.

21.4.4 Toughening by Graphene Nanoplatelets

For the current investigation, fracture toughness values were measured using direct crack measurement (DCM) method. Samples with proper radial cracks were used for toughness measurement. Variation of fracture toughness of graphene-SiC composites is shown in Fig. 21.3. For AHPCS-2 wt% C samples 40 % increase in fracture toughness is observed compared to monolithic SiC at 2,000 °C sintering temperature. Addition of more nanoplatelets do not improve toughness after that. Similarly, we can see improvement of fracture toughness for AHPCS-2 wt% C samples over monolithic SiC at 2,100 °C sintering temperature. Interestingly, SiC-2 wt% C also shows improvement in fracture toughness compared to

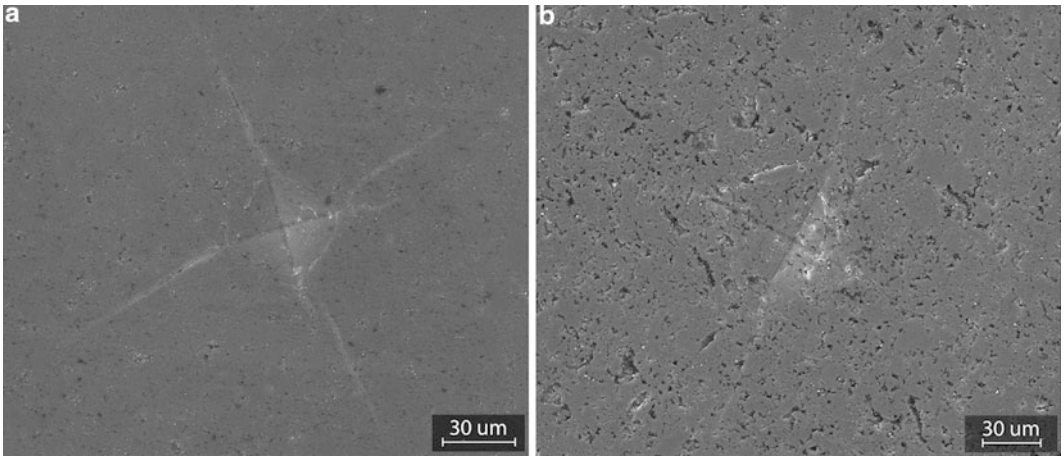

Fig. 21.4 Indentation radial crack shown for (**a**) AHPCS-2 wt% C and (**b**) SiC-2 wt% C sintered at 2,100 °C

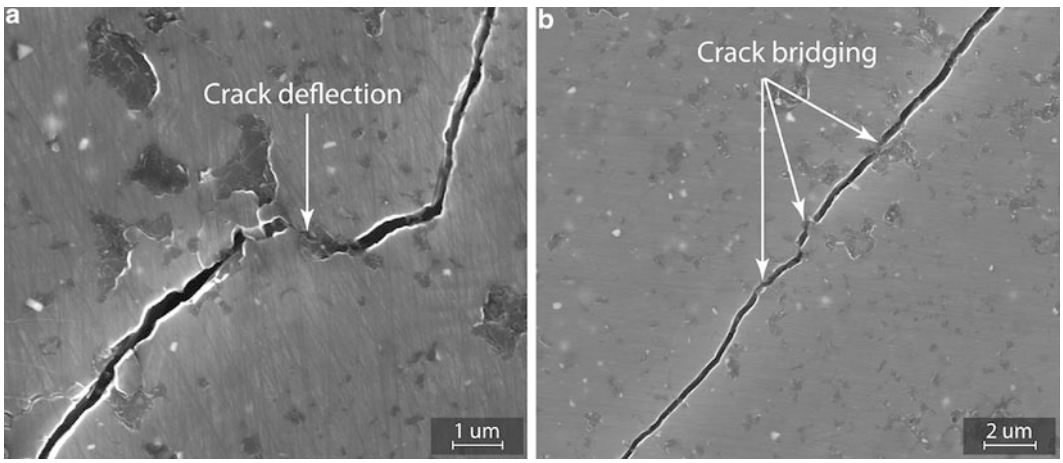

Fig. 21.5 Toughening mechanisms observed for AHPCS-%C samples

monolithic SiC at both sintering temperature. However, we call this improvement 'apparent'. As we know, in DCM method fracture toughness is a function of load, elastic modulus, hardness and radial crack length. If we consider the load and the crack length to be constant, then we get,

$$K_{IC} \propto \left(\frac{E}{H}\right)^{1/2} \tag{21.8}$$

From Eq. (21.8), one can see that fracture toughness is inversely proportional to hardness value. Therefore, reduction in hardness of the material will result in improvement in fracture toughness even though the radial crack length is unaffected by the filler addition. Note that for SiC-2 wt% C the hardness values were 62 % and 36 % lower compared to monolithic SiC sintered at 2,000 and 2,100 °C, respectively. Thus, the apparent improvement in fracture toughness for SiC-2 wt% C samples can not be considered due to any toughening by filler material. Figure 21.4 shows an example of indentation fracture of AHPCS-2 wt% C and SiC-2 wt% C samples sintered at 2,100 °C. SiC-2 wt% C shows a lot of porosity while AHPCS-2 wt% C is quite dense.

Toughening mechanisms can be identified by inspecting crack propagation in the composite using SEM. Figure 21.5 shows various toughening mechanisms that were observed for AHPCS-%C samples. It is evident from the figure that graphene nanoplatelets increased fracture toughness by intrinsic energy dissipation mechanisms. During crack bridging graphene nanopletelets resisted the tensile forces acted on them by the crack plane and pinned the crack. Moreover,

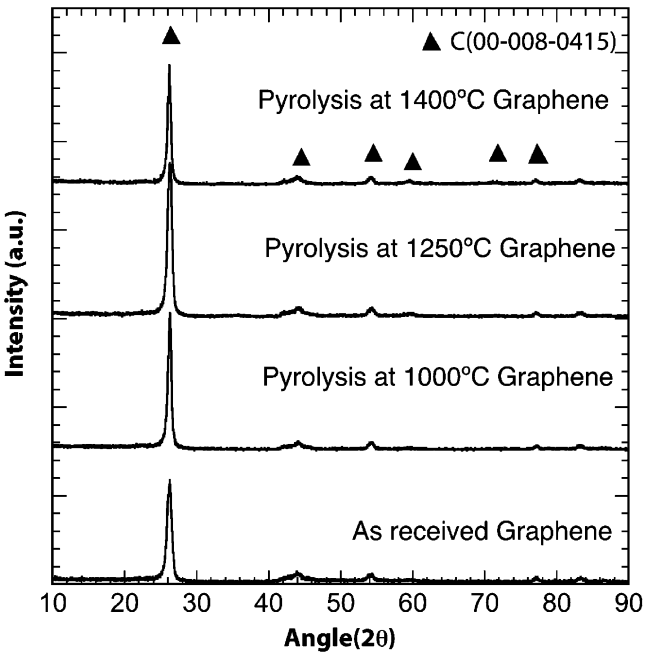

Fig. 21.6 XRD patterns for as-received graphene and pyrolyzed to different temperatures

interaction of crack front with graphene nanoplatelets resulted in deflection of the crack front due to high resistance provided by the filler. Thus, graphene nanoplatelet addition in SiC matrix effectively improve fracture resistance of this inherent brittle matrix material.

21.4.5 Thermal Stability of Graphene

Processing of SiC requires high sintering temperature and simultaneous pressure application for dense bulk form. These processing parameters are considered harsh for any carbon allotropes being introduced in the SiC matrix as filler material. Hence it is critical to obtain information regarding the structural defects that are being introduced due to these processing conditions. In the current study, as-received graphene nanoplatelets were subjected to different pyrolysis cycle to observe any change in the X-ray diffraction peak as shown in Fig. 21.6. It should be mentioned here that these are not exfoliated graphene that were subjected to pyrolysis cycle.

For as received graphene, we can see a prominent peak at 26.4° that corresponds to (002) plane of graphite. Four other small peaks are observed at 44.4°, 54.5°, 77.4°, and 83.3° corresponding to (100), (004), (110), and (112) planes of graphite. Pyrolysis to 1,000 °C or 1,250 °C showed no change in the peak positions or peak shape for the nanoplatelets. However, at 1,400 °C a new peak corresponding to (103) plane can be seen at 60°. This peak suggests crystallization of the nanoplatelets at 1,400 °C.

The experiment mentioned above subjects the nanoplatelets to higher pyrolysis temperature. To understand the complex effect of SPS sintering another set of experiments were performed on different graphene-SiC samples using Raman spectroscopy. For the current study, freshly cleaved SiC and graphene-SiC samples were studied using 532 nm laser excitation. The laser power was kept at 0.8 mW to prevent any heat induced change in the observed spectra. 100 μm spot size was used to collect information from a broad region. For 3C-SiC transverse optical (TO) band is observed at 796 cm^{-1} and longitudinal optical (LO) band is observed at 972 cm^{-1}. Figure 21.7 shows Raman spectra for all SiC and SiC-graphene samples sintered at 2,000 and 2,100 °C. Without any presence of carbon, the Raman spectra of 3C-SiC would only contain two peaks at 796 and 972 cm^{-1}. However, even for monolithic SiC samples D, G and G′ peaks were observed at 1,350, 1,583, and 2,701 cm^{-1}, respectively. This is due to the excess carbon present in the SiC matrix. Similar D, G and G′ peaks were also observed for all the other graphene-SiC samples. To determine the effect of SPS processing, we have to unambiguously identify the contribution of graphene nanoplatelets in these spectra. One way to deconvolute these spectra was to normalize these spectra with respect to a common peak. To do so, there are few assumptions. First of all, the absorption coefficient does not change in these materials. And a peak for SiC should have similar intensity in all these

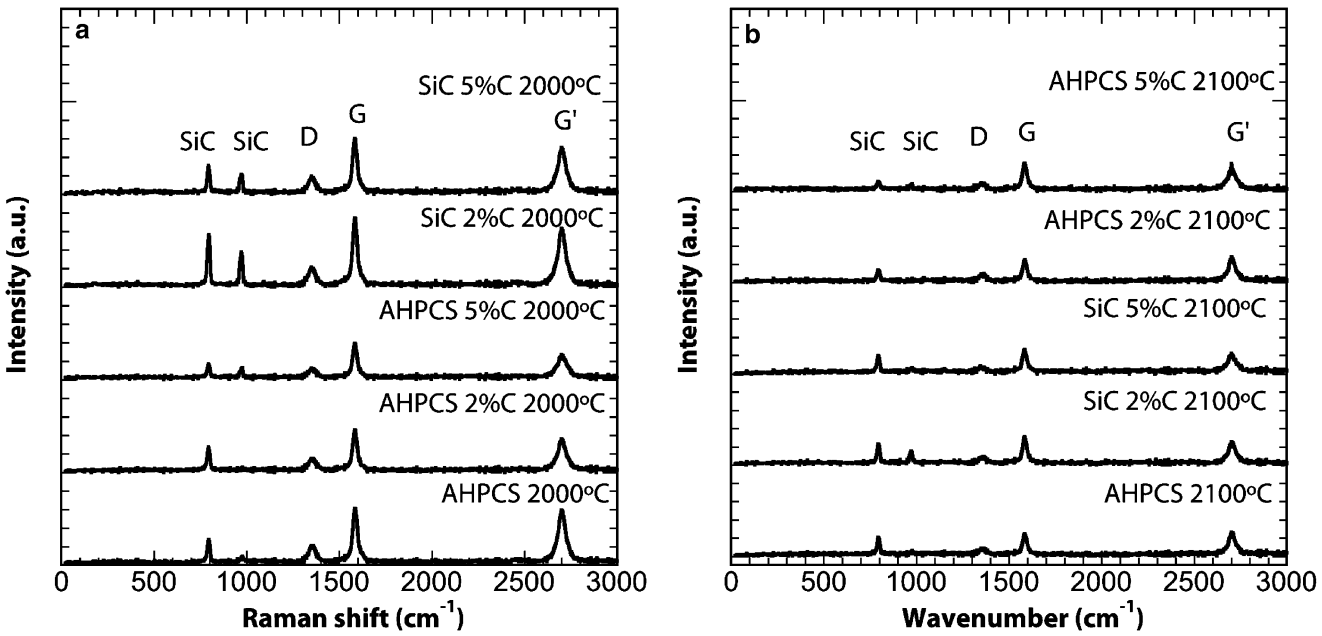

Fig. 21.7 Raman Spectra for (**a**) 2,000 °C samples and (**b**) 2,100 °C samples before normalization

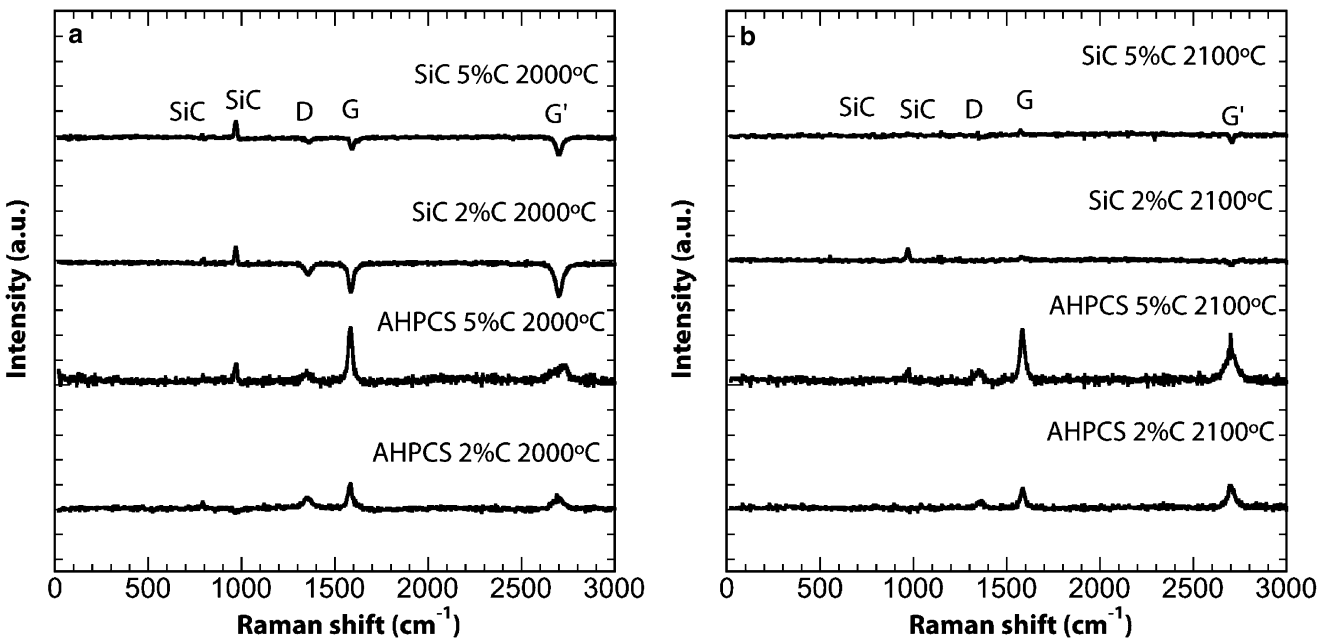

Fig. 21.8 Raman Spectra for (**a**) 2,000 °C samples and (**b**) 2,100 °C samples after subtraction of the spectra of monolithic SiC

materials since the spectrum is collected over a broad region. Considering these, 796 cm^{-1} TO peak intensity ratio was chosen as a normalizing factor for all the materials.

Finally, the spectra for monolithic SiC was subtracted from graphene-SiC spectra to get Raman signal only from graphene nanoplatelets as shown in Fig. 21.8. After subtraction, D, G, and G′ peaks can be identified for AHPCS-2 wt% C and AHPCS-5 wt% C samples sintered at 2,000 and 2,100 °C. However, negative D, G, and G′ were observed for SiC-2 wt% C and SiC-5 wt% C samples sintered at 2,000 °C. For 2,100 °C sintering temperature, no D, G, and G′ were observed for SiC-2 wt% C and SiC-5 wt% C samples. This warranted further investigation in this matter and is currently being undertaken.

21.5 Conclusion

Polymer pyrolysis technique followed by spark plasma sintering technique was used successfully to fabricate fine grained bulk SiC and graphene-SiC samples by in-situ crystallization of amorphous-SiC obtained from pyrolysis of polymer precursor. Based on experimental results the following has been observed:

1. Relative density measurement showed that addition of graphene can hinder densification process. Specially at higher weight fraction carbon acts as a barrier to densification mechanisms and results in lower density even at 2,000 °C. This was more prominent for samples prepared using IPA as dispersing media. On the other hand, addition of graphene as a filler material was shown to affect grain coarsening process. It acts as a barrier for surface diffusion leading to grain size refinement. Moreover, this effect is more prominent in case of higher sintering temperature (40 % reduction). One of the challenges in SiC sintering is restriction of grain growth during sintering and addition of graphene nanoplatelets have shown to be effective in doing so, particularly, at higher sintering temperature.
2. Hardness as a function of graphene weight fraction showed different trend for different processing routes. Analysis using Reuss–Voigt model indicated uniform dispersion of graphene content in case of AHPCS-%C samples as they showed hardness values close to upper bound hardness values. On the contrary, hardness of SiC-%C samples were close to lower bound hardness values referring to non-uniform dispersion. Addition of graphene nanoplatelet also affected fracture toughness of the composites. At 2 wt% C, AHPCS-2 wt% C sample showed 40 % improvement over monolithic SiC samples. Improvement in fracture toughness was attributed to different toughening mechanisms such as crack deflection and crack bridging.
3. Raman spectroscopic analysis confirmed presence of graphene in final composite structure. However, further investigation is required to understand the sole effect of sintering temperature and pressure on the structure of graphene.

References

1. Orange G, Tanaka H, Fantozzi G (1987) Fracture-toughnes of pressureless sintered silicon-carbide - a comparison of K_{Ic} measurement methods. Ceram Int 13(3):159–165
2. Ippolito M, Mattoni A, Colombo L, Cleri F (2005) Fracture toughness of nanostructured silicon carbide. Appl Phys Lett 87(14): 141912–141913
3. Lee S, Kim C (1994) Effects of α-SiC versus β-SiC starting powders on microstructure and fracture-toughness of SiC sintered with Al_2O_3-Y_2O_3 additives. J Am Ceram Soc 77(6):1655–1658
4. Ding Y, Dong S, Huang Z, Jiang D (2007) Fabrication of short c fiber-reinforced sic composites by spark plasma sintering. Ceram Int 33(1): 101–105
5. Shen Q, Li R, Wang C, Zhang L (2003) Densification of short carbon fiber reinforced silicon carbide by spark plasma sintering. Compos Mater III 249:133–135
6. Li R, Shen Q, Zhang L (2003) Fabrication of short-c-f/sic functionally graded materials. Funct. Graded Mater VII 423(4):253–256
7. Tang H, Zeng X, Xiong X, Li L, Zou J (2009) Mechanical and tribological properties of short-fiber-reinforced sic composites. Tribol Int 42(6): 823–827
8. He X, Guo Y, Zhou Y, Jia D (2008) Microstructures of short-carbon-fiber-reinforced SiC composites prepared by hot-pressing. Mater Charact 59(12):1771–1775
9. Zhan G, Kuntz J, Wan J, Mukherjee A (2003) Single-wall carbon nanotubes as attractive toughening agents in alumina-based nanocomposites. Nat Mater 2(1):38–42
10. Zhan G, Kuntz J, Garay J, Mukherjee A (2003) Electrical properties of nanoceramics reinforced with ropes of single-walled carbon nanotubes. Appl Phys Lett 83(6):1228–1230
11. Ma R, Wu J, Wei B, Liang J, Wu D (1998) Processing and properties of carbon nanotubes-nano-SiC ceramic. J Mater Sci 33(21):5243–5246
12. Geim AK, Novoselov KS (2007) The rise of graphene. Nat Mater 6(3):183–191
13. Kim H, Abdala A, Macosko C (2010) Graphene/polymer nanocomposites. Macromolecules 43(16):6515–6530
14. Lee C, Wei X, Kysar J, Hone J (2008) Measurement of the elastic properties and intrinsic strength of monolayer graphene. Science 321(5887):385–388
15. Lee C, Wei X, Li Q, Carpick R, Kysar JW, Hone J (2009) Elastic and frictional properties of graphene. Phys Status Solidi B 246(11–12): 2562–2567
16. Fan Y, Wang L, Li J, Li J, Sun S, Chen F, Chen L, Jiang W (2010) Preparation and electrical properties of graphene nanosheet/al2o3 composites. Carbon 48(6):1743–1749
17. Wang K, Wang Y, Fan Z, Yan J, Wei T (2011) Preparation of graphene nanosheet/alumina composites by spark plasma sintering. Mater Res Bull 46(2):315–318
18. Liu J, Yan H, Reece MJ, Jiang K (2012) Toughening of zirconia/alumina composites by the addition of graphene platelets. J Eur Ceram Soc 32(16):4185–4193
19. Walker LS, Marotto VR, Rafiee MA, Koratkar N, Corral EL (2011) Toughening in graphene ceramic composites. ACS Nano 5(4):3182–3190

20. Hvizdos P, Dusza J, Balazsi C (2013) Tribological properties of si_3n_4-graphene nanocomposites. J Eur Ceram Soc 33(12):2359–2364 [Nanoceramics and Ceramic-based Nanocomposites]
21. Rahman A, Singh A, Harimkar SP, Singh RP (2013) Spark plasma sintering and characterization of graphene reinforced silicon carbide nanocomposites. In: Composite materials and joining technologies for composites, vol 7. Springer, Berlin, pp 139–146
22. Zhao W, Fang M, Wu F, Wu H, Wang L, Chen G (2010) Preparation of graphene by exfoliation of graphite using wet ball milling. J Mater Chem 20(28):5817–5819
23. ASTM C830-00 (2011) Standard test methods for apparent porosity, liquid absorption, apparent specific gravity, and bulk density of refractory shapes by vacuum pressure. West Conshohocken: ASTM International. doi:10.1520/C0830-00R11, www.astm.org
24. Anstis G, Chantikul P, Lawn B, Marshall D (1981) A critical evaluation of indentation techniques for measuring fracture toughness: I, direct crack measurements. J Am Ceram Soc 64(9):533–538
25. Snead LL, Nozawa T, Katoh Y, Byun T-S, Kondo S, Petti DA (2007) Handbook of SiC properties for fuel performance modeling. J Nucl Mater 371(1–3):329–377; 1st symposium on nuclear fuels and structural materials for next generation nuclear reactors, Reno, 04–08 June 2006
26. Rijswijk WV, Shanefield DJ (1990) Effects of carbon as a sintering aid in silicon carbide. J Am Ceram Soc 73(1):148–149
27. Stobierski L, Gubernat A (2003) Sintering of silicon carbidei. Effect of carbon. Ceram Int 29(3):287–292
28. Ermer E, Wiesław P, Ludosław S (2001) Influence of sintering activators on structure of silicon carbide. Solid State Ion 141:523–528
29. Wang S, Zhang Y, Abidi N, Cabrales L (2009) Wettability and surface free energy of graphene films. Langmuir 25(18):11078–11081
30. Cheary RW, Coelho AA (1996) Programs xfit and fourya, deposited in ccp14 powder diffraction library, engineering and physical sciences research council, daresbury laboratory, Warrington, England
31. Wang K, Wang Y, Fan Z, Yan J, Wei T (2011) Preparation of graphene nanosheet/alumina composites by spark plasma sintering. Mater Res Bull 46(2):315–318
32. Fan Y, Estili M, Igarashi G, Jiang W, Kawasaki A (2014) The effect of homogeneously dispersed few-layer graphene on microstructure and mechanical properties of al2o3 nanocomposites. J Eur Ceram Soc 34(2):443–451
33. Hirota K, Hara H, Kato M (2007) Mechanical properties of simultaneously synthesized and consolidated carbon nanofiber (cnf)-dispersed sic composites by pulsed electric-current pressure sintering. Mater Sci Eng A 458(1):216–225
34. Kim HS (2000) On the rule of mixtures for the hardness of particle reinforced composites. Mater Sci Eng A 289(1):30–33

Chapter 22
Experimental Investigation of the Effect of CNT Addition on the Strength of CFRP Curved Composite Beams

M.A. Arca, I. Uyar, and D. Coker

Abstract Carbon nanotubes (CNT) have been attracting attention as a toughening material in composite matrix due to their excellent mechanical properties. However, superior properties of CNTs have not yet been realized in the strengthening of composites against fracture. This study focuses on investigating the effect of CNT variation in the epoxy resin on the strength of curved composite beams. Specimens are [0/90] fabric carbon/epoxy composite laminates manufactured by hand layup technique 3 % wt CNT fractions in the epoxy resin. Curved beam composite laminates were subjected to four point bending loading according to ASTM D6415/D6415M–06a and the load displacement plot is recorded. Digital Image Correlation technique is used to obtain deformation field in the laminate at the curved region just before delamination failure initiates. A high speed camera at 28,000 fps was used to capture the deformation sequence after initiation of failure. For the CNT added laminate, both CBS and failure load is found to decrease with the load-displacement behavior found to change from single load drop to multiple load drops. In addition, delamination is found to be constrained to the curved region for the CNT added laminate in contrast to the base laminate where delamination extends to the arms.

Keywords Delamination • Curved composite • Carbon nanotube • High-speed camera • DIC

22.1 Introduction

Composite material demand in aerospace and wind energy industries is flourishing as a primary load carrying members in complex shapes. Anisotropic behavior of composites changes the material response and fracture behavior from the metallic structure parts. However, use of composites in complex geometries such as curved composite beams is challenging for load carrying applications due to their weakness at the radius which causes delamination. The weakness is caused by high normal stresses in addition to shear stresses that may cause delamination with significant loss of mechanical toughness. Carbon nanotubes (CNTs) as a toughening material in composite matrix have attracted attention due to their very high mechanical properties and aspect ratios. However, superior properties of CNTs have not been yet realized in the fracture of composites. In the literature, Avalon and Donaldson showed in their studies [1] of curved beam composites showed that 5 % wt carbon nanofiber addition to the resin has no overall effect on the curved beam strength (CBS) while comparing curvature ratios. Carbon nanofiber added specimens tend to fail with stick slip behavior while base laminates fail with a rapid load drop. They also observed that increasing radius and thickness increases CBS and also decreasing radius and increasing thickness causes single crack with stick slip behavior. They also showed that the radial stress at failure was found to be independent of any parameters (radius, thickness, CNT), ranging between 30 and 32 MPa for all configurations for experimental and computational solutions [1]. Hao et al [2] investigated CBS and deformation field of 90° bend CRFP laminates by Digital Speckle Correlation Method and strain gages under bending for different thicknesses and radii. They showed that both increasing

M.A. Arca • I. Uyar
Department of Aerospace Engineering, Middle East Technical University, 06800 Ankara, Turkey

D. Coker (✉)
Department of Aerospace Engineering, Middle East Technical University, 06800 Ankara, Turkey

METU Center for Wind Energy, Middle East Technical University, 06800 Ankara, Turkey
e-mail: coker@metu.edu.tr

G. Tandon (ed.), *Composite, Hybrid, and Multifunctional Materials, Volume 4: Proceedings of the 2014 Annual Conference on Experimental and Applied Mechanics*, Conference Proceedings of the Society for Experimental Mechanics Series,
DOI 10.1007/978-3-319-06992-0_22,

radius and thickness increase the curved beam strength. With the increasing thickness stable fracture was observed. Increasing radius does not affect the delamination mechanism, only decreases the maximum load. DSCM results showed that maximum strain occurs where crack initiates and propagates. They also observed that for all kind of specimens delamination occur between 90/0 plies.

The objective of this study is to investigate the effect of CNTs on curved beam strength of curved composite beams experimentally using high speed cameras in conjunction with digital image correlation system (DIC) system in order to obtain deformation field and maximum stress locations and failure sequences. The curved beams are fabric carbon/epoxy composite laminates manufactured by hand layup technique with CNT fractions in the resin. Curved beam composite laminates were subjected to four point bending loading according to ASTM D6415/D6415M–06a. Micrographs of microstructures and fracture surfaces were examined.

22.2 Material

Four point bending test were conducted on two different types of carbon fiber/epoxy composite laminate specimens: (1) [0/90] fabric laminate, (2) [0/90] fabric laminate with CNT reinforcement. HexPly® AS4 family 5HS plain weave woven carbon dry fabrics having 0.35 mm ply thickness is used for CNT added specimens and HexPly® AS4 family 5HS plain weave woven carbon fabric prepregs having 0.25 mm ply thickness is used for base specimens. Both types of laminates were manufactured by hand layup technique and vacuum bagging. For CNT added laminates 3 % wt CNT addition to the resin is achieved by mixing Araldite® LY 5052 epoxy resin with EPOCYL™ NCR128-02 liquid bisphenol-A epoxy resin having 20 wt% fraction CNT produced by Nanocyl company. In Fig. 22.1 SEM images of bisphenol-A epoxy resin having 20 wt% fraction CNT are shown. In Fig. 22.1a CNT bundles in the epoxy are seen and in Fig. 22.1b dispersed CNTs in the epoxy resin is shown. The mixing ratio of epoxy resins bisphenol-A and Araldite® LY 5052 is 1–6. In order to manufacture CNT toughened specimens, dry fabrics are covered with CNT-epoxy resin by hand layup technique. Specimens manufactured as L-shaped beams containing a Teflon film at one leg in order to demonstrate the delamination as shown in Fig. 22.2a and then cut into two pieces using abrasive saw cutting tool in order to have fracture toughness (DCB and ENF) tests and four point bending test specimens. The dimensions are given in Fig. 22.2b.

22.3 Experimental Method

Four-point bending tests, in which pure moment is created at the corner, were carried out according to ASTM D6415/D6415M–06a [3] in order to obtain the curved beam strength of laminates. The experimental test setup is given in Fig. 22.1b. Shimadzu Autograph AGS-J 10 kN displacement controlled screw driven tensile testing machine is used for loading and a Photron SA5a million frame high speed camera with a full resolution of 1 MP up to 7,500 and 1,000,000 fps at reduced

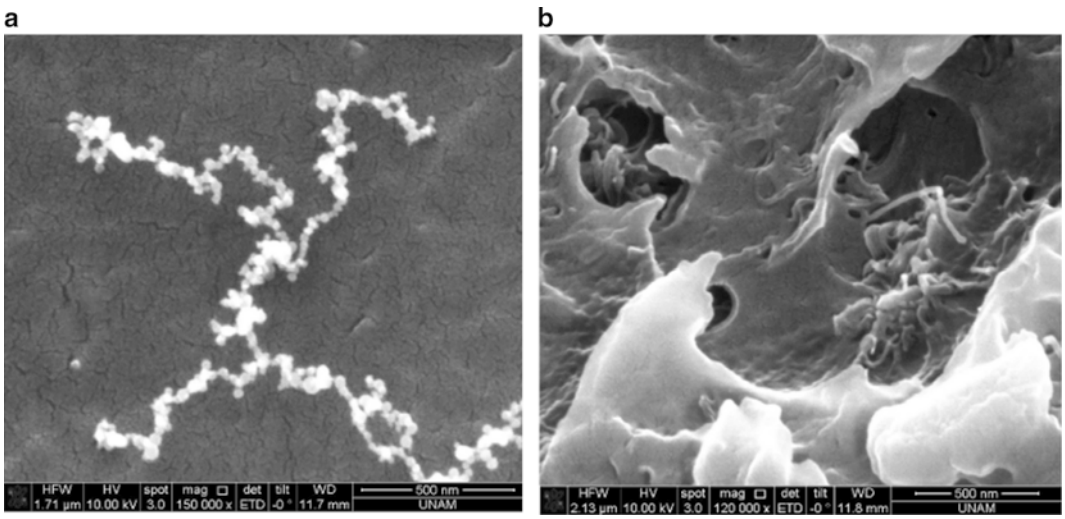

Fig. 22.1 (**a**, **b**) SEM images of EPOCYL™ NCR128-02 liquid bisphenol-A epoxy resin having 3 wt% fraction CNT

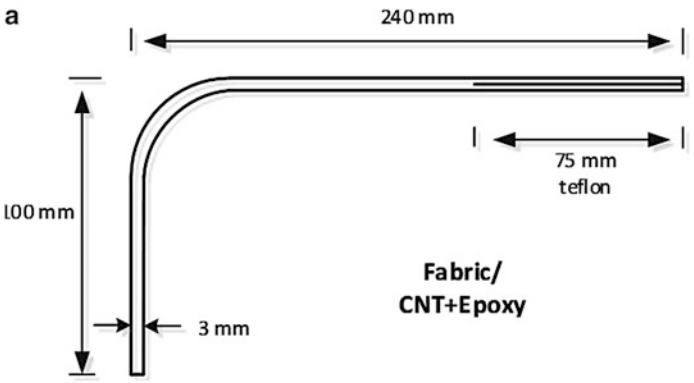

b

	4-pt bend	
	base	CNT
Ply #	12	9
dimensions	$L_1 = L_2 = 100$	$L_1 = L_2 = 100$
	w=25	w=25
	t=3	t=3
# of specimens	2	3

Fig. 22.2 (**a**) Specimen manufacturing geometry, (**b**) numbers and dimensions of specimens used in the tests

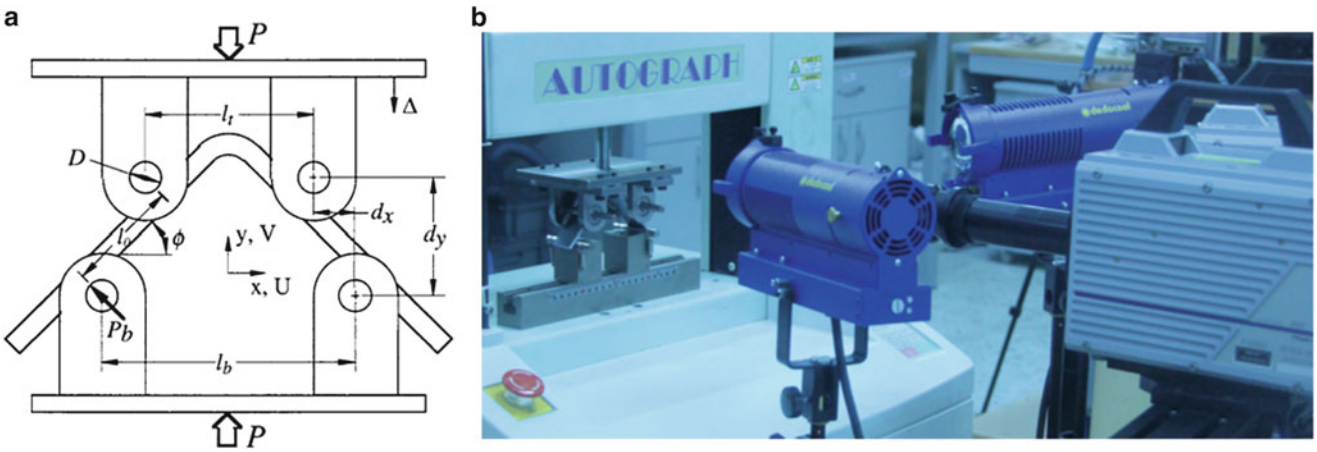

Fig. 22.3 (**a**) Four-point bending test-setup schematic; (**b**) test setup photograph

resolutions is used to record delamination initiation and propagation. Digital image correlation method in conjunction with the high speed cameras is used to obtain deformation field and maximum stress locations prior to failure. ARAMIS software developed by GOM is used for optical full-field strain measurements. During the test, specimen is positioned as shown in Fig. 22.3a and test setup is shown in Fig. 22.3b. Edge of the specimen is painted with the white paint to make failure (delamination) visible in the images. For the DIC experiments, specimen edges are first painted with the white paint and then speckle pattern is created using black spray paint in order to create facet field on specimen since the DIC software uses the facet field in the displacement measurement calculations. End trigger mode of High Speed Camera is used to capture the failure sequence photos after the cracking sound and load drop in the load displacement curve. Specimen is loaded at 0.5 mm/min crosshead speed and the test is stopped after a load drop of 50 % of the max load is attained in accordance with the ASTM standard.

Curved beam strength is calculated using relation given below, which is basically moment per unit length. The moment on the curved section of the specimen is the product of the force exerted by one of the cylindrical loading bars and the distance between two bars along one leg. Bar force is calculated from the maximum total force exerted on specimen at the first force drop and the distance between two bars along one leg is calculated from geometries of the loading fixture and test specimen and w refers to width and t to thickness of specimen. Other unknowns are shown on the experimental setup picture in Fig. 22.3a.

$$CBS = \frac{Pl_0}{w} = \frac{P}{2wcos(\varphi)} \left(\frac{d_x}{cos\,(\varphi)} + (D + t)\, tan\,(\varphi) \right)$$

P (load) and φ are two variables in CBS equation. Load value is read directly from measuring machine. φ value is determined from its stroke as following, where dy_i is measured initial value and Δ is stroke of measuring machine:

$$d_y = d_{yi} - \Delta$$

$$\varphi = sin^{-1} \frac{-d_x(D+t) + d_y\sqrt{\left(d_x^2 + d_y^2 - D^2 - 2Dt - t^2\right)}}{d_x^2 + d_y^2}$$

Interlaminar stress calculation was developed by Lekhnitskii [4] as given by

$$\sigma_r = -\frac{CBS}{r_o^2\, g}\left(1 - \frac{1-\rho^{k+1}}{1-\rho^{2k}}\left(\frac{r_m}{r_o}\right)^{k-1} - \frac{1-\rho^{k-1}}{1-\rho^{2k}}\left(\frac{r_m}{r_o}\right)^{k+1}\rho^{k+1}\right)$$

An approximate calculation of maximum interlaminar stress is given in the standard is:

$$\sigma_r^{\max} = \frac{3CBS}{2t\sqrt{r_i r_o}}$$

22.4 Results

Load-displacement curves for both base and CNT added specimens subject to four-point bending test are shown in Fig. 22.4. CNT addition is shown to decrease the maximum failure load in which the base specimen is seen to reach a maximum load of 2600 N whereas the CNT added specimen reaches a maximum load of 1700 N. Most significant difference is that CNT addition causes multiple load drops. At the first load drop single delamination occurs and the specimen continues to carry load without a significant change in slope. Upon further loading, a second load drop occurs at a higher load, leading to a catastrophic failure with multiple delaminations.

Curved beam strength and maximum radial stress values are given as bar graphs in Fig. 22.5a and b, respectively. Both CBS and radial stress values were found to decrease with 3 % wt CNT addition in contrast to the study in [1] where they were found not be affected by the addition of 5 % wt CNT. When the maximum stresses of two case are compared the maximum radial stress of CNT added specimens decreased about 64 %. While radial stress of non-CNT laminates is around 28 MPa, CNT addition decreases the stress to 10 MPa. Large standard deviation compared to the base specimens is also seen in four-point bending test results. These results supports the claim that reposition and concentration of CNTs in clusters with high density can lead to heterogeneity of the ply properties which also cause larger scatter in the results.

To visualize the strain field, DIC method was used on pictures taken of a 25 × 25 mm^2 area in the curved region at 20 N load increment up to a load of 1500 N. Since at high frame rates, the camera resolution is reduced to 256 × 185 pixels which are not sufficient to analyze strain variation with DIC method, high speed test and DIC test were conducted separately.

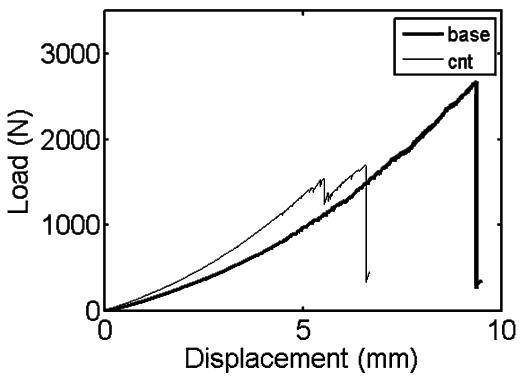

Fig. 22.4 Load displacement curves of base and CNT added laminates

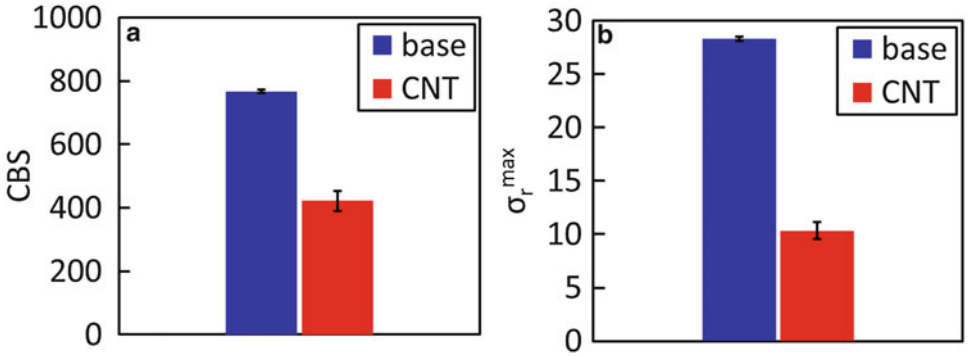

Fig. 22.5 (**a**) Curved beam strength results for base and CNT added laminates. (**b**) Maximum radial stress results for base and CNT added laminates

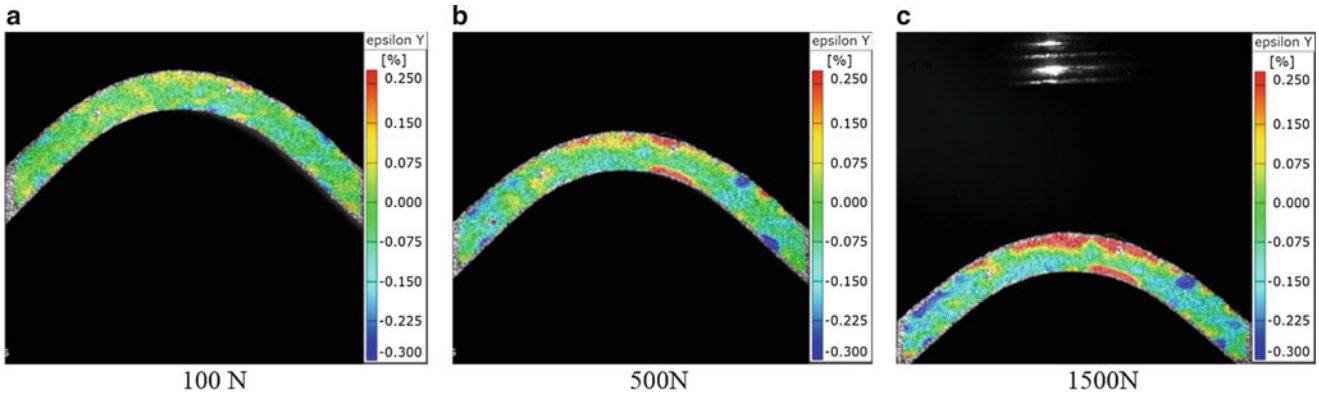

Fig 22.6 Full frame DIC images taken showing Epsilon Y strain corresponding to opening stresses (**a**) at 100 N, (**b**) at 500 N and (**c**) at 1,000 N

In Fig. 22.6 DIC images captured at 100, 500 and 1,500 N are given. Epsilon y stain corresponding to opening stresses which leads to delamination are located close to the outer radius. According to the DIC results delamination nucleation is expected at the upper side of the curved region.

High speed camera photos taken during experiments at fracture for base and CNT added specimens are given in Figs. 22.7 and 22.8, respectively. For base laminates photos were taken at 15,000 fps and for CNT specimens photos were taken at 28,000 fps.

In Fig. 22.7 nine sequential images with 0.66 μs time interval shows the failure sequence of base laminates. Catastrophic failure occurs in one load drop. The first delamination initiates close to the outer radius between third and fourth plies. This result is coherent with the DIC results. Failure started from the upper side of the curved region as expected since opening stresses located at this region as shown in Fig. 22.6c. Just after propagation of first delamination multiple delamination occurs simultaneously from outer radius to inner radius. In the propagation process different cracks merge and also fiber breakage is seen at the center line of the specimen.

In Fig. 22.8a, b failure sequence of CNT added specimens at first and second load drop is given respectively. Failure mechanism of CNT added specimens is different from base laminates. At the first load drop delamination initiates close to the outer radius between second and third plies and propagates slightly thorough the both arms as seen in Fig. 22.8a. At the second load drop while initial delamination continues to propagate, a second crack initiates at the last ply and propagates diagonally between different laminates. Third crack occurs above the second crack close to mid layer. Fourth crack initiates between first and third delamination and kinking can be clearly seen. Cracks mender to weak CNT clustered regions as a results of heterogeneity in plies due to concentration of CNTs in clusters with high density. This causes changes in the crack path as observed in the figures. No fiber breakage or merging cracks are observed, and the cracks are arrested in the curved region in contrast to the long cracks observed in the base laminates.

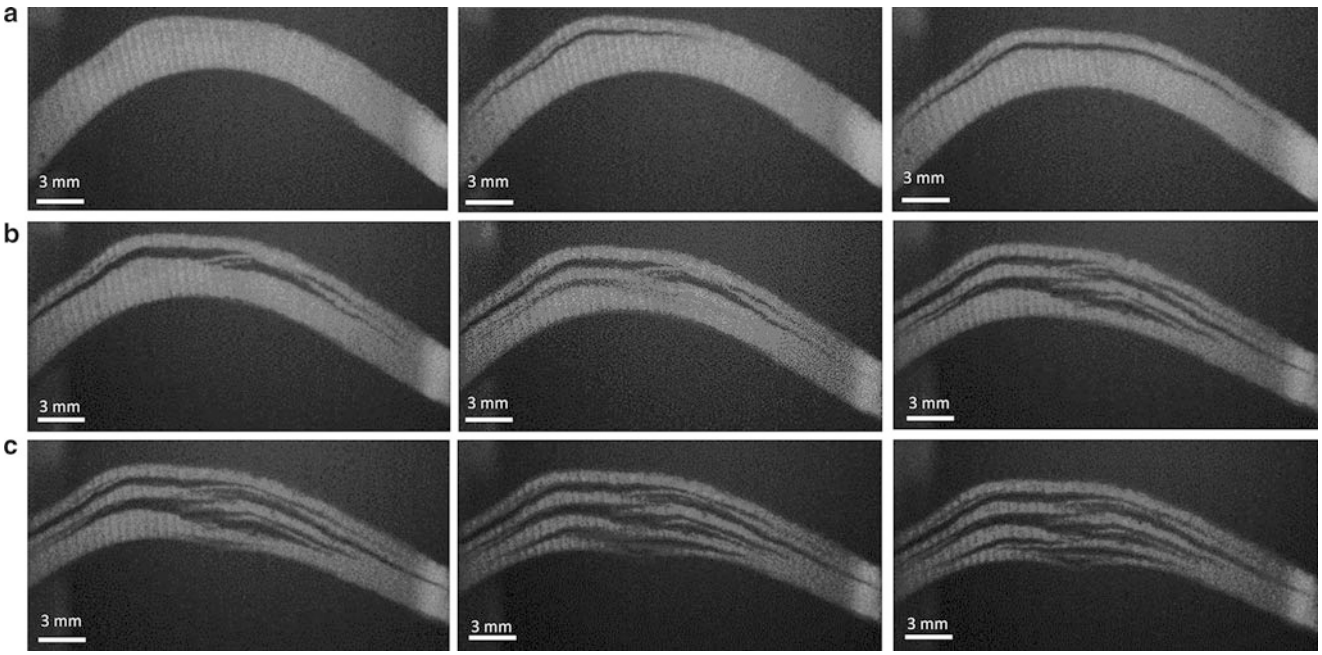

Fig. 22.7 (**a**–**c**) High speed camera photos showing failure sequence for base laminate at 15,000 fps

Micrographs of fracture surfaces is shown in Fig. 22.9. In Fig. 22.9a fracture surface of base laminate is shown. Part of a major crack between two layers can be seen in addition matrix cracks between fiber filaments. Different matrix cracks merge between layers. In Fig. 22.9b fracture surface of the CNT added laminate is shown. In this case, the cracks between the layers can be seen to originate from these vacancies. Reposition and concentration of CNTs in clusters with high density may cause the heterogeneity in the epoxy resin with corresponding vacancies (Fig. 22.9).

22.5 Conclusions

In this study four point bending tests were conducted in order to investigate change in the curved beam strength and maximum failure stress of carbon/epoxy fabric laminates with the 3 % wt CNT addition in the resin. CNT dispersion in the resin was provided by mixing epoxy resin with high fraction CNT and epoxy resin then covering the fabrics dissimilarly from the shear mixing or three rolling methods used in the literature [1, 3]. Both CBS and radial stress decreased about 50 % with 3 % wt CNT addition. In the test results large standard deviation was seen compared to the base specimens. Large standard deviation of CNT specimens in all types of tests supports the claim that reposition and concentration of CNTs in clusters with high density can lead heterogeneity in plies and non-isotropic mechanical properties which causes deviations in the results. High speed camera photos showed that the failure mechanisms of base laminates and CNT added laminates are different. While catastrophic failure occurs in one load drop for base laminates, at the first load drop close to the upper edge initial delamination initiates and propagates slightly and at the second load drop multiple delamination occur for CNT added laminates.

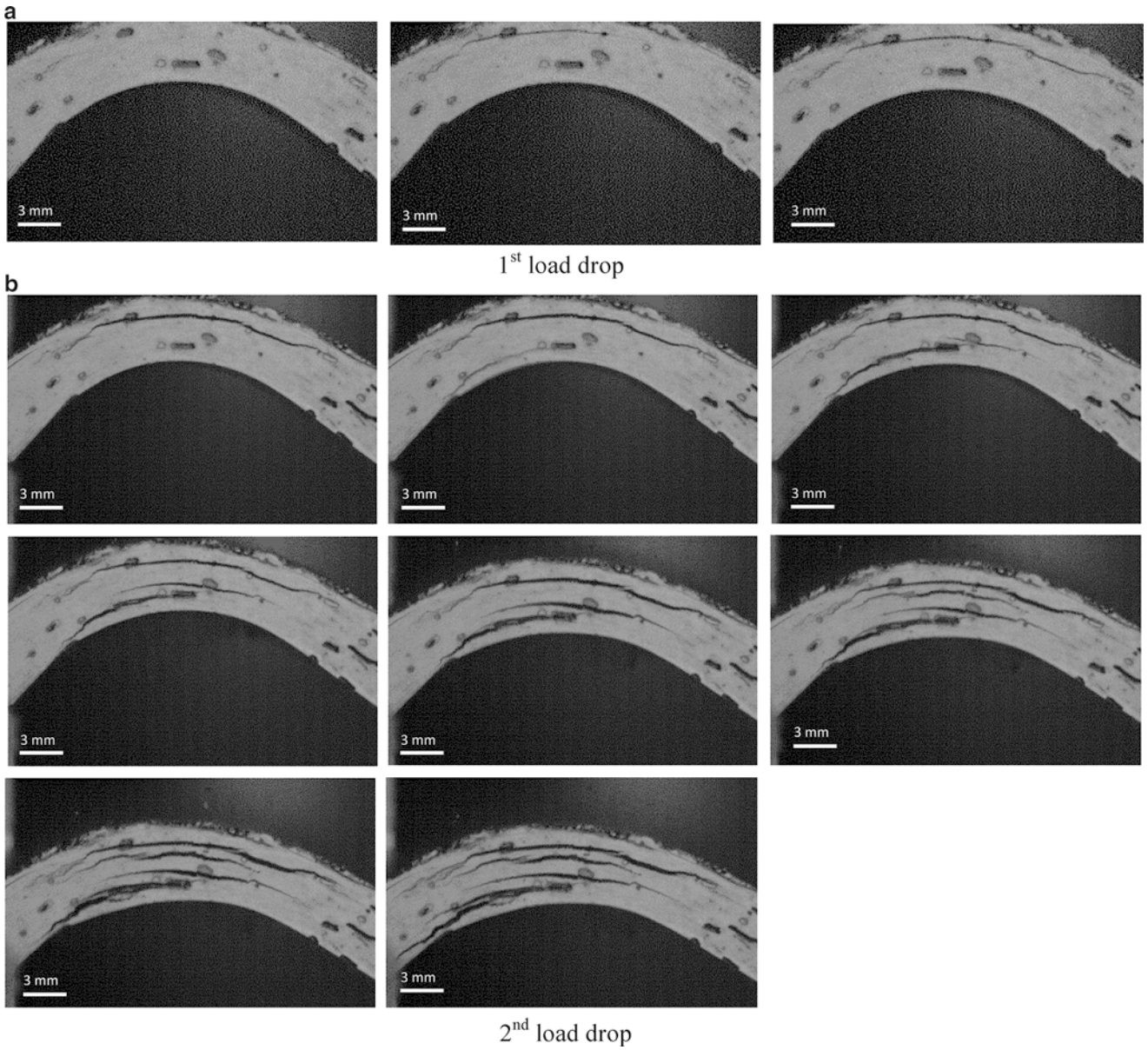

Fig. 22.8 (**a**) High speed camera photos for CNT added laminate after the first load drop at 28,000 fps. (**b**) High speed camera photos for CNT added laminate after second load drop at 28,000 fps showing failure sequence

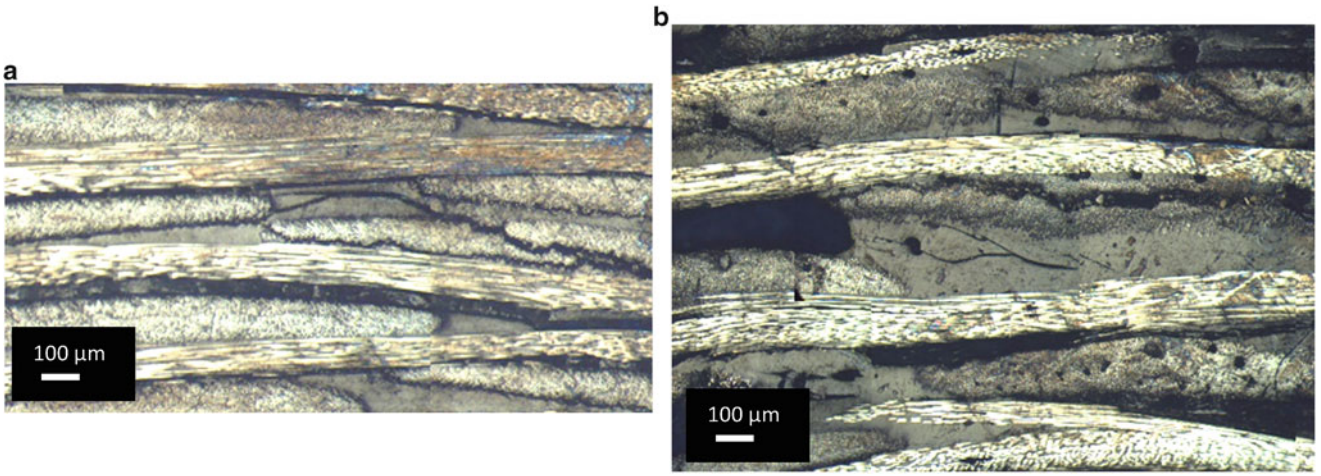

Fig. 22.9 Micrographs of fracture surfaces (**a**) base laminate, (**b**) CNT added laminate

Acknowledgements This work was supported by the Ministry of Science, Industry and Technology and Turkish Aerospace Industries through grant 00785.STZ.2011-1 and METU Center for Wind Energy. The authors would also like to thank Denizhan Yavas for his help in manufacturing the specimens.

References

1. Avalon SC, Donalson SL (2010) Strength of composite angle brackets with multiple geometries and nanofiber-enhanced resins. J Compos Mater 45(9):1017–1030
2. Hao W, Ge D, Ma Y, Yao X, Shi Y (2012) Experimental investigation on deformation and strength of carbon/epoxy. Polym Test 31:520–526
3. ASTM D6415/D6415M–06a (2007) Standard test method for measuring the curved beam strength of a fiber-reinforced polymer-matrix composite. ASTM International, West Conshohocken
4. Lekhnitskii SG (1981) Theory of elasticity of an anisotropic body. Mir, Moscow

Chapter 23
Mechanical and Tribological Performance of Aluminium Matrix Composite Reinforced with Nano Iron Oxide (Fe_3O_4)

E. Bayraktar, M.-H. Robert, I. Miskioglu, and A. Tosun Bayraktar

Abstract Aluminium matrix composite materials are used in aerospace, defence, automotive applications especially in the thermal management areas. Aluminium Matrix Composite (AMCs) reinforced with Nano Iron Oxide (Fe_3O_4) exhibit good physical and mechanical behaviour (electrical conductivity and wear resistance), which makes it an excellent multifunctional lightweight material. The present paper is based on low cost manufacturing of light and efficient materials for aeronautical applications. To that end, a study has been carried out on an aluminium matrix composite reinforced with Fe_3O_4-iron oxide and other alloying elements produced in our laboratory. Micro indentation tests were conducted on the AMC to investigate its elastic modulus, hardness, and scratch tests with very long cycles were performed to study its wear performance. Scanning Electron Microscopy examinations were made to study the morphology of damage surfaces. The goal was to get more information about the influence of fillers on the corresponding reinforcing and wear mechanism.

Keywords Wear • Scratch test • Aluminium matrix composites • Iron oxide (Fe_3O_4) • Damage analysis

23.1 Introduction

New types of metal matrix composites (MMCs) have made them attractive candidate materials for aerospace, automotive and numerous other applications. More recently, particulate reinforced MMCs have attracted considerable attention as a result of their relatively low cost and characteristic isotropic properties. Randomly reinforced aluminum metal matrix composites are a class of composite materials having trendy properties like low density, high specific stiffness, high specific strength, controlled coefficient of thermal expansion, increased fatigue resistance and superior dimensional stability in different environmental conditions (high temperatures etc.) [1–8]. These materials have appeared as a vital class of advanced materials providing engineers the possibility of tailoring the material properties to suit their needs [1, 3]. The particulate reinforced MMCs differ from the conventional engineering materials in that the structure and properties of these materials can be optimized by various processing techniques that have been improved over the last two decades. The processing methods utilized to manufacture particulate reinforced MMCs can be grouped based on the temperature of the metallic matrix during processing.

In the frame of the research project going on, this present work aims to evaluate certain parameters of the aluminium matrix composite (AMC) reinforced with nano iron oxide (Fe_3O_4) that we have recently designed by a simple and a low cost manufacturing technique [1, 2]. The good physical and mechanical behaviour (conductivity and wear resistance) obtained in

E. Bayraktar (✉)
Supmeca—Paris, School of Mechanical and Manufacturing Engineering, Paris, France
e-mail: bayraktar@supmeca.fr

M.-H. Robert
FEM, Mechanical Engineering Faculty, University of Campinas, UNICAMP, Campinas, Brazil

I. Miskioglu
ME-EM Department, Michigan Technological University, Houghton, MI, USA

A.T. Bayraktar
School of Chemistry, P. Vauqelin, 21, Avenue Boutroux, 75013 Paris, France

G. Tandon (ed.), *Composite, Hybrid, and Multifunctional Materials, Volume 4: Proceedings of the 2014 Annual Conference on Experimental and Applied Mechanics*, Conference Proceedings of the Society for Experimental Mechanics Series,
DOI 10.1007/978-3-319-06992-0_23,

this composite makes it an excellent multifunctional light weight and efficient material for engineering applications. At the first stage, a detail analysis was given on the continuous multi-cycle microindentation test at constant load to determine materials parameters such as indentation hardness, elastic modulus and stiffness. Dielectric properties (Permittivity (ε′) and dielectric loss angle tangent (tan delta)) were examined using a Dielectric Thermal Analyzer (Rheometric Scientific) at different frequencies over a temperature range varying from room temperature up to 280 °C. This study is necessary to optimise electrical conductivity of the composite (effect of Fe_3O_4). For the damage analysis during over very long cycles of loading, a special wear (scratch) test was carried out to better understand the reasons for the wear resistance of this composite. Damaged zone was measured by 3D optical surface roughness test device. Development of this composite will be used by French aeronautical company. In final stage of this ongoing project, optimization of electric and magnetic properties will be carried out.

23.2 Experimental Conditions

Preparation of Fe_3O_4 magnetic nano-particles: The preparation of Fe_3O_4 magnetic nano-particles was exclusively adapted from our simple low-cost method that was carried out at the chemical processing laboratory in Paris [1, 2, 6]. First of all, ferric chloride ($FeCl_3$, 820 mg) was dissolved in 30 mL deionized water by mechanical stirring under nitrogen atmosphere at 25 °C in a three neck flask. Ten milliliters of ferrous chloride tetra hydrate ($FeCl_2{\cdot}4H_2O$, 53 mg/mL) aqueous solution was then added into the flask under stirring. Ten minutes later, ammonia aqueous solution (4.5 g, 25 %) was slowly injected into the flask. The reacting solution has turned black with the injection of ammonia solution. The total amount of the reacting solution was about 45 mL. The reaction was maintained for 4 h. When the reaction was completed, the Fe_3O_4 nano-particles were separated and washed with deionized water several times with the help of a magnet until the deionized water was neutral. The purified Fe_3O_4 nano-particles were dispersed again into 45 mL deionized water. After this stage, Fe_3O_4 magnetic nano-particles were then collected and washed with deionized water for several times with the help of a magnetic bar. In the final stage, the nano-particles were dried and stored in a closed and dry environment. This method is a simple and safe way compared to the other approaches proposed in the literature [2, 9] to produce Fe_3O_4 nano-particles.

Low cost manufacturing of the composite samples: A simple tubular ceramic oven was used to sinter the compacted aluminium/iron oxide powder. The compact was prepared from aluminium and iron oxide (Fe_3O_4) powders. Aluminium with a purity of 99.7 % was used as the base material (Merck Co, France) with a grain size of <2 μm. The purity level of Fe_3O_4 was found to be 99.62 %, and its particle size varied from 45 to 70 nm. The mixtures were blended homogeneously by ball milling for 2 h. These Al matrix composites have resulted in higher mechanical properties and homogeneous microstructure as indicated in the former reports [1, 2]. Blended mixture was compacted by cold isostatic pressing (CIP) with a green compact pressure of 250 MPa, intending to produce an initial green density ranging from 85 to 95 %. The aspect ratio of the compact geometry was 0.85. The other series were also prepared with various aspect ratios at the green compact pressure range of 200–275 MPa in order to observe the effect of the compact pressure on the evolution of the density.

Sintering was performed under argon atmosphere to prevent oxidation and the sintering temperature was fixed for all the specimens at 600 °C in ceramic tubular oven.

Multicycle Microindentation test at Constant Load: CSM Indentation Tester with a Vickers diamond indenter was used for the microindentation experiments. Nine tests were performed and then averaged. The samples' thickness were approximately 5 mm. The maximum indentation load (F_{max}) was 1500 mN; the maximum load was reached in 30 s. The load was held at maximum for 5 s. The indentation hardness (H_{IT}), indentation modulus (E_{IT}) and the stiffness (S) were determined by using the Oliver and Pharr method [10]. In addition to the classical microindentation test, a multicycle indentation test under constant maximum load was used to investigate the evolution of indentation hardness, indentation modulus and the stiffness of the material as a function of number of indentation cycles. Three different maximum loads were used; 1,500, 2,000 and 2,500 mN. The maximum load was reached in 15 s. The load was held at maximum for 50 s. Fifty cycles were performed for each maximum load.

Dielectric properties: (Permittivity (ε′) and dielectric loss angle tangent (tan delta)) were investigated using a Dielectric Thermal Analyzer (Rheometric Scientific) at three different frequencies (1, 10 and 100 kHz) in the temperature range from room temperature up to 300 °C. The samples had a diameter of approximately 20 mm and were 2 mm thick.

Scratch tests: This type of damage analysis has been carried out by using a LISMMA-Paris Micro-Scratch Tester Device with a Vickers diamond indenter. Test conditions were set as 1.9 N normal load with the frequency of 10 Hz and the numbers of cycles were set at 25,000 and 50,000. Tangential and normal forces were controlled by software of LISMMA during the test their ratio was used to calculate the coefficient of friction. After the test, damaged zone were investigated by a 3D optical roughness meter to characterize the damage that occurred during the scratch test.

23.3 Results and Discussions

Microstructural evaluation: A typical analysis of the microstructure of the Al/Fe_3O_4 composite with 10 % Fe_3O_4 nanoparticles [1, 2] is given in Fig. 23.1a, b. In this composite iron oxide was doped with yttrium and SiO_2 before mixing it with the aluminum powder. This doping process was not used in our previous AMC designs. Due to the confidentiality agreement with our industrial partners, we cannot give more details about the composition.

Doping of iron oxide with certain elements at the first stage of alloying aluminum resulted in a more homogenous composite. It was observed that iron oxide was dispersed homogeneously and continuously in the aluminum matrix, mainly around the grain boundaries of aluminum. Also addition of zinc stearate during ball milling has prevented the joining and agglomeration phenomena and helped to improve the distribution of the alloying elements in the structure.

Multicycle Microindentation Test at Constant Load—Microindentation theory: Micro indentation techniques are advantageous as both hardness and local modulus of elasticity on small specimen can be determined simultaneously. This technique is widely used to characterize mechanical properties such as hardness, modulus of elasticity for various materials using Oliver–Pharr [10] equations.

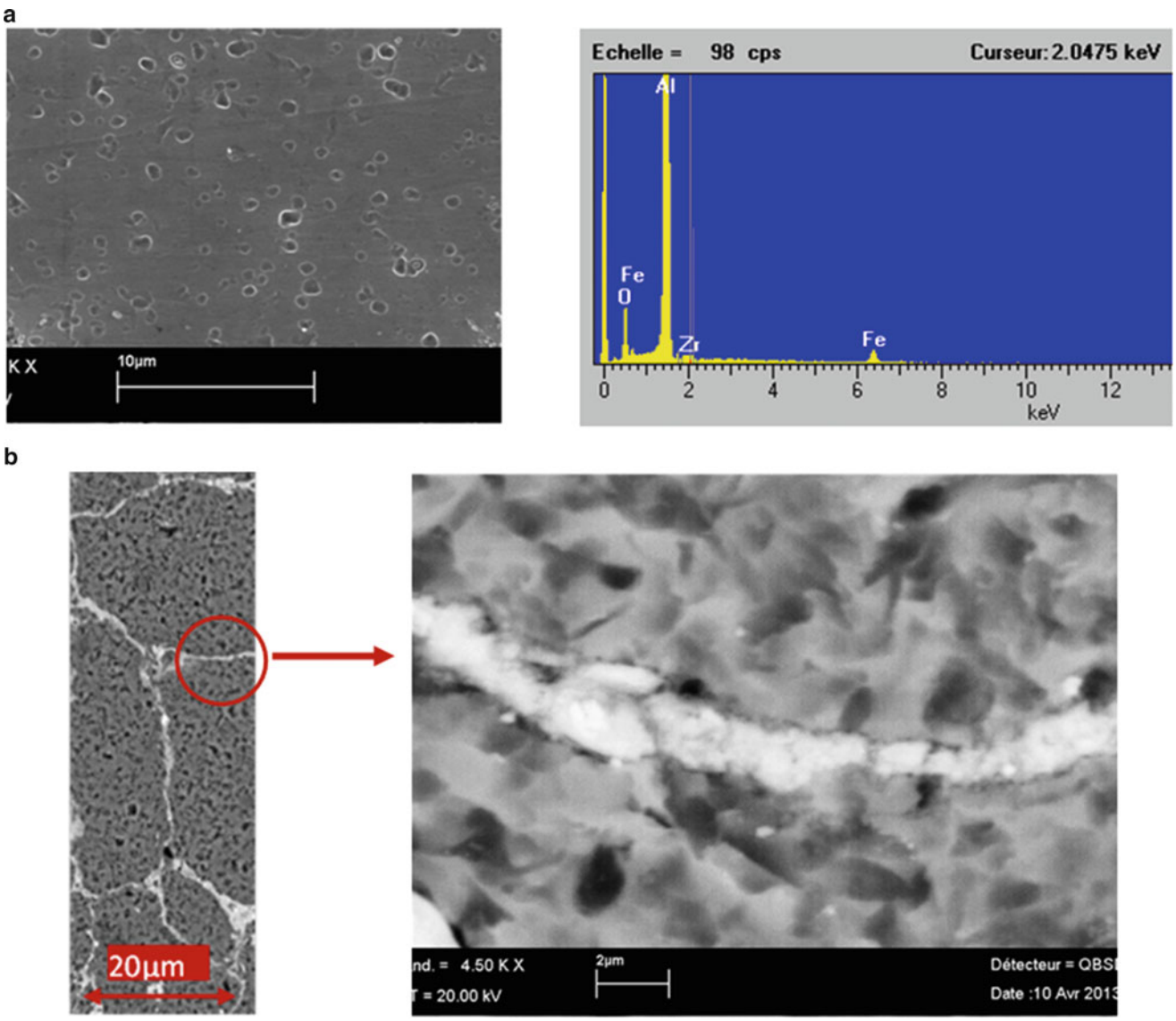

Fig. 23.1 (**a**) Distribution of Fe_3O_4 particles (10 %) on the Al-matrix and "EDS" analysis, AF8. (**b**) Arranging of Fe_3O_4 particles (10 %) on the aluminum matrix grain boundary, AF8

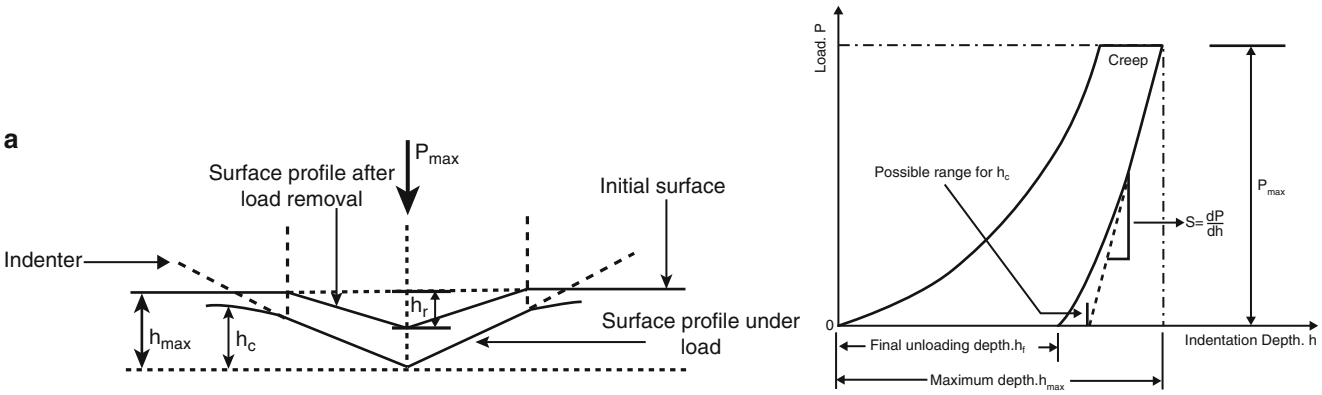

Fig. 23.2 Schematic graphs of (**a**) cross-section of an indentation and a typical load-penetration depth curve indicating key parameters needed for analysis [10]

The principal goal of microindentation testing is to extract modulus of elasticity and hardness of the specimen from the indenter load and depth of penetration data. In a typical test, force and depth of penetration are recorded as load is applied from zero to some maximum and then from the maximum force back to zero. The depth of penetration together with the known geometry of the indenter provides an indirect measure of the area of contact at full load, from which the mean contact pressure, and thus hardness, is estimated. When load is removed from the indenter, the material attempts to regain its original shape, but it is prevented from doing so because of plastic deformation. However, there is some degree of recovery due to the relaxation of elastic strains within the material. An analysis of the initial portion of this elastic unloading response gives an estimate of the elastic modulus of the indented material. A typical load-penetration depth diagram during a microindentation test is shown in Fig. 23.2.

Mechanical properties of materials in microscale are different from those of bulk materials. For this reason, we have chosen a special multicycle microindentation test at different constant loads. Figure 23.3 shows load (red curve) and depth (blue curve) profile as a function of time for the first 15 cycles at a constant load of 1500 mN for two samples. Indentation depth vs. time curve shows a strain hardening effect for both of the samples. In the same way, evolution of indentation hardness, modulus and stiffness depending on number of cycles justified these observations for all of the maximum loads (Figs. 23.4 and 23.5). In fact, there is considerable load effect on the evolution of these parameters. This gap between parameters is more remarkable in case of sample AF-8 for the three loads applied.

It is also shown that this composite exhibits not only variation in its elastic modulus but also in its hardness with number of cycles. **Dielectric properties**: The dielectric permittivity (ε) provides a measure of the ability of a material to be polarized in the presence of an applied electric field. The ratio of the dielectric permittivity of a material to that of a vacuum ($\varepsilon_o = 8.85 \times 10^{-12}$ F/m) is defined as the dielectric constant (k). Dielectric parameters of two samples were reported in Figs. 23.6, 23.7, 23.8, and 23.9. Permittivity, loss index and dissipation factor are characterized as a function of temperature in the range 20–300 °C and at three frequencies: 1, 10 and 100 kHz. Both of the samples have shown a higher permittivity and higher dielectric loss. An interfacial effect is visibly evident and glass transition temperature is unaffected (~90 to 100 °C) by the additional elements (amorphous filler effect of Fe_3O_4; this is important as parts of an aircraft can experience rather high and very low temperatures in service).

Damage analysis by means of scratch test and 3D optical roughness meter: Scratch tests results give a basic idea on the tribological behavior of the composite designed in the current research. Here, a simple software/LISMMA was used to control tangential and normal forces during the test. After the test, damaged zone was investigated by 3D optical roughness meter to measure damage depth with scratch, and average scratch roughness. In this study, various material parameters were determined during scratch test: normal and tangential forces on indenter, tangential stress on the surface and interfacial stresses. The high interfacial shear stress may be the main reason for damage of the matrix and reinforced filler interfaces. To simplify the evaluation, two test conditions 25,000 and 50,000 number of cycles were used. Fig. 23.10a, b indicate scratch damaged zone and characteristic parameters obtained by 3D optical roughness meter for both of numbers of cycles. Considerable difference was observed in case of damage-scratch depth values but SEM analyses carried out on the damage zone have shown no crack or other internal damage in both of the samples under our test conditions.

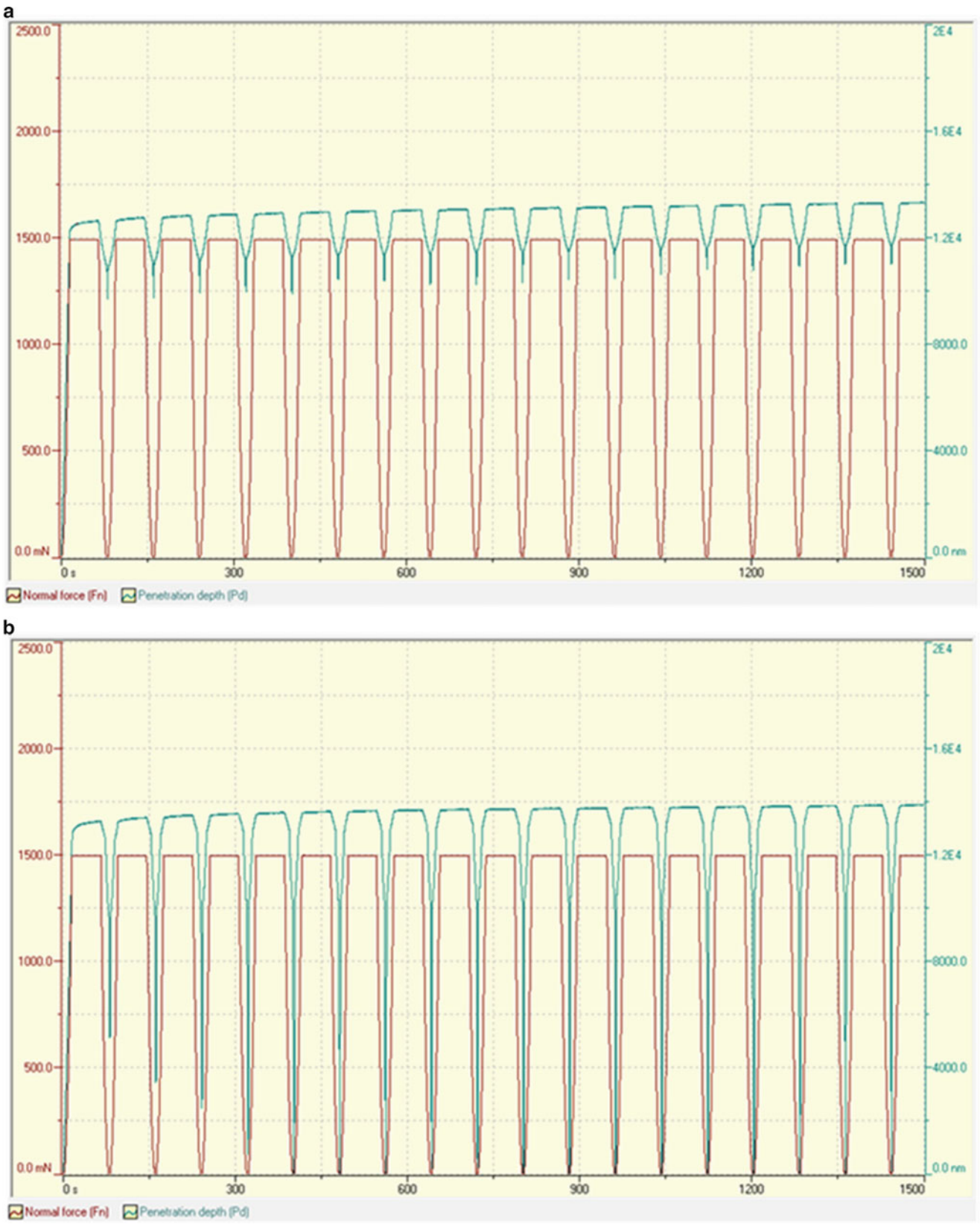

Fig. 23.3 Load (*red curve*) and depth (*blue curve*) profile as a function of time for first 15 cycles of multicycle microindentation at a constant load of 1,500 mN, (**a**) sample AF-5 and (**b**) sample AF-8

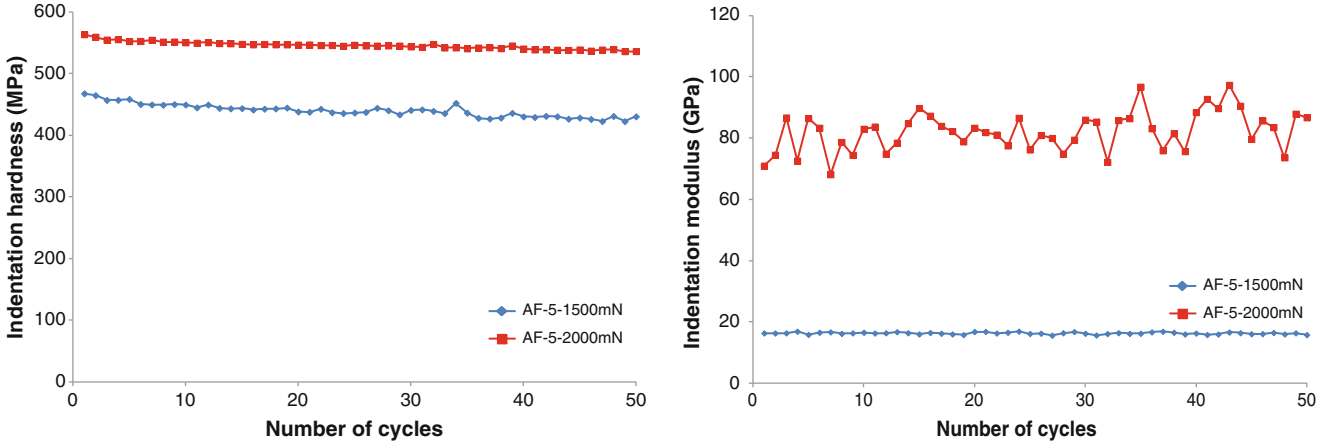

Fig. 23.4 Evolution of indentation hardness, modulus and stiffness as a function of number of cycles calculated from multicycle microindentation test at maximum loads of 1,500 and 2,000 mN, sample AF-5

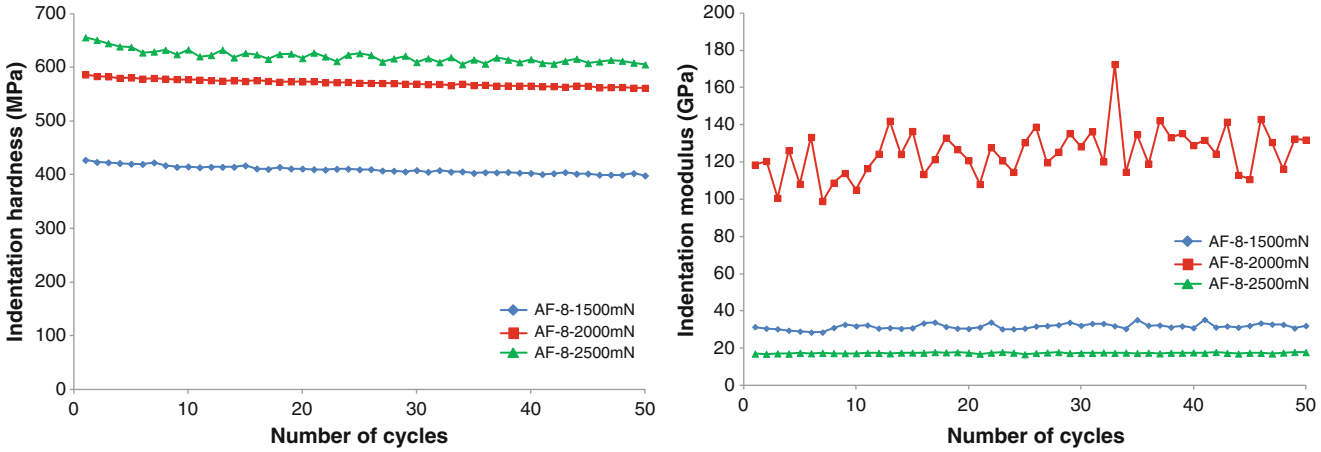

Fig. 23.5 Evolution of indentation hardness, modulus and stiffness as a function of number of cycles calculated from multicycle microindentation test at maximum loads of 1,500, 2,000 and 2,500 mN, sample AF-8

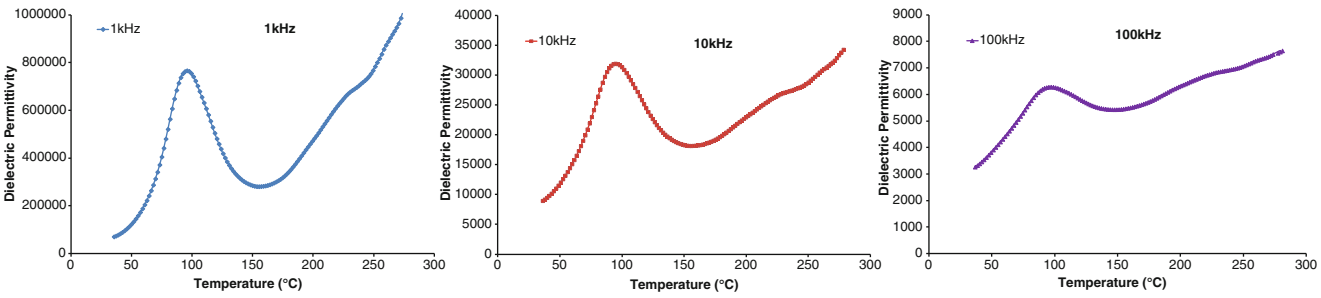

Fig. 23.6 Evolution of dielectric permittivity as a function of temperature for the sample AF-5

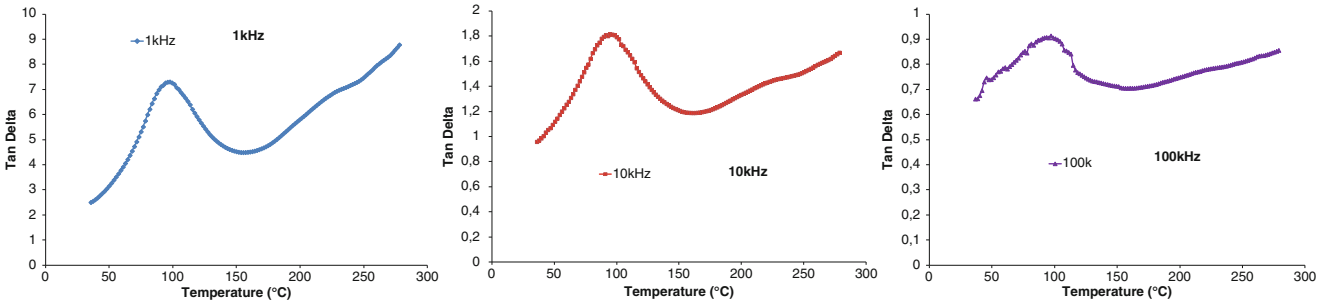

Fig. 23.7 Evolution of dielectric loss (tan delta) as a function of temperature for the sample AF-5

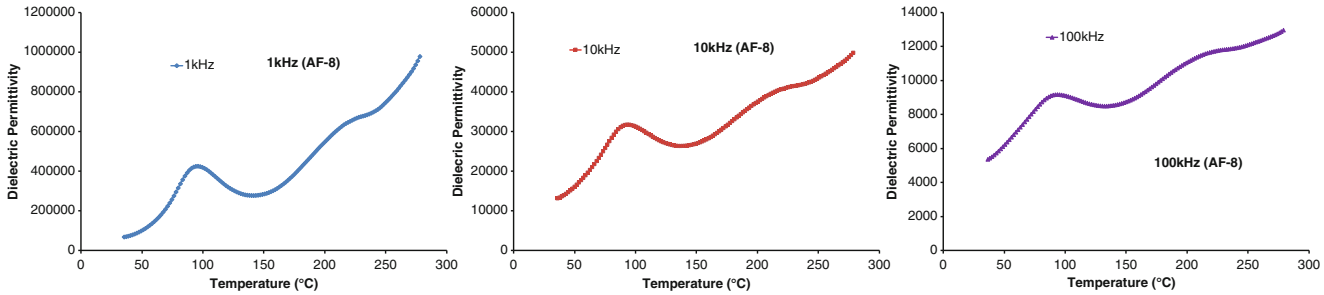

Fig. 23.8 Evolution of dielectric permittivity as a function of temperature for the sample AF-8

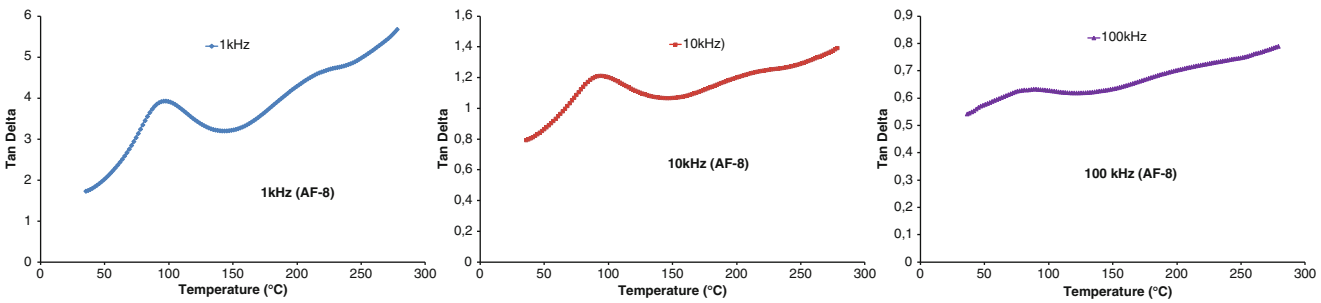

Fig. 23.9 Evolution of dielectric loss (tan delta) as a function of temperature for the sample AF-8

23.4 Conclusions

Multicycle microindentation damage analysis and tribological properties show that the newly designed Al based metal matrix composite reinforced with nano Fe_3O_4 particles is suitable aircraft applications. It was shown that this composite can be produced without difficulty by controlling the processing parameters very easily. However, a comprehensive study with modelling is needed when rigidity and toughness are important. This is an on-going project for French aeronautic company and final stage of this study will be completed after optimisation of electrical and magnetic properties.

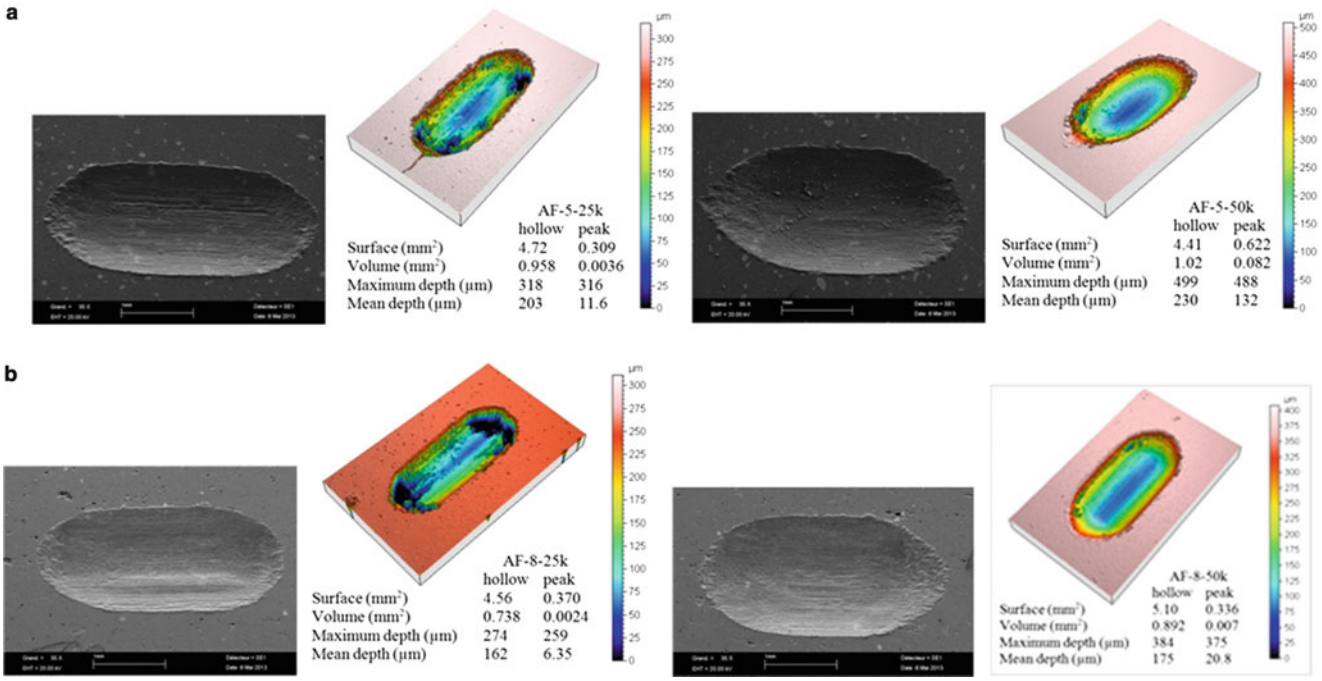

Fig. 23.10 (**a**) Damage traces achieved in the direction of width and length by scratch test after 25,000 (*left*) and 50,000 cycles (*right*) for the sample of AF-5. (**b**) Damage traces achieved in the direction of width and length by scratch test after 25,000 (*left*) and 50,000 cycles (*right*) for the sample of AF-8

References

1. Bayraktar E, Katundi D (2010) Development of a new aluminium matrix composite reinforced with iron oxide (Fe_3O_4). J Achiev Mater Manuf Eng 38(1):7–14
2. Katundi D, Ayari F, Bayraktar E, Tan M-J, Tosun Bayraktar A (2012) Design of aluminum matrix composites reinforced with nano iron oxide (Fe_3O_4). In: AMPT, 15th international conference on "advanced materials processing technologies", 23–26 Sept, Australia, vol 1, pp 1–12
3. Asif M, Chandra K, Misra PS (2011) Development of aluminum based hybrid metal matrix, composites for heavy duty applications. J Miner Mater Character Eng 10(14):1337–1344
4. Ibrahim IA, Mohamed FA, Lavernia EJ (1991) Particulate reinforced metal matrix composites—a review. J Mater Sci 26:1137–1156
5. Sinclair I, Gregson PJ (1997) Structural performance of discontinuous metal matrix composites. Mater Sci Technol 3:709–725
6. Katundi D, Ayari F, Bayraktar E, Tan M-J, Tosun Bayraktar A (2013) Manufacturing of aluminum matrix composites reinforced with iron-oxide (Fe3O4) nanoparticles: microstructural and mechanical properties. Metallur Mater Trans B 45(2):352–362. In: Laughlin DE (ed) ASM-TMS/USA. doi:10.1007/s11663-013-9970-1
7. Akhtar S, Sami Yilbas B, Bayraktar E (2013) Thermal stress distributions and microstructure in laser cutting of thin Al–Si alloy sheets (experimental and FEM). Int J LASER Appl (Am J) 25(4):1–12. In: Poprawe R (ed) Laser Institute of America. http://dx.doi.org/10.2351/1.4807081
8. Tolle LG, Craig RG (1978) Viscoelastic properties of elastomeric impression materials: polysulphide, silicone and polyether rubbers. J Oral Rehabil 5:121–128
9. Fang B, Wang G, Zhang W, Li M, Kan X (2005) Fabrication of Fe_3O_4 nano-particles modified electrode and its application for voltammetric sensing of dopamine. J Electroanal 17(9):744–748
10. Oliver WC, Pharr GM (1992) An improved technique for determining hardness and elastic modulus using load and displacement sensing indentation experiments. J Mater Res 7:1564–1583

Chapter 24
Particle Templated Graphene-Based Composites with Tailored Electro-mechanical Properties

Nicholas Heeder, Abayomi Yussuf, Indrani Chakraborty, Michael P. Godfrin, Robert Hurt, Anubhav Tripathi, Arijit Bose, and Arun Shukla

Abstract A capillary-driven particle level templating technique was utilized to disperse graphite nanoplatelets (GNPs) within a polystyrene matrix to form composites that possess tailored electro-mechanical properties. Utilizing capillary interactions, highly segregated composites were formed via a melt processing procedure. Since the graphene particles only resided at the boundary between the polymer matrix particles, the composites possess tremendous electrical conductivity but poor mechanical strength. To improve the mechanical properties of the composite, the graphene networks in the specimen were deformed by shear. An experimental investigation was conducted to understand the effect of graphene content as well as shearing on the mechanical strength and electrical conductivity of the composites. The experimental results show that both the mechanical and electrical properties of the composites can be altered using this very simple technique and therefore easily be tailored for desired applications.

Keywords Graphene • Polymer • Composites • Electrical properties • Mechanical properties

24.1 Introduction

Owing to its extraordinary mechanical and physical properties, graphene appears to be a very attractive filler material for the next generation of smart materials in devices such as batteries, supercapacitors, fuel cells, photovoltaic devices, sensing platforms and others [1, 2]. Along with the aspect ratio and the surface-to-volume ratio, the distribution of the filler in a polymer matrix has been shown to directly correlate with its effectiveness in improving material properties such as mechanical strength, electrical and thermal conductivity, and impermeability [3–8]. Although significant research has been performed to develop strategies to effectively incorporate nanoparticles into polymers, our ability to control the dispersion and location of graphene-based fillers to fully exploit their intrinsic properties remains a challenge [9–12].

One promising method to exploit certain properties of graphene is to create segregated composites, where the conductive particles are specially localized on the surfaces of the polymer matrix particles. When consolidated into a monolith, these conductive particles form a percolating three-dimensional network that dramatically increases the conductivity of the composite [13–18]. Sheets do not have to be distributed isotropically throughout a matrix to achieve percolation, overcoming a major limitation. These studies revealed that highly conductive composites can be created when graphene is segregated into organized networks throughout a matrix material. Although the highly segregated networks provide excellent transport properties throughout the composite, they inevitably result in poor mechanical strength, since fracture

N. Heeder • A. Yussuf • A. Shukla (✉)
Department of Mechanical, Industrial & Systems Engineering, Dynamic Photo Mechanics Laboratory, University of Rhode Island, Kingston, RI 02881, USA
e-mail: shuklaa@egr.uri.edu

I. Chakraborty • A. Bose
Department of Chemical Engineering, University of Rhode Island, Kingston, RI 02881, USA

M.P. Godfrin • A. Tripathi
School of Engineering, Center for Biomedical Engineering, Brown University, Providence, RI 02912, USA

R. Hurt
School of Engineering, Institute for Molecular and Nanoscale Innovation, Brown University, Providence, RI 02912, USA

G. Tandon (ed.), *Composite, Hybrid, and Multifunctional Materials, Volume 4: Proceedings of the 2014 Annual Conference on Experimental and Applied Mechanics*, Conference Proceedings of the Society for Experimental Mechanics Series,
DOI 10.1007/978-3-319-06992-0_24,

can occur easily in the continuous segregated graphene phase. Since most multi-functional materials are required to provide excellent transport properties while maintaining sufficient mechanical strength, alternative methods of distributing graphene need to be developed.

Despite recent progresses on the electrical characterization of graphene-based segregated composites, no results have been published yet regarding the combined electro-mechanical behavior of these highly conductive materials. In this work, a novel capillary-driven, particle-level templating technique was utilized to distribute graphite nanoplatelets into specially constructed architectures throughout a polystyrene (PS) matrix to form multi-functional composites with tailored electro-mechanical properties. By precisely controlling the temperature and pressure during a melt compression process, highly conductive composites were formed using very low loadings of graphene particles. To improve the mechanical properties, a new processing technique was developed that uses rotary shear during the compression molding process to gradually evolve the honeycomb graphene network into a concentric band structure. Two types of composites, organized and shear-modified, were produced to demonstrate the electro-mechanical tailoring of the composite material. An experimental investigation was conducted to understand the effect of graphene content as well as shearing on the mechanical strength and electrical conductivity of the composites.

24.2 Material and Specimen

24.2.1 Material

The graphite nanoplatelets used in this study were xGnP™ Nanoplatelets (XG Sciences, USA). These nanoparticles consist of short stacks of graphene layers having a lateral dimension of ~25 μm and a thickness of ~6 nm. The polymeric material chosen for this study was polystyrene (Crystal PS 1300, average molecular weight of 121,000 g/mol) purchased from Styrolution, USA. The PS pellets (~2 mm) used were elliptical prisms with a total surface area of 1.03 ± 0.01 cm^2.

24.2.2 Specimen

Two types of composites, organized and shear-modified, were produced to demonstrate the electro-mechanical tailoring of the composite material. A two-step process was utilized to produce the GNP/PS segregated composites [31]. For composites consisting of less than 0.2 v/v %, the desired amount of graphene platelets were measured and added directly to 7 g of dry PS pellets. The GNP spontaneously adheres to the dry polymer particles by physical forces, which may be van der Waals forces or electrostatic attraction associated with surface charges. This coating process works well for GNP loadings below 0.2 v/v %. However, at higher GNP loadings, this dry method leaves behind excess GNP because the charge on the pellets is neutralized after the initial coating.

To provide a means of temporarily attaching larger quantities of the GNP to the surface of the PS, an additional step is implemented during the fabrication procedure as shown in Fig. 24.1. For GNP loadings greater than 0.2 v/v %, the PS is first soaked in a methanol bath. The excess methanol is drained from the PS pellets. GNP is added, and the mixture is then shaken vigorously, creating a dense coating of graphene on each PS pellet. The methanol temporarily moistens the polymer pellets forming small liquid bridges. The capillary pressure created through these bridges allows the GNP to stick easily to the surface of the pellets. During the subsequent hot melt pressing, the temperature and mold pressure are precisely controlled allowing the pellets to be consolidated into a monolith while maintaining boundaries. In our experiments, a stainless steel mold consisting of a lower base and a plunger was heated to 125 ºC. The graphene coated PS was placed inside the cavity of the lower base and the plunger was placed on top. The temperature of both the plunger and the base mold was maintained for 20 min at which point it was hot-pressed at 45 kN using a hydraulic press. By precisely controlling the temperature and pressure during the melt compression process, highly conductive composites were formed using very low loadings of graphene particles.

Modified particle templated composites were fabricated by incorporating a shearing technique during the melt compression process. Following the same coating process as discussed earlier, the graphene coated pellets were placed inside a modified steel mold, which was equipped with guide pins to ensure that the base remained stationary. The plunger was then

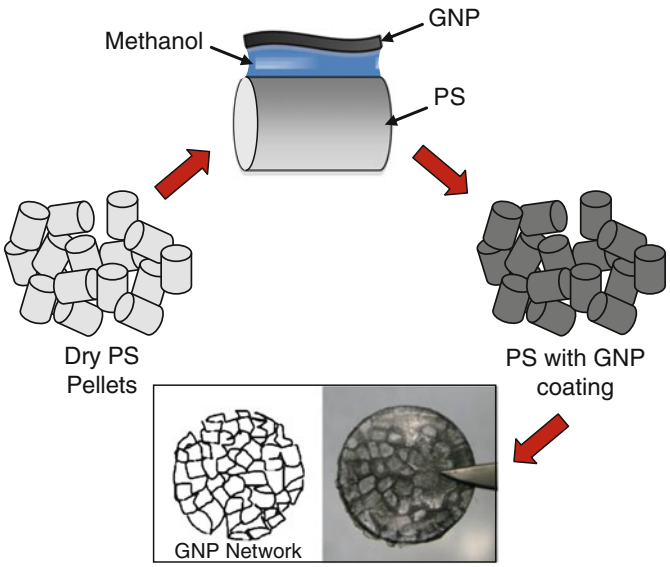

Fig. 24.1 Capillary-driven particle-level templating technique used to fabricate highly conductive GNP/PS composites

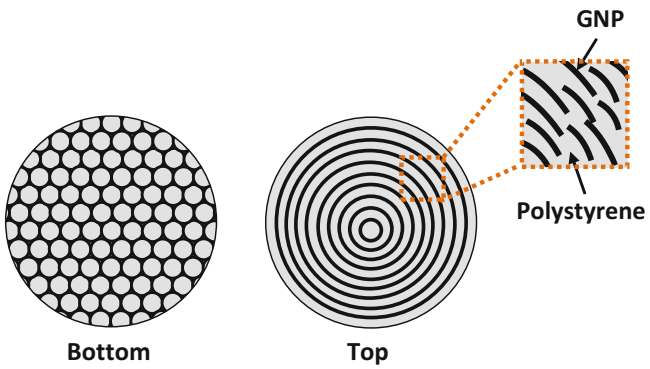

Fig. 24.2 Schematic of shear-modified particle templated

placed on top of the material and heated to 160 °C while the lower base mold was heated to 125 °C and maintained for 20 min. Next, 45 MPa was applied to the plunger and then rotated to various predetermined angles. All shear-modified composites were fabricated with 0.3 v/v % graphene platelets. By applying such a shear force to the top surface of the material, a gradient of graphene organization/orientation along the sample axis is formed which results in a composite possessing unique properties. A schematic of a shear-modified particle template composite is shown in Fig. 24.2.

24.3 Electrical Characterization

Electrical conductivity measurements were made on the GNP/PS composites using a volumetric two-point probe measurement technique. The bulk electrical conductivity was measured across the thickness of the sample (perpendicular to pressing). The resistance of the material was experimentally determined by supplying a constant current through the specimen while simultaneously measuring the voltage drop across the specimen. A constant current source was used to supply the DC current while two electrometers were used to measure the voltage drop. The difference between the two voltage readings was measured using a digital multimeter.

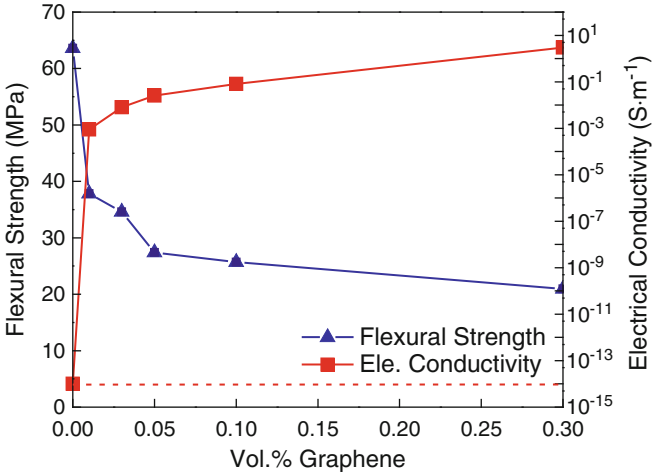

Fig. 24.3 Electro-mechanical behavior of GNP/PS organized particle templated composites loaded parallel to pressing

24.4 Mechanical Characterization

A screw-driven testing machine was implemented to load the specimens in a three point bending configuration. Specimens were cut into 5 mm × 6 mm × 38 mm rectangular prisms. A support span of 30 mm was used and the loading was applied at a rate of 0.1 mm/min.

24.5 Experimental Results and Discussion

Figure 24.3 shows the electrical conductivity as a function of graphene loading. A significant enhancement in electrical conductivity is demonstrated when 0.01 v/v % GNP was added to the PS. Since the boundaries located between the pellets are maintained, the graphene particles become interconnected throughout the material thus causing a significant increase in conductivity while using very low loadings of graphene. The capillary driven coating process enables more graphene to completely coat the surface of the PS which in turn increases the electrical conductivity of the composite approximately 4–5 orders of magnitude from 0.01 to 0.3 v/v %.

The effect of shear rotation on the electro-mechanical properties of the shear-modified GNP/PS composites was also investigated. By applying a shear force to the top surface of the highly segregated material, a gradient of graphene organization/orientation along the sample axis is formed which results in a 600 % increase in flexural strength while only sacrificing ~1–2 orders of magnitude of conductivity.

24.6 Conclusions

We demonstrate a simple, inexpensive and commercially viable technique that can be used to disperse conductive sheet-like particles, such as graphene, into a highly organized pattern within polymeric materials on either the micro- or macro-scale. Utilizing capillary interactions between polymeric particles and graphite nanoplatelets, liquid bridges on the surface of a polymeric material allows for coating of graphene onto the polymer surfaces. Following a melt compression process, highly conductive composites are formed using very low loadings of graphene particles. Since the graphene particles resided at the boundary between the polymer matrix particles, the composite exhibited poor mechanical strength. To improve the mechanical properties of the composite, a shear force was applied to the top surface of the material which created a gradient of graphene organization/orientation along the sample axis. Results showed that this novel fabrication technique can produce composite materials that possess both excellent transport properties and improved mechanical strength.

Acknowledgements The authors acknowledge the financial support provided by the Rhode Island Science & Technology Advisory Council as well as Research Experiences for Undergraduates National Science Foundation (CMMI 1233887).

References

1. Chakrabarti MH, Low CTJ, Brandon NP, Yufit V, Hashim MA, Irfan MF, Akhtar J, Ruiz-Trejo E, Hussain MA (2013) Progress in the electrochemical modification of graphene-based materials and their applications. Electrochim Acta 107:425–440
2. Huang X, Qi X, Boey F, Zhang H (2011) Graphene-based composites. Chem Soc Rev 41(2):666–686
3. Cardoso SM, Chalivendra VB, Shukla A, Yang S (2012) Damage detection of rubber toughened nanocomposites in the fracture process zone using carbon nanotubes. Eng Fract Mech 96:380–391
4. Heeder N, Shukla A, Chalivendra V, Yang S (2012) Sensitivity and dynamic electrical response of CNT-reinforced nanocomposites. J Mater Sci 47(8):3808–3816
5. Heeder NJ, Shukla A, Chalivendra V, Yang S, Park K (2012) Electrical response of carbon nanotube reinforced nanocomposites under static and dynamic loading. Exp Mech 52(3):315–322
6. Stankovich S, Dikin DA, Dommett GHB, Kohlhaas KM, Zimney EJ, Stach EA, Piner RD, Nguyen ST, Ruoff RS (2006) Graphene-based composite materials. Nature 442(7100):282–286
7. Vadlamani VK, Chalivendra V, Shukla A, Yang S (2012) In situ sensing of non-linear deformation and damage in epoxy particulate composites. Smart Mater Struct 21(7):075011
8. Vadlamani VK, Chalivendra VB, Shukla A, Yang S (2012) Sensing of damage in carbon nanotubes and carbon black-embedded epoxy under tensile loading. Polym Compos 33(10):1809–1815
9. Herrera-Alonso M, Abdala AA, McAllister MJ, Aksay IA, Prud'homme RK (2007) Intercalation and stitching of graphite oxide with diaminoalkanes. Langmuir 23(21):10644–10649
10. Paredes JI, Villar-Rodil S, Martínez-Alonso A, Tascón JMD (2008) Graphene oxide dispersions in organic solvents. Langmuir 24(19):10560–10564
11. Stankovich S, Dikin DA, Piner RD, Kohlhaas KA, Kleinhammes A, Jia Y, Wu Y, Nguyen ST, Ruoff RS (2007) Synthesis of graphene-based nanosheets via chemical reduction of exfoliated graphite oxide. Carbon 45(7):1558–1565
12. Stankovich S, Piner RD, Chen X, Wu N, Nguyen ST, Ruoff RS (2006) Stable aqueous dispersions of graphitic nanoplatelets via the reduction of exfoliated graphite oxide in the presence of poly(sodium 4-styrenesulfonate). J Mater Chem 16(2):155–158
13. Du J, Zhao L, Zeng Y, Zhang L, Li F, Liu P, Liu C (2011) Comparison of electrical properties between multi-walled carbon nanotube and graphene nanosheet/high density polyethylene composites with a segregated network structure. Carbon 49(4):1094–1100
14. Heeder N, Yussuf A, Guo F, Chakraborty I, Godfrin M, Hurt R, Tripathi A, Bose A, Shukla A (2013) Highly conductive graphene-based segregated composites prepared by particle templating. J Mater Sci 49(6):2567–2570
15. Hu H, Zhang G, Xiao L, Wang H, Zhang Q, Zhao Z (2012) Preparation and electrical conductivity of graphene/ultrahigh molecular weight polyethylene composites with a segregated structure. Carbon 50(12):4596–4599
16. Mamunya Y, Yellampalli DS (2011) Carbon nanotubes—polymer nanocomposites. InTech, Rijeka, pp 173–196
17. Pang H, Bao Y, Lei J, Tang J-H, Ji X, Zhang W-Q, Chen C (2012) Segregated conductive ultrahigh-molecular-weight polyethylene composites containing high-density polyethylene as carrier polymer of graphene nanosheets. Polym-Plast Technol Eng 51(14):1483–1486
18. Wang B, Li H, Li L, Chen P, Wang Z, Gu Q (2013) Electrostatic adsorption method for preparing electrically conducting ultrahigh molecular weight polyethylene/graphene nanosheets composites with a segregated network. Compos Sci Technol 89:180–185

Chapter 25
Novel Hybrid Fastening System with Nano-additive Reinforced Adhesive Inserts

Mahmoodul Haq, Anton Khomenko, and Gary L. Cloud

Abstract Structural joining of materials and components involves complex phenomena and interactions between several elements of either similar or dissimilar materials. This complex behavior, coupled with the need for lightweight structures and safety (human occupants in aerospace, automotive and ground vehicles), propels the need for better understanding and efficient design. A novel joining technique that incorporates the advantages of both bonded (lightweight) and bolted (easy disassembly) techniques was invented (Provisional Patent 61/658,163) by Dr. Gary Cloud at Michigan State University. The most basic configuration of this invention consists of a bolt that has a channel machined through the bolt-shaft that allows injection of an insert compound that fills the hole-clearance of the work-pieces and acts a structural component. The hole may contain additional sleeves or inserts. Several combinations of the proposed technique are possible, and in particular, the effect of the adhesive inserts, with and without nano-modification was studied in this work. Glass Fiber Reinforced Plastic (GFRP) composite plates were used as adherends with 12.5 mm holes, grade 8 bolts and preloaded to a torque of 35 N m. Pristine and Cloisite® 30B nanoclay reinforced SC-15 epoxy were used as adhesive inserts in the hybrid bolts. Tension lap-shear tests were performed on conventional (no-inserts) and hybrid bolted joints (inserts: adhesives + nanoclay), and their performance was compared. Results reveal that hybrid bolted joints can eliminate joint slip and considerably delay the onset of delamination. The addition of nanoclay increases the strengths but most importantly can prevent moisture from reaching the bolts shaft due to its excellent barrier properties. The proposed joining technique holds great promise for multi-material joining and a wide range of applications.

Keywords Novel joining technique • Hybrid bolted joint • Nano-modification • Cloisite® 30B nanoclay • SC-15 epoxy resin

25.1 Introduction

Lightweight and reliable dissimilar material joining is of special interest in automotive, aerospace, defense and marine industries. Conventional and well-established methods for dissimilar materials joining include friction stir welding (FSW), ultrasonic welding, arc welding, laser welding, plasma welding, explosive welding/bonding using chemical explosives, conventional brazing or soldering, rivets, bolts, and other conventional mechanical fasteners, and conventional adhesive joining [1]. However, each of those techniques has its own advantages and drawbacks.

FSW is widely used as its solid-state nature leads to number of advantages over fusion welding methods since porosity, solute redistribution, solidification cracking and liquation cracking do not arise during FSW [2]. Ultrasonic welding is well-established technique for joining both hard and soft plastics, such as semi-crystalline plastics, and metals [3]. But, it cannot allow joining for thick materials, making it difficult to join metals. Arc welding technique is not complicated and very well established, therefore it remains an important process for the fabrication of steel structures and vehicles [4, 5]. However, metallic corrosion in the weld area is a big concern. Other types of welding such as laser welding [5], plasma welding [6], explosive welding/bonding using chemical explosives [7], conventional brazing or soldering [8] all share the most common limitations of inability to join metals to FRP composites.

M. Haq (✉) • A. Khomenko • G.L. Cloud
Composite Vehicle Research Center, Michigan State University, 2727 Alliance Drive, Lansing, MI 48910, USA
e-mail: haqmahmo@egr.msu.edu

G. Tandon (ed.), *Composite, Hybrid, and Multifunctional Materials, Volume 4: Proceedings of the 2014 Annual Conference on Experimental and Applied Mechanics*, Conference Proceedings of the Society for Experimental Mechanics Series,
DOI 10.1007/978-3-319-06992-0_25,

Mechanical joining is one of the oldest, most important, and most neglected aspects of engineering design of machines and structures of all types and sizes. Such fasteners offer the advantage of being able to be removed without destroying the structure and they are not sensitive to surface preparation, service temperature, or humidity. On the other hand, bolts increase the weight of the resulting joint and create potential sources of stress concentration within the joint [9]. Moreover, the drilling of holes in laminated composites creates the serious problem of delamination in the joint, plus the clearance of the hole and the bolt can lead to bolt-adherend slip which is a serious concern in load re-distribution and stability of resulting components.

Adhesively bonded joints are gaining popularity in place of conventional fasteners as they provide light weight designs, reduce stress concentrations, enable joining of dissimilar materials, and are often cheaper than conventional fasteners. Bonded joints provide larger contact area than bolted joints thereby providing efficient stress distribution enabling higher efficiency and improved fatigue life [10]. Nevertheless, the quality of adhesively bonded joints depends on various factors including manufacturing techniques, manufacturing defects, physical damage and deterioration due to accidental impacts, moisture absorption, improper handling, etc. These factors can significantly affect the strength of resulting bonded joints and a successful monitoring technique that can provide information about the adhesive layer and its resulting joint is essential. Moreover, the resulting joint cannot be disassembled or reassembled anymore.

The joining technique presented in this work aims at overcoming the limitations of conventional joining techniques and incorporates the advantages of both bonded (lightweight) and bolted (easy disassembly) techniques. This novel technique was invented (Provisional Patent 61/658,163) by Dr. Gary Cloud at Michigan State University, and the first concept of the hybrid bolted joining was proposed in [9]. This system is particularly effective for applications in automotive, marine, air, and ground vehicles that are subject to severe service environments. As mentioned earlier, this technique has the advantages of both the adhesive and mechanical joining techniques, such as easy installation, repair and replacement, minimization of stress-concentration around holes, prevention of delamination in composites, and reduction of overall weight. Additionally, the use of structural inserts, specifically bonded inserts, allows filling of any delaminations or defects, reduces stress concentrations, creates compliance between adherends and introduces the advantages of adhesive bonding into the system. Most importantly, this technique can incorporate dissimilar material adherends efficiently. The tailorable nature of this technique allows selection of sleeve/insert that will create maximum compatibility among the dissimilar adherends and eliminate premature failures. Furthermore, the structural insert/sleeve can be tailored to modify the performance of resulting joints. Such joints need not be considered a weakness anymore, but rather a strength to control the overall structural behavior.

In this work, the effect of nano-modification of adhesive insert on the hybrid bolted joint behavior was studied. Tension lap-shear tests were performed on conventional (no-inserts) and hybrid bolted joints (inserts: pristine adhesive, and nanoclay reinforced adhesive), and their performance was compared. Results reveal that hybrid bolted joints eliminate joint slip and considerably delay the onset of delamination. The addition of nanoclay increases the strengths, but most importantly can prevent moisture from reaching the bolt shaft due to its excellent barrier properties. The proposed joining technique holds great promise for multi-material joining and a wide range of applications.

25.2 Hybrid Bolted Joining Technique and Sample Preparation

The most basic configuration of this invention (see Fig. 25.1) consists of a bolt that has a channel machined through the bolt-shaft that allows injection of an insert compound that fills the hole-clearance of the work-pieces and acts a structural component. The hole may contain additional sleeves or inserts.

In this work, the vacuum assisted resin transfer molding (VARTM) technique was used to manufacture the composite adherends for the lap joints. The reinforcement used for the adherend was S2-glass plain weave fabric (Owens Corning ShieldStrand S) with areal weight of 818 g/m^2. The resin used was a two part toughened epoxy, namely SC-15 (Applied Poleramics Inc., CA). Cloisite® 30B (Southern Clay Products, Inc., TX) with 2.5 wt% concentration was used as nano-reinforcement of the resin. The adherend had 16-layers of plain weave fabric with a resulting thickness of ~10 mm.

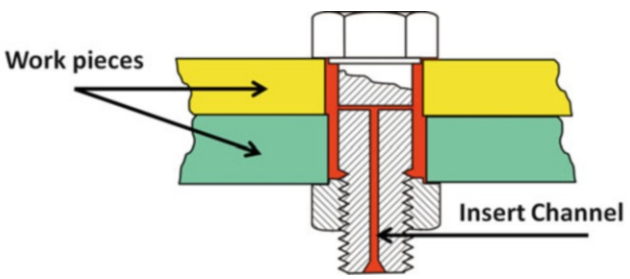

Fig. 25.1 Basic configuration of proposed hybrid bolted joining system

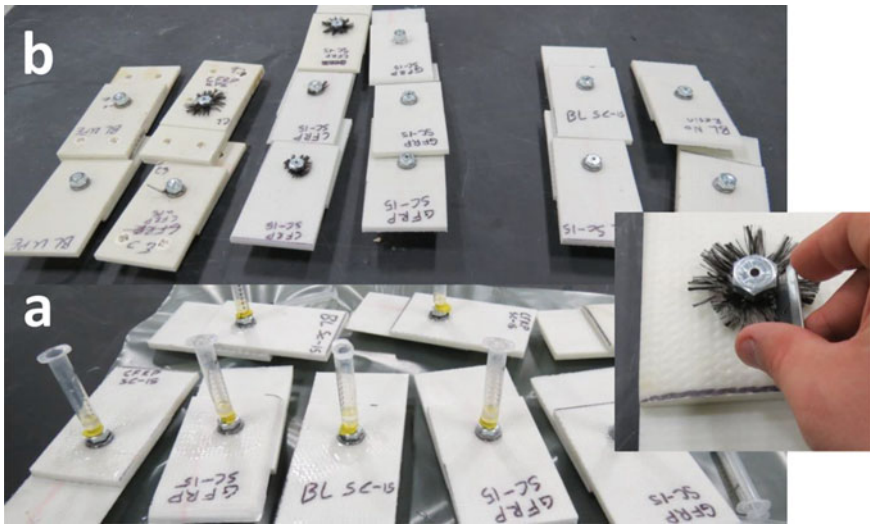

Fig. 25.2 (**a**) Manufacturing of hybrid bolted joints, (**b**) manufactured hybrid bolted joints

The adherend/plates were joined using ordinary grade 8 nominal 1/2 in. bolts and matching flat washers. Conventional bolted joints had no insert, and the bolts were not drilled. Bolts with drilled 2 mm diameter passageways for resin injection were used for the remaining specimens. All the bolts were torqued to 35 N m.

The nano-modification of SC-15 epoxy involved homogeneous mixing, and exfoliation of nanoclay in the resin. Initially, part A of SC-15 epoxy was mixed with the desired nanoclay content (2.5 wt%) and the resulting compound was sonicated using Vibra-Cell™ sonicator for around 30 min until the total applied energy was 30 kJ. Intermittent sonication energy (10 s energy: 5 s pause) was applied to control the rise in temperature of compound. Once 30 kJ was applied, the resulting mixture was cooled at room temperature for 10 min, followed by mixing of part B of SC-15 epoxy. The solution was mixed thoroughly, degassed and was made available for injection in the hybrid joining system. Once the adherends were joined with the applied torque level (35 N m), the pristine/n-modified resin was injected through the bolt, and the joint was cured in a convection oven at 60 °C for 2 h followed by post curing at 94 °C for 4 h.

Figure 25.2a, b illustrate the manufacturing process and resulting hybrid bolted joints respectively.

25.3 Experimental Results and Discussion

Three case studies were performed in this work, namely: (a) the conventional joint (control specimen), (b) the hybrid joint-pristine adhesive, and (c) the hybrid joint-nanoclay reinforced adhesive. The resulting lap-joints were tested in tensile-shear configuration until failure in displacement control at a rate of 1 mm/min. The displacement and applied load from MTS were recorded. Additionally, an external laser extensometer (LE-05 Epsilontech Laser Extensometer) was used to obtain precise relative displacements between the adherends.

25.3.1 Hybrid Bolted Joint with SC-15 Insert

In the first set of experiments, the performance of hybrid bolted joints with just SC-15 adhesive insert (no nano-modification) was compared to conventional bolted joints with no insert (see Fig. 25.3).

A few critical observations are highlighted in the plot in Fig. 25.3 to efficiently compare their performance. First, the graph for the conventional bolted joint shows a significant slip around 7 kN, where the applied tensile-shear load is sufficient to overcome the clamping forces (see Fig. 25.3, feature 1). At ~20 kN load, onset of delamination occurs in the vicinity of the point of contacts of the bolts with the adherend (see Fig. 25.3, feature 2). As the applied load increases, the delamination continues (see Fig. 25.3, feature 3), the washer deforms, and the bolt bends up to a maximum load of about 46 kN (see Fig. 25.3, feature 4). The delamination continues but the load carrying capacity considerably reduces after the peak load. Depending upon the desired application, the initial slip or reduction in load carrying capacity after peak load can be

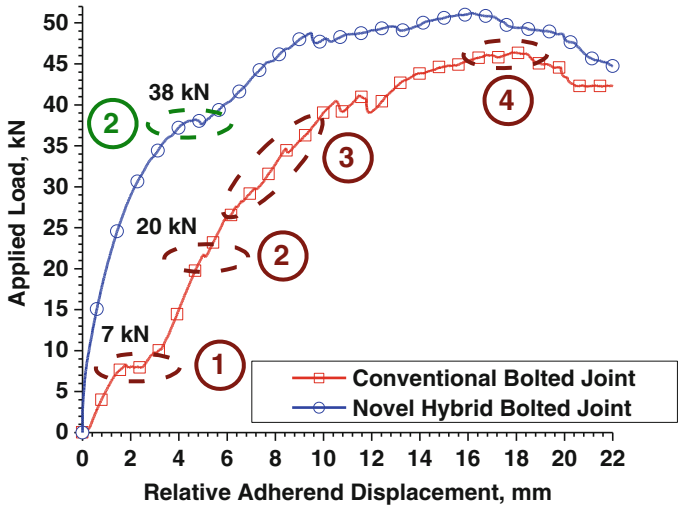

Fig. 25.3 Comparison of conventional bolted joint with novel hybrid bolted joint and some salient features: 1—joint slip, 2—onset of delamination, 3—growth of delamination, 4—maximum load capacity

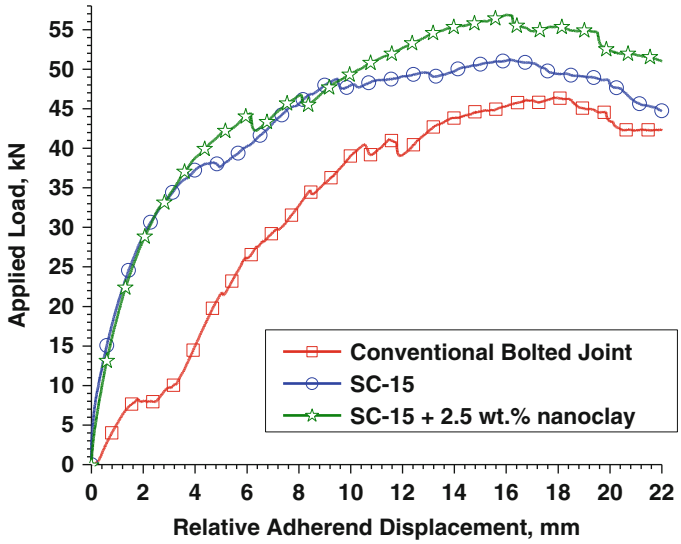

Fig. 25.4 Comparison of hybrid bolted joints containing nano-clay reinforced adhesive insert with hybrid bolted joint containing pristine adhesive and conventional bolted joint

considered as ultimate/failure loads for design purposes. Now, let's examine the response for the joint having pristine adhesive insert. Firstly, this joint does not exhibit any slip, and shows an increased stiffness up to 38 kN where the onset of delamination occurs. After the onset of delamination, the stiffness reduces, but the load-carrying capacity continues to increase up to 49 kN. Beyond this, similar to conventional joints, the delamination continues without any resistance to applied load until total joint destruction. Comparison of these data suggests that joint performance is enhanced although a simple, relatively "soft" adhesive insert is used. The degree of improvement can be further increased/tailored by using the appropriate structural adhesives. Furthermore, if slip is critical, then the joint with the adhesive can be considered infinitely better than the conventional one. If failure is defined as the onset of delamination, then the joint with the adhesive insert is ~90 % better. Similarly, if joint stiffness is the criterion, then the joints with adhesive insert perform better. Most importantly, the adhesive can be selected to tailor the performance of the joint and the resulting structures.

25.3.2 Hybrid Bolted Joint with Cloisite® 30B Modified SC-15 Insert

In the second set of experiments, the performance of hybrid bolted joints containing nanoclay reinforced adhesive insert was compared with both conventional and hybrid bolted joints containing pristine adhesive (see Fig. 25.4). The comparison of nanoclay reinforced adhesive insert and conventional bolted joint is analogous to that described for pristine adhesive insert

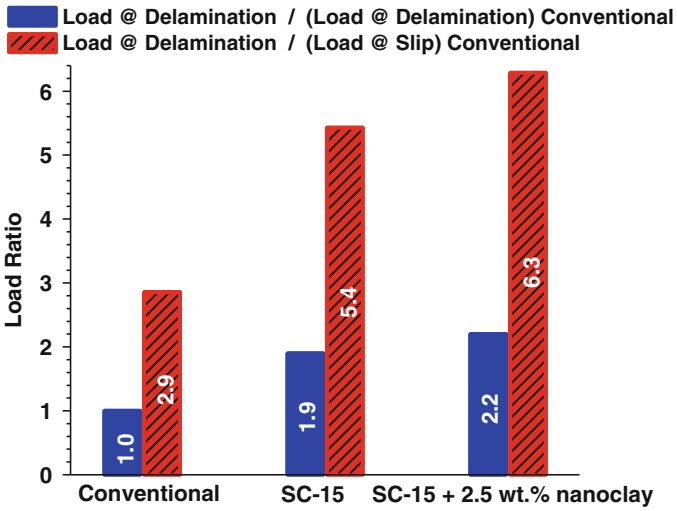

Fig. 25.5 Comparison of delamination and slip loads for novel hybrid joints relative to conventional bolted joint

joint (see previous section, Fig. 25.3). Nevertheless, the comparison of hybrid joints with pristine and nanoclay reinforced adhesive inserts reveals delay in onset of delamination. This can be attributed to the increase in toughness of the adhesive due to nanoclay reinforcement. Additionally, nanoclay reinforcements introduce tortuosity and crack-bridging properties that can further reduce brittleness and increase toughness.

As mentioned earlier, depending on applications, either the onset of slip or the onset of delamination can be considered as the failure load for design purposes. Hence comparisons of the hybrid joints in this study with the onset of slip and onset of delamination in conventional joint are shown in Fig. 25.5. If the onset of slip is considered, the hybrid bolted joints perform ~5 to 6 times better than conventional joint. If the onset of delamination is considered, the hybrid bolted joints with adhesive inserts perform ~2 times better. The effects of nanoclay are quite prominent considering the small addition of nanoclay (in this case 2.5 wt%) with increase in both the ultimate load carrying capacity and the load at onset of delamination in bolted joints relative to their counterpart with just pristine adhesive. Furthermore, nanoclay has excellent barrier properties and can considerably reduce moisture diffusion into the joint/bolt-shaft.

Overall, hybrid bolted joints can eliminate joint slip and considerably delay the onset of delamination. In this work, the effect of just adhesive inserts and nanoclay incorporation was explored. Considerable work that includes varying concentrations, different nano-reinforcements, structural adhesives and fiber-reinforced sleeves needs to be performed to fully exploit the benefit offered by this robust joint. Nevertheless, the results shown in this work show great promise for use of these novel hybrid joints for a wide range of multi-material joining applications.

25.4 Conclusions

A novel hybrid joining technique that incorporates the advantages of both bonded (lightweight, elimination of stress concentrations due to holes) and bolted (easy disassembly) techniques was studied. The most basic configuration of this invention consists of a bolt that has a channel machined through the bolt-shaft that allows injection of an insert compound that fills the hole-clearance of the work-pieces and acts a structural component. The effect of an adhesive structural insert was experimentally studied and compared to a conventional bolted joint. Furthermore, both pristine and nanoclay reinforced (2.5 wt%) adhesives were studied. Single lap-joints consisting of S-glass/SC-15 epoxy adherends and joined using ordinary grade 8 nominal 1/2 in. bolts and matching flat washers were manufactured and tested under tensile-shear configuration. Results revealed that the novel hybrid joints did not exhibit any joint-slip and had considerably higher load carrying capacities prior to onset of delamination, relative to conventional joints. If the onset of slip is considered, the hybrid bolted joints perform ~5 to 6 times better than conventional joint. If the onset of delamination is considered, the hybrid bolted joints with adhesive inserts perform ~2 times better. The effects of nanoclay are quite prominent considering the small addition of nanoclay (in this case 2.5 wt%) with increase in both the ultimate load carrying capacity and the load at onset of delamination relative to joints with just pristine adhesive. Furthermore, nanoclay has excellent barrier properties and can considerably reduce moisture diffusion into the joint/bolt-shaft. Considerable work that includes varying concentrations,

different nano-reinforcements, structural adhesives and fiber-reinforced sleeves needs to be performed to fully exploit the benefit offered by this robust joint. Nevertheless, the results shown in this work show great promise for use of these novel hybrid joints for a wide range of multi-material joining applications.

Acknowledgements This work was supported by US Army under TACOM/MSU Cooperative Agreement No. W56HZV-07-2-0007. The authors also acknowledge the in-kind material contribution by Southern Clay Products Inc., TX.

References

1. Jenney CL, O'Brien A (eds) (2001) Welding handbook: welding science and technology, 9th edn. American Welding Society, Doral
2. Sidhu M, Chatha S (2012) Friction stir welding—process and its variables: a review. Int J Emerg Technol Adv Eng 2(12):275–279
3. Matsuoka S, Imai H (2009) Direct welding of different metals used ultrasonic vibration. J Mater Process Technol 209(2):954–960
4. Fahimpour V, Sadrnezhaad S, Karimzadeh F (2012) Corrosion behavior of aluminum 6061 alloy joined by friction stir welding and gas tungsten arc welding methods. Mater Des 39:329–333
5. Yunlian Q, Ju D, Quan H, Liying Z (2000) Electron beam welding, laser beam welding and gas tungsten arc welding of titanium sheet. Mater Sci Eng A 280(1):177–181
6. Tan H, Wang Z, Jiang Y, Han D, Hong J, Chen L, Jiang L, Li J (2011) Annealing temperature effect on the pitting corrosion resistance of plasma arc welded joints of duplex stainless steel UNS S32304 in 1.0M NaCl. Corros Sci 53(6):2191–2200
7. Findik F (2011) Recent developments in explosive welding. Mater Des 32(3):1081–1093
8. Lin S, Song J, Yang C, Fan C, Zhang D (2010) Brazability of dissimilar metals tungsten inert gas butt welding–brazing between aluminum alloy and stainless steel with Al Cu filler metal. Mater Des 31(5):2637–2642
9. Cloud GL (2013) 2012 William M. Murray lecture: some curious unresolved problems, speculations, and advances in mechanical fastening. Exp Mech 53(7):1073–1104
10. Lin W-H, Jen M-HR (1999) The strength of bolted and bonded single-lapped composite joints in tension. J Compos Mater 33(7):640–666